

# **Characterization of Tearing Resistance of Automotive Grade Steel Sheets**

**Sayan Kalyan Chandra**

**Department of Physics**

**A thesis submitted for the degree of  
Doctor of Philosophy (Science)**

**Faculty Council of Science**

**Jadavpur University**

**Kolkata, India**

**2021**

## Certificate from the supervisors

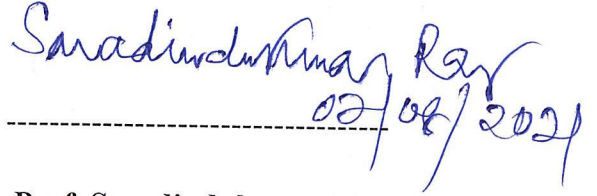
This is to certify that the thesis entitled “**Characterization of Tearing Resistance of Automotive Grade Steel Sheets**” submitted by Shri **Sayan Kalyan Chandra**, who got his name registered on **14<sup>th</sup> June, 2013** for the award of Ph.D. (Science) degree of Jadavpur University, is absolutely based upon his own work under the supervision of Prof. Pravash Chandra Chakraborti and Prof. Saradindukumar Ray and that neither this thesis nor any part of it has been submitted for either any degree/diploma or any other academic award anywhere before.

  
02/08/2021

Prof. Pravash Chandra Chakraborti  
Metallurgical and Material Engg. Dept.  
Jadavpur University  
Kolkata - 700032

-----  
**Prof. Pravash Chandra Chakraborti**

Supervisor  
Professor  
Metallurgical and Material Engineering  
Department  
Jadavpur University  
Kolkata – 700 032  
e-mail: pc.chakraborti@jadavpuruniversity.in

  
02/08/2021

-----  
**Prof. Saradindukumar Ray**

Supervisor  
Former Ministry of Steel Chair Professor  
Metallurgical and Material Engineering  
Department  
Jadavpur University  
Kolkata – 700 032  
e-mail: saradindu.ray@gmail.com

# JADAVPUR UNIVERSITY KOLKATA – 700 032, INDIA

REGISTRATION NO.D-7/SC/869/14

INDEX NO. 155/14/Phys./23

**1. Title of the thesis:** Characterization of Tearing Resistance of Automotive Grade Steel Sheets

**2. Name, Designation & Institution of the supervisors:**

- 1. Prof. Pravash Chandra Chakraborti**  
Professor,  
Metallurgical and Material Engineering Department  
Jadavpur University, Kolkata 700 032
- 2. Prof. Saradindukumar Ray**  
Former Ministry of Steel Chair Professor  
Metallurgical & Material Engineering Department  
Jadavpur University, Kolkata-700032

**3. List of Publications:**

- 1) S.K. Chandra, R. Sarkar, A.D. Bhowmick, P.S. De, P.C. Chakraborti, and S.K. Ray, "Fracture toughness evaluation of interstitial free steel sheet using Essential Work of Fracture (EWF) method," *Engineering Fracture Mechanics*, vol. 204, pp. 29-45, 2018.**
- 2) S.K. Chandra, R. Sarkar., A.D. Bhowmick, P.S. De, P.C. Chakraborti, and S.K. Ray, "Crack tip opening angle (CTOA) and  $\delta_5$  measurements on SENT and DENT specimens of a thin interstitial-free steel sheet," *Engineering Fracture Mechanics*, vol. 225,106861, 2020..**
- 3) S.K. Chandra, R. Sarkar, A.D. Bhowmick, P.S. De, P.C. Chakraborti, and S.K. Ray, "Evaluation of ductile tearing resistance of an interstitial free steel sheet using SENT specimens," *Engineering Fracture Mechanics*, vol. 238,107257 , 2020.**
- 4) S.K. Chandra, R. Sarkar, Sukalpa Choudhury, Mrinmoy Jana, P.S. De, P.C. Chakraborti, and S.K. Ray, "Determination of  $\eta_p$  factor for clamped SENT thin sheet specimens of an Interstitial Free Steel" *International Journal of Fracture*, vol. 227, pp. 137-152, 2021.**

5) **S.K. Chandra**, R. Sarkar, M.K. Patel, J.K. Mahato, P.S. De, P. C. Chakraborti, and S. K. Ray, “Characterization of Ductile Crack Growth Resistance Behaviour of Interstitial-Free Steel Sheet using Energy Dissipation Rate Parameter” **Theoretical and Applied Fracture Mechanics**, vol. 114,102994 , 2021.

6) Riddhi Sarkar, **Sayan Kalyan Chandra**, Partha Sarathi De, P.C. Chakraborti, and S.K. Ray, “Evaluation of ductile tearing resistance of dual-phase DP 780 grade automotive steel sheet from Essential Work of Fracture (EWF) tests,” **Theoretical and Applied Fracture Mechanics**, p. 102278, 2019.

4. **List of patents:** Nil

5. **List of Presentations in  
National/international conference:** Nil

# Declaration

I certify that

1. The work contained in this thesis is original and has been done by me under the guidance of my supervisors.
2. The work has not been submitted to any other Institute/University for any degree or diploma.
3. I have followed the guidelines provided by the University in preparing the thesis.
4. I have conformed to the norms and guidelines given in the Ethical Code of Conduct of the University.
5. Whenever I have used materials (data, theoretical analysis, figures, tables and text) from other sources, I have given due credit to them by citing them in the text of the thesis and giving their details in the references. Further, I have taken permission from the copyright owners of the sources, whenever necessary.

**Sayan Kalyan Chandra**

2021 / Kolkata



# Acknowledgements

Firstly, I would like to express my sincere gratitude to my supervisors, **Dr. Pravash Chandra Chakraborti**, Professor, Metallurgical and Material Engineering Department, Jadavpur University and **Dr. Saradindukumar Ray**, Former Ministry of Steel Chair Professor, in the same department, for their valuable guidance during the course of my research work. I have been motivated in doing research in the area embodied in the present thesis by their inspiration and encouragement. Without their valuable advice, discussion including timely criticism and guidance it would have been impossible to complete the research goals. Their valuable guidance and comments helped me a lot during experimental work, critically think over experimental results, drafting research papers and finally this thesis. I also learned from my supervisors lot beyond the immediate scope of the present research work, which helped me considerably in professionally maturing. I am fortunate enough to enjoy complete and free access to all experimental and computational facilities during the course of my research. This opportunity has instilled in me lots of confidence in carrying out experimental research independently.

I am very much grateful to my friends, seniors and juniors, without whom this journey would not have been complete. I sincerely thank **Dr. Partha Sarathi De** who helped me a lot with his technical expertise during the entire work. Besides, all the help and support rendered by Jayanta kumar Mahato, Riddhi Sarkar, Abhishek De Bhowmik, Subhajit Mukherjee, Manish Kumar Patel, Rahul Kumar, Ujjwal Bera and other past and present scholars/students are gratefully acknowledged. I would also like to express my gratitude to the teaching and non-teaching staff of Metallurgical and Material Engineering Department, Jadavpur University for their cooperation, whenever needed. I also thank Centre of Excellence in Phase Transformation and product Characterisation for providing research contingency. Finally, I sincerely thank Dr. Mahadev Shome of TATA Steel, Jamshedpur, India for providing the required steel sheet which has been used in the present research.

**Sayan kalyan Chandra**  
2021 / Kolkata





# Abstract

INDEX NO. 155/14/Phys./23

**Title of the thesis:** Characterization of Tearing Resistance of Automotive Grade Steel Sheets

**Submitted by:** Sayan kalyan Chandra

The present study aims at a comprehensive characterization of tearing resistance of a 1 mm thick automotive grade interstitial free (IF) steel sheet, a material with a very high strain hardening exponent. The tests comprise of deforming at chosen quasi-static strain rate notched (tip radius 0.1 mm) or fatigue pre-cracked double edge notched tensile (DENT) or single edge notched tensile (SENT) specimens clamped on both edges.

In this study, the crack initiation parameters examined are the initiation energy per unit ligament area ( $w_i$ ), in addition to the critical values for the  $J$ -integral and CTOD (respectively  $J_c$  and  $\delta_c$ ). For determining the initiation parameters, it is first necessary to identify the crack initiation event with sufficient accuracy, a non-trivial problem for a ductile thin sheet with large plasticity, crack tip necking and tunneling. In the present study a new method based upon comparing test data with those from 3-D finite element analysis (FEA) for non-growing crack has been adopted for detecting the crack initiation event. Notwithstanding the extensive plasticity and the related effects, the use of  $J_c$  has been validated for the SENT specimens of the present test material from the 3-D FEA computed path independent line integral values of  $J$ , in addition to determining the  $\eta_p$  factor for these specimens. The crack growth parameters examined are the CTOA ( $\varphi$ ) and its critical value for stable crack growth ( $\varphi_c$ ), the  $\delta_5$  parameter, and also the energy dissipation rate parameter ( $R$ ) and its value for stable crack growth ( $R_\infty$ ). The  $R$  parameter has hitherto been used almost exclusively for thick specimens. An attempt has been made to search for normalized energy dissipation rate ( $R_N$ ) to be determined from  $R_\infty$  such that  $R_N$  would be independent of specimen geometry. Of these parameters, only CTOA determination has been standardized for sheet metals (ASTM E 2472); however, the testing and measurement procedures prescribed by this standard require both experimental resources and skill, and are as such not very attractive for routine industrial applications. Optical measurements of CTOA and  $\delta_5$  for SENT and DENT specimens reported here adopted an experimental procedure developed in the course of the present study. The values for the crack initiation and growth parameters thus determined are compared with the corresponding parameters from the Essential Work of Fracture (EWF)

method determined using DENT specimens as is widely practiced, and also SENT specimens, ramp loaded to (near) fracture. The EWF test yields three parameters pertaining to tearing resistance of sheets: (i) the essential work of fracture,  $w_e$ , (ii) the opening across the fracture process zone (FPZ),  $\delta_c^e$ , and (iii) the flank angle of the FPZ,  $\psi^e$ . Dependence of the values of these various parameters determined on specimen geometry has also been examined. Additionally, notched SENT specimens have been used for exploring the use of the EWF method for the initial mixed mode regime of crack growth.

Results from the present investigation show that among all the possible tearing resistance parameters examined in the present study, four crack initiation parameters namely  $J_C$ ,  $\delta_c$ ,  $w_e$  and  $w_{ie}$  (the value of  $w_i$  data back extrapolated to zero ligament length) determined with fatigue pre-cracked specimens, and the three crack growth parameters ( $\varphi_c$ ,  $\psi^e$  and  $\delta_5$ ) appear to be material parameters independent of specimen geometry. Therefore, these parameters can be used for tearing resistance characterization of the present test material. In particular, it is confirmed that the  $\psi^e$  parameter, determined by the very simple experimental EWF procedure, is an actual measure of the stable CTOA  $\varphi_c$  optically measured in the present study. Use of SENT specimens is advantageous when determining the initiation based parameters that require fatigue pre-cracking the specimens.

Cohesive zone modelling (CZM) considering Mode I crack growth proved successful in simulating crack growth in notched or fatigue pre-cracked SENT and DENT specimens; also, the corresponding CZM parameters values are consistent with specimen geometry independence of crack growth parameters in sheet specimens. These studies need to be extended to other automotive grade steels, particularly with higher strengths and lower strain hardening indices.

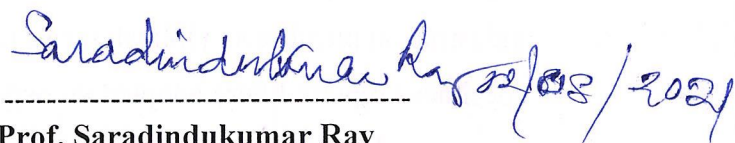
Supervisor(s)

  
02/08/2021  
Prof. Pravash Chandra Chakraborti  
Metallurgical and Material Engg. Dept.  
Jadavpur University  
Kolkata - 700032

-----  
**Prof. Pravash Chandra Chakraborti**  
Professor  
Metallurgical & Material Engineering  
Department  
Jadavpur University; Kolkata – 700 032

  
04/08/2021

**Sayan Kalyan Chandra**  
2021 / Kolkata

  
02/08/2021

-----  
**Prof. Saradindukumar Ray**  
Former Ministry of Steel Chair Professor  
Metallurgical & Material Engineering  
Department  
Jadavpur University; Kolkata – 700 032

# Contents

Contents	i
List of Symbols and Abbreviations	v
List of Figures	ix
List of Tables	xvii

## 1. Introduction

1.1 Characterizing tearing resistance of steel sheets - an overview....	1
1.2 Objectives of the present research.....	6
1.3 Scope of the present research.....	6

## 2. Literature review

2.1 Introduction.....	9
2.2 J-integral and CTOD for characterizing crack initiation in sheet metals.....	11
2.3 Energy dissipation rate Parameter $R$ .....	13
2.4 Crack tip opening angle, CTOA ( $\varphi$ ) .....	15
2.5 The $\delta_5$ parameter:.....	16
2.6 The Essential work of fracture (EWF) method .....	17
2.7 Cohesive zone modelling (CZM) simulation of ductile fracture .....	23
2.8 Tearing resistance of automotive grade steel sheets .....	26

## 3. Material and testing

3.1 Test Material .....	29
3.2 Experimental procedures.....	29
3.2.1 Tensile testing.....	30
3.2.2 EWF testing.....	31
3.2.3 Fatigue pre-cracking the specimens .....	32
3.2.4 Testing for CTOA determination .....	33

## 4. Fracture characterization using DENT specimens

4.1. Introduction.....	35
4.2. Experimental details .....	35

4.3. Results and discussion.....	36
4.3.1 EWF tests.....	36
4.3.1.1 Determining the valid ligament length range .....	36
4.3.1.2 Effect of notch tip radius on EWF parameters .....	40
4.3.1.3 Effect of ramp rates on EWF parameters .....	43
4.3.2 SEM of the fractured specimens .....	45
4.3.3 CTOA ( $\varphi$ ) determination by optical microscopy .....	46
4.3.4 Crack initiation parameters.....	50
4.3.4.1 FE simulation for identifying crack initiation event.....	50
4.3.4.2 Determining crack initiation parameters.....	53
4.4. Conclusions .....	55
 <b>5. <math>\eta_p</math> factor for clamped SENT sheet specimens</b>	
5.1 Introduction.....	57
5.2. Experimental .....	58
5.3. Results and discussion.....	59
5.3.1 $\eta_p$ determination from mechanical test data .....	59
5.3.2 Determination of $\eta_p$ using 3-D FE simulation data .....	64
5.3.3 Effect of notch tip radius $\rho$ on $\eta_p$ .....	75
5.3.4 $\eta_p$ determination from $J$ contour integral values for notched specimens.....	78
5.3.5 Evaluation of $J_p$ at crack initiation for notched SENT specimens .....	84
5.4. Conclusions .....	85
 <b>6. Fracture characterization using SENT specimen geometry</b>	
6.1. Introduction.....	87
6.2. Experimental .....	88
6.3. Results and discussion.....	89
6.3.1 EWF Tests.....	89
6.3.1.1 Determining the valid ligament length ranges for EWF tests.....	89
6.3.1.2 EWF analyses for tests at ramp rate $0.006 \text{ mm.s}^{-1}$ .....	93

6.3.1.3 Effect of ramp rate and specimen geometry on EWF parameters .....	95
6.3.2 CTOA ( $\varphi$ ) determination by optical method.....	99
6.3.3 Finite element modeling for non-growing crack.....	102
6.3.3.1 Notched SENT specimens .....	103
6.3.3.2 Pre-cracked specimens.....	110
6.4 Conclusions .....	113

## **7. Crack growth characterization: CTOA( $\varphi$ ) and $\delta_5$ measurements**

7.1. Introduction:.....	117
7.2. Experimental .....	117
7.2.1 Specimens and testing.....	117
7.2.2 CTOA determination.....	119
7.3. Results and discussion.....	120
7.3.1 Selection of optical CTOA ( $\varphi$ ) determination method.....	120
7.3.2 Effect of notch root radius ( $\rho$ ) and ligament lengths ( $l$ ) on $\varphi$ - $\Delta a$ plots.....	121
7.3.3 $\delta_5 - \Delta a$ and $\delta_7 - \Delta a$ plots: the corresponding $\varphi$ estimates .....	123
7.4. Conclusions .....	130

## **8. Crack growth characterization: Energy dissipation rate**

8.1. Introduction.....	131
8.2. Experimental .....	131
8.3. Results and discussion.....	132
8.3.1 Method 1: $R - \Delta a$ plot from $P - v_s - \Delta a$ data.....	132
8.3.2 Method 2: Determining $R_\infty$ .....	138
8.3.3 Normalization of the $R$ -resistance curve .....	142
8.4. Conclusions .....	144

## **9. Cohesive zone modelling (CZM) of crack growth**

9.1 Introduction.....	147
9.2 Determination of the CZM parameters .....	148

9.2.1 Notched ( $\rho = 0.1$ mm) specimens.....	148
9.2.2 Pre-cracked specimens.....	149
9.3 Transferability of CZM parameters .....	150
9.4 Verification of EWF results .....	154
9.5 CZM simulation for $\varphi(\delta_5) - \Delta a$ and $\varphi - \Delta a$ plots for pre-cracked specimens .....	159
9.6 Effect of crack tunneling on $\varphi - \Delta a$ curves.....	163
9.7 Simulation of dissipation energy rate ( $R$ ) resistance curve .....	165
9.8 Conclusions .....	166
<b>10. Thesis conclusions and suggestions for future research</b>	
10.1 Thesis conclusions.....	169
10.2 Recommendations .....	173
10.3 Suggestions for future research .....	174
<b>References</b> .....	177

## List of Symbols and Abbreviations

$A$	actual crack surface area
$A_P$	plastic component of work done
$a, \Delta a$	notch/crack length, crack extension, maximum crack extension
$\delta a, a_0$	increment in crack length, initial crack length
$\Delta a_{max}$	maximum crack extension
$A_M$	constant in Eq. (5.4)
$G(l/W), H(v_p/W)$	functions in Eq. (5.4)
$C_M, C_S$	machine elastic compliance, specimen elastic compliance
$E$	Young's modulus
$f_Y$	“geometry function” in $R_{ref}$ for $R$ normalization
$H$	free length of specimen between the two jaw grips
$J; J_e, J_p$	$J$ integral parameter; elastic, plastic components of $J$
$J_c, J_p^c$	critical value of the $J$ -integral, $J_p$ at crack initiation
$J_p^{max}$	maximum value of path independent contour $J$ integral for fixed $z$ computed with the adopted FE meshing
$J_p^{avg}$	average $J_p$ value of path independent contour $J$ integral along thickness computed with the adopted FE meshing
$K$	stress intensity factor
$l$	ligament length
$l_{max}, l_{min}$	maximum, minimum $l$ for applying EWF method
$L, d$	parameters used in optical measurement of CTOA
$m$	parameter in CZM
$n$	strain hardening exponent
$P, P_{max}$	load, maximum load
$R^2$	linear correlation coefficient
$R$	energy dissipation rate per unit crack area

$R_0, R_\infty$	value of $R$ at physical crack initiation ( $\Delta a = 0$ ), stationary value of $R$
$R_{ref}, R_N$	reference $R$ , normalized $R$ ( $R_N = R/R_{ref}$ )
$S_k$	load separation factor
$T_n, T_0$	cohesive normal traction, maximum cohesive strength
$t, t_n$	sheet specimen thickness, ligament width at neck
$U_{diss}$	energy dissipated (external work done minus elastic strain energy stored)
$v, v_a$	gage extension, actuator displacement
$v_{af}$	final actuator displacement (data at 90% load drop)
$v_f$	final gage/extensometer displacement (data at 90% load drop)
$v_s, v_p$	specimen free length extension, plastic displacement
$W$	specimen width
$W_e, W_p$	total energy spent in FPZ, in PDZ enclosing FPZ
$w_e, w_e^m$	plane stress, mixed mode essential work of fracture
$W_f, w_f$	total work of fracture, specific work of fracture
$W^{in}, W^{gr}$	work for fracture initiation, growth
$w_i, w_{ie}$	plane stress crack initiation energy per unit ligament area, value of $w_i$ back extrapolated to $l = 0$
$w_p$	non-essential work of fracture
$z$	distance from specimen surface in the thickness direction
$\alpha$	shape parameter (CZM)
$\beta, \beta w_p$	plastic zone shape factor, volumetric plastic work density in the PDZ,
$\Gamma_0$	cohesive energy
$\delta, \delta_c$	crack tip opening displacement, critical value of $\delta$ for crack initiation
$\Delta_n, \delta_n$	normal separation (CZM), final value of $\Delta_n$ at which $T_n = 0$ (CZM)



$\delta_c^e$	opening across the FPZ for a fully growing crack
$\delta_c^{e,m}$	CTOD at crack initiation (mixed mode)
$\delta_5, \delta_7$	displacement at original notch/crack tip for gage length 5 mm, 7 mm
$\varepsilon_p$	true plastic strain
$\eta_p$	cohesive energy, plastic “eta factor”
$\lambda$	parameter controlling decrease from $R_0$ to $R_\infty$
$\rho, \rho_{crit}$	notch root radius, critical value of $\rho$ ( $\rho \leq \rho_{crit}$ ) for obtaining $\rho$ -independent properties
$\rho_{crit}^{\delta_c^e}, \rho_{crit}^{w_e}$	critical value of $\rho$ for obtaining $\rho$ -independent $\delta_c^e, w_e$
$\sigma$	true stress
$\sigma_n, \bar{\sigma}_n$	maximum net section ligament stress, mean of the $\sigma_n$ values
$\sigma_u, \sigma_y, \sigma_f$	ultimate tensile strength, yield stress, flow stress
$\varphi, \varphi_c$	CTOA (optically measured), critical CTOA (optically measured)
$\varphi(\delta_5), \varphi_c(\delta_5)$	CTOA estimate from $\delta_5$ measurement, critical CTOA estimate from $\delta_5$ measurement
$\psi^e$	estimate of critical CTOA determined from EWF testing
CTOA	crack tip opening angle
CTOD	crack tip opening displacement
C(T)	compact tension (specimens)
DENT	double edge notched tension (specimens)
DP	dual phase
EWF	essential work of fracture
FE, FEA	finite element, finite element analysis
FPZ	fracture process zone
GTN	Gurson, Tvergaard and Needleman (micromechanical model)

IF	interstitial free (steel)
M(T)	middle tension (specimens)
PDZ	plastic deformation zone
SENT	single edge notched tension (specimen)
SEM	scanning electron microscopy
TSL	traction-separation law
YS	yield stress

## List of Figures

2.1	Schematic diagram of TSL law for ductile materials, the PPR law	26
3.1	Microstructure of IF steel (RD is the Rolling direction)	30
3.2	Schematic diagrams of <b>(a)</b> SENT and <b>(b)</b> DENT specimen	31
3.3	Representative $P - v_s$ plot showing loading – relaxation – unloading sequences in CTOA testing, Inset shows enlarged view for one such cycle.	34
4.1	<b>(a)</b> $v_f - l$ and <b>(b)</b> $w_f - l$ plots with linear fits for determining valid $l$ range for notched DENT specimens (ramp rate = $0.006 \text{ mm.s}^{-1}$ ).	37
4.2	$\sigma_n - l$ plots to determine valid $l$ - range for <b>(a)</b> notched DENT specimens (ramp rate = $0.006 \text{ mm.s}^{-1}$ ); <b>(b)</b> pre-cracked DENT specimens (ramp rate = $0.006 \text{ mm.s}^{-1}$ ); <b>(c)</b> notched DENT specimens (ramp rate = $0.06 \text{ mm.s}^{-1}$ ); and <b>(d)</b> notched DENT specimen (ramp rate = $0.6 \text{ mm.s}^{-1}$ ). In each figures, the pair of dashed horizontal lines define the $0.9\bar{\sigma}_n - 1.1\bar{\sigma}_n$ range for identifying $l$ -validity range following the criterion of Clutton [103].	39
4.3	<b>(a)</b> $w_f - l$ and <b>(b)</b> $v_f - l$ plots of notched and pre cracked DENT specimens for ramp rate $0.006 \text{ mm.s}^{-1}$ . Firm lines show linear fits of the data.	41
4.4	Shapes of plastic zones for notched DENT specimens with <b>(a)</b> $l = 3 \text{ mm}$ and <b>(b)</b> $l = 6 \text{ mm}$ .	43
4.5	<b>(a)</b> $w_f - l$ and <b>(b)</b> $v_f - l$ plots for notched DENT specimens for three different ramp rates.	44
4.6.	Representative scanning electron micrographs of different zones in the fracture ligament of the pre-cracked DENT specimen ( $l = 7.96 \text{ mm}$ ).	46
4.7	SEM image showing predominant flat fracture ( $l = 7.96 \text{ mm}$ ).	46
4.8	A representative photograph showing measurement of CTOA.	47

4.9	Choice of CTOA measurement basis $L$ for DENT specimens. SD is the standard deviation computed for the stable CTOA values (determined for the chosen $L$ ) between the two vertical bars.	48
4.10	$\varphi - \Delta a$ plots for fatigue pre-cracked DENT specimens at three different deformation rates.	49
4.11	Simulated $P - v_s$ plots for notched ( $\rho = 0.1$ mm) DENT specimens having mesh size of <b>(a)</b> 0.125 mm, 0.1 mm and 0.05 mm along thickness, <b>(b)</b> in plane meshing of $0.2 \times 0.2$ mm and $0.1 \times 0.1$ mm around notch..	52
4.12	FEM simulated $P - v_s$ plot superimposed on the experimental curve for notched ( $\rho = 0.1$ mm) DENT specimen with $l = 10$ mm, point ‘b1’ is the crack initiation point.	53
4.13	CTOD determined at point ‘b1’ of the Figure 4.12.	54
4.14	Variation of $J_p^c$ and $\delta_c$ with ligament length for notched DENT specimens.	55
5.1	$P - v_s$ curves for notched SENT specimens with different $a/W$ ratios from mechanical tests.	59
5.2	For notched SENT specimens, $A_p$ plotted as a function of notch length $a$ for different $v_p$ levels.	62
5.3	Comparison of $\eta_p$ computed using different approaches	63
5.4	Parameter $S_k$ plotted against normalized plastic displacement $v_p/l_k$ for different $a/W$ ratios.	63
5.5	Variation $S_k$ (average) with $l_k/W$ ratio	64
5.6	<b>(a)</b> Plane view of the finite element mesh showing smaller mesh size around the notch and larger mesh size rest of the SENT specimen; <b>(b)</b> enlarged view of the mesh around notch tip.	65

5.7	(a) Experimental and simulated (assuming non-growing crack) $P - v_s$ plots of notched SENT specimens. Inset shows for the plot for $a = 21$ mm, point “a1” where the two plots starts deviating, and a nearby point “b” at a slightly higher $v_p$ . (b) Necking at point “a1” (37%). (c) Necking at point “b” (37.7%).	67
5.8	$P - v_s$ plots from 3-D FE simulations of SENT specimen with $\rho = 0.1$ mm and $a = 21$ mm. For the three simulations, element size along thickness direction was 0.2 mm, 0.1 mm, or gradient meshing using 14 layers; for the corresponding in-plane mesh dimensions, see text.	68
5.9	(a) Representative SEM micro graph showing extensive necking ( $a = 8$ mm); (b) processed image by ImageJ software using edge detection technique in order to measure the necking percentage.	69
5.10	$\eta_p$ for the SENT sheet specimens evaluated from FE simulation (see Fig. 5.3), compared with $\eta_p$ computed from the functions for thick specimens with comparable $n$ reported in literature.	70
5.11(a)	Variation of $\eta_p$ with $a/W$ for various $v_p$ levels. The firm line shows the optimal linear fit of the data; and filled circles show for each $a/W$ , the mean $\eta_p$ computed for the chosen $v_p$ levels.	74
5.11(b)	Variation of % necking with $a/W$ for indicated $v_p$ levels. The filled symbol shows the % necking measured from FE mesh at crack initiation points (e.g., point “a1” in Fig. 5.7(a) inset) in these specimens.	74
5.11(c)	Variation of $\eta_p$ with $v_p$ for various $a/W$ levels	75
5.12	$P - v_s$ plots for SENT specimens with $a = 21$ mm, and with notch tip radius $\rho = 0.02$ mm and $\rho = 0.01$ mm.	77
5.13	Effect of $\rho$ on (a) $\eta_p$ and (b) $J_p$ values	78
5.14	Through thickness meshing with C3D8R elements having element size (a) 0.2 mm (b) 0.1 mm and (c) gradient meshing, with the red dot denoting the location $z = 0.4t$ , i.e., for $J_p^{max}$ as defined in this study.	80

5.15(a)	Path independence of $J_p^{max}$ - $v_p$ plots for contour radii 0.75 mm, 1 mm and 1.2 mm around the notch determined at $z = 0.4t$ .	81
5.15(b)	Through thickness variation of $J_p$ integral and $J_p^{max}$ (at $z = 0.4t$ ) and $J_p^{avg}$ value for SENT specimen with $a = 21$ mm, $\rho = 0.1$ mm.	82
5.16	For the SENT specimen with $a = 21$ mm, comparison of $J_p^{max}$ (at $z = 0.4t$ ) and $J_p^{avg}$ values considering the contour of 1mm for the three meshing used in this study.	83
5.17	For SENT specimen with $a = 21$ mm, comparison of the $v_p$ -dependence of <b>(a)</b> $J_p$ and <b>(b)</b> $\eta_p$ determined from contour integral (considering both $J_p^{max}$ and $J_p^{avg}$ values), and Method 1 with FE simulated $P$ - $v_p$ data.	84
5.18	For notched ( $\rho = 0.1$ mm) SENT specimens, variation of $J_p^c$ with $a/W$ ratio	85
6.1	<b>(a)</b> $v_f$ - $l$ and <b>(b)</b> $w_f$ - $l$ plots of notched SENT specimens	90
6.2	$\sigma_n$ - $l$ plots to determine valid $l$ ranges for <b>(a)</b> notched, <b>(b)</b> pre-cracked SENT specimens tested at ramp rate $0.006$ mm.s <sup>-1</sup> ; <b>(c)</b> notched SENT specimens tested at ramp rate $0.06$ mm.s <sup>-1</sup> ; and <b>(d)</b> notched SENT specimens at $0.6$ mm.s <sup>-1</sup> . Pairs of dashed vertical lines identify the valid $l$ ranges.	92
6.3	<b>(a)</b> $w_f$ - $l$ and <b>(b)</b> $v_f$ - $l$ plots of notched and pre-cracked SENT specimens for ramp rate $0.006$ mm.s <sup>-1</sup> .	95
6.4	$w_f$ - $l$ plots of <b>(a)</b> notched and <b>(b)</b> pre-cracked SENT and DENT specimens. (Data for DENT specimen from Chapter 4)	96
6.5	Different plastic zone shapes for pre-cracked <b>(a)</b> DENT ( $l = 4.6$ mm) and <b>(b)</b> SENT ( $l = 4.3$ mm) specimens	97
6.6	$v_f$ - $l$ plots for <b>(a)</b> notched and <b>(b)</b> pre-cracked SENT and DENT specimens. (DENT specimen data from Figs. 4.3(b), 4.5(b)).	98
6.7	For SENT specimens, choice of CTOA measurement basis $L$ for the two point method. SD is the standard deviation computed for the stable CTOA values (determined for the chosen $L$ ) between the two vertical bars.	101

6.8	$\varphi - \Delta a$ plots for pre-cracked SENT specimens at different ramp rates. SD is the standard deviation computed for the stable CTOA values (determined for the chosen $L = 1.5$ mm) between the two vertical bars.	102
6.9	For notched ( $\rho = 0.1$ mm) SENT specimen with $l = 9$ mm, FE simulated $P - v_s$ plot superimposed on the corresponding experimental curve; point ‘b’ is the crack initiation point.	104
6.10	CTOD determined at point ‘b’ of the Figure 6.9 by the method described in the text.	104
6.11	Variation of $J_p^c$ and $\delta_c$ values with ligament length, $l$ in SENT specimens.	105
6.12	For notched ( $\rho = 0.1$ mm) SENT specimens ramped at $0.006 \text{ mm.s}^{-1}$ , $w_i - l$ plot for the EWF valid $l$ range, compared with similar data for DENT specimens (see Fig. 4.14)..The dashed lines show linear least square fits for the two sets of data, Eq. 2.8.	107
6.13	For notched ( $\rho = 0.1$ mm) SENT specimens, <b>(a)</b> comparison of $w_e$ for plane stress with $w_e^m$ and $w_i^e$ for mixed stress zone; <b>(b)</b> comparison of $\delta_c^e$ for plane stress with $\delta_c^{e,m}$ and $\delta_c$ extrapolated to $l = 0$ for the mixed stress regime.	109
6.14	Representative FE simulated $P - v_s$ plot superimposed on the corresponding experimental curve for pre-cracked <b>(a)</b> SENT ( $l = 9.58$ mm) and <b>(b)</b> DENT ( $l = 8.33$ mm); point “b1” is the crack initiation point.	111
6.15	Variations of $J_p^c$ and $\delta_c$ values with ligament length $l$ for pre-cracked <b>(a)</b> SENT and <b>(b)</b> DENT specimens	112
6.16	For pre-cracked SENT and DENT specimens ramped at $0.006 \text{ mm.s}^{-1}$ , $w_i - l$ plots ( $l$ within corresponding valid $l$ ranges). The dashed lines show linear least square fits for the two sets of data, Eq. 2.8.	113
7.1	Schematic of microhardness indentations for $\delta_5$ and $\delta_7$ measurements	118
7.2	Four point method for determining the CTOA.	120

7.3	For a pre-cracked SENT specimen, $\varphi - \Delta a$ curves using two point method (data from Fig. 6.7, with $L = 1.5$ mm, the best choice) and four point method.	121
7.4	$\varphi - \Delta a$ curves of pre-cracked and notched SENT specimens (pre-cracked specimen data from data from Fig. 6.7 for $L = 1.5$ mm)	122
7.5	$\varphi - \Delta a$ plots of pre-cracked SENT specimens with different $l$ (data for $l = 23.98$ mm from Fig. 6.7 for $L = 1.5$ mm)	122
7.6	For a pre-cracked SENT specimen <b>(a)</b> $\delta_5 - \Delta a$ and $\delta_7 - \Delta a$ plots and <b>(b)</b> the corresponding $\varphi(\delta_5) - \Delta a$ and $\varphi(\delta_7) - \Delta a$ plots	124
7.7	<b>(a)</b> $\delta_5 - \Delta a$ and <b>(b)</b> corresponding $\varphi(\delta_5) - \Delta a$ plots for pre-cracked SENT specimens with different ligament lengths.	126
7.8	<b>(a)</b> $\delta_5 - \Delta a$ and <b>(b)</b> the corresponding $\varphi(\delta_5) - \Delta a$ plots for pre-cracked SENT and DENT specimens	127
7.9	<b>(a)</b> $\delta_5 - \Delta a$ and <b>(b)</b> the corresponding $\varphi(\delta_5) - \Delta a$ plots for pre-cracked and notched SENT specimens.	128
7.10	Comparison of $\varphi - \Delta a$ and $\varphi(\delta_5) - \Delta a$ curves of pre-cracked SENT specimen	129
8.1	<b>(a)</b> A representative $P - v_s$ plot for repeated cycles of loading-relaxation-unloading imposed on a specimen. <b>(b)</b> Illustrating measurement of increment in energy dissipated ( $\delta U_{diss}$ ) for the very first cycle in Fig. 8.1(a).	131
8.2	$R - \Delta a$ curves for pre-cracked SENT and DENT specimens at ramp rate $0.006 \text{ mm.s}^{-1}$	134
8.3	$R - \Delta a$ curves for notched and pre-cracked SENT specimens at ramp rate $0.006 \text{ mm.s}^{-1}$ .	134
8.4	$R - \Delta a$ curves for SENT specimens with different ligament lengths for ramp rate $0.006 \text{ mm.s}^{-1}$ .	135
8.5	Effect of ramp rates on $R - \Delta a$ plots of fatigue pre-cracked <b>(a)</b> SENT and <b>(b)</b> DENT specimens	136



8.6	$\varphi - \Delta a$ curves and $R - \Delta a$ curves for <b>(a)</b> SENT and <b>(b)</b> DENT specimens for three quasi-static ramp rates. ( $\varphi - \Delta a$ data for SENT specimens from Fig. 6.8 and for DENT specimens from Fig. 4.10).	137
8.7	$P - v_s$ plot from 3-D FE simulation for non-growing crack superimposed on the $P - v_s$ plot from mechanical test for a pre-cracked DENT specimen. The point of onset of deviation between the plots, point ‘b’, is the crack initiation point, and $W^{gr}$ is the dissipation energy to (nearly) complete fracture.	140
8.8	$R_\infty$ determination from EWF tested notched and pre-cracked <b>(a)</b> SENT and <b>(b)</b> DENT specimens (ramp rate $0.006 \text{ mm.s}^{-1}$ ).	141
8.9	$R_N - \Delta a$ curve of pre-cracked SENT and DENT specimens at ramp rate range of $0.006 - 0.6 \text{ mm.s}^{-1}$ . ( $R_{ref}$ defined by Eqs. (8.5) and (8.6))	143
9.1	CZM simulated $P - v_s$ plots of <b>(a)</b> notched DENT specimens ( $l$ range: 3 - 10 mm), <b>(b)</b> notched SENT specimens ( $l$ range: 4 - 15 mm), <b>(c)</b> pre-cracked SENT specimens ( $l$ range: 4.33 - 9.58 mm), <b>(d)</b> pre-cracked DENT specimens ( $l$ range: 4.36 - 8.33 mm), superimposed on the corresponding experimental $P - v_s$ plots. (Ramp rate $0.006 \text{ mm.s}^{-1}$ ).	153
9.2	Comparison of CZM simulated and experimental $w_f - l$ plots for <b>(a)</b> notched ( $\rho = 0.1 \text{ mm}$ ) DENT specimens; <b>(b)</b> notched ( $\rho = 0.1 \text{ mm}$ ) SENT specimens; <b>(c)</b> pre-cracked SENT specimens; and <b>(d)</b> pre-cracked DENT specimens. (Ramp rate $0.006 \text{ mm.s}^{-1}$ ).	156
9.3	Comparison of CZM simulated and experimental $v_f - l$ plots for <b>(a)</b> notched ( $\rho = 0.1 \text{ mm}$ ) DENT specimens; <b>(b)</b> notched ( $\rho = 0.1 \text{ mm}$ ) SENT specimens; <b>(c)</b> pre-cracked SENT specimens; and <b>(d)</b> pre-cracked DENT specimens. (Ramp rate $0.006 \text{ mm.s}^{-1}$ ).	158
9.4	$P - v_s$ plots for pre-cracked SENT ( $l = 23.98 \text{ mm}$ ) and DENT ( $l = 19.41 \text{ mm}$ ) specimens from mechanical tests and CZM simulations. (Ramp rate $0.006 \text{ mm.s}^{-1}$ ).	160

9.5	Comparison of experimental and CZM simulated <b>(a)</b> $\delta_5 - \Delta a$ and <b>(b)</b> $\varphi(\delta_5) - \Delta a$ curves. (Experimental data from Figs. 7.6(a) and 7.6(b)).	161
9.6	Comparison of $\varphi - \Delta a$ curves using data from mechanical tests (2-point method) and from CZM simulation (4-point method) for <b>(a)</b> SENT and <b>(b)</b> DENT specimens. (SENT specimen data by 2-point optical method from Fig.6.7; DENT specimen data from Fig.4.10).	162
9.7	Effect of crack tunneling on $\varphi - \Delta a$ curves.	164
9.8	The crack initiation points (through-thickness and on the surface) determined from the CZM model, and from surface photography.	164
9.9	Comparison of $R - \Delta a$ curves for pre-cracked SENT and DENT specimens from experiments and CZM simulations. (Data for experiments from Fig. 8.2).	166

## List of Tables

3.1	Tensile properties of the test material at different strain rate	30
4.1	Comparison of $w_e$ , $\beta w_p$ , $\delta_c^e$ and $\psi^e$ for notched and pre-cracked DENT specimen calculated from extensometer and actuator data, with and without extrapolation. (Ramp rate $0.006 \text{ mm.s}^{-1}$ ).	42
4.2	Effect of ramp rate on tearing resistance parameters determined from EWF testing of notched DENT specimens for $l = 3$ to $10 \text{ mm}$	45
4.3	Comparison of $\varphi_c$ for pre-cracked DENT specimens with $\psi^e$ from EWF tests for notched DENT specimens at three quasi-static ramp rates	49
5.1	Evaluation of $\eta_p$ of sheet SENT specimens by analyzing FE simulation data ( $0.2 \leq a/W \leq 0.9$ )	72
6.1	EWF parameters for notched and pre-cracked SENT specimens for ramp rate $0.006 \text{ mm.s}^{-1}$ (for descriptions of Data sets, see text)	94
6.2	Effect of specimen geometry on the energy based EWF parameters $w_e, \beta w_p$ (DENT specimen data from Tables 4.1 and 4.2)	97
6.3	Comparison of $\delta_c^e$ and $\psi^e$ for SENT and DENT specimens	99
6.4	Comparison of $\varphi_c$ for pre-cracked SENT specimens with $\psi^e$ from EWF tests for notched SENT specimens at three quasi-static ramp rates	101
7.1	Comparison of $\varphi_c$ and $\varphi_c(\delta_5)$	129
8.1	Comparison of $R_\infty$ computed using Methods 1 and 2 (Ramp rate $0.006 \text{ mm.s}^{-1}$ )	140
8.2	Effect of ramp rate and normalization on $R_\infty$ of pre-cracked SENT and DENT specimens. ( $R_{ref}$ defined by Eqs. (8.5) and 8.6))	144
9.1	Comparison of EWF results computed using data from mechanical tests and from CZM simulations	154



## 1.1 Characterizing tearing resistance of steel sheets - an overview

Ductile sheet metals combining high strength with good formability are being increasingly used in several technologically important applications like aircrafts [1], rockets [2] and automobiles [3]. As such, characterization of ductile tearing resistance of such thin sheet metals is attracting increasing attention [4-6]. For thick specimens, the significance and the procedures for determining the fracture mechanics parameters characterizing crack initiation and growth are well established [7, 8]. The situation, however, is more complex for sheet metals [9, 10]. The reasons can be understood by considering the essential features of ductile sheet metal deformation and fracture: (i) large scale plasticity, (ii) necking around the crack tip, and (iii) crack tip tunneling (which, depending on the test material, can be quite extensive) because of variation of constraint from plane stress at surface to plane strain at the mid plane [10, 11]. Consequently, with specimen thickness increasing from close to zero, initiation fracture toughness first increases to a maximum value (for a thickness that depends upon the test material) beyond which it gradually decreases, ultimately reaching the plane strain limit, as characteristic for a thick plate. A material with thickness in the first regime can be called a sheet material. For example, for an Al 6082-O alloy [2, 12, 13], this thickness limit for the initial rising toughness regime was determined to be 6 mm. Thus, initiation toughness of thin sheets need to be determined for the specific sheet thickness of interest [12, 14]. In a sheet material, the crack actually initiates under a complex state of stress; a small extent of initial crack growth in Mode I (flat fracture) under higher constraint is followed by typically extensive stable tearing under (quasi-) plane stress, which is followed by the final unstable fracture. Also, in some sheet metal specimens, after some extent of initial crack growth in Mode I, the crack twists and further crack growth takes place in mixed Mode I + Mode III, resulting

in slant fracture. Hachez [12] has carried out an extensive research to identify the conditions for crack growth by flat fracture in sheet specimens. These problems prompted the researchers to critically examine the limits of applicability of the well-established fracture mechanics parameters for thick plates for the case of thin ductile sheets, and also to search for alternative tearing resistance parameters specifically for thin sheets.

For characterizing crack initiation, an obvious choice appears to be the energy per unit ligament area required for crack initiation,  $w_i$ . The value of  $w_i$  depends upon the exact crack tip constraints at initiation, and thus systematically varies with the specimen ligament length  $l$  by an extent depending upon the test material and experimental conditions [15-17]. Two dimensional (2-D) formulations are commonly used for determining the value of the  $J$ -integral parameter (the path independent line integral) at crack initiation ( $J_C$ ) in the case of plates. Using such 2-D formulation for the case of thin sheets with prominently 3-D deformation is *prima facie* a doubtful proposition [4, 14]. Formally, one can ignore this, and directly apply the 2-D formulation for thin sheets. Faccoli et. al [18] rationalized use of 2-D  $J$ -integral formulation for the case of sheet DENT specimens clamped across the edges; these specimens are under predominantly tensile loading. For DENT specimens of an Al 6082-O alloy sheet, Pardoen et. al. [2, 17] showed that at the crack initiation point,  $J$  integral values evaluated using the 2-D formulation, and by 3-D finite element (FE) modelling invoking the basic line integral definition of  $J$ , agreed to within 10%. That is, in this instance, the extent of crack tip plasticity and necking at crack initiation did not invalidate the 2-D  $J$ -integral formulation.

For adopting either  $J_C$  or  $w_i$  - based approach, the difficulty lies in identifying the crack initiation point. High resolution videography of specimen surface has been used for this purpose [19], but it detects only surface crack initiation whereas crack actually initiates at the mid plane of the sheet where constraint is the highest [20]. The direct method of determining CTOD at crack initiation,  $\delta_c$ , involves scanning electron microscopy (SEM) measurements that are experimentally intensive and require time and skill [14, 21]. A simpler and faster alternative method developed in the GKSS groups [4, 5] is the  $\delta_5$  method;  $\delta_5$  is the opening displacement at the

original crack tip, measured over a gage length of 5 mm by an attached gage. The  $\delta_5$  parameter avoids the shortcomings of the  $J$ -integral and conventional definitions of CTOD with respect to thin-walled geometries. However,  $\delta_5$  measurement requires a special  $\delta_5$  gage. The existing studies using  $\delta_5$  measurement are limited to large size compact tension (C(T)) and middle tension (M(T)) specimens of aluminum alloys.

Actually, integrity assessment of a ductile sheet metal in terms of any initiation parameter would be unduly conservative because of the large stable crack growth and corresponding increase in tearing resistance preceding unstable fracture. Thus, prediction of failure of sheet structures in terms of crack growth becomes essential for realistic assessment of safety and reliability of the structural component. In this context, Newman et al. [11] proposed crack tip opening angle (CTOA),  $\phi$ , particularly the value of the stable CTOA,  $\phi_c$ , which remains constant over the stable crack growth regime, as a parameter for characterizing crack growth resistance of thin sheets. Since it was introduced, the CTOA parameter has been successfully applied for several metallic sheet materials, both for material qualification [4, 11, 20, 22-28], and for integrity assessment [29-32]. The CTOA concept proved successful in characterizing crack growth resistance; also, it allows transferability of data from the laboratory tested specimen to structural components. The experimental methods for determining CTOA in sheet specimens have been standardized in ASTM E 2472 [33]. But the testing and measurement procedures are time consuming and experimentally intensive, and as such may not be attractive for routine industrial application. From this perspective, the use of  $\delta_5$ - $\Delta a$  curves may be more attractive. The reported studies with both these parameters are mainly limited to large sized C(T) and M(T) sheet specimens [10, 14, 25, 34] as prescribed by the testing standards [33]. Kayamori et al [35] pointed out that using clamped single edge notched tension (SENT) specimens for such tests can significantly reduce the experimental burden as anti-buckling guides are not necessary; the same advantage extends to clamped DENT specimens. The energy dissipation rate,  $R$ , introduced as an alternative measure of tearing resistance in thick specimens, has been identified as a structural property [36, 37] because of its dependence on specimen geometry. The report by Brocks et al [38] till date appears

to be the only report on the application of the dissipation rate concept for characterizing crack growth in thin sheets; large size thin aluminum C(T) and M(T) specimens were used in this study.

In 1977, Cottrell and Reddel [39] introduced the Essential Work of Fracture (EWF) method for characterizing ductile tearing of thin sheets. They also demonstrated it by ramp loading to fracture a series of DENT specimens of a cold rolled low alloy steel sheet ( $t = 1.55$  mm), with identical external dimensions but varying ligament lengths. The EWF method is based upon a simple consideration: for crack growth in a thin sheet, the processes of necking and of separation together contribute to the essential work of fracture (EWF) spent in the fracture process zone (FPZ), measured per unit ligament area by the EWF parameter,  $w_e$ . Further, for crack growth under plane stress,  $w_e$  should be a material constant. Now, irrespective of specimen geometry, the plastic deformation zone (PDZ) enclosing the FPZ dimensionally will be of the order of  $l^p$ , with generally  $p > 1$  [40, 41]. If the average accumulated plastic work in the PDZ can be assumed to be a constant, then  $w_e$  can be extracted from the  $l$ -dependence of  $w_f$ , the total energy of fracture per unit ligament area. For this, however, certain conditions must be met, including both upper and lower limits for the ligament lengths (the  $l$ -validity range) to ensure dominant contributions from the plane stress regime of crack growth [10, 42, 43]. Limited efforts to apply the EWF method for the energy data in the initial mixed mode regime have been reported in literature [15, 44].

Even though the EWF method was first demonstrated and then applied for a variety of sheet materials using DENT specimens, the same philosophy should also extend to SENT sheet specimens. Unlike in DENT specimens, the plastic zone in a SENT specimen approaches the specimen boundary [15]. But this would not prove to be a limitation as long as the specimen geometry independence can be illustrated for the chosen  $l$ -range. The extension of EWF method to different specimen geometries in fact was first addressed [45] within ten years of the first proposal of EWF methodology using DENT specimens. However, the initial effort specifically with metallic sheet SENT specimens was not successful [45].



For EWF testing of DENT specimens, the specimen load line displacement at fracture is a linear function of ligament length with a non-zero offset [10, 39]. The offset of this line,  $\delta_c^e$ , should be close to the CTOD at crack initiation, and the slope of this line,  $\psi^e$ , should be a measure of CTOA [10]. It must be noted that  $\delta_c^e$  is different from the actual CTOD measured at the crack tip at initiation, because the EWF test data pertain to the main contribution to crack growth in plane stress regime. Similarly,  $w_e$  cannot be used as a measure of the extrapolated value of  $w_i$  for  $l = 0$ . The parameter  $\psi^e$ , however, is free from such limitations as it characterizes a growing crack that is already in the plane stress regime [41]. It appears that for the purpose of integrity assessment by the method of Newman et al [11], the inferred initiation CTOD and CTOA from EWF test may be preferred over the actual initiation CTOD and CTOA measured by relatively difficult experiments. For integrity assessment, the EWF parameters  $w_e$  and  $\delta_c^e$  should be independent of the notch tip radius. This can be achieved by fatigue pre-cracking the specimens [42]. For a given material and sheet thickness, the fracture resistance property of a sheet metal should be independent of specimen geometry. There is a very limited amount of evidence about the geometry independence of  $w_e$  and  $w_i$  [45]; the geometry independence of the parameters  $\delta_c^e$  or  $\psi^e$  has not at all been examined in literature. In sheet metals where crack initiates in flat mode [12,14] but crack growth eventually shifts to the slant mode, the physical significance of  $w_e$  and  $\delta_c^e$  parameters, determined by extrapolating data primarily from the slant fracture regime for representing parameters for flat crack initiation, requires careful consideration.

Also, it will be interesting to simulate crack growth in the test specimens (showing flat fracture) using 3-D cohesive zone modelling (CZM). In spite of its attraction compared to the other numerical crack growth simulation models because of its simplicity, the CZM method does not seem to have been applied for ductile thin steel sheets. The adjustable parameters in a CZM formulation may be considered as alternative parameters characterizing ductile tearing.

## 1.2 Objectives of the present research

The objective of the present study is formulating for comprehensive characterization of tearing resistance of automotive grade steel sheets, using one test material. A 1 mm thick interstitial free (IF) steel sheet has been selected for the present study. Interstitial-free (IF) steels offer a high degree of formability and freedom in design and have been used for the manufacturing of very complex products like inner door panels, side parts, inner wheelhouses, hoods, etc of a car body. The selection of an IF steel for the present study is primarily because of its high strain hardening index ( $n$ ) leading to accentuated specimen plasticity and necking effects, and also promoting flat mode of fracture (see Hachez et al. [46]). It may be expected that the conclusions drawn from research with this test material will generally apply for other automotive grade steels with lower strain hardening exponents.

The various crack initiation and growth parameters discussed in Section 1.1 are to be covered in the study. For a crack initiation or growth parameter to qualify as a material parameter, it must be shown to be independent of test specimen geometry. Therefore, testing both DENT and SENT specimens gripped across their entire widths are envisaged. Also, for potential applications in integrity assessment, it is necessary to use parameter values that are independent of notch tip radius. Therefore, tests are to be carried out using specimens with sharp mechanical notches (notch tip radius  $\rho = 0.1$  mm), or fatigue pre-cracks. The other test variables planned to be covered include specimen ligament length, and quasi-static ramp rate.

## 1.3 Scope of the present research

It may be convenient to frame the scope of research in terms of a few key issues that need to be addressed:

1. Possibility of extending the EWF methodology (well established with the DENT specimen geometry) to SENT specimen geometry. This will facilitate examining the geometry independence of the EWF parameters  $w_e$ ,  $\delta_c^e$  and  $\psi^e$ . Related issues are the possibility of extending the EWF paradigm to the

initial mixed stress regime, and determining initiation parameters for the highest physical constraint in the test sheet corresponding to  $l \rightarrow 0$ .

2. Possibility of finding a suitable method for identifying the crack initiation event with adequate resolution. This is necessary for determining the crack initiation parameters  $J_c$ ,  $\delta_c$  and  $w_i$  with DENT and SENT specimens.
3. Determining the  $\eta_p$  factor for the test sheet SENT specimens, for determining  $J_c$  with SENT specimens. It is necessary also to validate the method to be adopted for this purpose.
4. Characterizing crack growth by optically measured  $\varphi - \Delta a$  plot and hence  $\varphi_c$ , and also optically measured (without using a  $\delta_5$  gage)  $\delta_5 - \Delta a$  plot and hence  $\varphi(\delta_5) - \Delta a$  plots, and the corresponding critical values for the stable crack growth regime. A related question is: if the data generated in the course of these tests can be used to generate  $R - \Delta a$  plots as well.
5. Comparing the various crack initiation and growth parameters with their counterparts from the EWF tests.
6. Carrying out 3-D CZM simulation of crack growth in notched as well as pre-cracked DENT and SENT specimens of the present test material showing flat fracture, and also examining the possible uses of such CZM simulations.

The scheme of the presentation in this thesis is as follows. Chapter 2 presents a literature review. Chapter 3 introduces the test material, and also the four testing methods mainly used (with minor modifications in some cases) in the present study. Because the characterization studies include a rather wide range of topics, it was considered prudent to divide the study in thematic Chapters 4 - 9, each describing the experiments (if any) specific to the scope of the chapter, presentation and detailed analysis of the results, and conclusions therefrom. Finally, Chapter 10, summarizes the key results derived in the course of the present results, with a view to identifying areas for further research.



### 2.1 Introduction

The experimental measurement and standardization of tearing resistance plays important roles in assessing integrity and damage tolerance of engineering components and structures of thin ductile sheet metals, and also in such applications as product development and quality control. Tearing resistance of a specimen or a component is related to its capacity of dissipating energy before failure; the term “tearing” implies that a cracked body or a structure experiences stable crack extension and undergoes extensive plastic deformation before fracture [47]. The extent of plasticity strongly depends on the stress state, structural dimensions, loading configuration and resistance to plastic deformation [48]. For thick specimens, the significance and the procedures for determining the standard fracture mechanics parameters characterizing crack initiation and growth are well established [7, 8]. The same does not apply for thin sheet metals [9]. The reasons can be understood by considering the essential features of ductile sheet metal fracture.

1. Invariably, a ductile sheet shows large scale plasticity, necking around the crack tip [10] and crack tip tunneling (due to the presence of plane stress condition at two surfaces and plane strain condition at mid-plane, so that the crack tip tunnels through mid-plane [11]); the tunneling can be quite extensive depending on the test material.
2. Because of the extensive plasticity and necking, with increasing specimen thickness from close to zero, initiation fracture toughness first increases to a maximum value for a thickness that depends upon the test material, and beyond this it gradually decreases ultimately to the plane strain limit, as characteristic for a thick plate material. Thus, unlike thick specimens under plane strain condition, fracture toughness values for thin sheets are only valid for specific sheet thickness [12, 14]. Materials with thickness

corresponding to the first regime are called sheet material. For example, for an Al 6082-O material (strain hardening exponent  $n = 0.05$ ), the thickness limit for the initial rising toughness regime was 6 mm [2, 12, 13].

3. Typically a ductile sheet metal shows an extensive regime of stable tearing prior to onset of unstable fracture.

In a sheet material, the crack actually initiates under a complex state of stress, and only after a small extent of crack growth, further crack growth can be considered to take place under plane stress. This can be anticipated to continue up to close to final fracture, when the tip of the growing crack approaches sufficiently close to the free boundary (e.g., in a single edge notched tension (SENT) specimen), or in the case of a double edge notched tension (DENT) specimen, the tips of the two growing cracks come sufficiently close. For either case, again the state of stress becomes complex [4]. Further, depending upon the test material, the mode of fracture may be flat, or slant beyond some extent of initial flat fracture.

The classical elastic-plastic fracture mechanics parameters pertain to cracked plates with 2-D elastic-plastic stress-strain fields under load, ranging from plane stress to plane strain. The elastic-plastic fracture mechanics parameters are the crack tip opening displacement (CTOD,  $\delta$ ), and the  $J$ -integral. It may be recalled that the  $J$ -integral parameter is a path independent line integral defined for a non-linear elastic material [49]. Therefore, its use for elastic-plastic fracture is strictly permissible up to crack initiation (i.e., no unloading at crack tip), or may be allowed for a limited extent of crack growth such that the extent of crack tip unloading is acceptably small. Accordingly, crack initiation is characterized by the critical values of CTOD parameter ( $\delta_c$ ), or of the  $J$ -integral parameter ( $J_c$ ). The  $J$ -integral concept is used for characterizing crack growth in thick plates by the  $J$ -resistance curve, called the  $J_R$  (or  $J - R$ ) curve, the variation of  $J$  with crack growth  $\Delta a$ . Similarly, CTOD based resistance curves have also been used. The test standard ASTM E1820 discusses in detail the procedures for such characterization for plate materials, and also defines the various applicable limits. Using the  $J$ -integral parameter for such applications in the case of thin sheets become questionable because of the presence of extensive plasticity, necking, crack tunnelling, change of fracture mode during crack growth in some sheet metals, and the 3-D character

of the stress and strain fields [4, 14]. Consequently, several alternative approaches of characterizing crack initiation and growth in sheet metals have been proposed in the literature, and this is a vibrant area of research.

## 2.2 $J$ -integral and CTOD for characterizing crack initiation in sheet metals

For the thicker plate specimens, the current practice (ASTM E1820 [7]) is to evaluate  $J$ -integral for a non-growing crack as the sum of its elastic and plastic components,  $J_e$  and  $J_p$  respectively:

$$J = J_e + J_p = \frac{K^2}{E'} + \frac{\eta_p A_p}{tl} \quad (2.1)$$

$K$  is the stress intensity factor,  $E'$  is the effective elastic modulus,  $A_p$  is the area under the load  $P$  - plastic displacement  $v_p$  curve,  $t$  and  $l$  are respectively the thickness and the ligament length of the specimen, and  $\eta_p$  is the plastic “eta factor” which in general, depends on specimen geometry and dimensions, and may also depend upon the strain hardening property of test material [7]. This equation makes it very convenient to evaluate  $J$  for a non-growing crack from a single load - displacement record. The reservation about the applicability of this concept for sheet metals notwithstanding, there are a few reports adopting  $J_c$ , computed using the standard  $\eta_p$  formulation for thick plates, for characterizing crack initiation in deeply cracked double edge notched tension (DENT) sheet specimens gripped across the entire specimen width. In such tests, deformation is tension dominated, and the specimen does not buckle during testing, and therefore anti-buckling guides are not required. From 2-D formulations (i.e., for thick specimens), for deeply cracked DENT specimens,  $\eta_p = 1 - n$  (Table A7.4, Ref [9]). The report by Faccoli et al. [18] used standard  $J$  formulation for plate DENT specimens for determining the strain at crack initiation in a few automotive grade steel sheets. Their report includes a brief discussion rationalizing the applicability of  $J$  integral approach for characterizing crack initiation event in the sheet DENT specimens. Pardo et al. [2, 17] showed that for DENT specimens of an Al 6082-O alloy sheet (with  $\sigma_y = 50$  MPa,  $\sigma_u = 130$  MPa and  $n = 0.05$ ), at the experimentally determined crack initiation point, there was agreement within 10% between  $J$ -integral evaluated using

the standard formulation with  $n_p = 1 - n$ , and  $J$ -integral computed by 3-D finite element (FE) modelling invoking the basic line integral definition of  $J$ . That is, for their test material and the chosen specimen geometry (DENT), the extents of crack tip plasticity and necking, and crack tunneling, at crack initiation did not invalidate the 2-D  $J$ -integral formulation. It is not obvious that the same conclusion would extend to DENT specimens of other sheet metals, particularly with higher  $n$ . For the plasticity dominated scenario of ductile thin sheets,  $J \cong J_p$  [4]; also, the energy per unit ligament area for crack initiation  $w_i \cong A_p/(lt)$  so that  $J_p = \eta_p w_i$  [4].

In determining  $J_c$  by testing sheet DENT specimens, a practical problem has been identifying the crack initiation event with adequate resolution. In some reports, crack has been assumed to initiate at maximum load [50]; this assumption cannot be justified for a strain hardening material. Some sheet metal DENT specimens show sharp large drop in load during ramping. When this happens, the point of such load drop can be unequivocally identified as the crack initiation point [18]. Such sharp load drops, however, are not common in ductile sheet metals. For Al 6082-O alloy sheet, Pardoen and co-workers [2, 10, 13, 17] identified the point of appearance of thumb nail type impression on the specimen surface as crack initiation point. Dot [19] used high resolution videography for identifying crack initiation on the specimen surface; this method ignores the role of crack tunneling. There is a need for exploring for a suitable method for identifying crack initiation in sheet specimens of DENT, and also other, geometries.

As in DENT specimens, also in single edge notch tension (SENT) specimens gripped across the entire specimen width, and loaded in tension, deformation is tension dominated and the specimen does not buckle under load. Therefore, it should be possible to determine  $J_c$  using SENT specimens of sheet materials. For this application, it is however necessary to determine the value(s) of  $\eta_p$  to be used with ductile sheet SENT specimens. This is because, from results for thick plate SENT specimens,  $\eta_p$  is known to depend on  $n$  and also specimen dimensions, including thickness [51-60]. The viability of the  $\eta_p$  computed may be rigorously verified by comparing the (plastic components) of  $J_c$  determined experimentally using Eq. (2.1), and  $J_c$  computed invoking its basic line integral definition, as



demonstrated for the DENT sheet specimens tested by Pardoen et al [2, 17]. Further, if for a given sheet metal, the transferability of  $J_c$  (or its plastic component,  $J_p^c$ ) between SENT and DENT specimen geometries is established, it would establish  $J_c$  as a material parameter.

CTOD at crack initiation,  $\delta_c$ , measured by scanning electron microscopy (SEM) of the crack tip stretch zones on fractured surfaces, proved successful in characterizing crack initiation in thick [21, 61, 62] as well as thin plates [63, 64]. However, in thin sheets, the presence of extensive necking and plastic deformation at crack tip may complicate  $\delta_c$  measurements. The necessity for time consuming and painstaking SEM measurements limits its attraction, particularly for industrial application. Following the pioneering research by Newman et. al. [11, 20], CTOD based resistance curves have been used for predicting stable crack growth in thin sheets (Section 2.4). The definition of CTOD in such formulations is very different from the CTOD definition adopted for SEM measurements.

### 2.3 Energy dissipation rate parameter $R$

In the course of the discussions on the geometry dependence of  $J_R$  curves, Turner and co-workers [37, 65, 66] proposed the energy dissipation rate parameter,  $R$ , for characterizing extensive crack growth in any structures.  $R$  is defined as [67, 68]

$$R = \frac{dU_{diss}}{tda} \quad (2.2)$$

$U_{diss}$  is the plastic work dissipated during crack growth i.e., the difference between external work done and the recoverable elastic strain energy stored. For quasi-static isothermal deformation and fracture,  $U_{diss}$  equals the energy dissipated in plastic work, plus local separation energy necessary to create new surfaces. For specimens with thickness  $t$  the increment of crack area is  $tda$ . It has been experimentally shown that  $R$  initially has high values for crack initiation and small crack growths. With increasing crack growth  $\Delta a$ ,  $R$  decreases, and eventually attains a steady value  $R_\infty$  for relatively large  $\Delta a$  [36, 68]. Therefore, for large  $\Delta a$  values, the relevant characterising parameter is  $R_\infty$ . The high initial values of  $R$  are generally associated

with the initial blunting of the crack tip and the decaying shapes of the curve may be fitted to an exponential curve [50] as,

$$R = \frac{dU_{diss}}{tda} = R_{\infty} + (R_0 - R_{\infty}) \cdot \exp\left(-\frac{\lambda \Delta a}{W}\right) \quad (2.3)$$

Here,  $R_0$  is the initial value of the dissipation rate,  $R_{\infty}$  denotes the “crack propagation energy” for steady state crack growth, and the parameter  $\lambda$  governs the intensity of the decay from  $R_0$  to  $R_{\infty}$ . Turner and Kolednik [67] also pointed out that for determining  $R - \Delta a$  curves, fatigue pre-cracked specimens are not required - specimens with sufficiently sharp mechanical notches can very well be used. In such a specimen, beyond a small extent of crack growth, the crack growth behaviour becomes independent of the initial crack tip radius.

The problem with the  $R - \Delta a$  curve or for that matter  $R_{\infty}$  is that  $R$  includes all irreversible contributions of the external work of the whole structure [36, 68]. Thus, it is not a material property but a structural one which depends on both the specimen geometry and the loading configuration [67]. However, if the remote work term can be filtered out, a material property (the local work of separation) can be recovered [38, 69]. Recent developments, both in experimental and analysis techniques such as the topology of the fractured surface [70] and models of damage mechanics such as Gurson model [71] or its modifications e.g., the Gurson, Tvergaard and Needleman (GTN) model [72, 73], and the cohesive zone models (CZM) [74] now allow performing this separation. However, such analyses require knowledge of finite element analysis and may not be attractive for routine applications. Also, such distinction between local and remote crack tip work has been criticized [8, 36, 50] because in order to advance the crack it is necessary to reach a certain local work rate to coalesce voids at the crack tip, but this can only be achieved by straining material which is remote from the crack tip whereas experimentally only external work dissipated and elastic energy stored can be measured.

In order to resolve the problem of geometry dependence and transferability of the test results, the use of a normalised total dissipation rate (including both local and remote work) has been proposed. For fully yielded test pieces, this normalization has been attempted by scaling  $R$  with plastic limit load [50, 75].

However, the existing literature dealing with normalization of  $R - \Delta a$  curves are limited in number and that too to C(T) and M(T) specimens of thick plates [38, 50, 69]. As the normalization factor depends upon specimen geometry and strain hardening exponent,  $n$ , it appears necessary that the normalization factor has to be determined for each specific material and specimen geometry under consideration; this adds to the problem.

The application of energy dissipation rate,  $R$ , has mainly been limited to thick plates of different materials and specimen geometries [36-38, 50, 65, 67-69]. Its application seems to be extremely limited for thin sheets. For a 3 mm thick Al-Mg alloy (Al 5083 H321) sheet, Brocks et al [76] had applied the energy dissipation rate for characterizing the crack growth in C(T) and M(T) specimens with width of 150 mm. In another study, Brocks and Siegmund [77] applied FE simulations incorporating a two parameter cohesive zone model in order to determine the dissipation rates for a 1 mm thick and 508 mm wide centre cracked Al panel (Al 2024 T3) with initial  $a/W$  ratios of 0.2, 0.35 and 0.55. A normalization method (based on plastic limit load factor) was attempted for reducing the  $a/W$  dependence of the results, however it was not very successful (see Fig. 5(b) of [77]). Specifically, there are no reports on the application of the dissipation energy method for high strain hardening automotive grade steel sheets.

## 2.4 Crack tip opening angle, CTOA ( $\varphi$ )

In view of the extensive stable crack growth regime prior to onset of unstable fracture in ductile sheet metals, failure prediction of sheet structures by crack extension is a major concern in the assessment of safety and reliability. In a sheet metal, after an initial transient regime associated with crack tip blunting and specimen tunneling, the CTOA,  $\varphi$ , attains a constant value (the critical value),  $\varphi_c$ , and maintains this value for a substantial regime of crack extension. Newman et al. [11] proposed  $\varphi$ , particularly its critical value  $\varphi_c$ , for characterizing crack growth resistance of thin sheets. Since it was introduced, the CTOA parameter has proved successful in characterizing crack growth resistance and transferability of data from the laboratory tested specimen to structural sheet components. It has been successfully applied for several metallic sheet materials, both for material

qualification [4, 11, 20, 22-28], and for integrity assessment [29-32]. Methods of CTOA determination have been discussed in literature, cf. [26, 27, 34, 78-80] and references cited therein. For experimental determination of  $\varphi_c$  in metallic sheets, the ASTM E2472 standard [33] recommends C(T) and M(T) specimens with large (nearly 200 mm) width, and use of anti-buckling guides. This standard is quite comprehensive in terms of the alternative experimental approaches that can be used: it basically recommends two direct (optical microscopy and digital image correlation, DIC) and two indirect (microtopography and finite element analysis), methods of CTOA measurements in case of thin sheets. Among these methods, optical microscopy is the most commonly adopted method of measuring CTOA [4, 11, 20, 22-28] because of its relative simplicity. The application of the others methods (DIC [79, 81, 82], microtopography [83, 84] and 2-D and 3-D elastic-plastic FE analyses [11, 34, 85] are somewhat limited as these are rather complex in terms of experimentation and analysis. An important advantage of  $\varphi_c$  is, its value does not depend upon the initial notch tip radius. In the context of CTOA determination with 2.6 mm thick carbon-manganese steel sheets, Kayamori et al [35] had noted that anti-buckling guides are not necessary for clamped single edge notched tension (SENT) specimens, thus reducing the experimental difficulties. Needless to add that the same would apply for using DENT specimens.

## 2.5 The $\delta_5$ parameter

A simpler and faster alternative to CTOD determination developed by the GKSS group [4, 5] is the  $\delta_5$  method:  $\delta_5$  is the opening displacement at the original crack tip, measured over a gage length of 5 mm by an attached gage. The  $\delta_5$  parameter avoids the shortcomings of the  $J$ -integral and also of conventional definitions of CTOD for SEM measurements on thin-walled geometries. It is particularly convenient for characterizing large crack extensions in thin-walled structure. Therefore, in addition to  $\varphi$ , the  $\delta_5$  parameter has also been standardized for fracture resistance characterization of specimens with low constraint [4]. Further studies [38, 86] also showed that though both the definitions of the CTOD, i.e.,  $\delta_5$  at crack initiation and the conventional  $\delta_c$ , may yield practically identical results, the main difference between these methods consists in the applicability to test piece

geometry. Heerens et al [87] and Schwalbe et al [88] successfully used the  $\delta_5 - \Delta a$  curves for characterizing crack growth in large sized C(T) and M(T) specimens of an Al alloy. They also showed that within the validity limit, the slope of  $\delta_5 - \Delta a$  curves correlated with the optical CTOA value:

$$\varphi = \varphi(\delta_5) = \tan^{-1} \left( \frac{d\delta_5}{d\Delta a} \right) \approx \frac{d\delta_5}{d\Delta a} \quad (2.4)$$

This removes the necessity of laborious and painstaking angle measurements at the crack tip, and provides a much easier alternative for CTOA determination that does not require sophisticated experimental skills. However, Heerens et al. [87] subsequently found that as the  $\delta_5$  gauge position does not follow the tip position of the extending crack, it loses its meaning as a local parameter beyond some extent of crack growth and the question arises whether  $\delta_5$  based CTOA can be a true measure of actual CTOA,  $\varphi$ , or not. Most of the studies using both  $\delta_5$  and the optical  $\varphi$  measurement methods are mainly limited to the specimen thickness range of 2.3 mm typical of sheet materials to plate thickness of 35 mm; published reports dealing with thickness lower than 2 mm appear extremely limited [89]. However, the necessity for a  $\delta_5$  gauge and fixing it on a thin sheet specimen may limit the attraction of this method.

## 2.6 The Essential work of fracture (EWF) method

The Essential Work of Fracture (EWF) method provides a much simpler method in terms of experimentation and analysis for characterizing tearing resistance of thin sheets in plane stress regime. As such, it is no surprise that the EWF method has been used extensively for polymeric sheets [43, 44], and also for a number of ductile metallic sheets [2, 16, 19, 90, 91]. However, only a few reports are available in the literature on the application of the EWF method for automotive and similar grade steel sheets, e.g., [19, 41, 92].

Broberg [93] proposed that the plastic region can be divided into two regions: an end region where the fracture process takes place (the fracture process zone, FPZ), and an outer region (the plastic deformation zone, PDZ) where screening plastic deformation is necessary to accommodate the strains in the FPZ. Based on this idea, Cotterell and Reddel [39] formulated the EWF method for plane stress regime for

separating out the essential work of fracture for the process of crack propagation, a material property, from the total work of fracture. They also demonstrated the application of the EWF method by carrying out tests with DENT specimens made of a cold rolled low alloy steel sheet. The necessary criteria for proper implementation of the EWF concept have been given by Cotterell and Reddel [39] as:

- i) The ligament (length  $l$ ) of the DENT specimen is under plane state of stress.
- ii) The plastic zone is confined to the notched ligament.
- iii) The ligament is fully yielded prior to crack initiation and small enough to avoid edge effects.

To meet the above conditions, Cottrell and Reddel [39] empirically proposed a range of valid ligament length ( $l$ ) values as  $(3 - 5)t \leq l \leq W/3$ , where  $W$  is the specimen width. This ligament length range is generally considered as the “rule of thumb” for selecting ligament lengths for DENT specimens for EWF testing. In this equation, the lower limit  $l_{min}$  is necessary to reduce the effects of the small extent of initial crack growth under higher constraint (see Section 2.1). The upper limit  $l_{max}$  is meant to ensure full yielding of the ligament before the onset of fracture. When these criteria are fulfilled, an autonomous Fracture Process Zone (FPZ) can be identified inside the large plastic zone near the crack. The critical processes of necking and fracture are confined in the FPZ. The total energy dissipated can be partitioned into two components: the work of fracture ( $W_e$ ) associated with FPZ, and the plastic work ( $W_p$ ) dissipated in the outer PDZ. While  $W_e$  scales with ligament area,  $W_p$  depends on the volume of the plastic zone. Accordingly, the total energy can be expressed as follows

$$W_f = \int_0^{v_f} P dv = W_e + W_p = w_e l t + \beta w_p l^2 t \quad (2.5)$$

$P$  is load,  $v$  the specimen gage extension with value  $v_f$  for fracture,  $t$  is the specimen (original) thickness and  $\beta$  is a shape factor denoting shape of the plastic zone. After normalizing by the ligament area,  $l t$ , the specific work of fracture,  $w_f$  can be written as

$$w_f = \frac{W_f}{lt} = w_e + \beta w_p l \quad (2.6)$$

where  $w_e$  is the Essential Work of Fracture.

Also for a DENT specimen, the following important relationship between the final displacement,  $v_f$  and the ligament length,  $l$ , has also been proposed by Cotterell et al [10] (see also Ref [39]):

$$v_f = \delta_c^e + (\psi^e / 2)l \quad (2.7)$$

$\delta_c^e$  is identified as the inferred average critical crack tip opening displacement and  $\psi^e$  as the inferred CTOA from EWF testing. The EWF method thus yields four parameters:  $w_e$ ,  $\beta w_p$ ,  $\delta_c^e$  and  $\psi^e$  pertaining to tearing resistance. Of these four possible fracture resistance parameters, the focus of research in EWF method has been on the parameter  $w_e$ , and also its relation with  $J_c$ . Considerably less attention has been paid to the parameter  $\delta_c^e$  and its relation with  $\delta_c$  and virtually little attention has been paid to  $\psi^e$  and its relation with critical CTOA,  $\varphi_e$ .  $\beta w_p$  has been reported to be strongly dependent upon the amount of plastic deformation and specimen geometry; therefore, it cannot be considered as a fracture resistance parameter.

To determine these parameters, DENT specimens of identical external dimensions and sheet thickness  $t$  but with varying ligament lengths  $l$  are taken. For each specimen, the two edges are gripped across the entire width, and the specimen is quasi-statically ramp loaded in Mode I to complete fracture, recording the load ( $P$ ) and gauge extension ( $v$ ) data for the entire process. Since the buckling problem is avoided for these specimens, the EWF test and analysis procedures are very simple. Moreover it has been reported [92, 94] that an extensometer is not essential for EWF testing which too adds to its attraction.

The starting point of EWF testing is the selection of valid ligament length ( $l$ ) range for the test sheet specimens [95, 96]. The “thumb rule” proposed by Cotterell and Reddel [39] has been found unsatisfactory for some materials. For example, the lower limit ( $l_{min}$ ) was reported to be much higher than the proposed value of  $(3 - 5)t$  for low density polymeric film [75, 97]. For some Al and Zn alloys,

Marchal et al. [98] determined  $l_{min}$  as  $(6 - 8)t$ . On the other hand, the upper bound of the proposed “thumb rule” ( $l_{max} \leq W/3$ ) has been considered to be conservative by several researchers, cf. [99, 100]. A simple method is to visually identify the linearity ranges from plots showing linear least square fits of  $w_f - l$  data (Eq. (2.6)) and of  $v_f - l$  data (Eq. (2.7)). A more rigorous (and computation intensive) statistical procedure may be found in the report of Marchal, Walhin and Delanny [98]. For DENT specimens of a rigid-ideal plastic material, Hill [101] showed that for the plane stress condition, the maximum net section stress ( $\sigma_n$ ) calculated by dividing the maximum load with the ligament cross section area, should be independent of the ligament and show a constant value of  $\sim 1.15 \sigma_y$  (see also [39]). This has been presented in the ESIS test standard for polymeric material. Existing literatures [40, 96, 102] show that  $\sigma_n$  is nearly independent of  $l$  in the plane stress domain, though the value of  $\sigma_n$  can deviate from  $1.15 \sigma_y$ . For determining  $l_{min}$  in a strain hardening material, Clutton [103] suggested determining  $\bar{\sigma}_n$ , the mean of the maximum net sectional ligament stress  $\sigma_n$  values for all the specimens, and then discarding data for any specimen with  $\sigma_n$  outside the band  $\bar{\sigma}_n \pm 10\% \bar{\sigma}_n$ . Also, the number of specimens to be tested and their distribution over the valid ligament range for sufficiently good statistics, depends upon material. Some results on polymeric materials indicate that more than 20 specimens are required for the ratio of standard deviation to mean value of  $w_e$  to be less than 0.1 [44, 103]. However, for metallic material much smaller number of specimens (6-8) proved to be adequate [10, 16].

Subsequently Mai and Cotterel [15] extended the EWF methodology to energy for crack initiation in DENT specimens in plane stress by partitioning the total work of fracture  $W_f$  into the work for crack initiation  $W^{in}$ , and the work for crack growth  $W^{gr}$ , such that

$$w_i = \frac{W^{in}}{lt} = w_{ie} + \beta_i w_{ip} l \quad (2.8)$$

The method has been applied mostly for polymeric materials [97, 104, 105], and also for dual phase (DP) 780 and 1000 grade steel sheets [19]. From these studies,  $w_{ie}$  emerged as another parameter for material qualification. However, sufficiently



accurate detection of the crack initiation point is necessary for adopting this approach; this is not an easy problem. Also, attempt has been made to apply the EWF method for the energy data in the initial mixed mode regime [15, 44].

It is well recognized in literature that in order to determine  $w_e$  and  $\delta_c^e$  values that are independent of notch root radius  $\rho$ , the DENT specimens should be fatigue pre-cracked. This would require some experimental skill, and considerably increase the duration of a test campaign, and consequently, the EWF method will lose much of its simplicity and attraction. Because of significant specimen necking, the parameters  $w_e$  and  $\delta_c^e$  are thickness dependent. Depending upon the whether work of necking or separation dominates  $w_e$ , the thickness effect on  $w_e$  can be either large or small. Recent research on dual phase (DP) 590 and 780 grades of automotive steel sheets [41, 92] suggests that determining  $\rho$ -independent  $w_e$  and  $\delta_c^e$  may be necessary only for their potential use in integrity assessment. For routine material qualification and also possibly for product development,  $w_e$  and  $\delta_c^e$  determined using standard DENT specimens with a standardized low  $\rho$  value (such as achievable by electro-discharge machining) might be quite acceptable. It was also noted that  $\psi^e$  was statistically the best determined parameter. Also, because  $\psi^e$  pertains to a propagating crack, it is not seriously affected by the constraint for crack initiation (i.e., the value of  $\rho$ ) and specifically, fatigue pre-cracking is not necessary to determine  $\psi^e$ . Thus the  $\psi^e$  value as such determined from testing the notched specimens should qualify also for integrity assessment. A very significant result from these studies is:  $\psi^e$  values determined by EWF method were very similar to actual critical CTOA value,  $\varphi_c$ , determined by testing fatigue pre-cracked DENT specimens following a procedure that adapts ASTM E 2472 [33], leading the possibility of avoiding the painstaking CTOA measurement at the crack tip.

When comparing for metallic sheets the ( $\rho$ -independent) EWF parameters for crack initiation ( $w_e$ ,  $\delta_c^e$ ) with their fracture mechanics counterparts ( $J_c$ ,  $\delta_c$ ), the fracture morphology of sheet metals should also be considered. In case of age-hardened Al - alloys and high strength steels, it is reported that the ductile crack typically starts with crack tip tunneling, and an initially flat crack (i.e, Mode I) coplanar with the pre-crack twists into a slant crack (i.e., mixed Mode I+III) after a

very limited amount of crack extension; also, the extent of necking is small. In contrast, pure flat fracture with “bath-tub” type fracture profile, associated with extensive crack tip necking, was observed for sheets of Al 6082-O alloy [17], and also for various metallic sheets [13]. Hachez et al. [46] carried out fracture tests on thin DENT specimens of a large number of sheet metals and alloys (including AISI 316L steel and Al 6082-O alloy) with wide ranges of yield strength, work hardening capacity, extents of crack tip necking, and mean initial microvoid spacing, all showing mode I fracture profiles. From their experimental results, backed by 3-D FE modelling, they concluded that while a quantitative answer was not available, qualitatively, the slant fracture mode probably results from a relatively low strain hardening capacity and small fracture strain. Slant fracture is avoided when the fracture strain is large enough to allow the development of significant necking prior to crack initiation; this constrains the crack growth to the plane of the ligament. If necking has not developed enough, the crack is not constrained to remain in the plane of the ligament and can tilt at  $45^\circ$ . Reservation has been expressed [41, 92] on the physical significance of comparing the initiation values  $J_c$  and  $\delta_c$  which pertain to the flat mode in which crack initiates, with  $w_e$  and  $\delta_c^e$  respectively determined by back extrapolating data pertaining to dominantly slant mode of fracture, such as DP 590 or DP 780 grade steel sheets. Obviously, this limitation does not apply in comparing  $\psi^e$  and  $\varphi_c$ , as the relevant test data for both these parameters pertain to the same fracture mode. These reports [41, 92] also pointed out the need of extending these studies to relatively high ductility steels with higher work hardening rates.

In order to qualify as a material parameter, an EWF parameter must be independent of specimen geometry. Mai and Cotterell [45] investigated the effect of specimen geometry on  $w_i$  and  $w_e$  using large sized specimens of four different geometries made of 1.6 mm thick sheet specimens of an Al alloy with strain hardening exponent  $n = 0.052$ .  $w_i$  was found to be essentially independent of specimen geometry. However, for  $w_e$ , the specimen geometry independence could not be established with the SENT specimens, because deformation by rotation caused the loading geometry to change as fracture progressed, and geometrical similarity could not be maintained. Subsequently, however, for tests on polymeric sheets with sharp notched DENT and SENT specimens gripped across the entire

width, generally  $w_e$  values were found to be some 10-15% higher for the SENT geometry compared to the DENT geometry, and thus generally consistent with geometry independence of  $w_e$  [15, 16, 102, 106]. These studies also confirmed that  $\beta w_p$  shows strong dependence on specimen geometry, and therefore does not qualify as a material parameter. Apparently this transferability issue has never been examined for  $\delta_c^e$  or  $\psi^e$ . It also appears that apart from this first (failed) attempt by Mai and Cotterell [45], this geometry independence of  $w_e$  has not been sought to be established by testing both DENT and SENT specimens of metallic sheets.

The brief survey presented above underscores the potential of the EWF method for both routine quality control and material qualification, as well as integrity assessment of automotive and similar grade steels.

## **2.7 Cohesive zone modelling (CZM) simulation of ductile fracture**

The development of computational techniques provides an alternative method of integrity assessment of a component, by numerical simulation of the fracture process. Such efforts, however, have been mainly restricted to thick components: a constitutive description of the material behaviour in the process zone, which can mirror the local loss of stress carrying capacity, is difficult in thin sheets due to the presence of necking, tunnelling, and large plastic deformation at the crack tip. The two alternative approaches that have been adopted for the numerical simulations are reflected in the micromechanical damage models, and phenomenological cohesive models.

Several damage models based on the micro-mechanism of ductile rupture i.e., nucleation, growth and coalescence of voids, have been developed [72, 107]. For example, the well known Gurson, Tvergaard and Needleman model (GTN model) [72, 73] has been used for characterizing ductile crack growth especially in thick plates [71, 108] and also to a limited extent in thin sheets [109-111]. A micromechanical model can easily take into account the constraint effects (specimen size and geometry), and can describe the fracture mode: flat or slant. The main problem in applying a micromechanical damage model is the difficulty in

determining the values of a large number of micromechanical material parameters (GTN model needs eight parameters) [112]. Moreover, the use of damage models for large scale simulations can be difficult as the requirement of fine mesh resolution can lead to enormous CPU time requirements. As such application of GTN model, for example, is limited to research purposes; it has not been popular for industrial applications [113].

In contrast, a cohesive zone model (CZM) is a phenomenological finite element model that considers fracture as a gradual process of crack initiation and propagation where crack appears in the cohesive zone. Thus, unlike a micromechanical model such as the GTN model, CZM requires a pre-defined crack path along the boundaries of solid elements. For this, particular surface elements are introduced at the boundaries of solid elements and the constitutive relation of these interface elements represents its effective mechanical behaviour. For mode I crack growth, fracture resistance is simulated by normal cohesive traction,  $T_n$ , and the corresponding normal separation,  $\Delta_n$ , related by the traction-separation law (TSL) or cohesive law. As the surface begin to separate, the opening stress first increases until a maximum is reached and then it gradually decreases to zero, which results in complete separation. The variation in  $T_n$  with  $\Delta_n$  is plotted on a curve known as traction-separation curve. The area of the curve is the energy needed for separation. Since the model is sensitive to the shape of the TSL, the cohesive parameters cannot be considered as model-independent material parameters. Cohesive laws can also be established for mixed mode separation processes, which will require an additional stipulation on the interaction of tensile and shear modes.

The main advantage of the CZM over micromechanical models (including the GTN model) is that as few as two parameters, i.e. a cohesive strength and a critical separation, can define the cohesive law. Thus CZM numerical simulations of crack growth in metals are less susceptible to convergence problems. Another important advantage of CZM simulations compared to the continuum models of damage is that a CZM does not show pathological mesh dependence, and thus can be used with coarser mesh with reduced CPU time. A major drawback of CZM is the restriction to pre-defined crack paths along the boundaries of solid elements. Also, as the TSL is purely phenomenological, its parameters cannot be directly

experimentally measured, and must be determined by fitting of finite element results to experimental data.

Various TSL relations have been proposed in the literature for simulating mode I crack growth. Needleman [114] was the first to propose in 1987 a potential based on a polynomial function. Subsequently, in 1990, Needleman [115] proposed an exponential potential to accommodate large shear displacements. In 1992, Tvergaard and Hutchinson [116] proposed a trapezoidal law. However, the stiff slope often led to numerical problems in compatibility between the cohesive elements and the surrounding continuum elements. This problem was to some extent mitigated by the modified trapezoidal law introduced Cornec et al in 2003 [117]. Though this model was more realistic, it failed to properly simulate softening behaviour of ductile metals.

Park et. al. [118, 119] proposed the cohesive PPR model where polynomial based potential is defined for the cohesive interaction (softening) region where fractured surfaces transfer cohesive tractions. This potential can successfully model both mode I and mixed mode crack propagations [118, 120]. Since its introduction, this model has been applied mainly for thick brittle material [119, 121] and to a limited extent for thin ductile specimens [122]. Figure 2.1 presents a schematic diagram for a PPR model TSL. The mode I cohesive traction-separation ( $T_n$ - $\Delta_n$ ) PPR law takes the form [123] (Fig. 2.1)

$$T_n = \left(\frac{\Gamma_0}{\delta_n}\right) \left(\frac{\alpha}{m}\right)^m \left(1 - \frac{\Delta_n}{\delta_n}\right)^{\alpha-1} \left(\frac{\alpha}{m} + \frac{\Delta_n}{\delta_n}\right)^{m-1} (\alpha + m) \frac{\Delta_n}{\delta_n} \quad (2.9)$$

Here,  $T_n$ = normal (mode I) cohesive traction;  $\Gamma_0$ = mode I cohesive energy;  $\Delta_n$ = normal opening displacement,  $\delta_n$  = final value of  $\Delta_n$  at which  $T_n = 0$ ; and  $\alpha$  is a shape parameter defining the softening part of the traction-separation law.

$m$ , the non-dimensional exponent, is written as

$$m = \alpha(\alpha - 1)(\delta_c/\delta_n)^2/(1 - \alpha(\delta_c/\delta_n)^2) \quad (2.10)$$

where,  $\delta_c$  is the critical crack opening displacement at crack initiation, at which  $T_n = T_0$ , the maximum traction. There are thus four independent unknown parameters:  $\Gamma_0$ ,  $T_0$ ,  $\delta_c$  and  $\alpha$ , which need to be determined in order to fully define

this cohesive interaction. It may be noted that CZM simulation of crack growth in thin sheets is rather rare in literature.

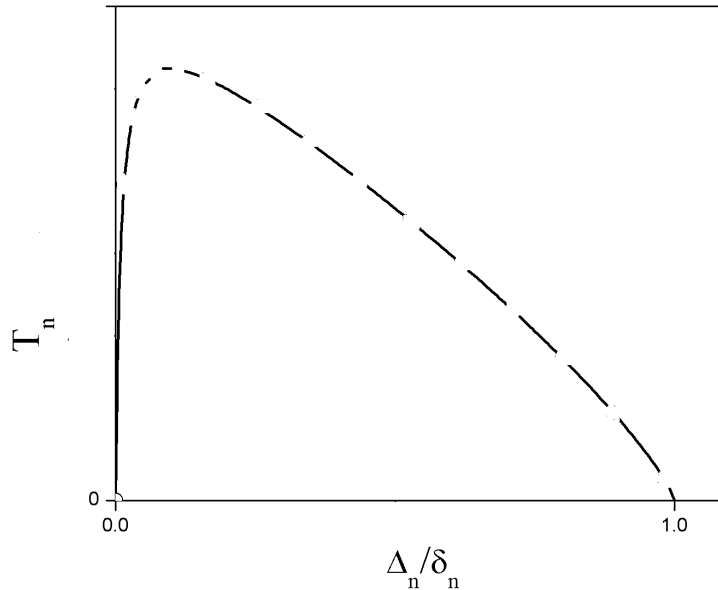


**Figure 2.1:** Schematic diagram of TSL law for ductile materials, the PPR law

## 2.8 Tearing resistance of automotive grade steel sheets

Apparently, there are only a few reports in open literature on characterizing tearing resistance of automotive grade steel sheets. ASTM E2472 standard [33], discussed in Section 2.4, is the only standard available for characterizing tearing resistance of ductile sheet metals. The value of critical CTOA  $\varphi_c$  of a 1 mm thick interstitial free high strength steel sheet has been determined by testing 200 mm wide CT specimens (with anti-buckling guides) following the optical method of this standard [89]. The testing procedures of this standard are rather demanding with respect to experimental resources and operator skill. This section summarises some important results reported for automotive (and similar) grade steel sheets obtained by adopting other test methods.

All the experimental results reported in this paragraph were obtained by testing DENT specimens. For DP 780 and 1000 grade steel sheets, Dot [19] determined the EWF parameter  $w_e$ . Also, crack initiation energy per unit ligament area  $w_i$  were determined for specimens with  $l$  in the EWF validity range;  $w_{ie}$  determined from linear fit of the  $w_i - l$  data (see Eq.(2.8)) was proposed as a material characterizing

parameter. High resolution videography was used for detecting crack initiation. Similarly,  $w_e$  values have been determined by testing sheet specimens of DP steel [124], a transformation-induced plasticity (TRIP) grade steel [125] and an advanced high strength steel (AHSS) [126]. For a DP grade steel sheet, Martin et al. [127] determined  $w_e$  at 1000 and 1200 °C and successfully used this  $w_e$  value for optimizing the microstructure. It will be noted that none of these studies examined the displacement based EWF parameters  $\delta_c^e$  or  $\psi^e$ . More recently, systematic studies have been carried out on characterizing crack initiation and growth in DP 590 and DP 780 grade automotive steel sheets in terms of the three EWF parameters  $w_e$ ,  $\delta_c^e$  and  $\psi^e$  [41, 92]. As recorded in Section 2.6, several important results were derived from these studies, such as close similarity of the values of EWF parameter  $\psi^e$  and critical CTOA  $\varphi_c$  determined by an optical method closely adapting the ASTM E2472 for DENT specimens.

Since the reports cited in the last paragraph had tested only DENT specimens for obtaining the results, whether any crack initiation or growth parameters examined is independent of specimen geometry could not be examined. Further, no attempts had been made for determining the standard fracture mechanics crack initiation parameters  $J_c$ ,  $\delta_c$ , and comparing these with their EWF counterparts  $w_e$ ,  $\delta_c^e$  respectively. Similarly, it will be interesting to compare crack growth characterization by different approaches, particularly the parameters for stable crack growth regime ( $\psi^e$  from EWF,  $\varphi_c$ ,  $\varphi_c(\delta_5)$  and  $R_\infty$ ) in terms of their physical significance. A related issue is the possible additional insight from CZM simulations of crack growth in the test specimens. These aspects were taken into consideration in framing the Objectives (Section 1.2) and the Scope of the present research (Section 1.3) is presented in the previous chapter.





## 3.1 Test Material

The test material for the research reported in this thesis is a 1 mm thick cold-rolled Interstitial-free (IF) steel with chemical composition (wt%): C - 0.0018; Mn - 0.064; Si - 0.002; P - 0.009; Al - 0.0359; N - 0.0018; Ti - 0.04 and balance Fe. Truly the investigated material belongs to the high-strength category of IF steel. The material was received from M/s TATA Steel, Jamshedpur, India. A small specimen sawed from the as-received steel sheet was used for the development of microstructure using standard metallographic technique. In this effort, the specimen was metallographically polished in successively finer silicon carbide base emery papers and finally cloth polished using alumina suspension. After final polishing, the specimen was thoroughly cleaned in water and then in acetone. The polished and cleaned specimen was etched using modified Lopera reagent and observed in an optical microscope, Leica 2500M. Optical images of the microstructure were captured using a digital camera and stored in a personal computer for grain size analysis. The analysis of grain size was carried out using an automatic image analyser, Leica Materials Workstation. The as-received material has an average grain size of 8.1 micron in LT direction and 8.3 micron in TL direction (Fig 3.1).

## 3.2 Experimental procedures

Mainly the four following test methods have been used for the present study. In some cases, minor modifications of these experimental procedures have been adopted. Also occasionally additional test procedures have been adopted. These modifications and additions are described in the relevant chapters. All the mechanical tests have been conducted in a computer controlled servo-hydraulic universal testing machine of  $\pm 100$  kN capacity, INSTRON 8501R, under ambient condition ( $\sim 25^\circ\text{C}$ ).

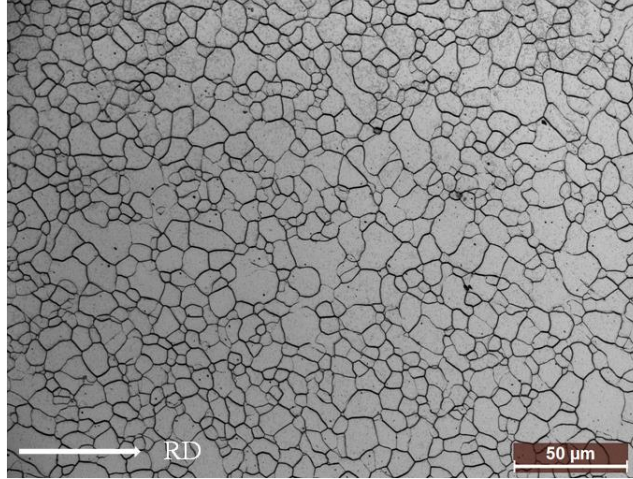


**Figure 3.1:** Microstructure of IF steel (RD is the Rolling direction)

### 3.2.1 Tensile testing

Dog-bone tensile specimens were fabricated keeping long axis of the specimens parallel to the rolling direction. Tensile tests have been conducted under strain-control mode at three different strain rates of  $10^{-2}$ ,  $10^{-3}$  and  $10^{-4}$   $s^{-1}$  in the testing machine using INSTRON BlueHill tensile test software. A tensile extensometer with 25 mm gauge length and full range capacity of the +50% to -10% was used for these tests. Tensile properties obtained at three different nominal strain rates are reported in Table 3.1.

The tensile test records did not show any evidence of strain aging and its Young's modulus ( $E$ ) is 142.7 GPa. With a 100-fold increase in the nominal (quasi-static) strain rate, the yield stress  $\sigma_y$ , ultimate tensile strength  $\sigma_u$ , and strain hardening exponent  $n$  increased respectively by 13.6%, 7.4% and 2.9%, whereas the percentage of elongation to failure decreased by 4.5%.

**Table 3.1:** Tensile properties of the test material at different strain rate

Strain Rate ( $s^{-1}$ )	Yield Strength (MPa)	Tensile Strength (MPa)	Total Elongation (%)	Strain hardening exponent ( $n$ )
$10^{-4}$	162	324	44	0.241
$10^{-3}$	168	338	43	0.247
$10^{-2}$	184	348	42	0.248

### 3.2.2 EWF testing

DENT and SENT specimens of size  $90 \times 30 \times 1$  mm with different ligament lengths ( $l$ ) were machined in longitudinal (L-T) orientation having dimensions free length  $H = 60$  mm, width  $W = 30$  mm, thickness  $t = 1$  mm and notch tip radius  $\rho = 0.1$  mm (Fig. 3.2). The specimens do not buckle in tensile loading, and hence, do not require anti-buckling guides during tests, making the experimentation simpler.

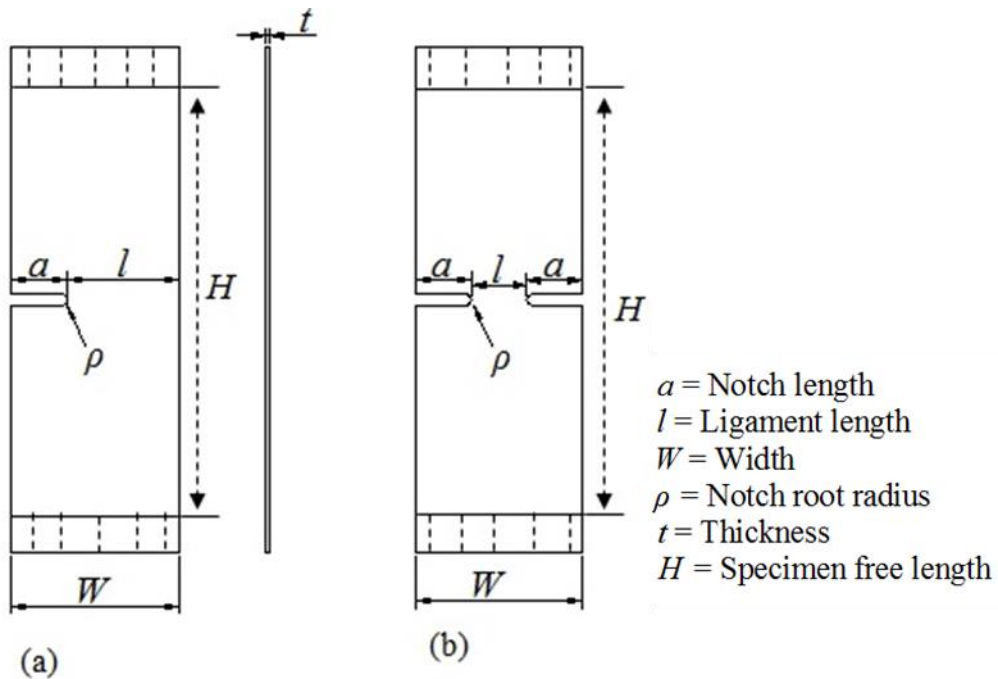


**Figure 3.2:** Schematic diagram of (a) SENT and (b) DENT specimen

The EWF testing of the notched ( $\rho = 0.1$  mm) specimens (SENT and DENT) were conducted by tensile loading the specimens at three different ramp rates of 0.6, 0.06 and 0.006  $\text{mm}\cdot\text{s}^{-1}$ , corresponding to nominal strain rates of  $10^{-2}$ ,  $10^{-3}$  and  $10^{-4}$   $\text{s}^{-1}$ . An extensometer with 25 mm gage length and 50% range was used for the EWF testing. Specimen ramping was stopped at 90% drop from the peak load, to prevent any potential damage to the extensometer, and also to preserve the fracture surface for subsequent fractographic observations. During the test, load ( $P$ ), gage extension ( $v$ ), and actuator displacement ( $v_a$ ) data were recorded in the computer for subsequent analyses. The EWF testing was also carried out for pre-cracked specimens at a ramp rate of 0.006  $\text{mm}\cdot\text{s}^{-1}$  following the procedure described for the notched specimens.

### 3.2.3 Fatigue pre-cracking the specimens

ASTM E1820-01 standard [7] *inter alia* prescribes the guidelines of fatigue pre-cracking the thick C(T), SEBT and disk-shaped C(T) specimens. In absence of a suitable testing code for fatigue pre-cracking of metallic sheet specimens of DENT and SENT geometry, it was decided to be guided by the prescriptions of ASTM E1820-01. Fatigue pre-cracking for either DENT or SENT specimens was conducted under load controlled mode using a sinusoidal tension-tension load waveform with a load ratio of 0.1. The target crack extension by fatigue pre-cracking a DENT or a SENT specimen for EWF testing was only about 0.5 mm. ASTM E1820-01 code specifies that the maximum load during fatigue pre-cracking should be less than limit load,  $P_L$ . For fatigue pre-cracking the notched DENT specimens,  $P_L$  for DENT specimens in plane stress condition was first estimated from the equation (Ref [9], Table A 9.15),

$$P_L = (4/2\sqrt{3})tl\sigma_{flow} \quad (3.1)$$

where  $\sigma_{flow}$  is the flow stress, taken as the average of yield and tensile strengths. For the present campaign, throughout fatigue pre-cracking, the maximum loads for fatigue cycling  $P_{max}$  was kept as at  $\leq 30\%$  of current  $P_L$ . In fatigue pre-cracking a DENT specimen, maintaining the symmetry of fatigue crack growths from both the crack starter notches is a major concern. While pre-cracking a specimen, after every  $\sim 5000$  cycles, (i) the fatigue cycling was stopped; (ii) the extents of crack growths were optically measured on both notch tips on both surfaces to determine the average values of crack growth and also any asymmetry; (iii) the specimen was flipped (alternately vertically and horizontally) to facilitate symmetry and uniformity of the fatigue crack growths at both notches on both sides; and (iv) the quantum of load shedding for the next fatigue cycling step was decided based upon prior experience and also the accumulating results, to keep  $P_{max}$  at  $\leq 30\%$  of current  $P_L$  to ensure sufficiently small crack growth during the next  $\sim 5000$  cycles. (For the very small extents of crack growths involved in each step, it is not practicable to plan the load shedding based on the accumulating  $\Delta K - \Delta a$  data). The average fatigue crack extensions were used in all computations. The maximum difference of the both notch tip pre-crack length of DENT specimens was about 0.05 mm. A

typical pre-cracking campaign required about 80,000 cycles. For SENT specimens in plane stress condition,  $P_L$  was computed as (Ref [9], Table A 9.15),

$$P_L = 1.072 \eta t l \sigma_{flow}, \text{ with } \eta = \sqrt{1 + \left(\frac{a}{l}\right)^2} - a/l \quad (3.2)$$

In this case, and specimen flipping was not necessary. As could be anticipated, fatigue pre-cracking is considerably simpler with the SENT specimens with single crack starter notch, than with the DENT specimens with two crack starter notches.

### 3.2.4 Testing for CTOA determination

Pre-cracked DENT specimens, and pre-cracked as well as notched SENT specimens have been tested for CTOA determination by a method that adapts the essence of the optical method of ASTM E 2472 [33]. CTOA values have been determined at three different ramp rates of 0.6, 0.06 and 0.006 mm.s<sup>-1</sup>. In this test, the specimen was first polished to metallographic finish. Then (i) the specimen was loaded at the chosen ramp rate up to a pre-determined actuator displacement; then (ii) the actuator movement was arrested and load was allowed to relax; and finally (iii) the specimen was unloaded to a load value of ~1 kN. This load-relax-unload sequence (Fig. 3.3) was repeated several times – and the whole load-displacement curve was generated.

During the each relaxation step, the crack tips visible on the specimen's surfaces were photographed by using a light microscope integrated with a digital camera. By this technique, a series of photographs was obtained for each test and these photographs were used for further analysis. The unloading step was included to have an alternative means to calculate the crack length using elastic compliance method, if optical measurement of crack tip were found unsatisfactory due to large crack tip tunnelling in thin sheets; however, it transpired that this was redundant, at least for the present tests. The actual method of determining CTOA values from each set of the photographs is explained with actual set of test data, see Section 4.3.3.

Though the test has been introduced here as the CTOA determination, it transpires that the data from this test can be used for determining  $R - \Delta a$  curves

(section 8.3.1). Also, as shown in Chapter 7 (section 7.2), the same basic experimental procedure with minor modifications, can be used to determine the  $\delta_5$  -  $\Delta a$  curves.

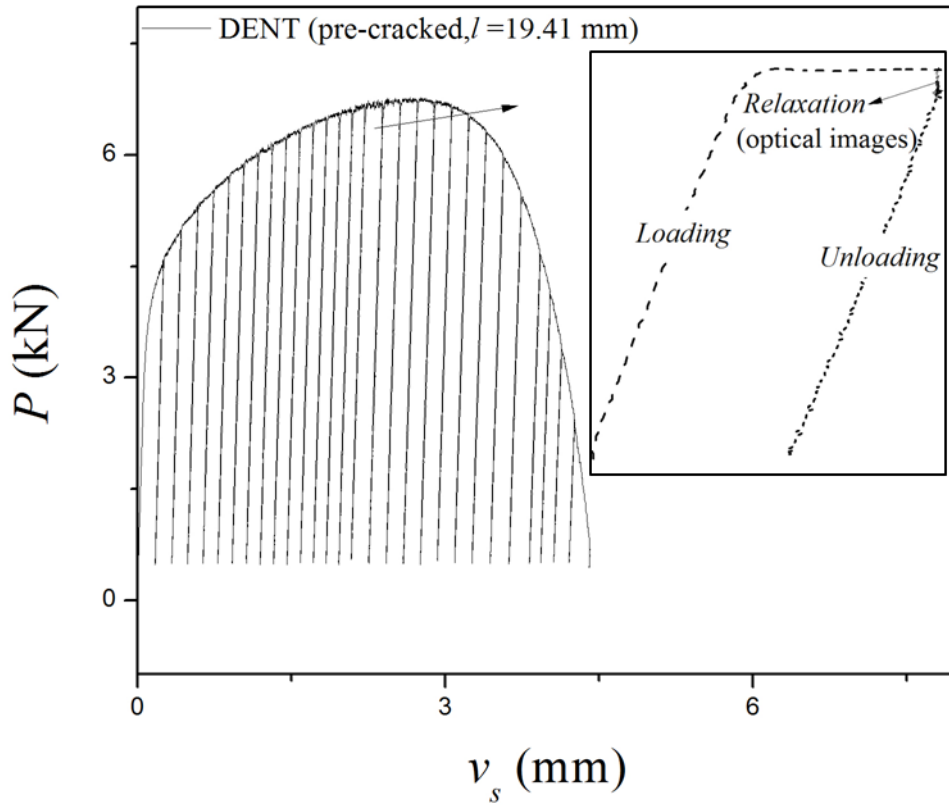


**Figure 3.3:** Representative  $P - v_s$  plot showing loading-relaxation-unloading sequences in CTOA testing, Inset shows enlarged view for one such cycle.

## 4.1 Introduction

This chapter reports the results from characterization of crack initiation and growth in the test sheet material using DENT specimens. An important component of this study is generating EWF parameters  $w_e$ ,  $\delta_c^e$  and  $\psi^e$  using notched and fatigue pre-cracked specimens. The influence of deformation rate and notch root radius on the EWF parameters are also examined  $\varphi - \Delta a$  plots have been generated by testing fatigue pre-cracked DENT specimens adopting the optical method described in Section 3.2.4, and analyzing the photographs thus obtained as described subsequently in Section 4.3.3. This enables comparing the crack growth parameter  $\psi^e$  from EWF test with its fracture mechanics counterpart,  $\varphi_c$ . As described in Section 4.3.4, a novel method has been developed for identifying the crack initiation event in ramped specimens with acceptable resolution. It involves comparing for a test specimen the load-displacement plot from the ramp test with the corresponding plot generated using 3-D large strain FE simulation of the ramp loaded specimens with non-growing cracks. With the crack initiation point identified, it becomes possible to determine the fracture mechanics initiation parameters  $J_c$ ,  $\delta_c$  for the test specimens with different ligament lengths. This enables comparing for the notched specimens the crack initiation parameters  $w_e$ ,  $\delta_c^e$  from EWF tests with their fracture mechanics counterparts,  $J_p^c$  (the plastic component of  $J_c$ ) and  $\delta_c$ , respectively.

## 4.2 Experimental details

EWF testing has been carried out with a set of ten notched ( $\rho = 0.1$  mm) DENT specimens with  $l$  in the range 2 to 10 mm, and also a set of six DENT specimens, fatigue pre-cracked following the procedure in Section 3.2.3, with  $l$  in the range 4.4

to 8.3 mm. The EWF tests were performed at a ramp rate of  $0.006 \text{ mm.s}^{-1}$  following the procedure in Section 3.2.2. In addition, sets of notched ( $\rho = 0.1 \text{ mm}$ ) DENT specimens with  $l = 2$  to  $10 \text{ mm}$  were tested at quasi-static ramp rates of  $0.06$  and  $0.6 \text{ mm.s}^{-1}$  in order to determine the effect of ramp rates on the EWF parameters of the present test material. The critical CTOA ( $\varphi_c$ ) values have been determined for three different quasi-static ramp rates of  $0.6$ ,  $0.06$  and  $0.006 \text{ mm.s}^{-1}$  by testing three pre-cracked DENT specimens with  $l$  range of  $19.41 \text{ mm}$  to  $20.06 \text{ mm}$ . The test procedure has been described in Section 3.2.4.

## 4.3 Results and discussion

### 4.3.1 EWF tests

#### 4.3.1.1 Determining the valid ligament length range

The  $v_f - l$  and  $w_f - l$  plots for notched DENT specimens (ramp rate =  $0.006 \text{ mm.s}^{-1}$ ) are shown in Figs. 4.1(a) - (b). From the linearity of these plots, the entire  $l$  range of  $2$ - $10 \text{ mm}$  appears acceptable for EWF analysis, though the corresponding minimum ligament of  $2 \text{ mm}$  clearly violates the “thumb rule” (Section 2.6) proposed by Cotterell and Reddel [39].

Figures 4.2(a)-(d) depict the variation of  $\sigma_n$  with  $l$  for the 4 sets of EWF tested specimens. For each of the data sets plotted, the  $0.9 \bar{\sigma}_n - 1.1 \bar{\sigma}_n$  band was defined following Clutton's [103] prescription. For each of the four data sets examined, the value of  $\sigma_n$  becomes nearly independent of  $l$  for the range  $l = 3 - 10 \text{ mm}$ , with average values much higher than  $\sigma_n \sim 1.15 \sigma_y$ , the value derived by Hill [101] for a rigid-ideal plastic sheet specimen in plane stress. Clearly, Hill's criterion does not apply for the present test material, with a very high strain hardening exponent. Compared to Hill's criterion, or Clutton's prescription, an empirical criterion  $\sigma_n \sim 1.15 \sigma_u$  appears to be a better choice for the present test material, especially for the pre-cracked specimens, Fig. 4.2(b). However, this is open to verification for other materials covering a wide range of strain hardening materials. Since Clutton's criterion is essentially statistical, it is possible that for applying this criterion, the number of specimens should be large. It appears that a mixed mode stress state develops in the notched specimen with  $l = 2 \text{ mm}$  for all deformation rates,



especially for the two higher rates, viz. 0.06 and 0.6 mm.s<sup>-1</sup>, Figs. 4.2(a), 4.2(c) and 4.2(d). Therefore, this ligament length was excluded for plane stress analysis. The plots Figs. 4.2(a)-(d) underscore the inadequacy of plots like Figs. 4.1(a) and 4.1(b) for identifying the  $l$ -validity range.

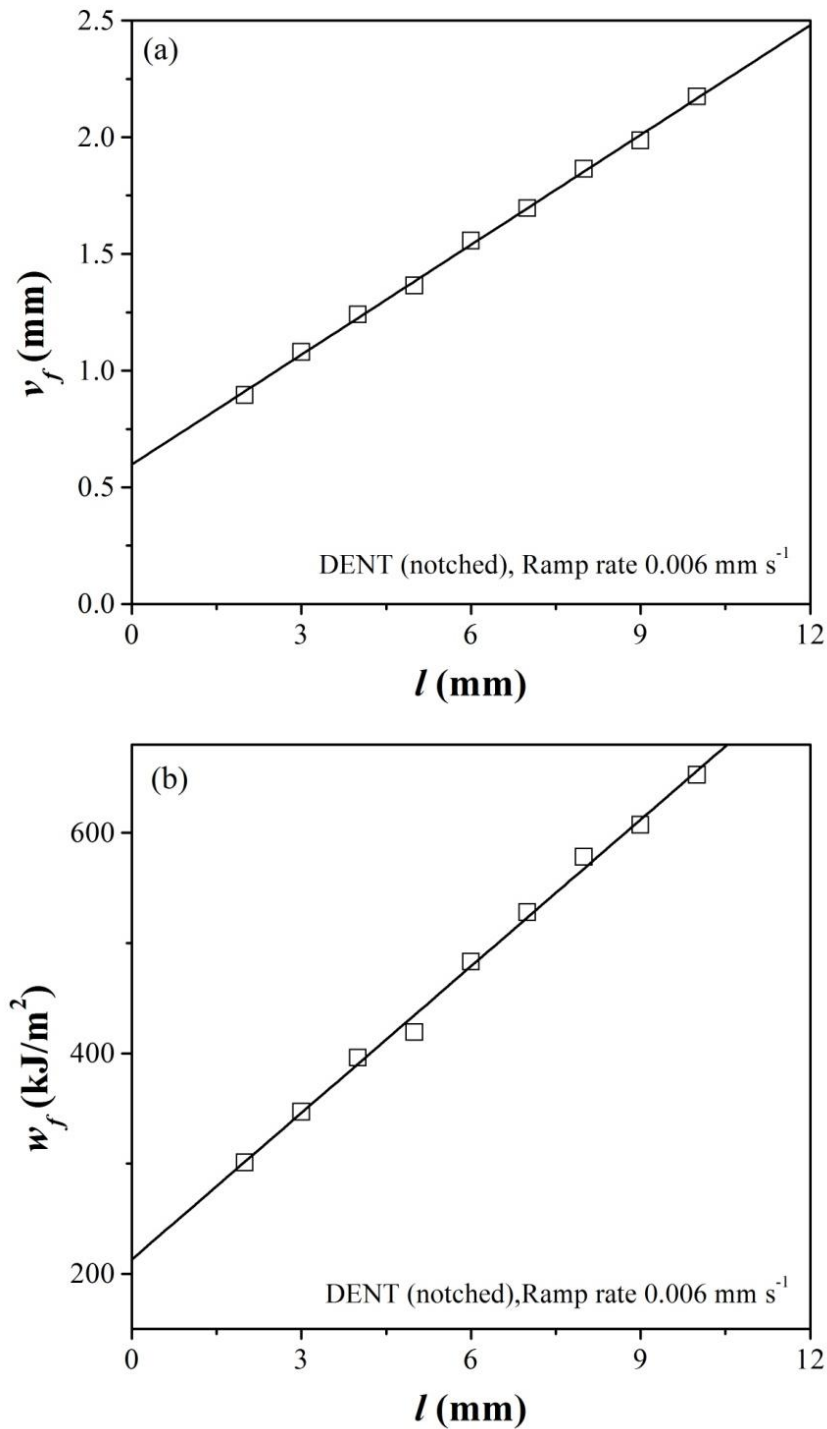
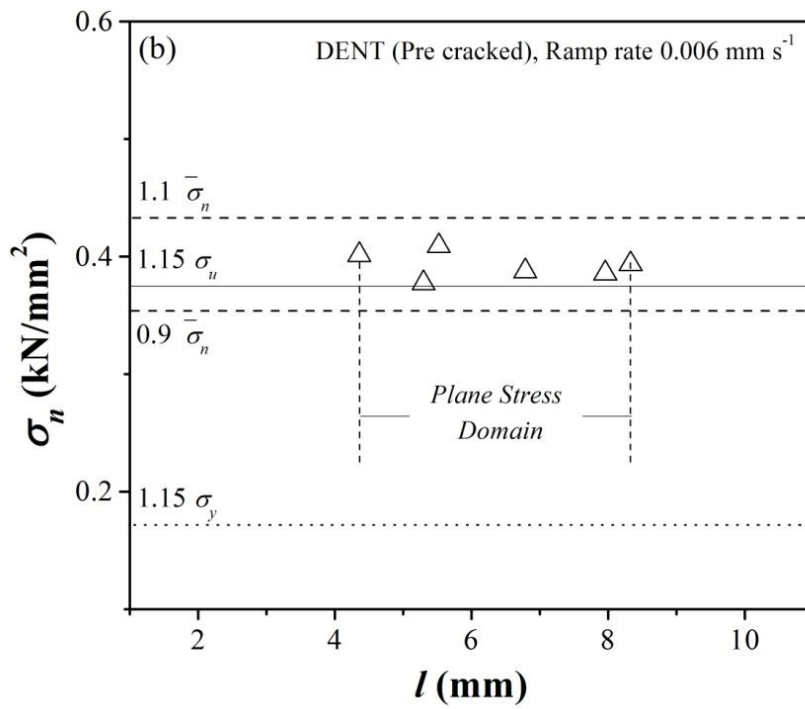
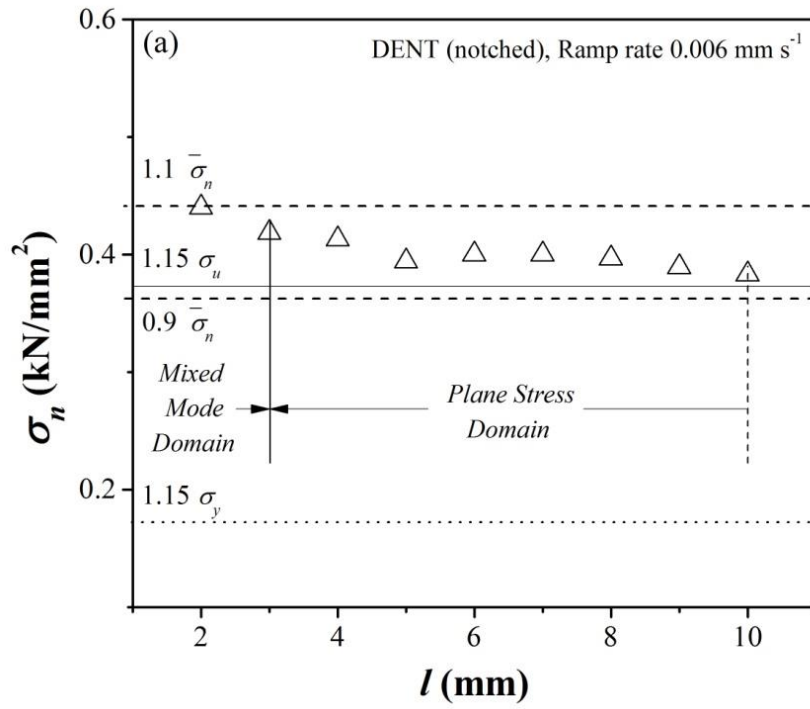


**Figure 4.1:** (a)  $v_f$ - $l$  and (b)  $w_f$ - $l$  plots with linear fits for determining valid  $l$  range for notched DENT specimens (ramp rate = 0.006 mm.s<sup>-1</sup>).



(Continued)

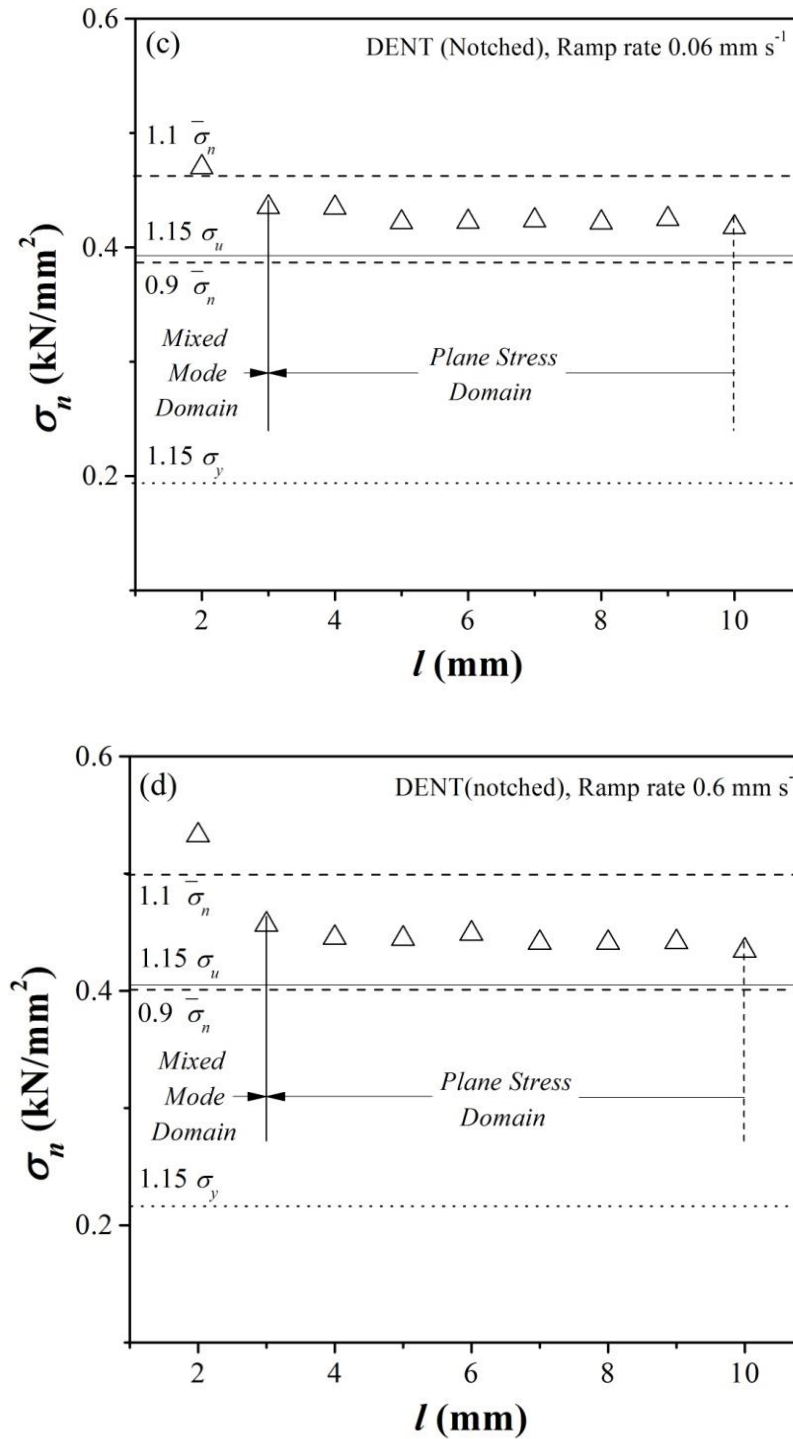


**Figure 4.2:**  $\sigma_n$ - $l$  plots to determine valid  $l$ - range for (a) notched DENT specimens (ramp rate =  $0.006 \text{ mm.s}^{-1}$ ); (b) pre-cracked DENT specimens (ramp rate =  $0.006 \text{ mm.s}^{-1}$ ); (c) notched DENT specimens (ramp rate =  $0.06 \text{ mm.s}^{-1}$ ); and (d) notched DENT specimen (ramp rate =  $0.6 \text{ mm.s}^{-1}$ ). In each figures, the pair of dashed horizontal lines define the  $0.9\bar{\sigma}_n$  -  $1.1\bar{\sigma}_n$  range for identifying  $l$ -validity range following the criterion of Clutton [103].

### 4.3.1.2 Effect of notch tip radius on the EWF parameters

The  $l$ -dependence of  $w_f$  and  $v_f$  data (within the  $l$ -validity range) for notched and pre-cracked specimens are compared in Figs. 4.3(a) and 4.3(b) respectively. Both these parameters show satisfactory linear dependence on  $l$ . Results for these linear fits are shown in Table 4.1. From these results, it can be inferred that the value of  $w_e$  and  $\delta_c^e$  are significantly reduced on reducing notch tip radius ( $\rho$ ) by fatigue pre-cracking: the value of  $w_e$  is reduced by  $\sim 48\%$  and of  $\delta_c^e$  by  $\sim 15\%$ . Similar observations have been reported by several other researchers [128, 129]. In the present instance, the value of  $\beta w_p$  increased by  $\sim 17\%$  by pre-cracking. In contrast to these results,  $\psi^e$  is found to be independent of  $\rho$ . Therefore, for integrity assessments, in terms of  $\rho$ -independence,  $\psi^e$  is a more convenient parameter than either  $w_e$  or  $\delta_c^e$ . Now,  $w_e$  and  $\delta_c^e$  are associated with the crack initiation phenomenon, whereas  $\psi^e$  characterizes crack growth. Therefore, the effect of crack tip blunting will be more pronounced for the parameters  $w_e$  and  $\delta_c^e$  than for  $\psi^e$  because after a certain amount of crack growth, the effect of crack blunting would become insignificant. Interestingly, the present results indicate that  $\delta_c^e$  is less sensitive to  $\rho$  than  $w_e$ , so the critical notch root radius  $\rho_{crit}^{\delta_c^e}$  for determining  $\rho$ -independent  $\delta_c^e$ , and the critical notch root radius  $\rho_{crit}^{w_e}$  for determining  $\rho$ -independent  $w_e$  are not expected to be the same: the percentages of variation in  $w_e$  ( $\sim 48\%$ ) and  $\delta_c^e$  ( $\sim 15\%$ ) with variation in  $\rho$  suggest that  $\rho_{crit}^{w_e} < \rho_{crit}^{\delta_c^e}$ .

Table 4.1 (Set 1) demonstrates negligible variations in the values for the parameters ( $w_e$ ,  $\beta w_p$ ,  $\delta_c^e$  and  $\psi^e$ ) calculated using either extensometer or actuator data. Therefore, all these parameters ( $w_e$ ,  $\beta w_p$ ,  $\delta_c^e$  and  $\psi^e$ ) could be determined by EWF tests using the actuator data, at least for the material under investigation. Rink et al [40] made similar observation and suggested the use of actuator travel as measure of displacement. A practical implication of this observation is: use of extensometer may altogether be avoided in EWF tests. Since these tests were stopped at 90% load drop from  $P_{max}$ , i.e., before final fracture, the values for displacements at fracture have also been approximated using linear extrapolation from the last segment of the load displacement plots. Though the choice of a linear extrapolation introduces a degree of subjectivity, Table 4.1 (Set 1 and Set 2) shows

that using extrapolated data (corresponding to 100% load drop from  $P_{\max}$ ) and actual test data (i.e., up to 90% load drop from  $P_{\max}$ ) give almost results. Thus, the final test data point (at 90% load drop from  $P_{\max}$ ) has been considered as the data point of final separation.

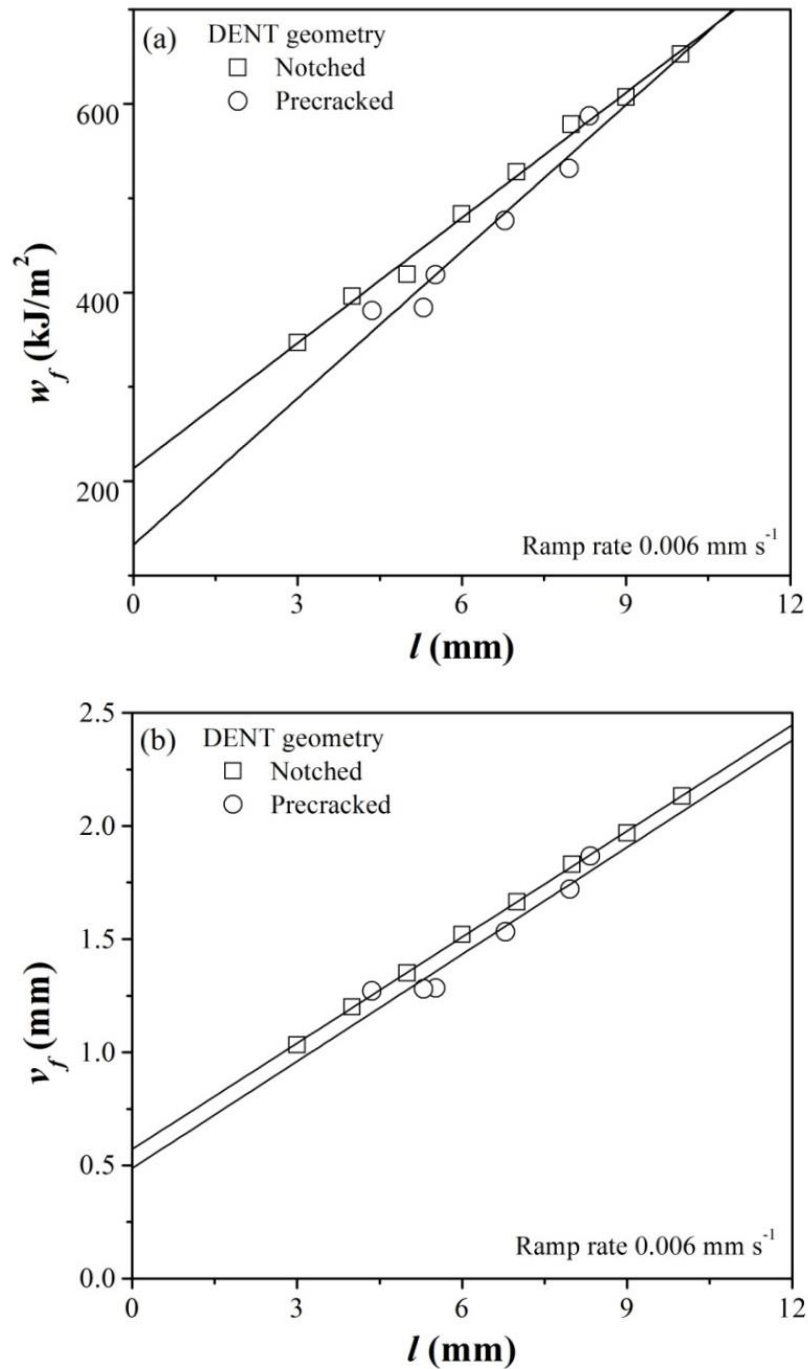


**Figure 4.3:** (a)  $w_f$ - $l$  and (b)  $v_f$ - $l$  plots of notched and pre cracked DENT specimens for ramp rate 0.006 mm.s<sup>-1</sup>. Firm lines show linear fits of the data.

**Table 4.1:** Comparison of  $w_e$ ,  $\beta w_p$ ,  $\delta_c^e$  and  $\psi^e$  for notched and pre-cracked DENT specimen calculated from extensometer and actuator data, with and without extrapolation. (Ramp rate 0.006 mm.s<sup>-1</sup>).

DATA SET 1 Test Data (90% load drop from $P_{max}$ )	(Results from extensometer data)						
	<b>Fitting Eq:</b>	$w_f = \beta w_p l + w_e$			$v_f = (\psi^e/2)l + \delta_c^e$		
	<b>DENT specimen</b>	$R^2$	$\beta w_p$ (MJ.m <sup>-3</sup> )	$w_e$ (kJ/m <sup>2</sup> )	$R^2$	$\psi^e$	$\delta_c^e$ (mm)
	Notched	0.997	44.26	213.62	0.999	17.9°	0.572
	Pre-cracked	0.997	51.83	132.7	0.967	17.99°	0.487
	(Results from actuator data)						
	<b>Fitting Eq:</b>	$w_{af} = \beta w_p l + w_e$			$v_{af} = (\psi^e/2)l + \delta_c^e$		
	<b>DENT specimen</b>	$R^2$	$\beta w_p$ (MJ.m <sup>-3</sup> )	$w_e$ (kJ/m <sup>2</sup> )	$R^2$	$\psi^e$	$\delta_c^e$ (mm)
	Notched	0.997	44.26	213.7	0.999	17.85°	0.578
	Pre-cracked	0.996	51.83	133.2	0.967	18.03°	0.492
DATA SET 2 Extrapolated data (100% load drop)	(Results from extensometer data)						
	<b>Fitting Eq:</b>	$w'_f = \beta w_p l + w_e$			$v'_f = (\psi^e/2)l + \delta_c^e$		
	<b>DENT specimen</b>	$R^2$	$\beta w_p$ (MJ.m <sup>-3</sup> )	$w_e$ (kJ/m <sup>2</sup> )	$R^2$	$\psi^e/2$	$\delta_c^e$ (mm)
	Notched	0.996	44.26	214.12	0.999	17.87°	0.580
	Pre-cracked	0.997	51.68	133.8	0.967	18.04°	0.490
	(Results from actuator data)						
	<b>Fitting Eq:</b>	$w'_{af} = \beta w_p l + w_e$			$v'_{af} = (\psi^e/2)l + \delta_c^e$		
	<b>DENT specimen</b>	$R^2$	$\beta w_p$ (MJ.m <sup>-3</sup> )	$w_e$ (kJ/m <sup>2</sup> )	$R^2$	$\psi^e/2$	$\delta_c^e$ (mm)
	Notched	0.996	44.26	214.2	0.999	17.79°	0.590
	Pre-cracked	0.996	51.48	134.8	0.967	18.1°	0.496

To obtain  $w_p$  from the value of  $\beta w_p$  determined from EWF test, it is necessary to know  $\beta$ . A circular plastic zone is usually associated with metallic material [2]. Figures 4.4(a)-(b) show the shapes plastic zones for notched DENT specimens having (a)  $l = 3$  mm and (b)  $l = 6$  mm. From these figures, it appears that for the present test material, the plastic zone is more of an elliptical shape for longer ligaments and circular for shorter ligaments. Similar observation has also been reported for zinc sheets [16]. Thus determining  $\beta$  factor is difficult, as a proper measurement of plastic zone shape is required. As locating the plastic zone

boundaries from the photographs like Figs. 4.4(a)-(b)) is difficult,  $\beta w_p$  is used instead of  $w_p$  throughout the present study.

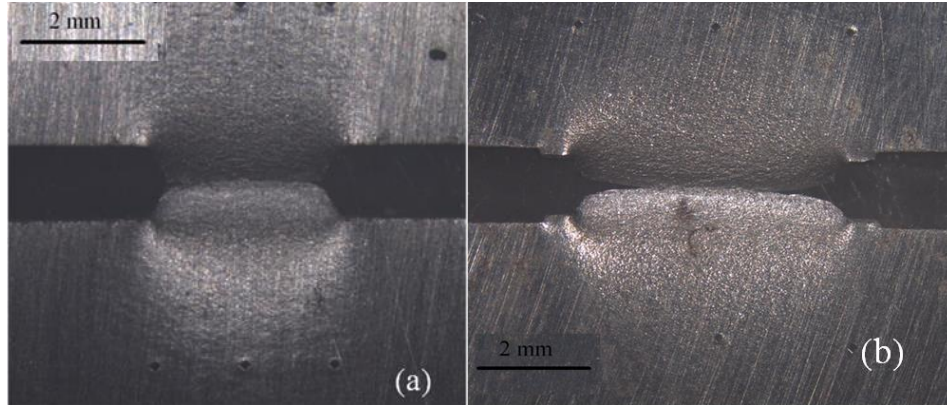


**Figure 4.4:** Shapes of plastic zones for notched DENT specimens with (a)  $l = 3$  mm and (b)  $l = 6$  mm.

#### 4.3.1.3 Effect of ramp rates on EWF parameters

The ramp rate has a significant effect on the  $P$ - $v_s$  traces of notched DENT specimens: the maximum load  $P_{max}$  increased with increase in ramp rate. The  $w_f$ - $l$  and  $v_f$ - $l$  plots for three different ramp rates of 0.6, 0.06 and 0.006 mm.s<sup>-1</sup> are shown in Figs.4.5 (a) and 4.5(b) respectively. To ensure that the selected data points belong to the plane stress regime, based on the results presented in Section 4.3.1, only data for  $l \geq 3t$  have been chosen.

Values for  $w_e$ ,  $\beta w_p$ ,  $\delta_c^e$  and  $\psi^e$  for the different ramp rates are presented in Table 4.2. From this Table, no clear trend in the variation of  $w_e$  with deformation rate is discernible, although  $\beta w_p$  is noted to increase with increase in ramp rate. This observation is consistent with the findings of other researchers [128, 130] for polymeric materials. The values of  $\delta_c^e$  depict clear increase with increase in ramp rate. The  $\psi^e$  parameter is found to be virtually independent ( $\sim 1.2\%$  variation) of deformation rate. However, it should be noted that the same conclusions may not hold good for dynamic deformation rates, where inertial effects would be important.

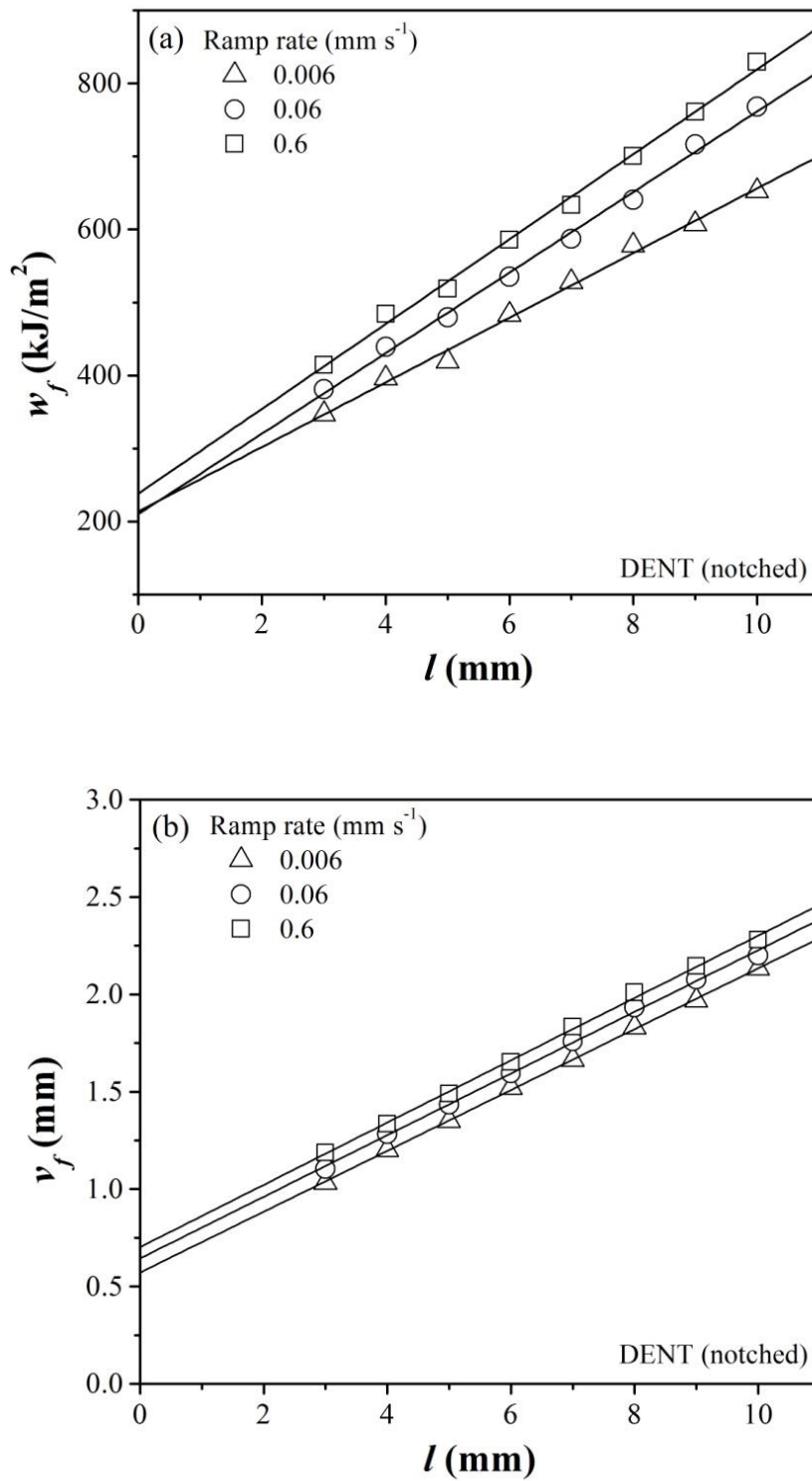


**Figure 4.5:** (a)  $w_f - l$  and (b)  $v_f - l$  plots for notched DENT specimens for three different ramp rates.



**Table 4.2:** Effect of ramp rate on tearing resistance parameters determined from EWF testing of notched DENT specimens for  $l = 3$  to 10 mm

Fitted equation:		$w_f = \beta w_p l + w_e$			$v_f = (\psi^e/2)l + \delta_c^e$		
Ramp rate (mm.s <sup>-1</sup> )	$R^2$	$\beta w_p$ (MJ.m <sup>-3</sup> )	$w_e$ (kJ.m <sup>-2</sup> )	$R^2$	$\psi^e/2$ ( $\psi^e$ )	$\delta_c^e$ (mm)	
0.006	0.997	44.26	213.62	0.999	0.1562 (17.9°)	0.572	
0.06	0.997	55.14	210.1	0.999	0.158 (18.10°)	0.64	
0.6	0.997	58.10	238.10	0.999	0.159 (18.22°)	0.70	

### 4.3.2 SEM of the fractured specimens

Scanning electron microscopy (SEM) of fatigue pre-cracked DENT specimens were ramp loaded to fracture reveals the different zones associated with the fracture process, Fig.4.6. The machined notch is followed by the fatigue pre-crack; this is followed by the stretched zone, where crack tip blunting takes place, prior to the onset of ductile fracture. It is observed from Fig.4.6 that the magnitude of specimen necking increases sharply over a short distance from the starting notch tip. Beyond this distance, necking reaches a constant value (maximum ~ 36% of  $t$ ) over the rest of the ligament. It may also be noted that the extent of crack tunnelling is not severe in Fig. 4.6, justifying the measurements of crack extension optically on the specimen surface for the present tests. Figure 4.7 shows a predominant flat fracture of the ligament. Clearly, there is no transition from flat to slant fracture in the present test material. The same observation has been made for all the ligament length values. Apparently, the extent of necking was adequate to restrain the initiated crack to grow in the flat mode.

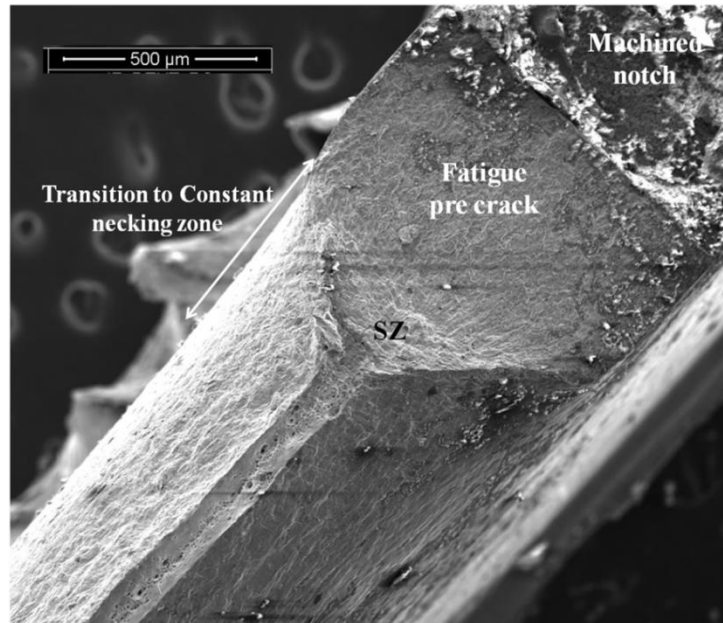


**Figure 4.6:** Representative scanning electron micrographs of different zones in the fracture ligament of the pre-cracked DENT specimen ( $l = 7.96$  mm).

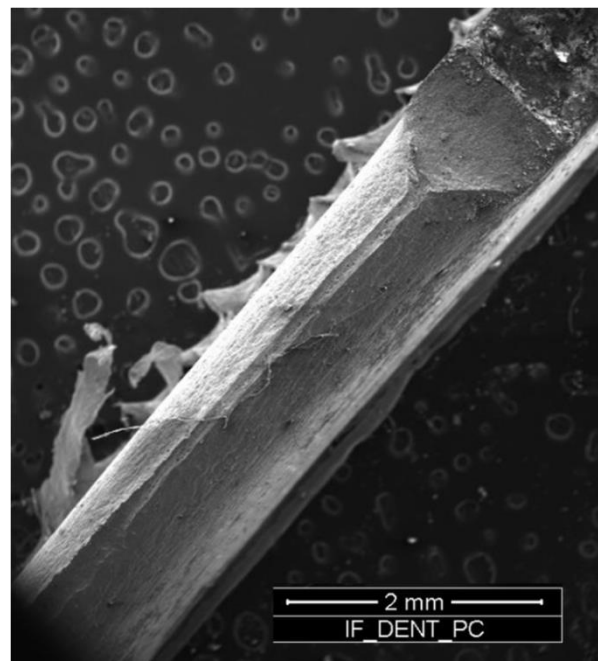


**Figure 4.7:** SEM image showing predominant flat fracture ( $l = 7.96$  mm).

### 4.3.3 CTOA ( $\varphi$ ) determination by optical microscopy

The results of CTOA measurements on fatigue pre-cracked DENT specimens are presented here. Following the test method described in Section 3.2.4, a series of

photographs was obtained for each test. From each photograph, CTOA was measured along with the crack extension,  $\Delta a$ , on the specimen surface. In the present study, the two-point method described in ASTM E2472 has been followed [23], where the crack tip is always included in the calculation of the CTOA. Thus firstly the crack tip in the photographs has been located, and then a pair of points along the crack profile, located at a distance in the range between 0.5 to 1.5 mm behind the crack tip have been selected for determining CTOA (Fig.4.8) using the following equation:

$$(\varphi)_{\Delta a} = \left( \frac{d_i}{L_i} \right)_{\Delta a} \quad (4.1)$$

Here,  $d_i$  is the distance between the two points located at the position  $i$ , and  $L_i$  is the distance between the crack tip and the location  $i$ . It should be noted that an accurate measurement of CTOA requires proper selection of length  $L$  [87]. A high value of  $L$  may introduce size and geometric effects on CTOA measurement. Following ASTM E2472 [33],  $L$  has been chosen in the range 0.5 to 1.5 mm.

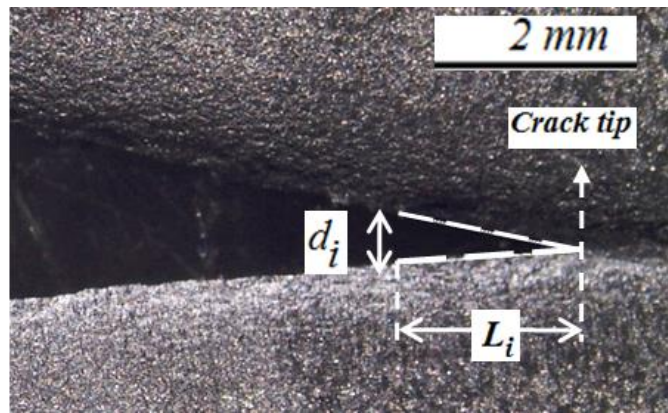


**Figure 4.8:** A representative photograph showing measurement of CTOA.

Figure 4.9 presents results from a test, where for each photograph, three CTOA measurements were carried out for  $L = 0.5, 1.0$  and  $1.5$  mm. From Fig. 4.9, it can be observed that the critical CTOA and the corresponding  $\Delta a$  remain unaffected by the choice of  $L$  in this range. For convenience, subsequent CTOA values for the tested specimens were determined only for  $L = 1.5$  mm behind the crack tip.

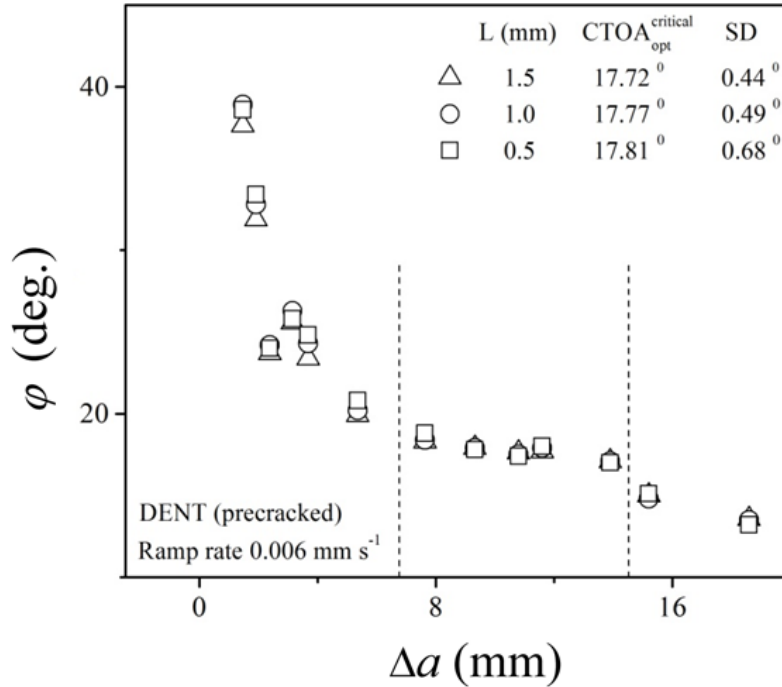


**Figure 4.9:** Choice of CTOA measurement basis  $L$  for DENT specimens. SD is the standard deviation computed for the stable CTOA values (determined for the chosen  $L$ ) between the two vertical bars.

The  $\varphi - \Delta a$  curves for different deformation rates have been plotted in Fig.4.10. The plot follows the usual trend: from high initial values, CTOA decreases, and as the crack growth stabilizes it reaches a fairly constant value. It may be noted that the transition distance for all the cases is  $\sim 5.5$  mm with a negligible variation of less than 2%. This is the distance over which the crack traverses to attain a steady CTOA value,  $\varphi_c$ . For the three ramp rates, Table 4.3 compares the  $\varphi_c$  optically determined with fatigue pre-cracked specimens, with the corresponding  $\psi^e$  estimated from linear extrapolation of the EWF test data for notched DENT specimens with ligament lengths  $l = 3 - 10$  mm has been shown in Table 4.3 (Data Set 1). The maximum difference between the  $\varphi_c$  and  $\psi^e$  values is only 4%. Evidently,  $\psi^e$  determined from EWF testing of notched DENT specimen can very well be used as a measure of the critical CTOA ( $\varphi_c$ ). Similar comparison has also been made for  $\psi^e$  determined with notched DENT specimens with  $l = 6 - 10$  mm (Data Set 2, Table 4.3). Ligament lengths in this range exceed the minimum transition distance ( $\sim 5.5$  mm) before onset of the stable regimen evaluated from the  $\varphi - \Delta a$  curve (Fig. 4.9). It is found that for this ligament length range, the maximum difference

between  $\psi^e$  and  $\varphi_c$  is further reduced to 2%. It would be interesting to examine this aspect with larger number of specimens with ligament lengths higher than the maximum value used in the present study.

**Table 4.3:** Comparison of  $\varphi_c$  for pre-cracked DENT specimens with  $\psi^e$  from EWF tests for notched DENT specimens at three quasi-static ramp rates

Ramp rate (mm.s <sup>-1</sup> )	$\varphi_c$ (pre-cracked specimens)	Data set 1		Data set 2	
		$l$ (mm)	$\psi^e$ from EWF	$l$ (mm)	$\psi^e$ from EWF
0.006	17.72 <sup>0</sup>		17.90 <sup>0</sup>		17.54 <sup>0</sup>
0.06	17.6 <sup>0</sup>	3-10 (Notched)	18.10 <sup>0</sup>	6-10 (Notched)	17.54 <sup>0</sup>
0.6	17.5 <sup>0</sup>		18.22 <sup>0</sup>		17.91 <sup>0</sup>

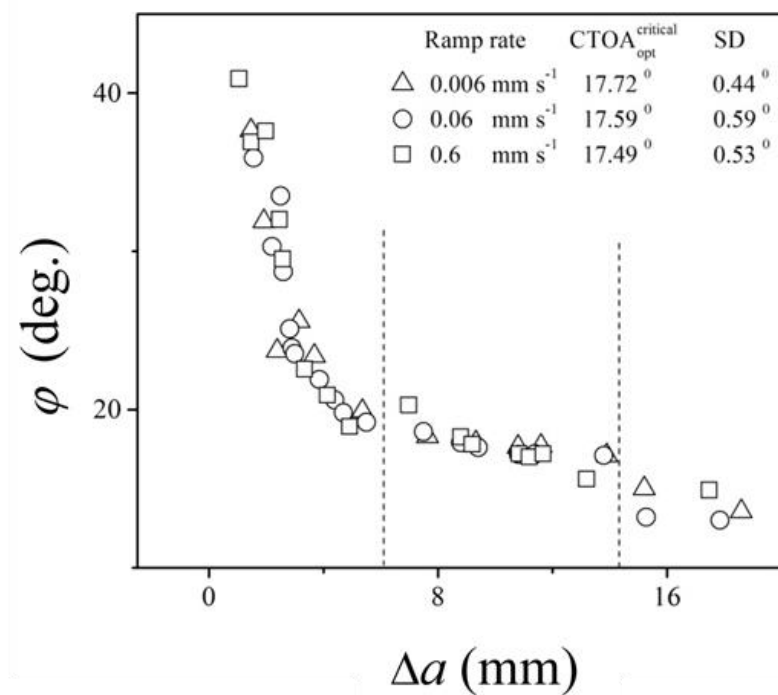


**Figure 4.10:**  $\varphi - \Delta a$  plots for fatigue pre-cracked DENT specimens at three different deformation rates.

### 4.3.4 Crack initiation parameters

#### 4.3.4.1 FE simulation for identifying crack initiation event

In order to determine the fracture mechanics based crack initiation parameters  $J_c$ ,  $\delta_c$  or even  $w_i$ , the energy for crack initiation, it is necessary to first identify the crack initiation event during ramping a specimen, such as in the course of an EWF test. The brief review on this point in Section 2.2 concluded that there is a need for exploring for a suitable method for identifying crack initiation in sheet specimens, particularly DENT and SENT specimens. For the research reported in the present thesis, the crack initiation points are determined by a novel method comparing mechanical test data from EWF tests with results from a 3-D large strain FE formulation for non-growing crack. Obviously, a crack initiation point thus identified would refer to a point averaged for the variation of through thickness constraint. It makes sense to carry out this comparison using variation of load with specimen free length extension,  $v_s$ .  $v_s$  values for the mechanical test data were determined from the actuator displacement values using the equation:  $v_s = v_a - C_M P$ , where  $C_M$  is the “machine” elastic compliance, i.e., the elastic compliance of the entire load train excluding the free length of the specimen. In the present study  $C_M = 0.01305 \text{ mm.kN}^{-1}$  has been determined using a simple calibration procedure developed earlier [41]; the estimated accuracy of the computed  $v_s$  values was about  $3 \mu\text{m}$ .

For the first step, 3-D time independent large strain FE simulations for non-growing crack had been carried out for all the notched DENT specimens ( $l$  range: 3 to 10 mm) for ramp rate of  $0.006 \text{ mm.s}^{-1}$ . The finite element software, ABAQUS 6.10 was used for these simulations, and 3-D 8 node solid hexahedral elements C3D8R with reduced integration and 1 integration point were used. The elastic-plastic tensile material properties determined for nominal strain rate of  $10^{-4} \text{ s}^{-1}$  (Section 3.1) which corresponds to the chosen ramp rate were assumed for these elements. The simulations were continued well beyond the maximum load in each case. It was assumed that the Hollomon work hardening relationship ( $\sigma = k\varepsilon_p^n$ ), with parameter values determined using data up to maximum load (Section 3.2.1), could be applied for the entire strain range covered in the simulations.

For the specific case of notched ( $\rho = 0.1$  mm) DENT specimen with  $l = 10$  mm, FE simulations for non-growing crack have been carried out using a mesh size of 0.2 mm around the notch and 1 mm in the rest of the specimen (i.e., in-plane dimension of the elements was 0.2 mm  $\times$  0.2 mm around the notch to accommodate large deformation and the element size gradually increased to 1 mm  $\times$  1 mm away from notch). The elements had 0.125 mm, 0.1 mm or 0.05 mm widths along the thickness of the sheet specimen (i.e., 8, 10 or 20 layers along the specimen thickness direction). The computed  $P - v_s$  data for these three sizes of meshing along thickness showed excellent matching, with maximum difference in  $P$  being 0.15% at the highest  $v_s$  value of 1.8 mm, Fig. 4.11(a). Thus the element of thickness 0.125 mm along thickness direction is adequate for identifying crack initiation with acceptable accuracy, without unduly increasing the computational burden. The mesh convergence has been verified for the same DENT specimen with  $l = 10$  mm, keeping the through thickness element size fixed at 0.125 mm, while the in-plane mesh size gradually increasing from 0.1  $\times$  0.1 mm (in place of 0.2  $\times$  0.2 mm) around the notch to 1  $\times$  1 mm away from the notch. Even after such considerable refinement in mesh sizes near the notch with consequent drastic increase in the computational burden, at the highest  $v_s$  level of 1.8 mm, the difference in the computed  $P$  was only 0.13%, Fig. 4.11(b). Thus, it was concluded that for the intended application, in plane minimum mesh size of 0.2 mm is adequate.

As mentioned above, these simulations were carried out to identify the crack initiation points. Figure 4.12 shows an example; it compares the experimental, and the simulated  $P - v_s$  plots of notched DENT specimen with  $l = 10$  mm. As the figure shows, the simulation results match well with the early portion of the experimental curve, but starts deviating from the experimental plot at point 'b1'. As this simulation does not incorporate damage, this deviation can only be ascribed to crack initiation. (That this deviation cannot be ascribed to difference in the degree of necking has been shown subsequently with an example of a SENT specimen, see Fig. 5.7, Section 5.3.2). This method of visually identifying the initiation point 'b1' inevitably involves a degree of subjectivity, which can be reduced by using some criterion such as a fixed percentage (such as 1%) of load drop. It was verified that for the resolutions of test data and analyses in the present study, the resultant

uncertainty was acceptable small. In this figure it is also noted that crack initiation point appears before reaching the maximum load (Point 'a'). Similar results were obtained for all the ligament lengths.

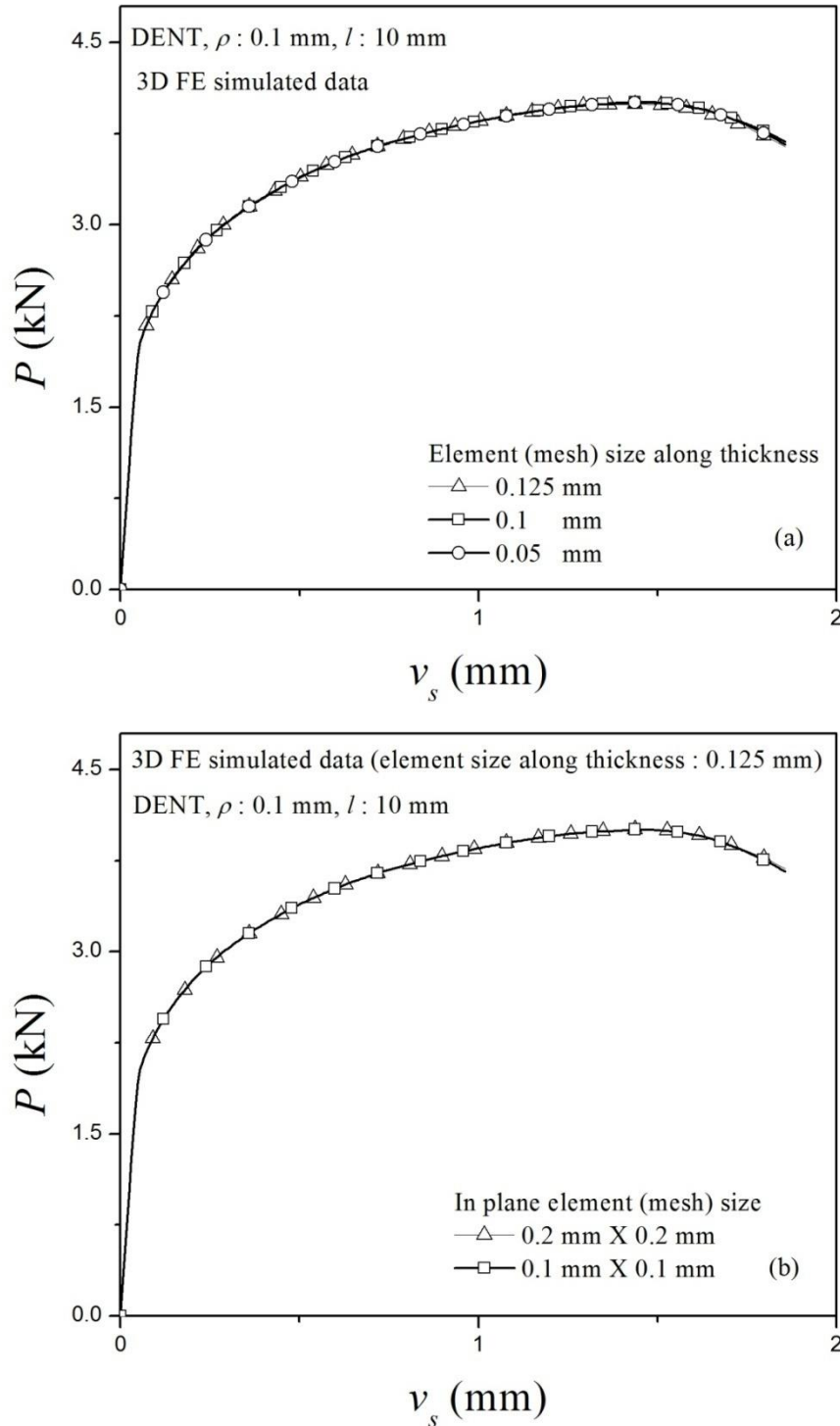


**Figure 4.11:** Simulated  $P - v_s$  plots for notched ( $\rho = 0.1$  mm) DENT specimens having mesh size of (a) 0.125 mm, 0.1 mm and 0.05 mm along thickness, (b) in plane meshing of  $0.2 \times 0.2$  mm and  $0.1 \times 0.1$  mm around notch.



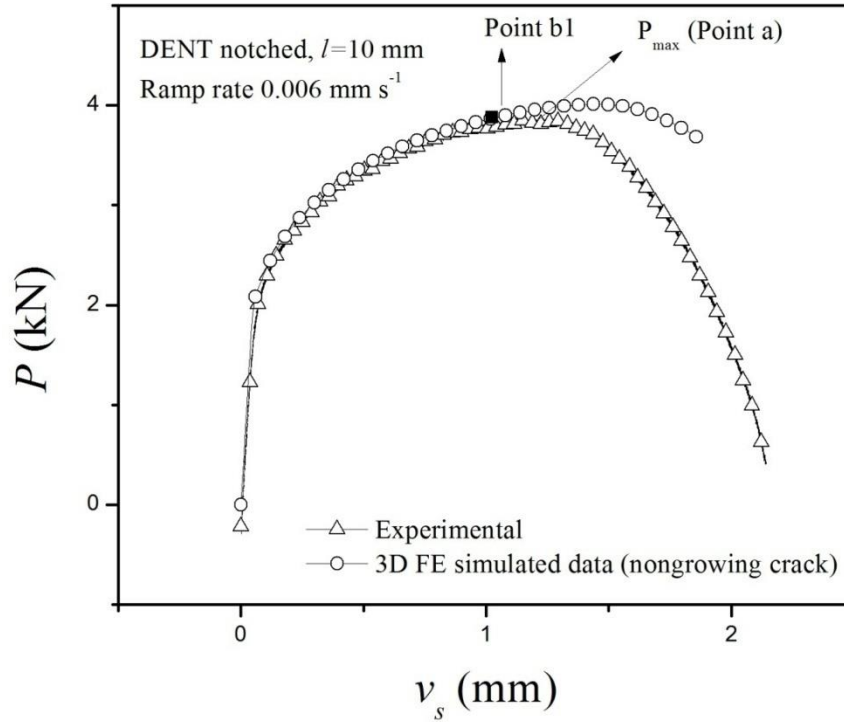


**Figure 4.12:** FEM simulated  $P - v_s$  plot superimposed on the experimental curve for notched ( $\rho = 0.1$  mm) DENT specimen with  $l = 10$  mm; point ‘b1’ is the crack initiation point.

#### 4.3.4.2 Determining crack initiation parameters

Using the initial notch tip radius,  $\rho = 0.1$  mm, the CTOD obtained from FE simulation at point ‘b1’ in Fig.4.12 was  $\sim (0.86 - 0.2) = 0.66$  mm (Fig. 4.13). CTOD is defined here as the distance between two points situated on the intersection of the crack faces with two perpendicular planes at  $45^\circ$  from the crack plane minus the initial opening [16]. CTOD values for crack initiation,  $\delta_c$ , for different ligament lengths have been shown in Fig. 4.14.  $J_p^c$ , the  $J_p$  value at the crack initiation point ‘b1’ was calculated using the following equation (see Eq. (2.1))

$$J_p = \frac{\eta_p A_p}{lt} \quad (4.2)$$

In a plot like Fig. 4.12, a line parallel to the initial elastic loading line was drawn from the crack initiation point (point ‘b1’) to  $P = 0$ ; the area of the  $P - v_s$  plot on the left of this elastic unloading line equals  $A_p$ .

As noted in Section 2.2,  $J_p^c$  can be taken to equal  $\eta_p w_i$ . For the present specimens,  $J_p^c$  values are computed using  $n_p = 1 - n$ , the  $n_p$  value derived for

deeply cracked thick DENT specimens. As noted in Section 2.2, use of  $n_p$  thus calculated has been validated by Pardoen et al [2, 17] for DENT sheet specimens of an Al 6082-O alloy ( $\sigma_y = 50$  MPa,  $\sigma_u = 130$  MPa and  $n = 0.05$ ). There may, however, be reservations about extending this validation to the present test material with much higher strength as well as strain hardening exponent (Table 3.1). The  $J_p^c$  values computed for the different ligament lengths are also shown in Fig. 4.14. Figure 4.14 shows slight variations in the  $J_p^c$  and of  $\delta_c$  values with  $l$ . Further, the variations are more for the lower ligament lengths,  $l = 3$  and 4 mm. It is possible that higher constraint for crack initiation for these two smallest ligament lengths leads to lower initiation values, compared to those for the higher ligament lengths. But, this requires further scrutiny. Considering the entire data set, the average  $J_p^c$  value of  $199.8 \text{ kJ.m}^{-2}$  shows reasonable agreement with the  $w_e$  for notched specimens ( $\sim 213.6 \text{ kJ.m}^{-2}$  with extensometer/actuator travel data, Table 4.1). It will be interesting to carry out such comparison for pre-cracked specimens.

The  $J_p^c$  data trend does not necessarily validate using the  $n_p$  from 2-D formulations for the present specimens, and could instead very well reflect that  $w_i$  is the actual crack initiation parameter. The mean  $\delta_c$  value from Fig. 4.14 (0.64 mm) is considerably higher than the  $\delta_c^e$  values determined for notched specimens (0.57 - 0.58 mm, Table 4.1). It is possible that the difference reflects the difference in the definitions of these two parameters; here too, such comparison appears desirable for pre-cracked specimens.

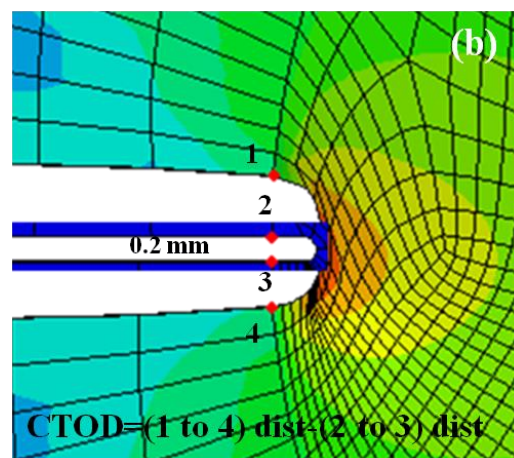


**Figure 4.13:** CTOD determined at point 'b1' of the Figure 4.12.

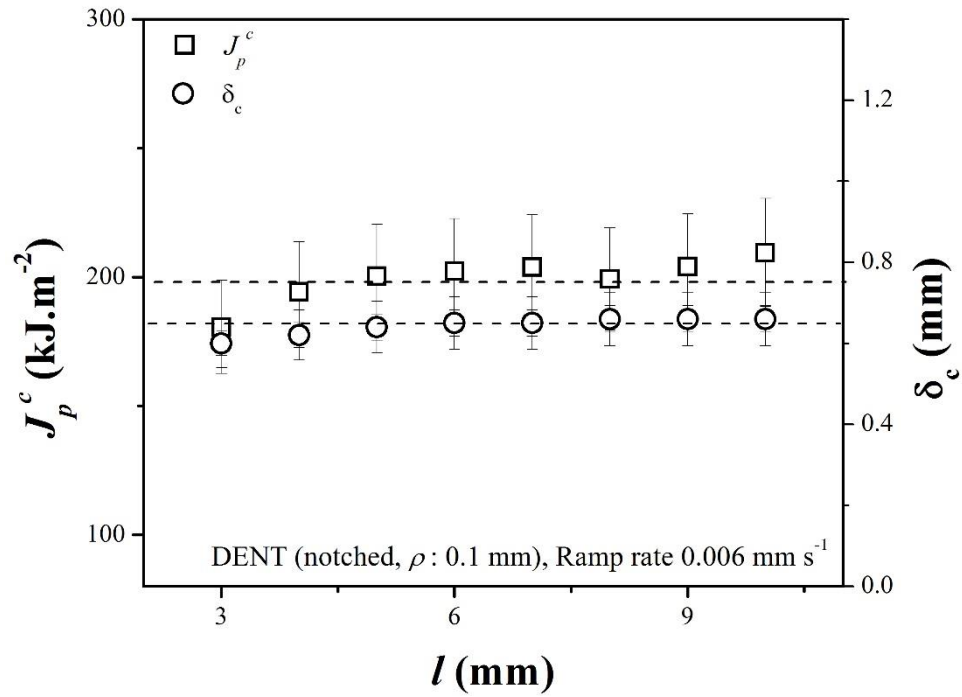


**Figure 4.14:** Variation of  $J_p^c$  and  $\delta_c$  with ligament length for notched DENT specimens

#### 4.4 Conclusions

1. The present DENT specimens show flat fracture, and 36% crack tip necking.
2. It was confirmed that EWF parameters ( $w_e, \beta w_p, \delta_c^e$  and  $\psi^e$ ) can be determined using actuator displacement ( $v_a$ ), data, and an extensometer is strictly not require; this simplifies the EWF testing.
3. For identifying the  $l$ -validity range for EWF analysis with notched or pre-cracked DENT specimens, the criterion of a (nearly) constant  $\sigma_n$  with a value about  $1.15\sigma_u$  seems to be more appropriate than Clutton's criterion [103].
4. Fatigue pre-cracking is necessary for determining  $\rho$ -independent  $w_e$  and  $\delta_c^e$  values. But  $\psi^e$  is found to be independent of  $\rho$  and is therefore a more convenient parameter for integrity assessment. For the notched specimens, with quasi-static ramp rate increasing from  $0.006 \text{ mm.s}^{-1}$  to  $0.6 \text{ mm.s}^{-1}$ ,  $\psi^e$  shows a variation of only  $\sim 1.2\%$ .

5. The  $\varphi_c$  values determined optically by testing fatigue pre-cracked DENT specimens at different ramp rates are found to be comparable to the  $\psi^e$  values estimated from the EWF tests with notched specimens; the agreement improved with  $\psi^e$  computed using data for specimens with  $l$  larger than the initial transient regime of crack growth before the stable regime.
6. A novel method is developed for identifying the crack initiation points during ramp loading of notched DENT specimens, by comparing  $P - v_s$  plots from mechanical tests and from 3-D large strain FE simulation of the specimen for non-growing crack. This makes it possible to compute  $J_p^c$  values as well as  $\delta_c$  values. The  $J_p^c$  and  $\delta_c$  values determined are found to be nearly constant particularly for the higher specimen ligament lengths. However, using  $n_p$  value from 2-D formulations for deeply cracked DENT specimen for the present test material should preferably be justified.

### 5.1 Introduction

The primary objective of the research reported in this chapter is to determine the  $\eta_p$  factor for the present SENT sheet test specimens, and to use the same for determining  $J_p^c$ , the plastic component of  $J$ -integral at crack initiation, in SENT specimens. Apparently, this is the first attempt at determining  $\eta_p$  of sheet SENT specimens in literature. Specifically, in literature, both 2-D [51-53] and 3-D [54-60] FE simulations have been used for evaluating  $\eta_p$  for thick SENT specimens using well established methods. In these investigations, the analyses covered material strain hardening parameter  $n$  in the range 0.05 - 0.5,  $a/W = 0.1 - 0.7$ ,  $H/W = 6, 10$ ,  $t = 20 - 40$  mm, and  $t/W = 1, 2$ . The results reported by different authors show that  $\eta_p$  depends upon both specimen dimensions and  $n$ , and also show rather large variations (see [131]). The specimen dimensions covered in these studies, particularly thicknesses, also differ considerably from that used in the present study: specimen free length between the two jaw grips  $H = 60$  mm,  $W = 30$  mm ( $H/W = 2$ ), crack depth ratio  $a/W = 0.2 - 0.9$ , sheet thickness  $t = 1$  mm, with  $\rho = 0.1$  mm for the machined specimens, Figure 3.2(a).

Following the well-established practice for thick fracture mechanics specimens, sheet SENT specimens with sufficiently sharp ( $\rho = 0.1$  mm) mechanical notches are used for determining  $\eta_p$ .  $\eta_p$  values are determined from  $P$  vs. specimen free length ( $H$ ) extension ( $v_s$ ) data prior to crack initiation from ramp loaded specimens adopting two different methods based on 2-D formulations (i.e., for thick specimens).  $\eta_p$  values are also determined using  $P - v_s$  data from 3-D large strain FE simulations of notched specimens for non-growing cracks using one of these methods, for  $v_p$  levels well beyond the corresponding  $v_p$  for crack initiation in the

tested specimens. The various data sets that can be used for  $\eta_p$  determination are also examined. Using FE simulation, it is verified that the  $\eta_p$  determined using notched specimens can be used with fatigue pre-cracked specimens, but fatigue pre-cracked specimens should be used for determining  $J_p$ .  $\eta_p$  determination reported here is validated for one specimen using FE simulation that computes  $J$ -integral invoking its fundamental path independent line integral definition (cf. the similar analyses with DENT specimens of an Al 6082-O alloy sheet by Pardoen et. al. [2, 17], cited in Section 2.2). Next follows the illustration of evaluating  $J_p^c$  values with mechanical test data for the entire chosen  $a/W$  range using the  $\eta_p$  derived in this report. The conclusions are presented in the final section.

## 5.2 Experimental

SENT specimens of the test material (IF steel sheet) with thickness,  $t = 1$  mm were machined in longitudinal (L-T) orientation having dimension of  $90 \times 30 \times 1$  mm and notch tip radius  $\rho = 0.1$  mm, with notch lengths ( $a$ ) varying in the range  $6 - 27$  mm, i.e.,  $0.2 \leq a/W \leq 0.9$ . All the mechanical tests were performed in a computer controlled servo-hydraulic universal testing machine, INSTRON 8501R, of  $\pm 100$  kN capacity (see Chapter 3). Each specimen was ramp loaded at cross head speed of  $0.006$  mm.s<sup>-1</sup> (corresponding to a nominal strain rate of  $\sim 10^{-4}$  s<sup>-1</sup>); the ramping was stopped when the load just beyond the maximum load, and the specimen was fully unloaded. No extensometers were used for these tests. Therefore, load line extension  $v_s$  for the specimen free length  $H$ , was determined from the actuator displacement data  $v_a$  using the equation  $v_s = v_a - C_M P$ , as discussed earlier in Section 4.3.6. The  $P - v_s$  plots of the SENT specimens with different  $a/W$  values are presented in Fig.5.1. For each specimen, the initial elastic compliance value,  $C_s$  was determined from the  $P - v_s$  data, which was then used to compute  $v_p$  values from the  $P - v_s$  data by subtracting specimen elastic deformation,  $v_p = v_s - C_s P$ . This method can be applied only to  $P - v_s$  data prior to crack initiation, and it is also assumed that the effects of crack tip blunting on the specimen elastic compliance is negligible. The same method applies for computing  $v_p$  values from the  $P - v_s$  data from FE simulation of specimens with non-growing cracks.

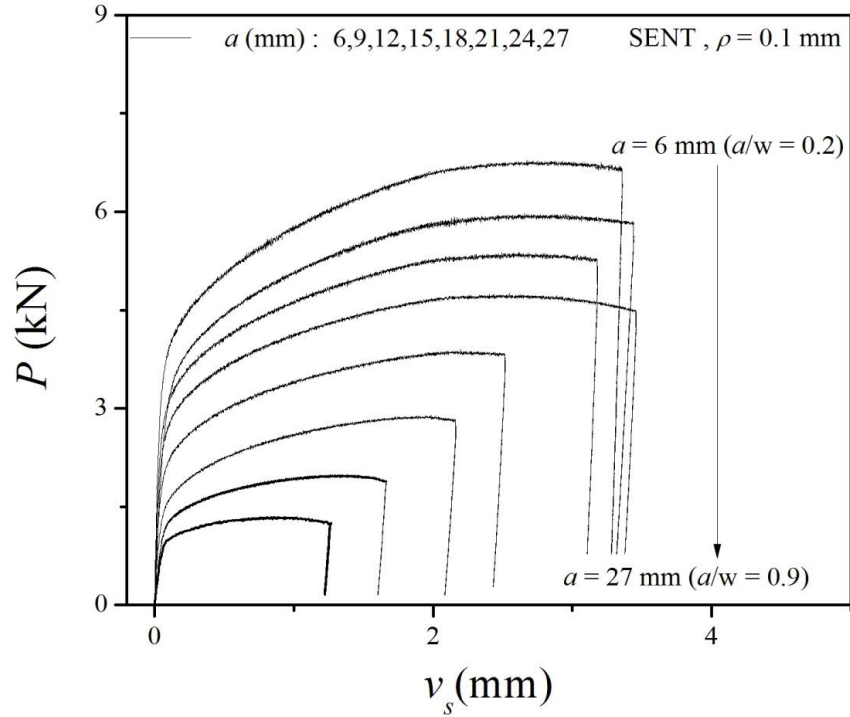


**Figure 5.1:**  $P - v_s$  curves for notched SENT specimens with different  $a/W$  ratios from mechanical tests.

## 5.3 Results and discussion

### 5.3.1 $\eta_p$ determination from mechanical test data

The determination of  $\eta_p$  uses the methods established for standard 2-D formulation of  $J$  integral [9, 49]. For a given specimen, the area under the load ( $P$ ) - plastic displacement ( $v_p$ ) plot, i.e., the plastic component of work done, is

$$A_p = \int_0^{v_p} P \, dv_p \quad (5.1)$$

For a non-growing crack,  $\eta_p$  can be determined by equating the expressions of  $J_p$  from the energy rate interpretation of  $J$ -integral (shown by Rice [49], Landes and Begley [132] and others as fundamental to elastic-plastic  $J$  testing) with the definition of  $J_p$  using the  $\eta_p$  (cf. Turner [8, 133]):

$$J_p = \left( -\frac{dA_p}{tda} \right)_{v_p} = \eta_p \left( \frac{A_p}{tl} \right)_{v_p} \quad (5.2)$$

This method is called as Method 1 in this chapter.

Method 2 directly invokes the Paris et al. [134] method of writing load  $P$  in a variable separable form as product of two functions, one with normalized ligament length  $l/W$  as argument, and the other with normalized plastic component of the specimen free length extension  $v_p/W$  as argument:

$$P = tW \cdot G\left(\frac{l}{W}\right) \cdot \left[A_M \cdot H\left(\frac{v_p}{W}\right)\right] \quad (5.3)$$

In this equation,  $A_M$  is a constant with dimension of stress. This variable separable form has been examined and rigorously verified for thick fracture mechanics specimens, [135, 136]. It is now known that this variable separable form is valid except for very small values of  $v_p/W$ . Appendix A15, Section 15.2.6 in ASTM E1820 [7] prescribes this cut off limit as  $v_p/W = 0.001$  for the plate compact tension and single edge notched specimen in three point bend loading; setting the basis for estimating  $J - \Delta a$  curves for limited extents of crack growth  $\Delta a$ . Similar guidelines are not available for sheet specimens. Equation 5.3 can be used to define a load separation factor with respect to an arbitrarily chosen reference configuration with a fixed ligament size  $l_0$ . For the specimen with ligament length  $l_k$ , the load separation factor may be expressed as the ratio of loads for any fixed  $v_p$  level:

$$S_k\left(\frac{l}{W}\right) = \left\{ \frac{P(l_k/W)}{P(l_0/W)} \right\} \quad (5.4)$$

where  $P(l_k/W)$  and  $P(l_0/W)$  are respectively the loads for specimens having ligament lengths  $l_k$  and  $l_0$ . Obviously, with Eq. 5.3 valid,  $S_k(l/W)$  should be independent of  $v_p$ . Then,  $\eta_p$  can be expressed as,

$$\eta_p = \left\{ \frac{(l/W)}{S_k(l/W)} \right\} \cdot \left\{ \frac{\partial S_k(l/W)}{\partial (l/W)} \right\} = \left\{ \frac{\partial \ln S_k(l/W)}{\partial \ln(l/W)} \right\} \quad (5.5)$$

For computation of  $\eta_p$  using Eq. (5.2) or Eq. (5.5), data with  $v_p$  values between an upper cutoff level and a lower cutoff level were only used. The upper cutoff level is dictated by the requirement that data must pertain to the regime prior to crack initiation in the specimens. This level was (arbitrarily) fixed as  $v_p = 0.5$  mm, which, from Fig. 5.1, should be well before crack initiation in all these specimens. It was considered prudent to adopt also a lower cut off level of  $v_p$  because of two reasons. Firstly, such a limit is prescribed for thick fracture mechanics specimens.



Secondly, small  $v_p$  values computed as described in Section 5.2 are susceptible to relatively large fractional errors because of limitations of measurement accuracies for elastic compliances of machine, and of specimens. In absence of any guidelines in literature for sheet specimens, this lower cut off limit was arbitrarily set as  $v_p \geq 0.2$  mm. Accordingly,  $\eta_p$  computations were restricted to  $0.5 \geq v_p \geq 0.2$  mm. While Method 2 requires a prior assumption about the functional form for  $H(v_p/W)$  in Eq. (5.3) (which must be validated by experimental results), Method 1 avoids this but requires numerical differentiation.

For Method 1, plastic energy  $A_p$  was evaluated for each ligament length as a function of  $v_p$  by integrating the corresponding  $P-v_p$  curve. For various fixed  $v_p$  values (covering the chosen range), the  $A_p$  vs  $a$  plots appear to be linear, Fig. 5.2. From the measured slopes of the plots, i.e.,  $(dA_p/da)_{v_p}$  values,  $\eta_p$  values were computed using Eq. 5.2 for each of the chosen  $v_p$  level. Now, for each  $a/W$  ratio, the mean of the computed  $\eta_p$  values for the different  $v_p$  levels used in  $J_p$  computations. With  $a/W$  increasing from 0.2 to 0.9, this mean  $\eta_p$  gradually decreases from  $\sim 0.87$  to  $\sim 0.77$ , i.e., by  $\sim 11\%$  that is comparable with the standard deviation of the data, Fig. 5.3. An alternative interpretation would be to take an average  $\eta_p = 0.81$  with standard deviation of 0.04.

For Method 2, the specimen with  $a/W = 0.4$  (i.e.,  $l_0 = 18$  mm) was arbitrarily chosen as the reference specimen. For the  $k$ -th specimen, the variation of  $S_k$  with  $v_p$  normalized by ligament length,  $l_k$ , are shown in Fig. 5.4. Obviously, for the reference configuration,  $S_k = 1$  for all the  $v_p/l_k$  values; for the other  $l_k$  values, the variations in  $S_k$  with  $v_p/l_k$  are generally small. For each  $l_k$  value, the average of the  $S_k$  values shown in Fig. 5.4 were computed; Fig. 5.5 shows the plot of this average  $S_k$  against the normalized ligament length,  $l_k/W$ .

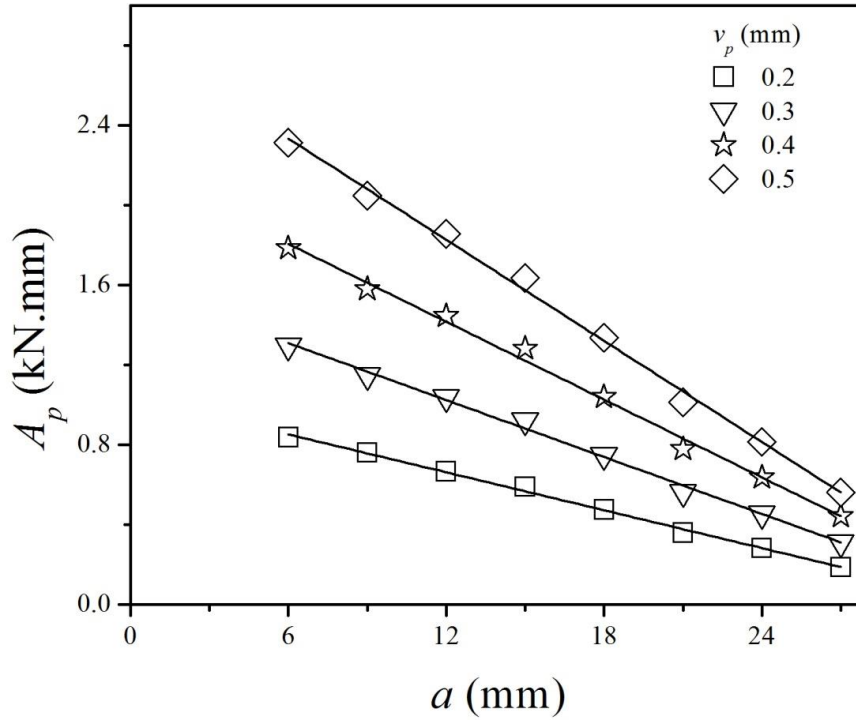


**Figure 5.2:** For notched SENT specimens,  $A_p$  plotted as a function of notch length  $a$  for different  $v_p$  levels

As Fig.5.5 shows, the data can be well correlated by a simple nonlinear least square fit to power-law equation,  $S_k = c(l_k/W)^{\eta_p}$  with  $c = 1.48$  (standard error = 0.032), and a constant  $\eta_p = 0.79$  (standard error = 0.038), with corresponding  $R^2 = 0.997$ . This constant  $\eta_p = 0.79$  (Method 2) is  $\sim 2.5\%$  less than the mean  $\eta_p = 0.81$  computed by Method 1. It must, however, be noted that  $\eta_p$  factor computed from the power law fit (Method 2) is constant while Method 1 shows a modest linear variation of  $\eta_p$  factor with  $a/W$ , Fig. 5.3. In this regard, one may consider the use of 2<sup>nd</sup> order polynomial function to fit  $S_k(l/W)$  vs  $l/W$ ; Figure 5.5 shows that this polynomial function is reasonably successful in fitting  $S_k(l/W)$  vs  $l/W$  data ( $R^2 = 0.992$ , i.e., the power law fit with  $R^2 = 0.997$  is statistically superior), but the trend of the  $\eta_p$  vs  $a/W$  plot from this polynomial fit (Method 2) is very different from the trend of the  $\eta_p$  vs  $a/W$  plot derived from Method 1, Fig. 5.3. Therefore, this 2<sup>nd</sup> order polynomial fit cannot be recommended.

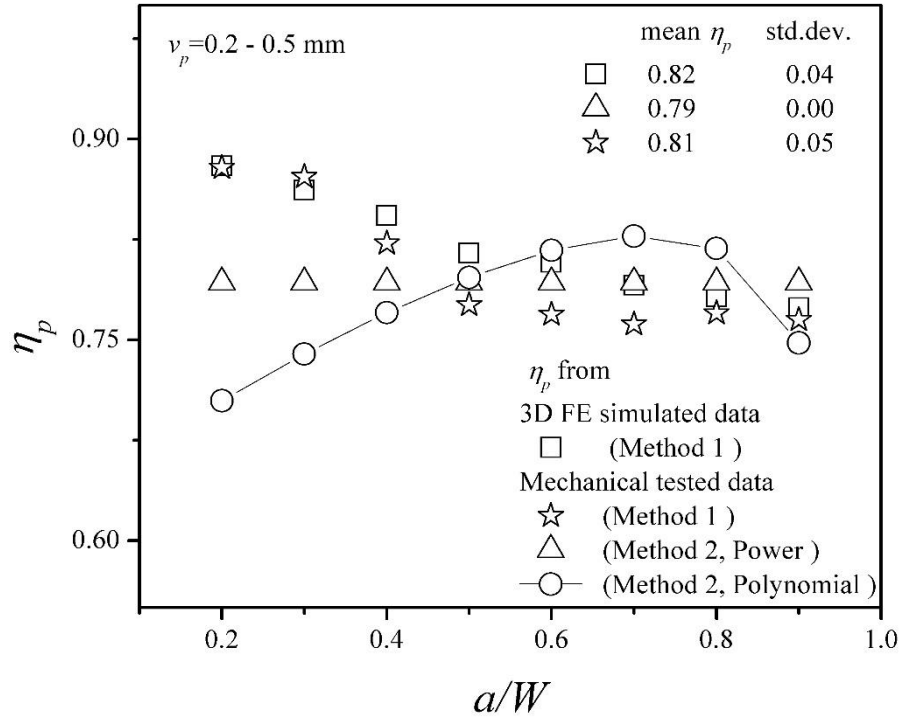


**Figure 5.3:** Comparison of  $\eta_p$  computed using different approaches.

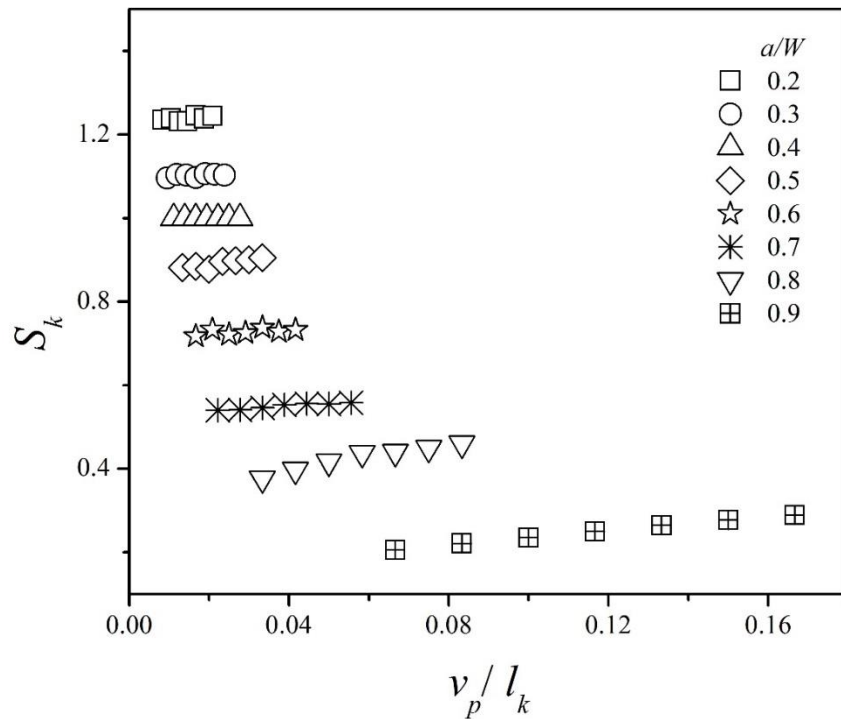


**Figure 5.4:** Parameter  $S_k$  plotted against normalized plastic displacement  $v_p/l_k$  for different  $a/W$  ratios

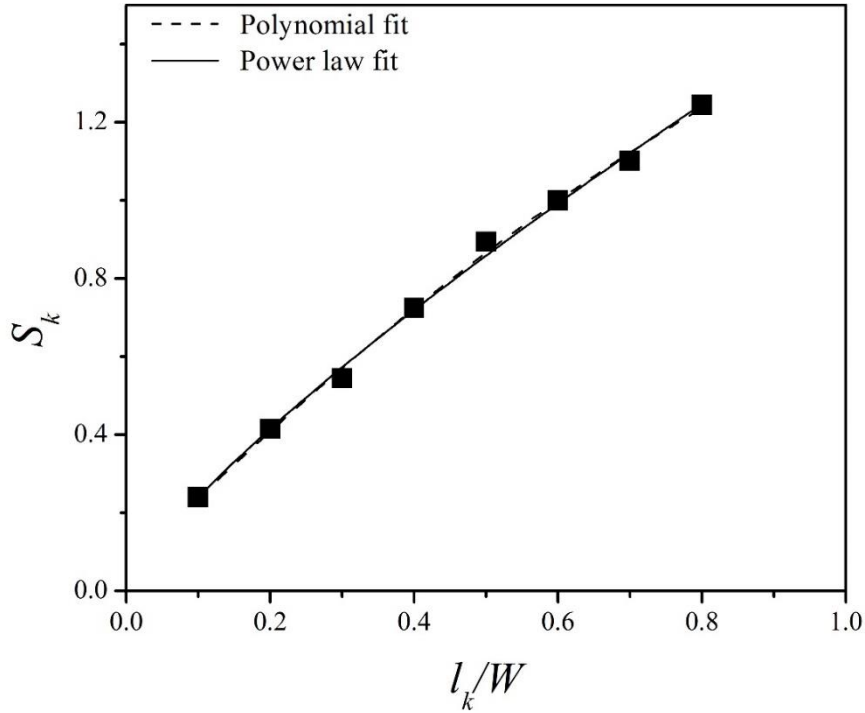


**Figure 5.5:** Variation  $S_k$  (average) with  $l_k/W$  ratio

### 5.3.2 Determination of $\eta_p$ using 3-D FE simulation data

Three dimensional (3-D) large strain rate-independent FE simulations have been carried out for notched (tip radius  $\rho = 0.1$  mm) SENT specimens of the test material with  $0.2 \leq a/W \leq 0.9$ , ramp loaded at  $0.006 \text{ mm.s}^{-1}$ . The objective of the simulations was to determine the variation of  $P$  with  $v_s$ , and also the corresponding extents of notch tip necking for non-growing cracks. The simulations were continued well beyond the maximum load in each case. The simulation procedure is similar to simulation for DENT specimens described in Section 4.3.4.1. To recount briefly, elastic-plastic material properties with Hollomon work hardening parameters for nominal strain rate of  $10^{-4} \text{ s}^{-1}$  (Section 3.1) were assumed to apply for the entire strain ranges for the simulations. The commercial finite element software, ABAQUS 6.10 was used for these simulations, and 3-D 8 node solid hexahedral elements C3D8R with reduced integration and 1 integration point were used. 5 slices of equal thickness of 0.2 mm were used in the direction of the sheet thickness. The in-plane dimension of the elements was  $0.2 \text{ mm} \times 0.2 \text{ mm}$  around the notch to accommodate large deformation, and the element size gradually increased to  $1 \text{ mm} \times 1 \text{ mm}$  away from notch, Figs. 5.6(a), 5.6(b).

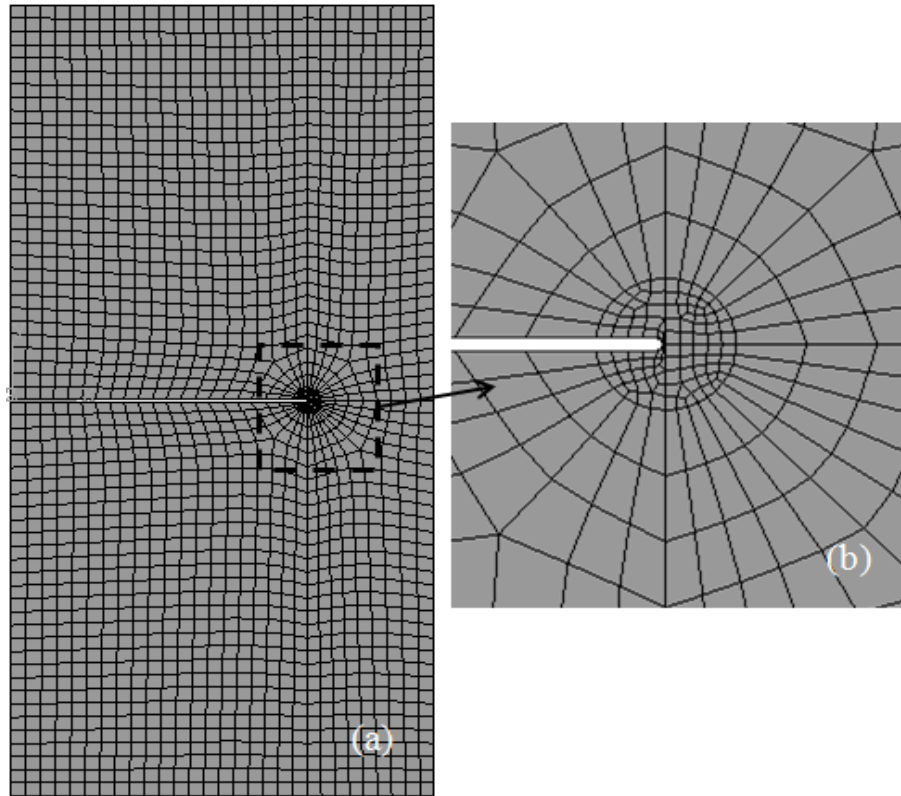


**Figure 5.6:** (a) Plane view of the finite element mesh showing smaller mesh size around the notch and larger mesh size rest of the SENT specimen; (b) enlarged view of the mesh around notch tip.

Mesh convergence studies had shown this in-plane meshing to be adequate for DENT specimens. The lower end face of a sheet specimen was clamped by specifying zero displacement boundary conditions for all nodes on this face. The specimen was loaded uniaxially along the longitudinal axis by specifying for all nodes on the upper end face a constant displacement along this direction, and setting displacements along the remaining two directions as zero. The  $P - v_s$  data from mechanical tests and the FE simulations for each notch length are compared in Fig. 5.7(a). For each notch length, the simulation results match well with the early portion of the experimental curve. But, as shown in the inset of Fig. 5.7(a) for the specimen with  $a = 21$  mm, from the point “a1”, the FE simulation plot starts increasingly deviating from the experimental plot even before the maximum load is reached. This deviation cannot be explained by the difference in the degrees of necking. For example, for the specimen with  $a = 21$  mm, the extent of necking (computed by FE analysis) at the nearby point “b” is 37.7%, merely 0.7% higher than that at the point “a1” (% necking is defined as (initial thickness of the ligament,

$t$ - current ligament thickness,  $t_n \times 100/t$ ), Figs. 5.7(b) and 5.7(c). Since the FE simulations were for non-growing crack situation, this onset of deviation in  $P - v_s$  data noted in Fig. 5.7(a) can only be ascribed to crack initiation and point “a1” is considered as the crack initiation point. The simulation results in Fig.5.7(a) also confirm that for all the specimens, cracks initiated at  $v_p$  values well beyond the upper cut off limit value of 0.5 mm adopted for applying Methods 1 and 2 in Section 5.3.1. The good match of  $P - v_s$  plots from mechanical tests and FE simulation (non-growing crack) prior to crack initiation for each of the  $a$ -levels validates the FE meshing adopted. Nevertheless, adequacy of the chosen meshing was also confirmed by carrying out a mesh convergence study for a specimen with  $a = 21$  mm ( $\rho = 0.1$  mm) using two different meshing strategy.

For the first simulation, C3D8R element size in thickness direction was kept as 0.1 mm (i.e., 10 layers in thickness direction) and element in-plane size was 0.1 mm  $\times$  0.1 mm around the notch gradually increasing to 1 mm  $\times$  1 mm away from the notch. For the second simulation, the element in-plane size was 0.2 mm  $\times$  0.2 mm around the notch gradually increasing to 1 mm  $\times$  1 mm away from the notch, but 14 layers were taken along the thickness directions, with element thickness of the 4 layers from each of the two sheet surfaces kept as 0.05 mm, and thickness of the remaining 6 layers kept as 0.1 mm. Even after such considerable refinement of mesh sizes with consequent drastic increase in the computational burden, the computed  $P - v_s$  data did not show any significant variations: the maximum variation in the computed  $P$  values for the three simulations was only 0.2% at the highest  $v_s$  level of 2.3 mm, Fig.5.8. Extension of this mesh convergence study for evaluating  $J$  by contour integration is discussed in Section 5.3.4.

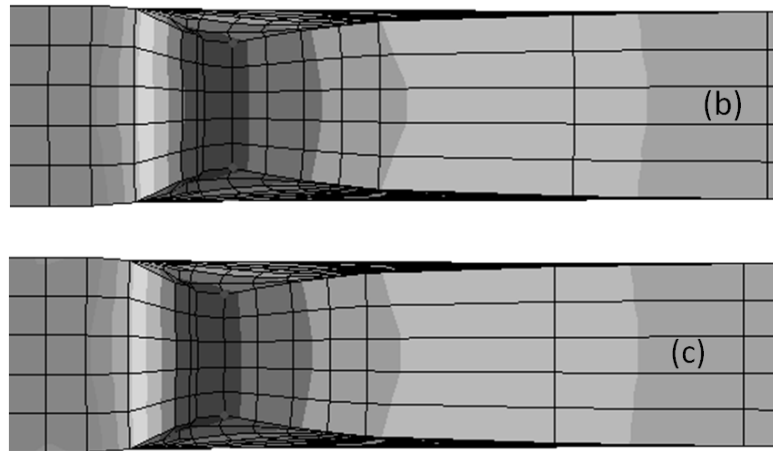
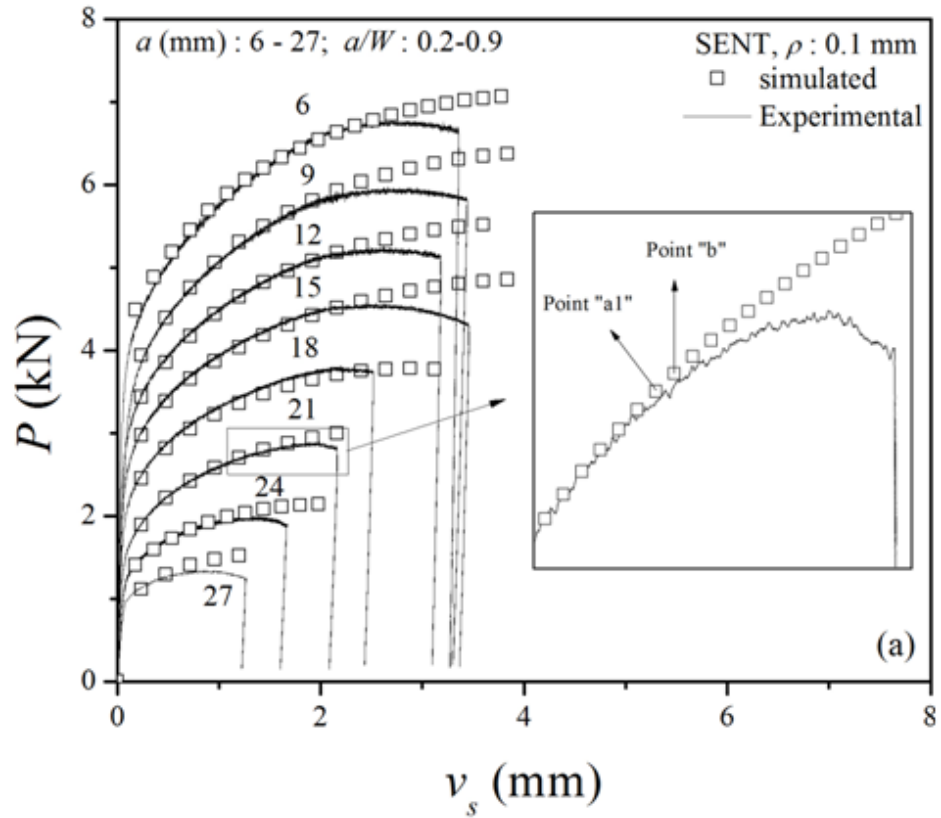


**Figure 5.7:** (a) Experimental and simulated (assuming non-growing crack)  $P - v_s$  plots of notched SENT specimens. Inset shows for the plot for  $a = 21$  mm, point "a1" where the two plots starts deviating, and a nearby point "b" at a slightly higher  $v_p$ . (b) Necking at point "a1" (37%). (c) Necking at point "b" (37.7%).

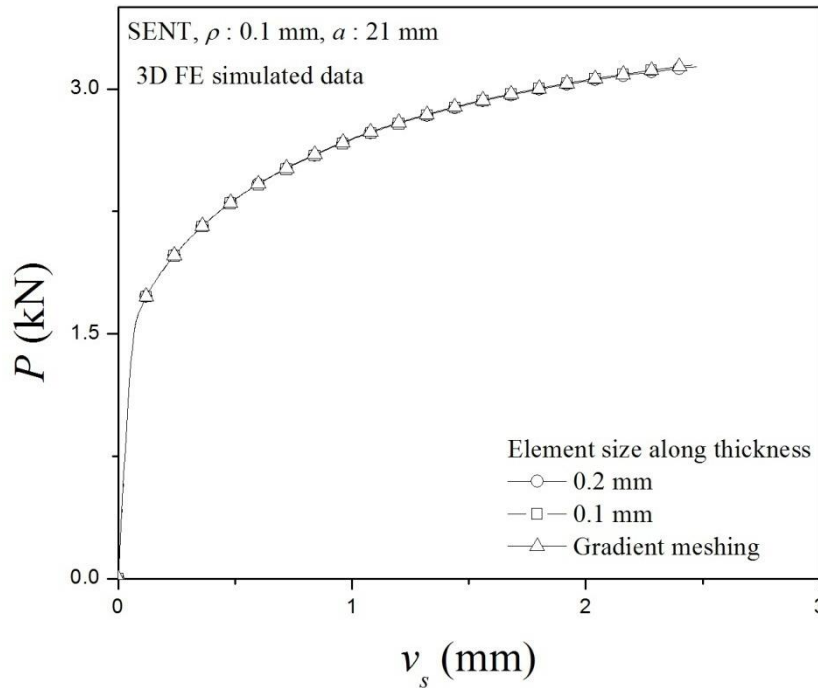


**Figure 5.8:**  $P - v_s$  plots from 3-D FE simulations of SENT specimen with  $\rho = 0.1$  mm and  $a = 21$  mm. For the three simulations, element size along thickness direction was 0.2 mm, 0.1 mm, or gradient meshing using 14 layers; for the corresponding in-plane mesh dimensions, see text.

Figure 5.9(a) shows a representative SEM micrograph of a fractured specimen ( $a = 8$  mm). For accurately measuring % necking in this figure, ImageJ software with edge detection technique [136] was used; Fig. 5.9(b) shows the result - the % necking thus determined was 36%, in reasonably good agreement with those assessed from Fig. 5.5(b-c). It may be noted that %necking for the present DENT specimens is also 36% (Fig. 4.6, Section 4.3.2). Also, in DENT sheet specimens showing flat fracture, for all initial crack lengths, %necking remains essentially constant after crack initiation [2, 13, 17] (see Fig. 4.6). The same may be expected for SENT sheet specimens. From the  $P - v_s$  data obtained from FE simulations, the corresponding  $P - v_p$  data were computed in the same manner as that followed for the mechanical test data (Section 5.2). With  $P - v_p$  data from 3-D FE simulations  $\eta_p$  values were computed by adopting Method 1 for  $v_p$  values in the range of 0.2 - 0.5 mm. These  $\eta_p$  results, also shown in Fig. 5.3, are, as expected, in good agreement with results from analysis of experimental  $P - v_s$  data as reported in Section 5.3.1. For  $0.2 \leq a/W \leq 0.9$ , the decrease of  $\eta_p$  with increasing  $a/W$  can be described



by a linear relation. It was verified that the quality of fit did not meaningfully improve by using a higher order polynomial. Because of the modest slope of the linear relation, a mean  $\eta_p = 0.825$  can also be assumed for the entire crack depth range. The relevant data from least square fits for these two models are recorded in Table 5.1 (Data set I).

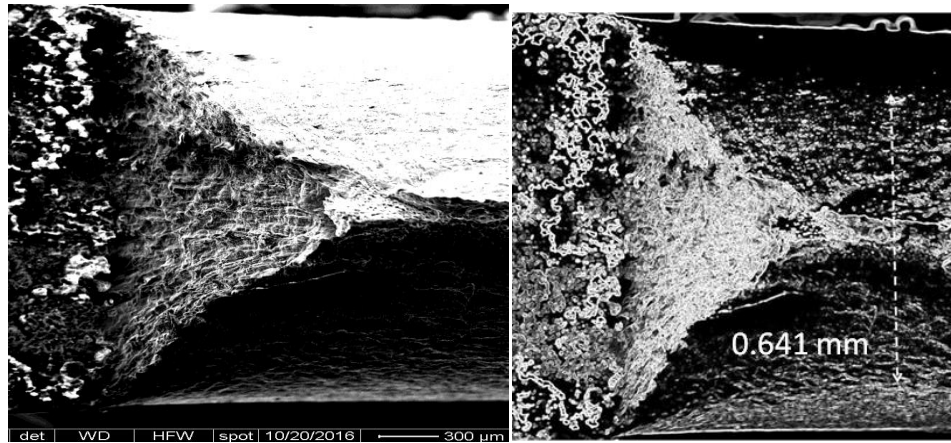


**Figure 5.9:** (a) Representative SEM micro graph showing extensive necking ( $a = 8$  mm); (b) processed image by ImageJ software using edge detection technique in order to measure the necking percentage.

The  $\eta_p$  vs  $a/W$  plot from the FE simulation data (using Method 1) is shown in Fig. 5.10; this figure also includes  $\eta_p$  vs  $a/W$  results from 3-D FE simulations by different researchers [54-56, 59, 60] for a material with  $N = 1/n = 5$  (comparable to  $N = 1/n \approx 4$  for the present test material), for specimens with dimensions  $a/W = 0.1 - 0.7$ ,  $H/W = 6, 10$ ,  $t = 20 - 40$  mm, and  $t/W = 1, 2$ . For the thick SENT specimens, with increasing  $a/W$ ,  $\eta_p$  first increases rather sharply to reach a near plateau, and then gradually decreases. For the present sheet specimens, on the other hand,  $\eta_p$  decreases marginally with  $a/W$  increasing in the range 0.2 to 0.9. Apparently, this difference in the trends for thick and sheet SENT specimens arises because of significantly reduced thickness and also crack tip necking in the sheet specimens. This area, however, requires further research. This basically justifies the present study.

Figure 5.3 presented the  $\eta_p$  values up to the plastic displacement,  $v_p = 0.5$  mm for the present tested SENT specimens. These  $\eta_p$  values have been derived by (i)

Method 1 (using experimental load vs. displacement data) (ii) Method 2 using a power law fitting with the experimental load vs. displacement data (here only power law has been considered for reasons discussed in Section 5.3.1) and (iii) Method 1 using load displacement data from 3-D FE simulations.

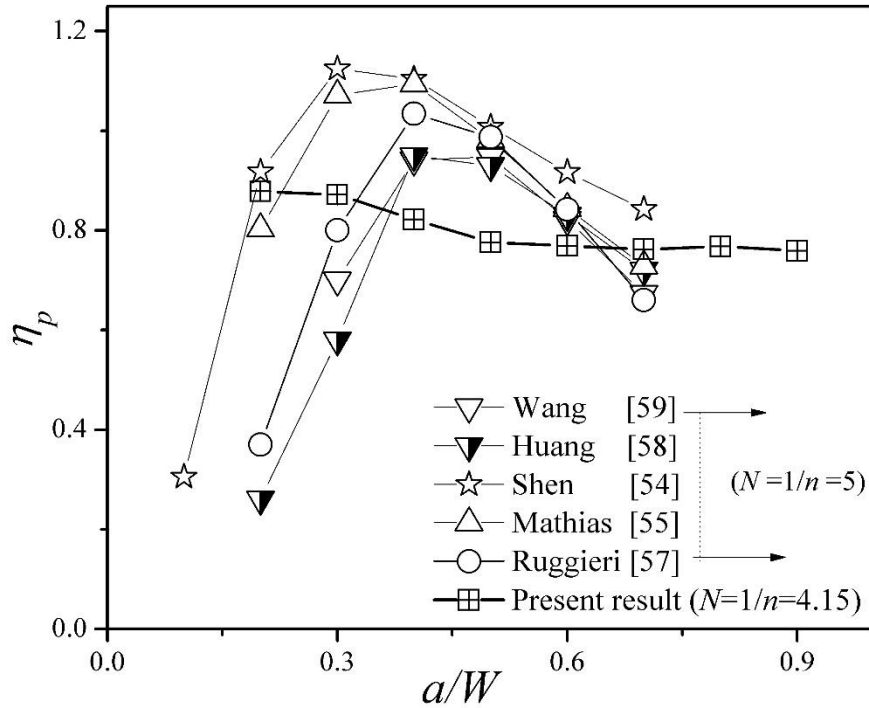


**Figure 5.10:**  $\eta_p$  for the SENT sheet specimens evaluated from FE simulation (see Fig. 5.3), compared with  $\eta_p$  computed from the functions for thick specimens with comparable  $n$  reported in literature.

Though  $\eta_p$  computed using Method 1 and Method 2 with the experimental load-displacement data show good agreements, Method 2 gives the result with smallest dependence on the  $a/W$  ratio.  $\eta_p$  from the 3-D FEM simulations data shows good agreement with  $\eta_p$  determined from experimental data (Method 1 and Method 2). Basically, this validates the FE simulation method used in the present study. From Fig. 5.3, it is clear that at least up to  $v_p = 0.5$  mm, the extent of necking (maximum  $\sim 19.2\%$ ) does not invalidate application of Methods 1 and 2. The analysis was extended to higher degrees of necking, by adopting Method 1 for analyzing the 3-D FE simulated  $P$ - $v_p$  data (non-growing crack) for  $v_p$  levels in the range 0.2 to 2.5 mm for all the test specimens. The corresponding data set is designated as Data set II. Figure 5.11(a) shows the variation of computed  $\eta_p$  with  $a/W$  for different  $v_p$ ;

this plot also includes for each  $a/W$  level, the average of the  $\eta_p$  values for the  $v_p$  levels. Figure 5.11(b) plots the variations in % necking (measured from the deformed FE mesh) with  $a/W$  for the  $v_p$  levels of 0.5, 1.0, 1.5, 2.0 and 2.5 mm. This figure also shows that the % necking thus measured, see Fig. 5.7(a) at crack instantiation points varies over a very small range of 34.8% - 39%. Figure 5.11(c) shows the variation of  $\eta_p$  with  $v_p/W$  for various  $a/W$  levels.

From Fig. 5.11(b), it is clear with  $v_p$  increasing from 0.5 mm to 2.5 mm, % necking increases from ~19.2% to 68.2%. Figure 5.11(a) shows that apparently Method 1 can still be applied for data up to  $v_p = 2.5$  mm. It is possible that the 2-D based Methods 1 and 2 would prove inadequate at some higher degree of crack tip necking; this aspect has not been examined. As with Data set I in Table 5.1, for the Data set II also, a linear  $\eta_p$ -  $a/W$  relation appears viable, and also because of the modest slope, an average  $\eta_p$  may very well be considered for the entire  $a/W$  range. As expected, for each  $a/W$  level, the  $\eta_p$  averaged over the  $v_p$  values are quite close to the linear fit, as can be seen from Fig. 5.11(a). The relevant results from the least square fits for this Data set II are recorded in Table 5.1. An alternative possibility is to analyse a Data set III, which includes data only prior to crack initiation for all the specimens. From the Data set II (shown in Fig 5.11(a)), Data set III was prepared by discarding, for each  $a/W$  level, data for  $v_p$  levels beyond crack initiation, Fig. 5.11(b). The results from the least square fits for Data set III are also included in Table 5.1. Figure 5.11(a) shows that for all crack lengths, all the  $\eta_p$  data only for  $v_p = 0.2$  mm and 0.3 mm show large positive deviations from the linear fit shown. This is not consistent with the Gaussian distribution of errors implied in least square fitting.

Figure 5.11(c) shows that for every  $a/W$  level,  $\eta_p$  gradually increases with  $v_p$  increasing from 0.1 mm to 0.3 mm, then sharply drops as  $v_p$  increases to 0.4 mm, and thereafter remains more or less constant (as theoretically expected) for  $v_p$  increasing to 2.5. This “hump” in the  $\eta_p$  -  $v_p$  plot for  $v_p < 0.4$  mm is discussed further in Section 5.3.3. In any event, by this evidence, the lower cut off  $v_p$  level should be set as,  $<0.4$  mm and not  $<0.2$  mm as (arbitrarily) assumed for the

analyses in Section 3.1. Data sets I, II and III were revised imposing this revised lower cut off  $v_p$  level, to obtain Data sets IA, IIA, and IIIA respectively. The results for linear fits, and also approximation of mean  $\eta_p$  for these revised data sets are also presented in Table 5.1.

**Table 5.1:** Evaluation of  $\eta_p$  of sheet SENT specimens by analyzing FE simulation data ( $0.2 \leq a/W \leq 0.9$ )

Data Set	No of data	Average $\eta_p$ (std. error of fit)	Linear $\eta_p - a/W$ relation (std. error of fit)
<b>I</b>	$v_p$ : 0.2 to 0.5 mm (4 levels) Sp. necking = 2.9% - 19.2%. (Fig. 5.3).		
	32	$\eta_p = 0.825$ (0.0490)	$\eta_p = 0.910 - 0.156 \cdot (a/W)$ (0.0318)
<b>II</b>	$v_p$ : 0.2 to 2.5 mm (8 levels) Sp. necking = 2.9% - 68.2% (Fig. 5.11(a))		
	64	$\eta_p = 0.808$ (0.0468)	$\eta_p = 0.895 - 0.158 \cdot (a/W)$ (0.0287)
<b>III</b>	$v_p$ : 0.2 mm to crack initiation. Sp. necking = 2.9% - 39%		
	43	$\eta_p = 0.822$ (0.0462)	$\eta_p = 0.896 - 0.144 \cdot (a/W)$ (0.0312)
<b>IA</b>	$v_p$ : 0.4 to 0.5 mm (2 levels) Sp. necking = 12.4% - 19.2%.		
	16	$\eta_p = 0.796$ (0.0427)	$\eta_p = 0.887 - 0.165 \cdot (a/W)$ (0.0130)
<b>IIA</b>	$v_p$ : 0.4 to 2.5 mm (6 levels) Sp. necking = 12.4% - 68.2%		
	48	$\eta_p = 0.793$ (0.0394)	$\eta_p = 0.882 - 0.161 \cdot (a/W)$ (0.0111)
<b>IIIA</b>	$v_p$ : 0.4 mm to crack initiation. Sp. necking = 12.4% - 39%		
	27	$\eta_p = 0.803$ (0.0408)	$\eta_p = 0.885 - 0.165 \cdot (a/W)$ (0.0120)

Clearly, imposing the lower cut off  $v_p$  level as 0.4 mm significantly reduced the standard error for the linear fits, and also reduced the spreads for the optimal values for the slopes and offsets for the linear fits. But overall, the resultant change in the optimal values of the various parameters in Table 5.1 was at most 3.5%. This reflects that for each specimen, compared to the average  $\eta_p$ , the magnitudes of these initial anomalies are small, Fig. 5.11(c). It may be noted from the results in Table

5.1 that assuming a mean  $\eta_p = 0.81$  leads to a maximum error of about 2% compared to the average  $\eta_p$  values, and 9% compared to the linear fits. This is akin to the case of deeply cracked DENT specimens (thick, or in sheet form) with constant  $\eta_p (= 1 - n)$  independent of  $a/W$ , section 2.2. For sheet SENT specimens, further researches are necessary to quantify the effects of sheet thickness,  $a/W$ ,  $n$  and also in-plane specimen dimensions on  $\eta_p$ .

As of now,  $\eta_p$  needs to be determined for SENT specimens of each test material and sheet thickness of interest. If a fully 3-D FE simulation (non-growing crack) based analysis is adopted, then it seems prudent to first validate the simulations by comparing with mechanical test results, cf. Fig. 5.8(a), and also to identify the crack initiation points. It is also desirable to first identify the lower cut off for  $v_p$  from a plot like Fig. 5.11(c). Operationally, Data sets IA and IIIA may be preferred, simply because these avoid the high degrees of % necking in Data set IIA, which strictly are not necessary for  $\eta_p$  determination. The computation intensive 3-D FE simulation based method does not seem to be very attractive for routine use. It is of course possible to determine  $\eta_p$  using only data from mechanic tests, without the support of FE analyses. It then becomes necessary to identify (or, estimate with reasonable conservatism), the crack initiation point(s), for the specimen with the highest crack length for a campaign using Data set I or IA, and for all the specimens for a campaign using Data set III or IIIA. It should be noted that all the discussion so far, excluding the results shown for Method 2 in Fig.5.3, is based on  $\eta_p$  computed using Method 1. This is because Method 2 using power law as implemented in Section 3.1 enforces a constant  $\eta_p$ . It is desirable to search for suitable alternatives functional forms for Method 2.

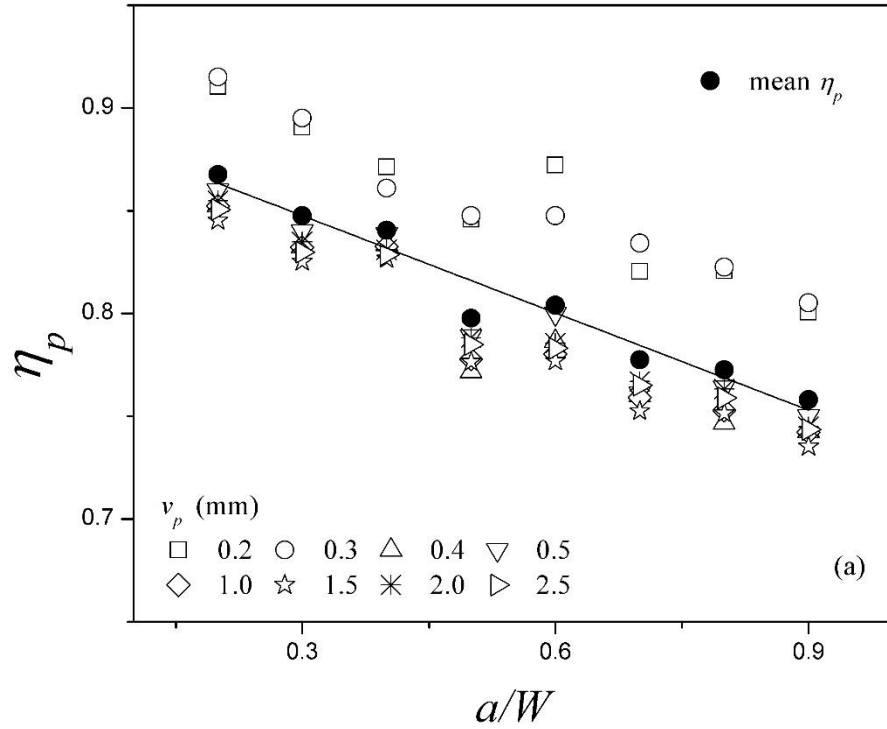


**Figure 5.11(a):** Variation of  $\eta_p$  with  $a/W$  for various  $v_p$  levels. The firm line shows the optimal linear fit of the data, and filled circles show for each  $a/W$ , the mean  $\eta_p$  computed for the chosen  $v_p$  levels.

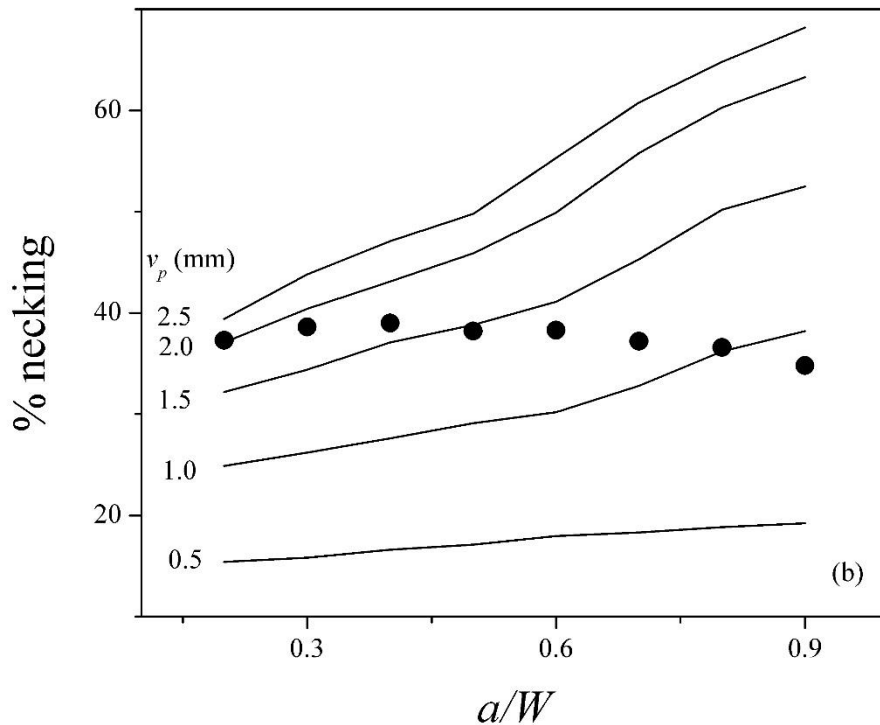


**Figure 5.11(b):** Variation of % necking with  $a/W$  for indicated  $v_p$  levels. The filled symbols show the % necking measured from FE mesh at crack initiation points (e.g., point “a1” in Fig. 5.7(a) inset) in these specimens.

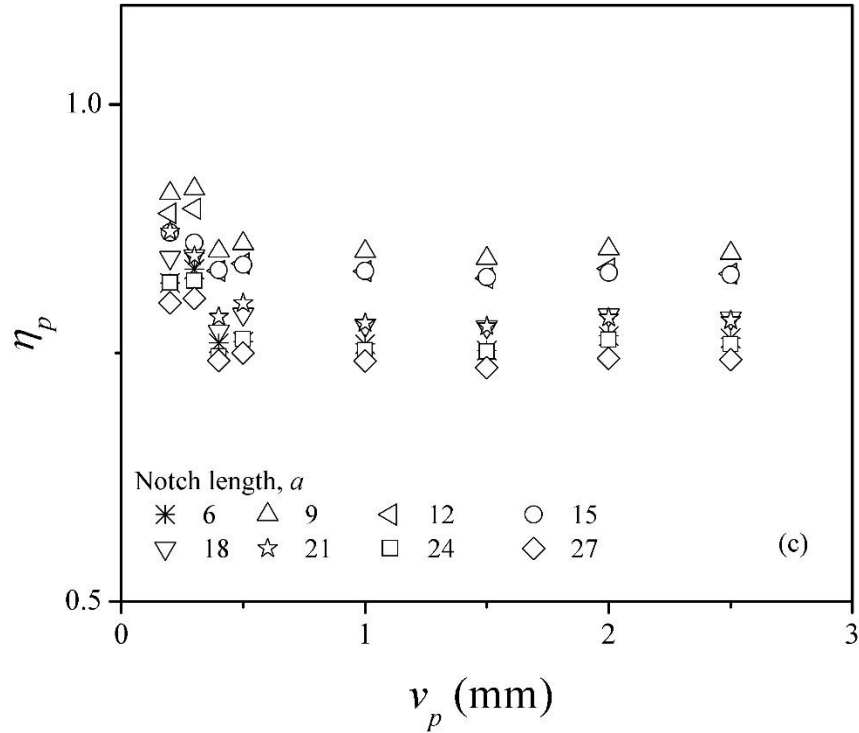


**Figure 5.11(c):** Variation of  $\eta_p$  with  $v_p$  for various  $a/W$  levels.

### 5.3.3 Effect of notch tip radius $\rho$ on $\eta_p$

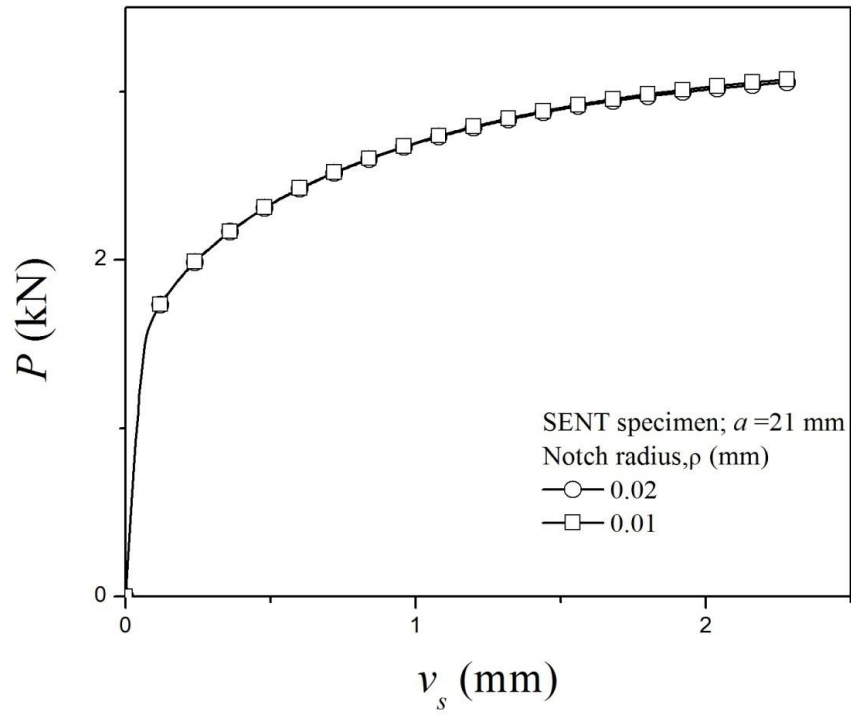
In common with the practice for thick fracture mechanics specimens, the results presented so far relied upon notched specimen data ( $\rho = 0.1$  mm) for evaluating  $\eta_p$  for sheet specimens also. It is necessary to verify that the  $\eta_p$  thus determined should apply for fatigue pre-cracked sheet SENT specimens also. For the present sheet material, the effect of  $\rho$  was checked by comparing  $\eta_p$  results for  $\rho = 0.1$  mm (Section 5.3.2) with those computed from FE simulation data (non-growing crack) for  $\rho = 0.02$  mm and also for  $\rho = 0.01$  mm. Accordingly, 3-D FE simulations were carried for SENT specimens with  $a = 21$  mm but with the chosen  $\rho$  values ramp loaded at the identical ramp rate. For both the simulations with  $\rho = 0.02$  mm and  $\rho = 0.01$  mm, 8 node 3-D solid hexahedral elements, C3D8R elements were used. The mesh thickness was 0.2 mm (i.e. 5 slices in thickness direction), and in-plane mesh size was  $0.05 \times 0.05$  mm around the notch gradually increasing to  $1 \times 1$  mm away from the notch. The reduction in in-plane mesh sizes near notch compared to those used for FE simulations of specimens with  $\rho = 0.1$  mm (in Section 5.3.2) was meant to accommodate the larger deformation around the notch. The computed  $P$  -

$v_s$  data for these two notch root radii showed excellent matching, with maximum difference in  $P$  being 0.15% at the highest  $v_s$  value of 2.3 mm, corresponding to  $v_p \sim 2.2$  mm for this specimen (Fig.5.12).

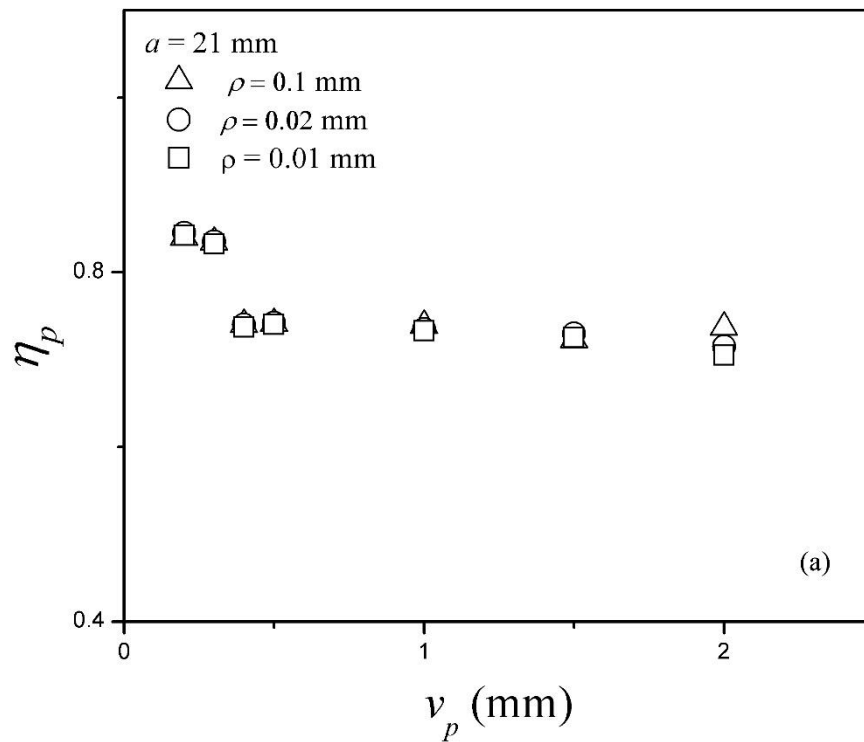
For both  $\rho = 0.02$  and 0.01 mm, with the specimen meshing described above, contour elastic-plastic  $J$  integral evaluation scheme available in ABAQUS 6.10 code [137] was used to compute the values for the parameter designated as  $J_p^{max}$  for the chosen values of  $v_p$ .  $J_p^{max}$  is the value of  $J_p$  for a contour of radius 1 mm lying on the element surface parallel to the front and back surfaces of the specimen and normal to the crack front, but located at a distance  $z = 0.4t$  from specimen surface. For the present meshing using element thickness of 0.2 mm,  $J_p^{max}$  is the highest computed contour integral, for the contours located at  $z = 0.4t = 0.6t$ . Further details about  $J_p^{max}$  are discussed in Section 5.3.4. From the  $J_p^{max}$  values for the chosen  $v_p$  levels, the corresponding  $\eta_p$  was determined by invoking Eq. (5.2), as  $\eta_p = J_p^{max} / (A_p / tl)_{v_p}$ . Figure 5.13(a) plots against  $v_p$  the  $\eta_p$  values computed by the contour integration route for  $\rho = 0.02$  and 0.01 mm, and using Method 1 with FE simulated  $P - v_p$  data for  $\rho = 0.1$  mm. For different  $v_p$  values,  $\eta_p$  values for  $\rho = 0.1$  to 0.01 mm are found to match very closely. Specifically, the initial anomalous variation in  $\eta_p$  for  $v_p < 0.4$  mm seen in Fig. 5.11(c) for all the specimens are reproduced by the contour integration results for  $\rho = 0.02$  and 0.01 mm, Fig. 5.13(a). This suggests that the initial anomalous behavior in Fig. 5.11(c) may be due to crack tip necking in sheet metals; more research is required to clarify this aspect.

Figure 5.13(b) shows that for a given  $v_p$ ,  $J_p^{max}$  values for  $\rho = 0.02$  and 0.01 mm nearly coincide for the entire  $v_p$  range investigated, but both are smaller than the corresponding  $J_p^{max}$  values for  $\rho = 0.1$  mm and the difference increases with increasing  $v_p$ . Also, exactly as for thick fracture mechanics specimens, for sheet SENT specimens also, sharp notch produced by fatigue pre-cracking is necessary for determining the value of  $\rho$ -independent critical  $J$  integral (for possible integrity evaluation purposes), but notches with  $\rho = 0.1$  mm are found adequate for  $\eta_p$  determination.





**Figure 5.12:**  $P - v_s$  plots for SENT specimens with  $a = 21$  mm, and with notch tip radius  $\rho = 0.02$  mm and  $\rho = 0.01$  mm.



(Continued)

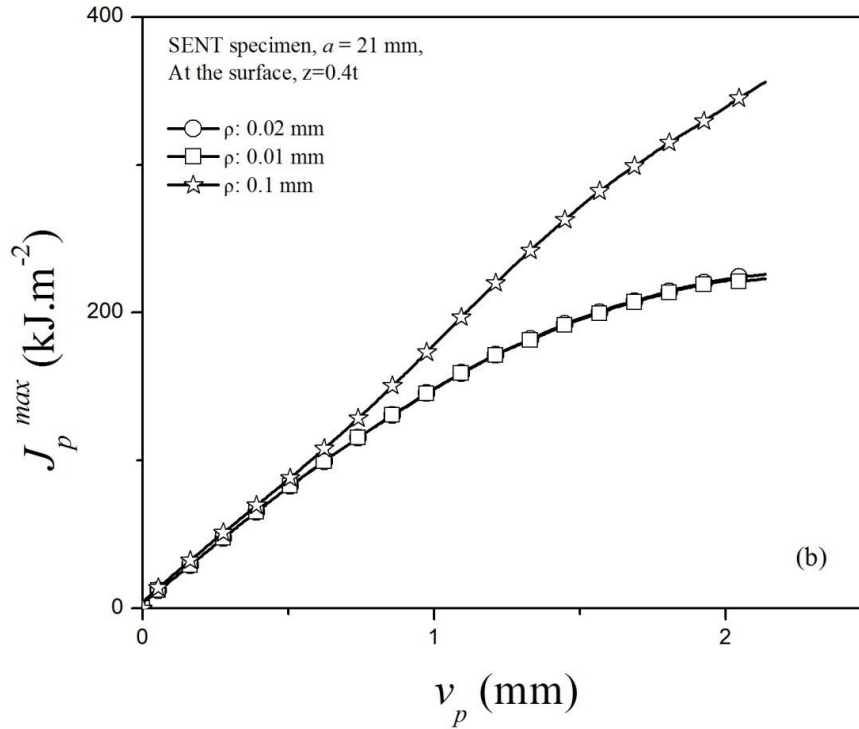


**Figure 5.13:** Effect of  $\rho$  on (a)  $\eta_p$  and (b)  $J_p$  values

Figure 5.13(b) also suggests that for the present test material,  $\rho = 0.02$  mm represents an “infinitely” sharp crack, because it is adequate to determine  $\rho$ -independent fracture properties. This was verified by a mesh convergence study for the specimens with  $\rho = 0.02$  mm specimen, using identical element thickness of 0.2 mm, but in-plane mesh size gradually increasing from  $0.01 \times 0.01$  mm (in place of  $0.05 \times 0.05$  mm) around the notch to  $1 \times 1$  mm away from the notch. Even after such considerable refinement in mesh sizes near the notch with consequent drastic increase in the computational burden, at the highest  $v_s$  level of 2.3 mm, the difference in the computed  $P$  was only 0.13%, and the difference in  $J_p^{max}$  value was only 0.9%.

### 5.3.4 $\eta_p$ determination from $J$ contour integral values for notched specimens

Section 5.3.3 presented limited results which *inter alia* verified that for the present sheet material,  $\eta_p$  determined using Method 1 (Sections 5.3.1 and 5.3.2) is consistent with the fundamental path-independent line integral definition of the  $J$  parameter (see [2]). In this Section, the path independent contour integral definition

of  $J$  has been used to compute the  $v_p$ -dependence of  $J_p$  for the SENT specimen with  $a = 21$  mm and  $\rho = 0.1$  mm. The ABAQUS 6.10 FE code was used for these  $J_p$  computations (see Section 5.3.3 for reference). The meshing adopted was identical to the one used for the FE results reported in Section 5.3.2: C3D8R elements were used with element thickness of 0.2 mm (i.e. 5 slices), and in-plane element size increased gradually from 0.2 mm  $\times$  0.2 mm around the notch to 1 mm  $\times$  1 mm away from the notch (Fig.5.14 (a)). Applying the divergence theorem, any contour integral can be converted into a volume integral in three dimensions, over a finite domain surrounding the crack. ABAQUS 6.10 uses this domain integral method to evaluate the elastic-plastic  $J$ -integral values for each contour defined. ABAQUS considers contours with the user specified radius on the x-y plane parallel to the sheet surfaces and perpendicular to the crack front, for each element layer in the sheet thickness ( $z$ ) direction. Taking into account the specimen symmetry, for the present meshing with 5 layers, the contour integral results are available for  $z = 0 = t$  (the two surfaces),  $z = 0.2t = 0.8t$ , and  $z = 0.4t = 0.6t$ , closest to the highest constraint plane at  $z = 0.5t$ . Therefore, with the present 5 layer meshing, the highest value for the computed contour  $J$  integral obtains for  $z = 0.4t (= 0.6t)$ , which is the closest estimate of  $J$  integral for  $z = 0.5t$ . ABAQUS also computes the elastic component of the contour  $J$  integral,  $J_e$ , by considering an elastic crack. Using these data, the plastic component of  $J$  integral,  $J_p$ , can be obtained from the equation  $J_p = J - J_e$ .

The path independence of the computed contour  $J$  integral was examined by considering three contours with radii 0.75 mm, 1 mm and 1.2 mm around the notch tip. The  $J_p - v_p$  plots for the plane at  $z = 0.4t$  (designated as  $J_p^{max}$  because this is the highest computed  $J_p$  with the present meshing) for these contours are shown in Fig. 5.15(a): the maximum difference for these three contour radii is only 2.1% for  $v_p$  as high as 2.2 mm. This path independence of these contour holds for all the six surfaces ranging from  $z = 0$  to  $z = t$ , with an interval of  $t/5 = 0.2$  mm along thickness direction. Based on these findings, the intermediate radius, namely 1 mm, has been chosen for computing path independent  $J_p$  values. Figure 5.15(b) confirms that  $J_p$  values increase from minimum at surface to maximum value at mid

thickness, consistent with increasing constraint from surface ( $z = 0 = t$ ) to centre ( $z = 0.5t$ ) of the specimen. This figure also confirms the symmetry in  $J_p$  values with respect to distance from mid-plane, at  $z = 0.5t$ . Thus  $J_p$  values can be defined either in terms of the maximum computed  $J_p$  value,  $J_p^{max}$  at  $z = 0.4t = 0.6t$  for the present meshing, or as the average  $J_p$  value,  $J_p^{avg}$ , determined by averaging  $J_p$  values for all the six layers, also shown in Fig. 5.15(b). For comparing with results from mechanical tests,  $J_p^{avg}$  should be more appropriate. It is interesting to note that for this SENT sheet specimen with  $a = 21$  mm,  $\rho = 0.1$  mm, at crack initiation (point “a1” in Fig 5.8(a), corresponding to  $v_p = 1.18$  mm), the through-thickness variation of  $J_p$ , from surface to mid-plane ( $z = 0.5t$ ), is only 7%. The difference between  $J_p^{max}$  and  $J_p^{avg}$  is only about 1.7% at the crack initiation point, rising to only 5.6% for  $v_p = 2.2$  mm.

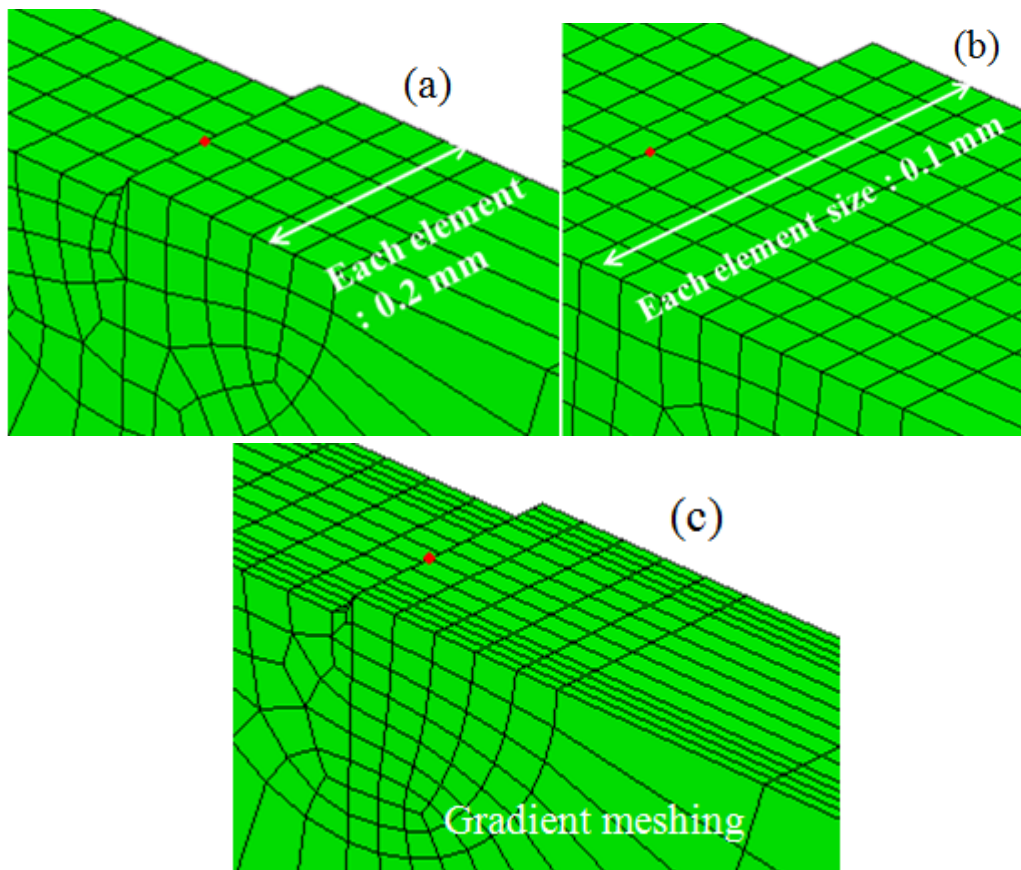


**Figure 5.14:** Through thickness meshing with C3D8R elements having element size (a) 0.2 mm, (b) 0.1 mm, and (c) gradient meshing, with the red dot denoting the location  $z = 0.4t$ , i.e., for  $J_p^{max}$  as defined in this study.

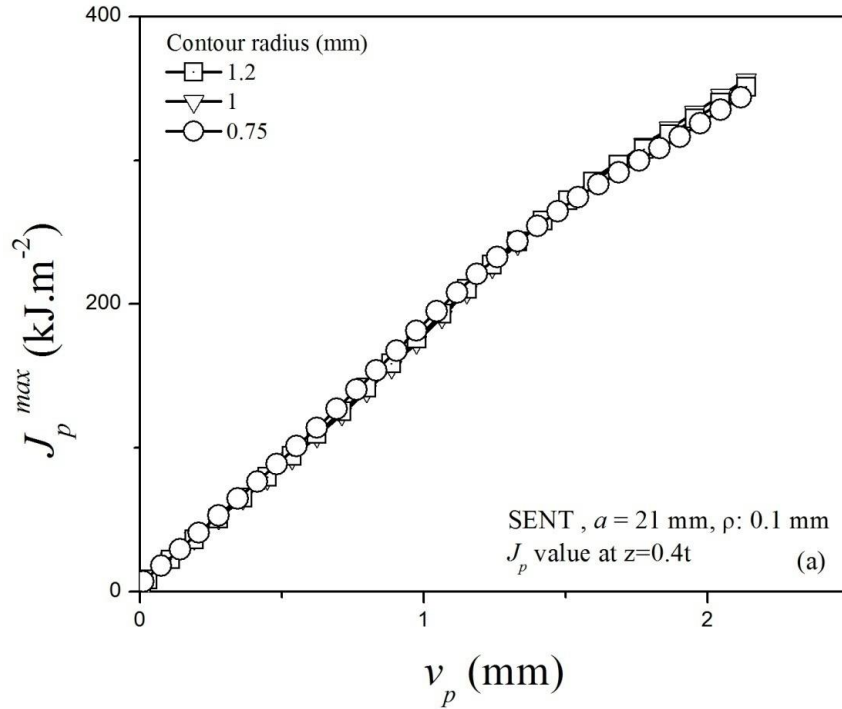


**Figure 5.15(a):** Path independence of  $J_p^{max}$ -  $v_p$  plots for contour radii 0.75 mm, 1 mm and 1.2 mm around the notch determined at  $z = 0.4t$ .

Mesh convergence study was also carried out for  $J_p$  -  $v_p$  plots for all the surfaces along the thickness direction by using the same meshing used for mesh convergence study for  $P$  -  $v_s$  plots in Section 5.3.2. That is, C3D8R elements were used with the two different meshing: (i) element thickness = 0.1 mm (i.e., 10 layers in thickness direction) and element in-plane size gradually increasing from 0.1 mm  $\times$  0.1 mm around the notch to 1 mm  $\times$  1 mm away from the notch (Fig.5.14(b)); and (ii) gradient meshing along thickness direction, with in-plane size 0.2 mm  $\times$  0.2 mm around the notch gradually increasing to 1 mm  $\times$  1 mm away from the notch (Fig.5.14(c)). With these two meshing and also the meshing used to compute the results in Figs. 5.15(a) and 5.15(b), for a  $v_p$  value of 2.2 mm, (i) the maximum difference in  $J_p^{max}$  (at  $z = 0.4t$ ) values was only 1.1% (Fig. 5.16); (ii) the maximum difference in  $J_p^{avg}$  values was only 0.8% (Fig. 5.16).; and (iii) the maximum difference between  $J_p$  for  $z = 0.5t$ , and  $J_p^{max}$  was 0.48%. From the data presented in Fig. 5.15(b) for the  $\rho = 0.1$  mm specimen, the six  $J_p$  values for the six  $z$  levels were obtained for  $v_p = 2.2$  mm; their interpolation yielded  $J_p$  for  $z = 0.5t$ . These results confirmed that meshing adopted for the results reported in Figs.

5.15(a) and 5.15(b) is adequate for the intended application, and are used for further computations. Also, almost negligible error is committed in designating  $J_p$  at  $z = 0.4t$  as  $J_p^{max}$  for the present analysis.

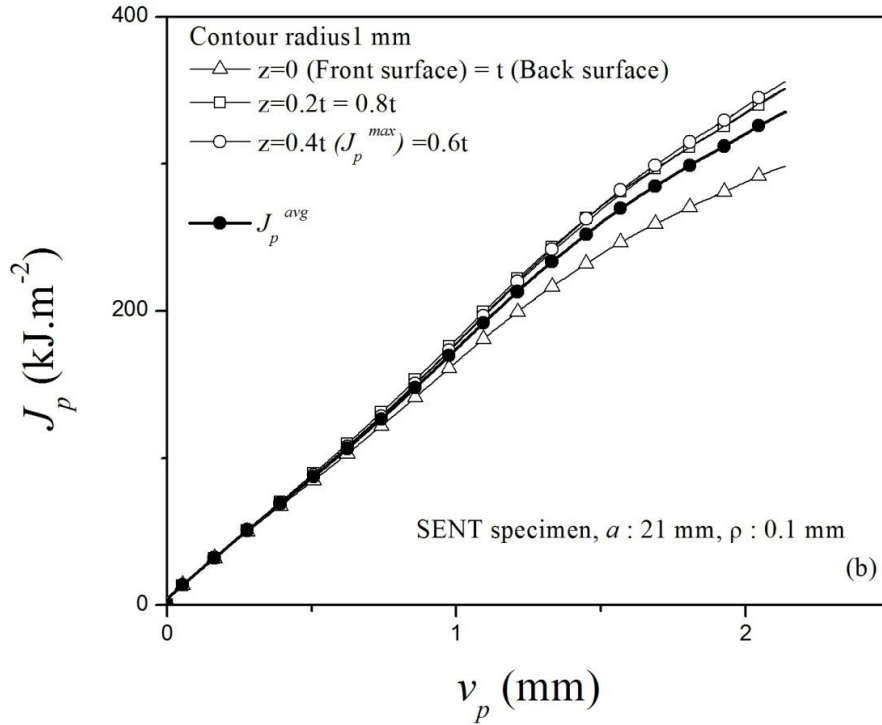


**Figure 5.15(b):** Through thickness variation of  $J_p$  integral and  $J_p^{max}$  (at  $z=0.4t$ ) and  $J_p^{avg}$  value for SENT specimen with  $a = 21$  mm,  $\rho = 0.1$  mm.

Figure 5.17(a). shows that for the SENT specimen with  $a = 21$  mm,  $\rho = 0.1$  mm,  $J_p$  values determined by using a mean  $\eta_p = 0.81$  with FE simulated  $P - v_p$  data (non growing crack), agree well with both  $J_p^{max}$  (at  $z=0.4t$ ) and  $J_p^{avg}$  derived from the contour integral (contour of radius 1 mm) up to  $v_p$  level similar to that for crack initiation, i.e., 1.1 mm (variation 3.4%); but start deviating increasingly for higher  $v_p$  levels. Figure 5.17(b) compares the  $\eta_p - v_p$  plots computed from the  $J_p^{max}$  and  $J_p^{avg}$  values in Fig. 5.15(b) with the  $\eta_p - v_p$  plot obtained for the specimen with  $a = 21$  mm,  $\rho = 0.1$  mm, by using Method 1 with FE simulated  $P - v_p$  data reported in Section 5.3.2. The three mean  $\eta_p$  values for the entire  $v_p$  range differ at most by 1.5%, and the initial anomalous variation in the  $\eta_p - v_p$  plot in Fig. 5.11(c) discussed in Sections 5.3.2 and 5.3.3 is also noted in Fig. 5.17(b).

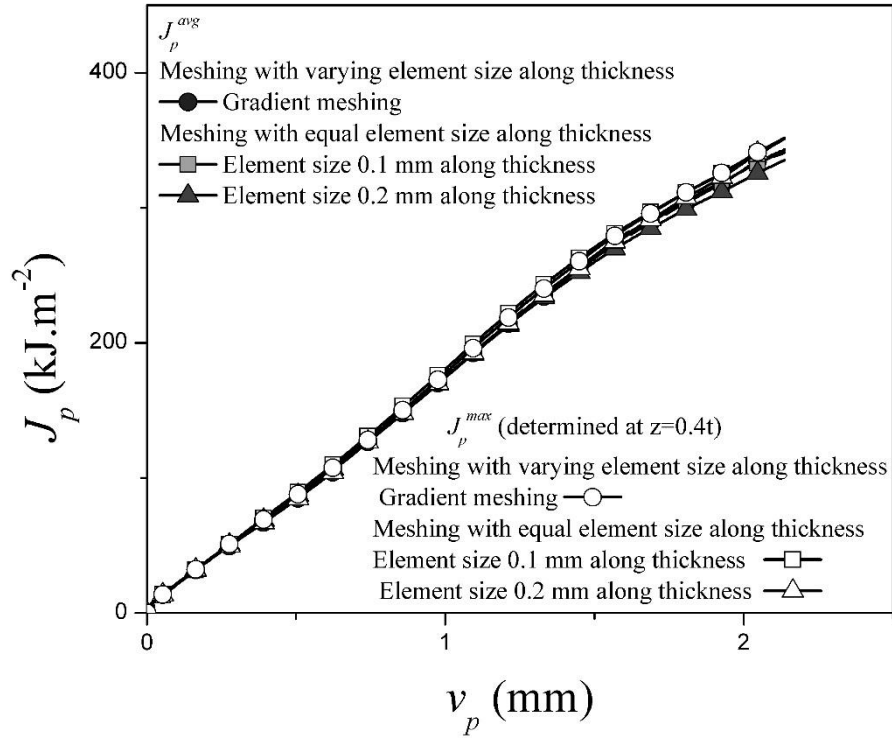
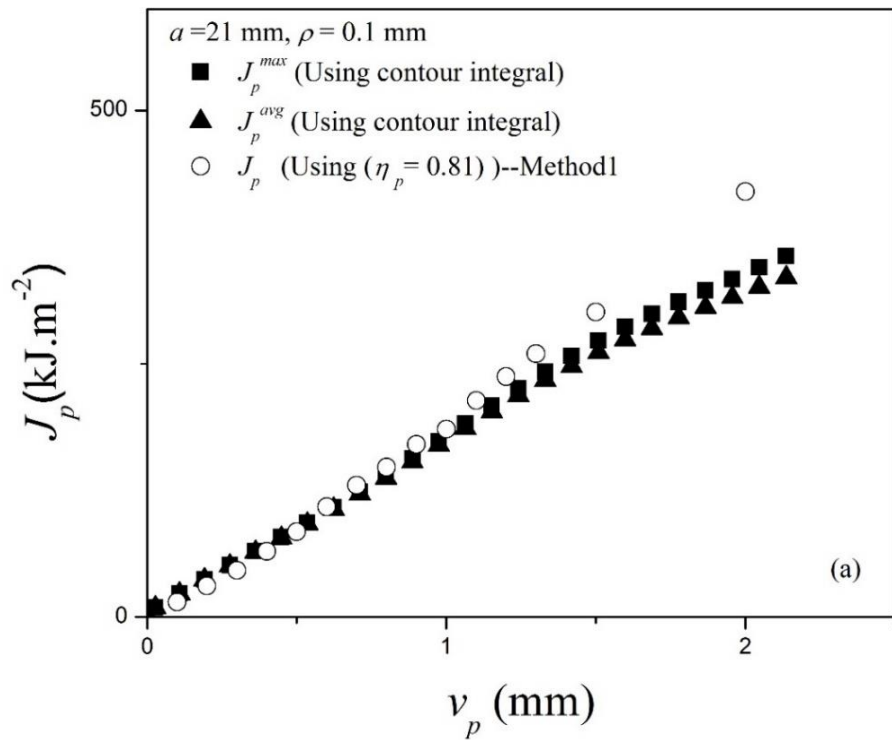


**Figure 5.16:** For the SENT specimen with  $a = 21$  mm, Comparison of  $J_p^{max}$  (at  $z=0.4t$ ) and  $J_p^{avg}$  values considering the contour of 1mm for the three meshing used in this study



(Continued)

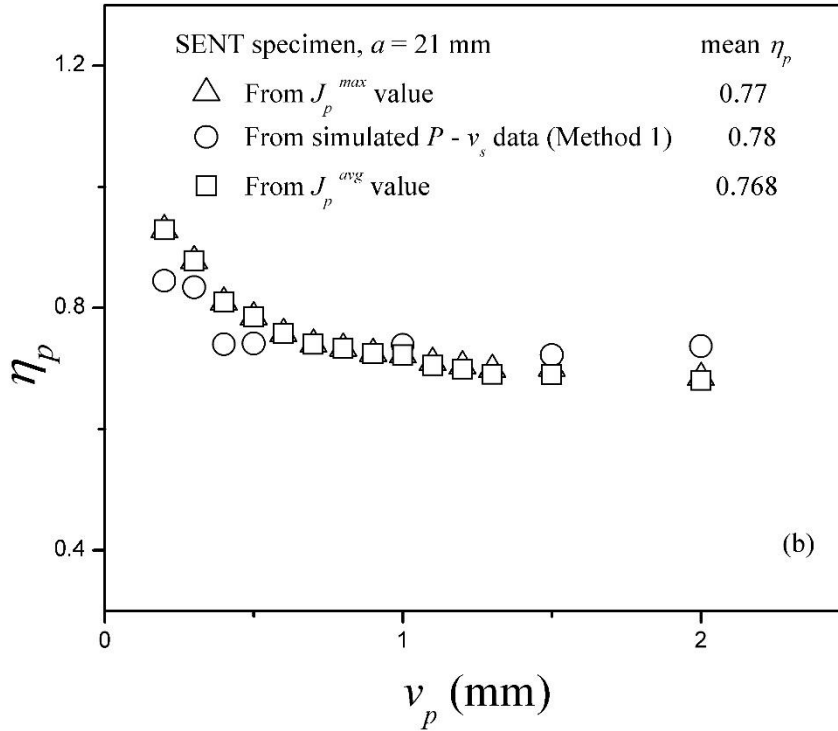


**Figure 5.17:** For SENT specimen with  $a = 21$  mm, comparison of the  $v_p$ -dependence of (a)  $J_p$  and (b)  $\eta_p$  determined from contour integral (considering both  $J_p^{max}$  and  $J_p^{avg}$  values) and Method 1 with FE simulated  $P$ - $v_p$  data.

### 5.3.5 Evaluation of $J_p$ at crack initiation for notched SENT specimens

As shown in Section 5.3.2, the 3-D FE simulations for non-growing crack can be used for identifying crack initiation points from test data for notched SENT specimens.  $J_p$  values for crack initiation,  $J_p^c$ , were calculated at these crack initiation points using Eq. (4.2), i.e.,  $J_p^c = \eta_p A_p / lt$ . In this equation, the previously determined  $\eta_p = 0.81$  (by Method 1, Sections 5.3.1) was used. The  $J_p^c$  values thus determined for  $0.2 \leq a/W \leq 0.9$  ( $24 \geq l \geq 3$  mm) are shown in Fig. 5.18.

As Fig. 5.18 shows,  $J_p^c$  shows slight variation with  $a/W$ . Ignoring this variation and considering the entire data set, the average  $J_p^c$  value is  $191.7 \text{ kJ.m}^{-2}$  (with standard deviation =  $4.3 \text{ kJ.m}^{-2}$ ). This agrees within  $\sim 4\%$  with the average  $J_p^c = 199.8 \text{ kJ.m}^{-2}$  determined using notched DENT specimens ( $\rho = 0.1$  mm) of the same sheet material for  $l = 3$  to  $10$  mm, Fig.4.14. The good agreement in the average  $J_p^c$  values determined using notched SENT and DENT specimens of the sheet material shows



that for the notched specimens of the present sheet material,  $J_p^c$  (and therefore,  $J_c$ ) qualifies as a material property that is independent of specimen geometry, SENT or DENT. This is discussed further in Section 6.3.3.1. This result appears to lend credence to using  $\eta_p = 1 - n$  for the present sheet DENT specimens (see Sections 2.2 and 4.3.4.2).

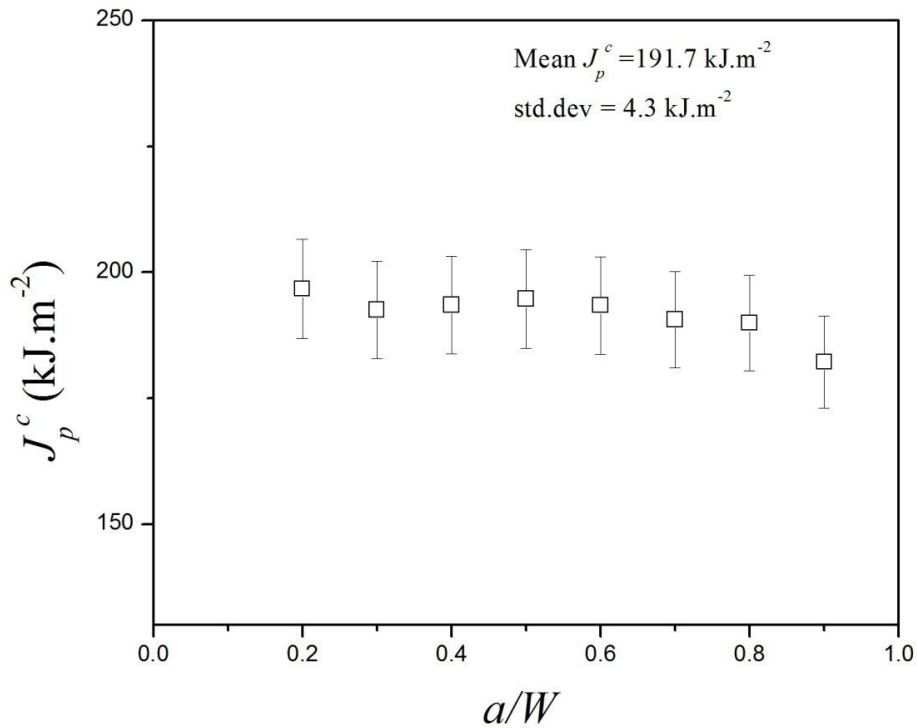


**Figure 5.18:** For notched ( $\rho = 0.1$  mm) SENT specimens, variation of  $J_p^c$  with  $a/W$  ratio

## 5.4 Conclusions

1. For determining  $\eta_p$  for notched ( $\rho = 0.1$  mm) SENT specimens of the present test material with  $0.2 \leq a/W \leq 0.9$ , two well-known formulations for thick specimens (designated as Method 1 and Method 2 in this report) were considered. Good agreements were obtained for  $\eta_p$  computed by Methods 1 and 2 with mechanical test data conservatively estimated to be prior to crack initiation, and also Method 1 with data from 3-D FE simulation for non-growing cracks. However, the functional forms for  $S_k(l_k/W)$  considered for implementing Method 2 proved inadequate; there is a need to search for better functional forms. The  $\eta_p$  values determined using Method 1 are consistent with the fundamental path-independent line integral definition of the  $J$  – parameter.

2. For the different specimens, the data from 3-D FE simulations for non-growing cracks for  $v_p$  as high as 2.5 mm (covering crack initiation in all the tested specimens) have been analysed using Method 1. The results suggest that the high crack tip necking does not affect the  $\eta_p$  factor significantly for  $2.5 \geq v_p \geq 0.4$  mm. A similar result may be anticipated for sheet DENT specimen of the present test material; it will be interesting to verify this conjecture.
3. The  $\eta_p$  results using Method 1 for the different data sets considered are quite similar: the decrease in the value of  $\eta_p$  with  $a/W$  increasing from 0.2 to 0.9, can be described by a linear relation with a modest slope, or even considering a mean  $\eta_p$  (such as 0.81) for the entire  $a/W$  range.
4. In defining the data sets to be analysed for determining  $\eta_p$ , it is advantageous to be able to identify the crack initiation points without undue conservatism. In the present study, both for DENT and SENT specimens, the crack initiation points have been determined with adequate resolution by comparing load-displacement data sets from experiments and from 3-D FE simulations for a non-growing crack. There is, however, scope for searching for alternative method(s) for identifying crack initiation point which avoid extensive FE computations.
5. For the sheet SENT specimen with  $a = 21$  mm, it has been verified that  $\rho = 0.1$  mm is adequate for determining  $\eta_p$ , but fatigue pre-cracked specimens should be used for determining  $\rho$ -independent  $J_p$ . For FE computations,  $\rho = 0.02$  mm proves to be satisfactory for representing a pre-cracked SENT specimen of the present test material.
6.  $\eta_p$  determination reported here is validated for one specimen by FE simulation that computes  $J$ -integral invoking its fundamental path independent line integral definition.
7. Mean  $J_p^c$  values for notched ( $\rho = 0.1$  mm) DENT and SENT specimens (Figs. 4.14 and 5.18 respectively) for the higher ligament lengths agree within  $\sim 4\%$ , consistent with  $J_p^c$  being a material property.

## 6.1 Introduction

Chapter 4 reported the results from a detailed characterization of crack initiation and growth in the test sheet material using DENT specimens. It included determining the EWF parameters and studying the effects of quasi-static ramp rate and notch root radius on these parameters.  $\varphi - \Delta a$  plots have been generated by testing fatigue pre-cracked DENT specimens following a test protocol that closely follows the optical method in ASTM E 2472 [33]. This enabled comparing the EWF crack growth parameter  $\psi^e$  with its fracture mechanics counterpart,  $\varphi_c$ . Adopting a novel 3-D FE simulation based method for identifying crack initiation, it was possible to determine then fracture mechanics based initiation parameters  $J_p^c$  (the plastic component of  $J_c$ ),  $\delta_c$  and also  $w_i$ , as functions of ligament length. It thus became possible to compare the crack initiation parameters  $w_e$ ,  $\delta_c^e$  from EWF tests with their fracture mechanics counterparts,  $J_p^c$  (the plastic component of  $J_c$ ) and  $\delta_c$ , respectively.

These results are interesting and useful. But for any crack initiation or growth parameter to be considered a material property, it must be demonstrated to be independent of the specimen geometry. In literature, there is very limited evidence only on the geometry independence of  $w_e$  and  $w_i$  [45], based on testing of DENT and SENT specimens of a polymeric material. The primary focus of this chapter is examining this geometry independence of the various parameters considered in Chapter 4. Towards this end, the various tests carried out with DENT specimens as reported in Chapter 4 are replicated with SENT specimens, and the results for these two specimen geometries are compared. An added benefit of this exercise is: if a parameter is to be determined using pre-cracked specimens, then considering the ease of fatigue pre-cracking, SENT and not DENT specimens are for choice (see Section 3.2.3). In addition, exploratory studies are carried out on extending the

EWF paradigm to the regime of complex state of stress for crack initiates and early crack growth.

However, before embarking in it is necessary to revise Eq. (2.7). This equation for DENT specimens is consistent with the kinetic equation

$$\frac{d(v_f - \delta_c^e)}{dl} = \psi^e$$

For a DENT specimen with ligament length  $l$ , fracture takes place when each of the two cracks extend by length  $l/2$ , i.e.,

$$\int_0^{l/2} \frac{d(v_f - \delta_c^e)}{dl} dl = \int_0^{l/2} \psi^e dl = (\psi^e) \frac{l}{2} = v_f - \delta_c^e;$$

Recognizing that a SENT specimen with a single notch, specimen fractures when crack growth equals  $l$ , and assuming that the same kinetic equation applies when  $l$  meets the appropriate validity criteria,

$$\int_0^l \frac{d(v_f - \delta_c^e)}{dl} dl = \int_0^l \psi^e dl = (\psi^e)l = v_f - \delta_c^e$$

That is, for SENT specimens, the equation to be used in place of Eq. (2.7).

$$v_f = (\psi^e)l + \delta_c^e \quad (6.1)$$

However, for fracture of either DENT or SENT specimens, with ligament length  $l$ , the ligament area fractured is  $lt$ . Therefore, for either specimen geometry, subject to validity criteria, Eq. (2.6), i.e.  $w_f = w_e + \beta w_p l$  applies.

## 6.2 Experimental

The EWF testing with notched ( $\rho = 0.1$  mm) or fatigue pre-cracked SENT specimens followed the scheme for the DENT specimens, Section 4.2. Briefly, SENT specimens (Fig. 3.2(a)) of size  $90 \times 30 \times 1$  mm (i.e., same as that of the DENT specimen tested in this research), machined in longitudinal (L-T) orientation with different ligament lengths  $l$  were taken for EWF testing. EWF testing was carried out following the procedure described in Section 3.2.2 at three different ramp rates of 0.6, 0.06 and 0.006 mm.s<sup>-1</sup> (corresponding to nominal strain rates of

$10^{-2}, 10^{-3}$  and  $10^{-4} \text{ s}^{-1}$ ) for the notched specimens. Also, five SENT specimens were fatigue pre-cracked following the procedure described in Section 3.2.3 to varying  $l$  in the range 4.3 - 9.6 mm, and EWF tested at ramp rate of  $0.006 \text{ mm.s}^{-1}$ . To determine the critical CTOA ( $\varphi_c$ ) value, pre-cracked SENT specimens were tested at three different ramp rates of 0.6, 0.06 and  $0.006 \text{ mm.s}^{-1}$  by the procedure described in Section 3.2.4.

## 6.3. Results and discussion

### 6.3.1 EWF tests

#### 6.3.1.1 Determining the valid $l$ ranges for EWF tests

Figures 6.1(a) and 6.1(b) show respectively the  $v_f - l$  and  $w_f - l$  plots for the notched SENT specimens with  $l = 1, 2, 3, 4, 5, 6, 7, 8, 9, 10, 12$  or  $15 \text{ mm}$ , tested at ramp rate of  $0.006 \text{ mm.s}^{-1}$ ; the lines in these figures were obtained from linear least square fits for the entire data sets. From these figures, it appears that for either plot, the linearity conditions hold for the data with  $l = 3-10 \text{ mm}$ , consistent with the “thumb rule” for DENT specimens proposed by Cotterell and Reddel [39]. It may be recalled that the corresponding  $l$ -validity range for the notched DENT specimens was  $2-10 \text{ mm}$ , Figs. 4.1(a)-(b)).

Figures 4.2(a)-(d) for the 4 sets of EWF tested DENT specimens showed that for identifying the  $l$ -validity range, the empirical criterion,  $\sigma_n \cong 1.15 \sigma_u$ , appears to be superior to either Hill’s [101] or Clutton’s [103] criterion (cf. Section 2.6). Figures 6.2(a)-(d) show the variations of  $\sigma_n$  with  $l$  for the EWF tested notched or fatigue pre-cracked SENT specimen. For each of the data sets plotted, the  $0.9 \bar{\sigma}_n$ - $1.1 \bar{\sigma}_n$  bands have been defined following Clutton [103].  $\sigma_y$  and  $\sigma_u$  values are also shown in the plots. The dispositions of the  $\sigma_n$  data in these figures suggest that for determining both  $l_{min}$  and  $l_{max}$  for the notched or pre-cracked SENT specimens, the criterion  $\sigma_n \cong \sigma_u$  is better than the alternatives [101]. Also, for all these data sets, the validity range was  $4 \leq l \leq 10 \text{ mm}$  (used for subsequent EWF analysis), or possibly  $5 \leq l \leq 10 \text{ mm}$  for notched specimens tested at the ramp rate of  $0.6 \text{ mm.s}^{-1}$  (Fig. 6.2(d)). As for DENT specimens, this result underscores the inadequacy of linear fits of data (Figs. 6.1(a)-(b)) for identifying the  $l$ -validity

range. Since for DENT specimens the corresponding criterion was  $\sigma_n \cong 1.15\sigma_u$  (Section 4.3.1.1), it appears that for the present test material and for specimens in the corresponding valid  $l$ -ranges, the constraint level was slightly higher for the DENT specimens compared to the SENT specimens.

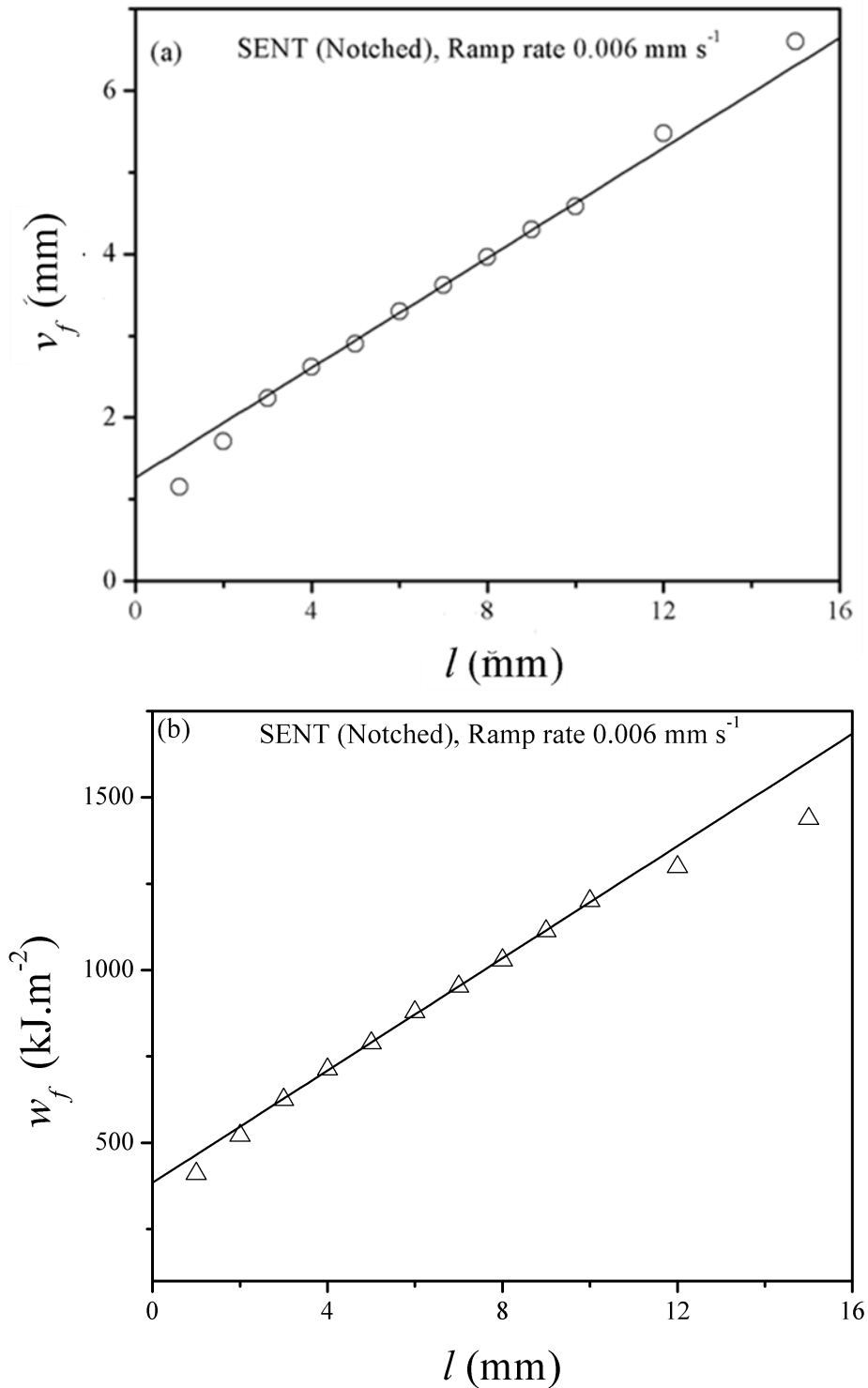
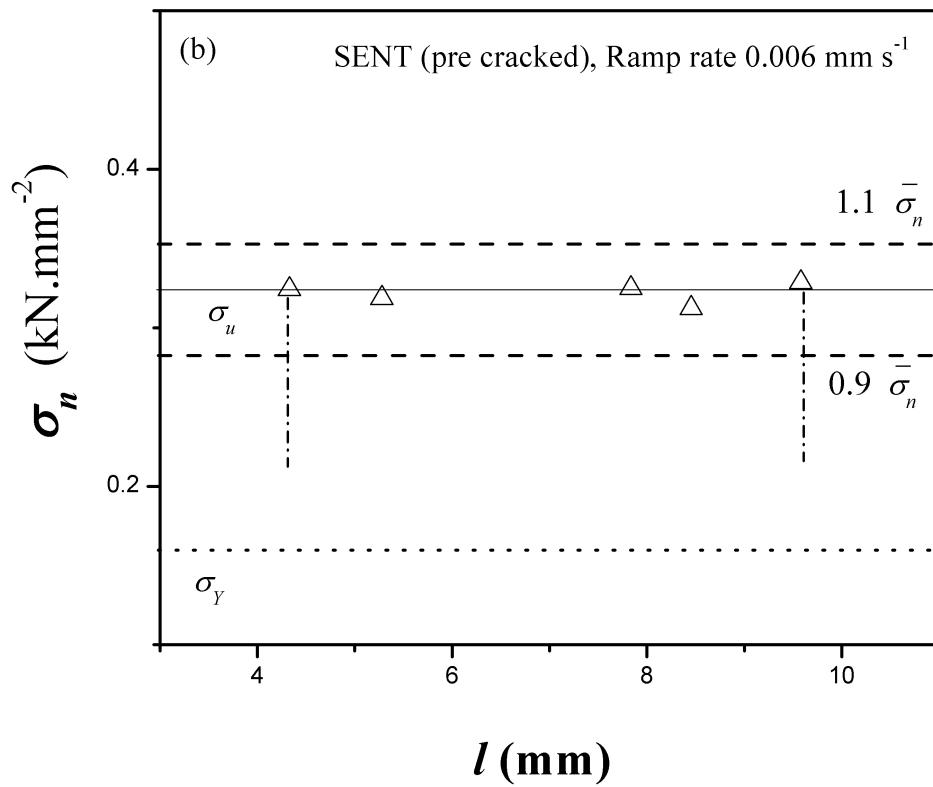
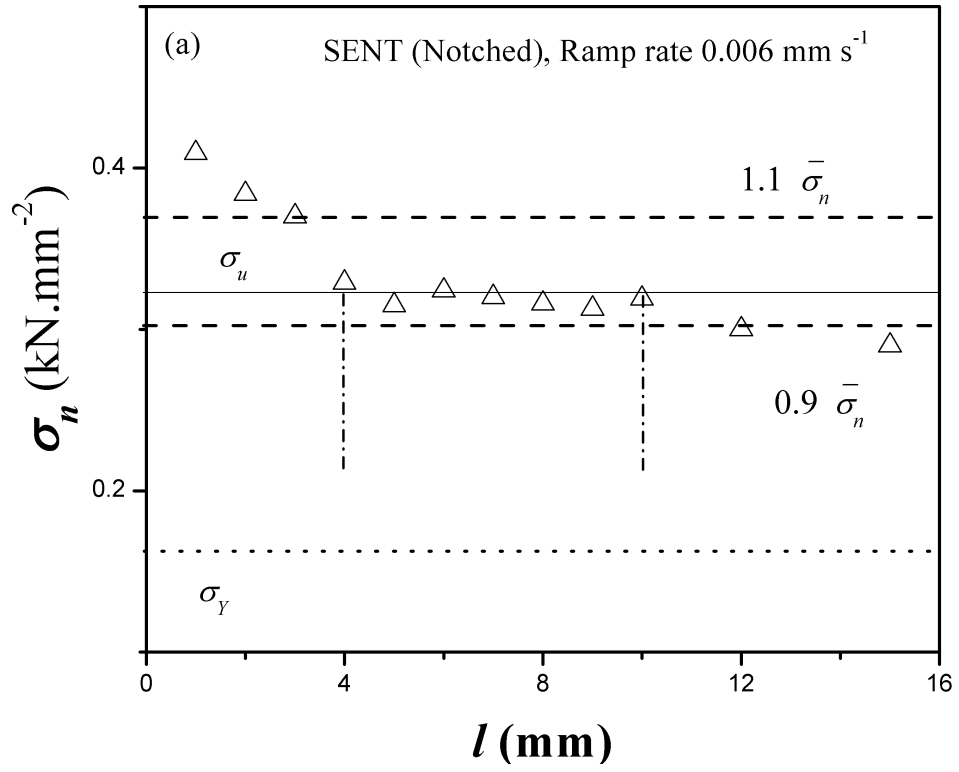


**Figure 6.1:** (a)  $v_f - l$  and (b)  $w_f - l$  plots of notched SENT specimens



(Continued)

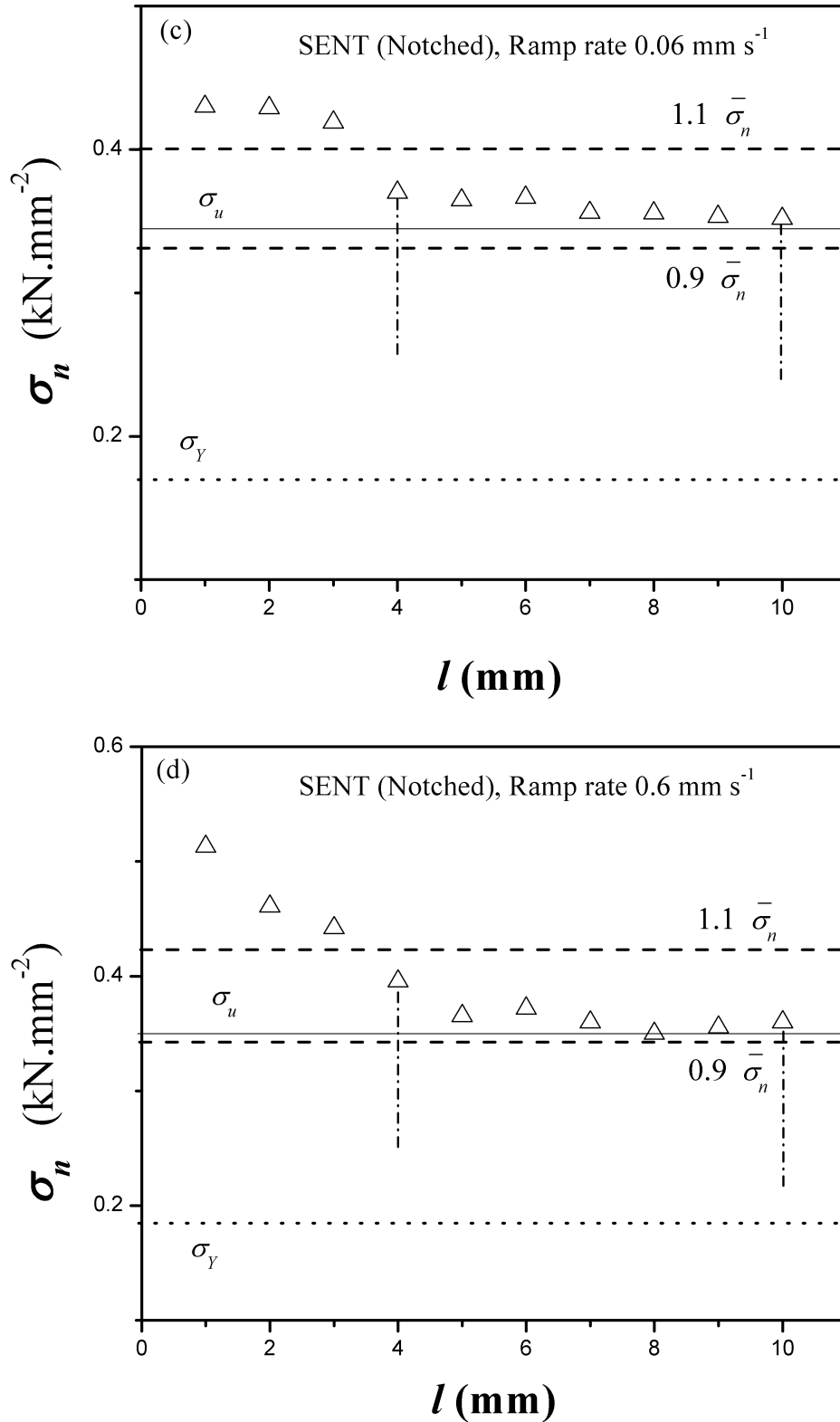


**Figure 6.2:**  $\sigma_n - l$  plots to determine valid  $l$  range for (a) notched, (b) pre-cracked SENT specimens tested at ramp rate  $0.006 \text{ mm.s}^{-1}$ ; (c) notched SENT specimens tested at ramp rate  $0.06 \text{ mm.s}^{-1}$ ; and (d) notched SENT specimens at  $0.6 \text{ mm.s}^{-1}$ . Pairs of dashed vertical lines identify the valid  $l$  ranges.



### 6.3.1.2 EWF analyses for tests at ramp rate $0.006 \text{ mm.s}^{-1}$

For tests carried out with notched and pre-cracked specimens at ramp rate  $0.006 \text{ mm.s}^{-1}$ , EWF least square data fitting was carried out using four different data sets:

Data set (i):  $P - v$  data sets from the tests carried out to 90% drop from peak loads were taken; the final values of  $v$  recorded were taken as  $v_f$ , and the corresponding areas  $P - v$  curves were taken as  $W_f$ .

Data set (ii):  $P - v$  data sets obtained from tests were augmented by linear extrapolation from the tail ends of generated test data to  $P = 0$ . The augmented data sets were used for determining  $v_f$  and  $W_f$ .

Data set (iii):  $P - v_a$  data sets from the tests carried out to 90% drop from peak loads were taken; the final values of  $v_a$  recorded were taken as  $v_f$ , and the corresponding areas under  $P - v_a$  curves were taken as  $W_f$ .

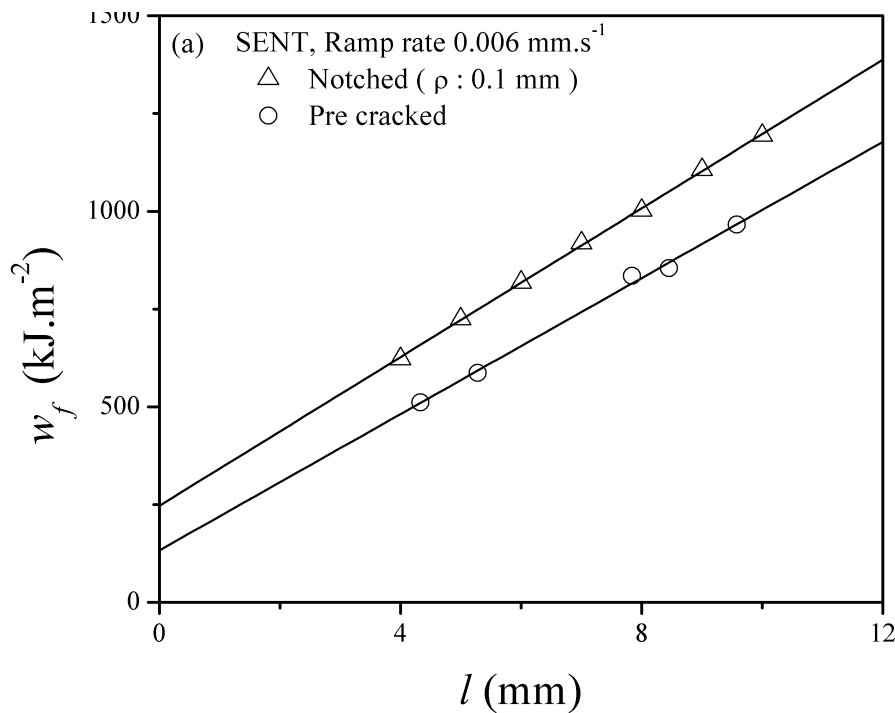
Data set (iv):  $P - v_a$  data sets obtained from tests were augmented by linear extrapolation from the tail ends of generated test data to  $P = 0$ . The augmented data sets were used for determining  $v_f$  and  $W_f$ .

The numerical results from these analyses are presented in Table 6.1. The linear correlation coefficients  $R^2$  for all the fits were quite satisfactory. Overall, the minor variations in estimates of the various parameters for the four data sets for either notched or pre-cracked specimens show that provided ramping the specimens are continued sufficiently close to fracture, then extrapolations from the tail ends of the  $P - v$  or  $P - v_a$  plots are not really necessary for improving the tearing resistance estimates, and for that matter, even an extensometer is not necessary. Similar exercises with results from DENT specimens of both a DP 780 automotive grade steel sheet [92], and the present test material (Table 4.1) led to the same conclusion. It may be recalled that Williams and Rink [40] had suggested measuring displacement using the actuator travel. From Table 6.1, it is also obvious that reducing radius  $\rho$  from 0.1 mm by fatigue pre-cracking resulted in reducing values of  $w_e$  and  $\delta_c^e$ . For example, analyses with Data set (i) are compared in Figs. 6.3(a) and 6.3(b): it shows with fatigue pre-cracking,  $w_e$  decreased by  $\sim 46\%$ ,  $\delta_c^e$  by a more modest  $\sim 11.8\%$ , while  $\psi^e$  was effectively independent of  $\rho$ . This  $\rho$ -

dependence of the initiation parameters  $w_e$  and  $\delta_c^e$  determined by testing DENT specimens are well known in literature (Section 2.6), and also confirmed for the present test material (Section 4.3.1.2), whereas  $\rho$ -independence of  $\psi^e$  from DENT specimens has been established for the present test material in Section 4.3.1.2. Data for pre-cracked SENT and DENT specimens are compared in Section 6.3.2.

**Table 6.1:** EWF parameters for notched and pre-cracked SENT specimens for ramp rate  $0.006 \text{ mm.s}^{-1}$  (for descriptions of Data sets, see text)

Specimen	Data set	Fit to Eq. (2.8) $w_f = \beta w_p l + w_e$			Fit to Eq. (6.1) $v_f = (\psi^e)l + \delta_c^e$		
		$R^2$	$\beta w_p$ (MJ.m <sup>-3</sup> )	$w_e$ (kJ/m <sup>2</sup> )	$R^2$	$\psi^e$	$\delta_c^e$ (mm)
Notched	(i)	0.999	95.06	247.06	0.999	0.33 (18.9°)	1.27
	(ii)	0.999	95.06	247.2	0.999	0.328 (18.8°)	1.273
	(iii)	0.998	95.07	247.9	0.999	0.328 (18.8°)	1.273
	(iv)	0.999	95.1	248.1	0.997	0.326(18.68°)	1.28
Pre-cracked	(i)	0.994	87.03	133.3	0.999	0.326(18.67°)	1.12
	(ii)	0.994	87.03	133.8	0.997	0.324(18.56°)	1.125
	(iii)	0.994	87.03	134.1	0.998	0.326(18.67°)	1.126
	(iv)	0.992	87.03	134.6	0.993	0.321 (18.4°)	1.134



(Continued)

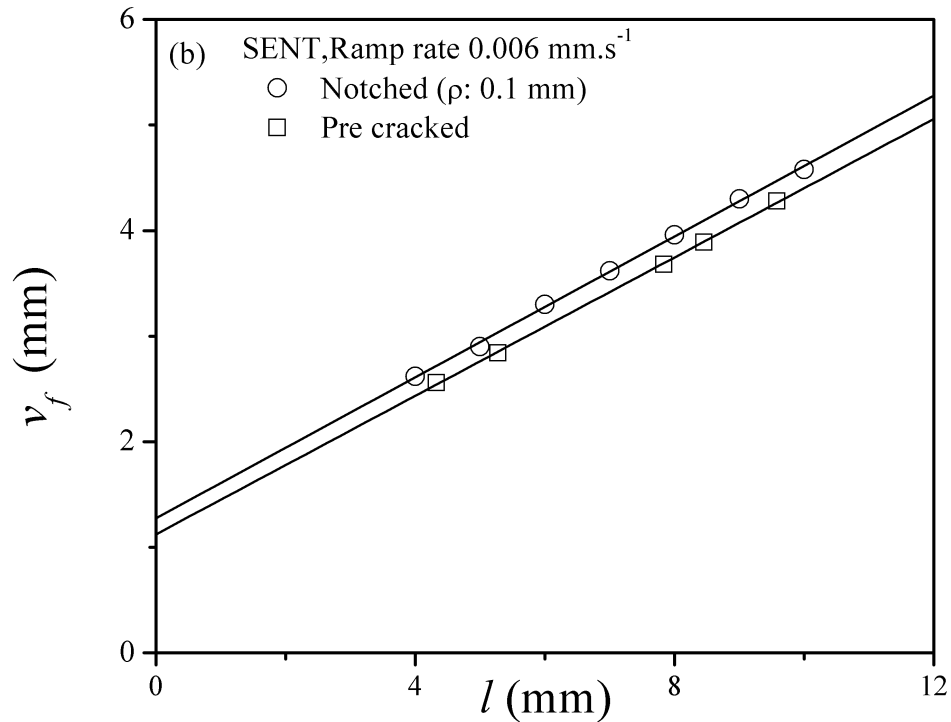


**Figure 6.3:** (a)  $w_f - l$  and (b)  $v_f - l$  plots of notched and pre-cracked SENT specimens for ramp rate  $0.006 \text{ mm.s}^{-1}$ .

### 6.3.1.3 Effect of ramp rate and specimen geometry on EWF parameters

For DENT as well as SENT specimens, Table 6.2 compares the effect of specimen geometry on the energy based EWF parameters  $w_e$  and  $\beta w_p$  determined for notched ( $\rho = 0.1 \text{ mm}$ ) specimens at three different ramp rates of 0.6, 0.06 and  $0.006 \text{ mm.s}^{-1}$ , and also pre-cracked SENT tested at ramp rate of  $0.006 \text{ mm.s}^{-1}$ . These EWF results have been obtained using Data set (i) for the specimens with  $l$  within the corresponding validity ranges, i.e., (i)  $4 \leq l \leq 10 \text{ mm}$  for SENT specimens (Section 6.3.1.1), and (ii)  $3 \leq l \leq 10 \text{ mm}$  for DENT specimens (Section 4.3.1.1). For the different ramp rates, the  $w_f - l$  plots for the SENT specimens with machined notches and fatigue pre-cracks are compared with the corresponding plots for DENT specimen in Figs. 6.4(a) and 6.4(b) respectively. With increasing quasi-static ramp rate in the indicated range,  $\beta w_p$  and  $w_e$  increased marginally for both the specimen geometries. Also, for the different ramp rates, notched ( $\rho = 0.1 \text{ mm}$ ) SENT specimens yielded  $\sim 7$ - $16\%$  higher  $w_e$  values than the notched ( $\rho = 0.1 \text{ mm}$ ) DENT specimens, but the difference was only  $\sim 1\%$  for the pre-cracked specimens.

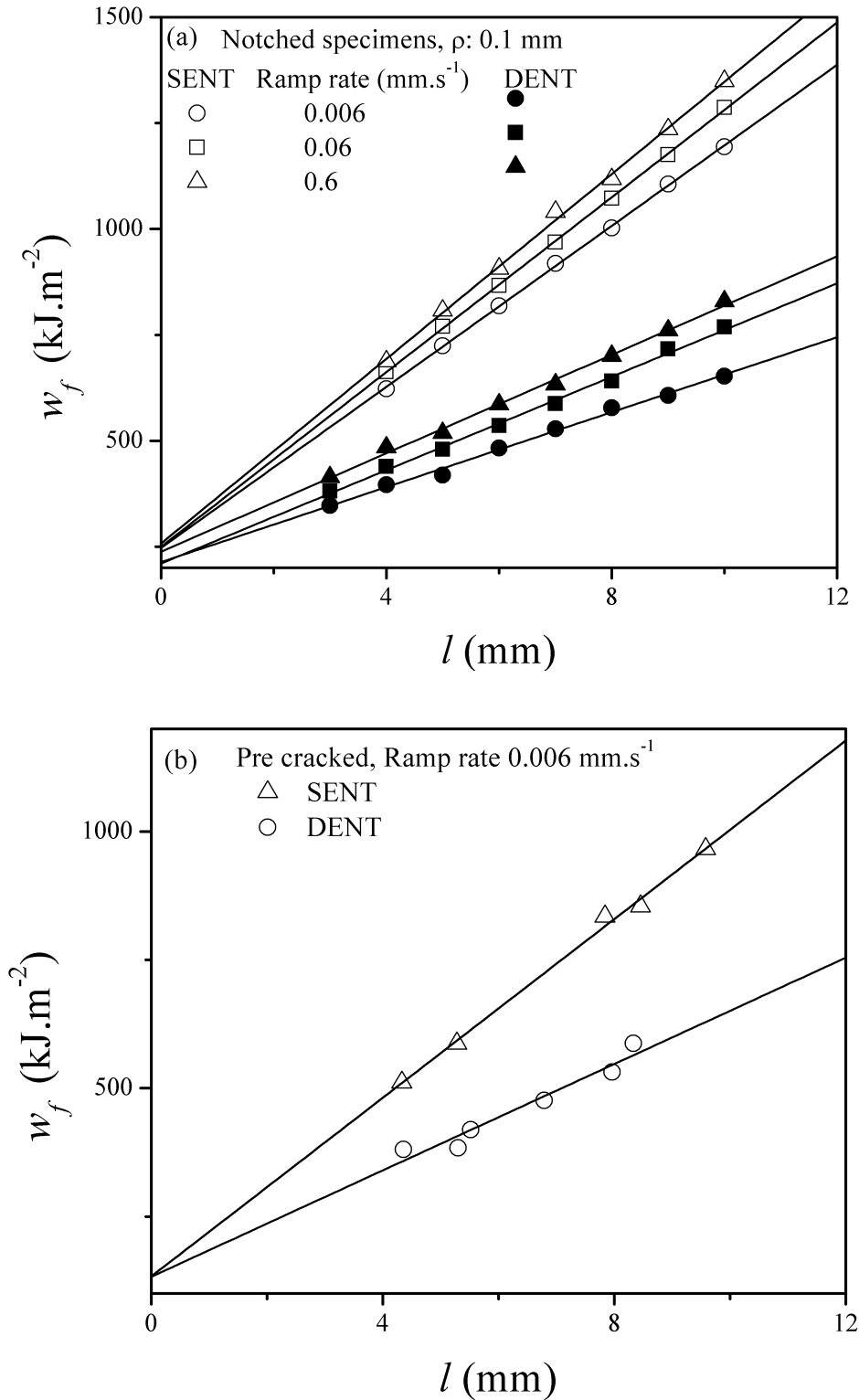


**Figure 6.4:**  $w_f - l$  plots of (a) notched and (b) pre-cracked SENT and DENT specimens. (Data for DENT specimen from Chapter 4)

These results confirm that for the present test material,  $\rho$ -independent  $w_e$  (determined using pre-cracked specimens) is a material parameter, independent

of specimen geometry. In contrast, for any ramp rate the  $\beta w_p$  parameter was consistently higher for the SENT geometry, being in the range 1.87-2.15 times for the notched specimens, and 1.69 times for the pre-cracked specimens. This difference in  $\beta w_p$  values can be attributed to the larger plastic zone size, and therefore higher values for the plastic zone shape factor  $\beta$ , for the SENT geometry. This becomes obvious by considering a typical example - the difference in the plastic zones for the present test material with fatigue pre-cracked DENT and SENT specimens with very similar ligament lengths, Figs. 6.5(a-b). The conclusion that  $\beta$  for SENT geometry is greater than that for DENT geometry has been reported in literature for polymer sheets [102, 106].

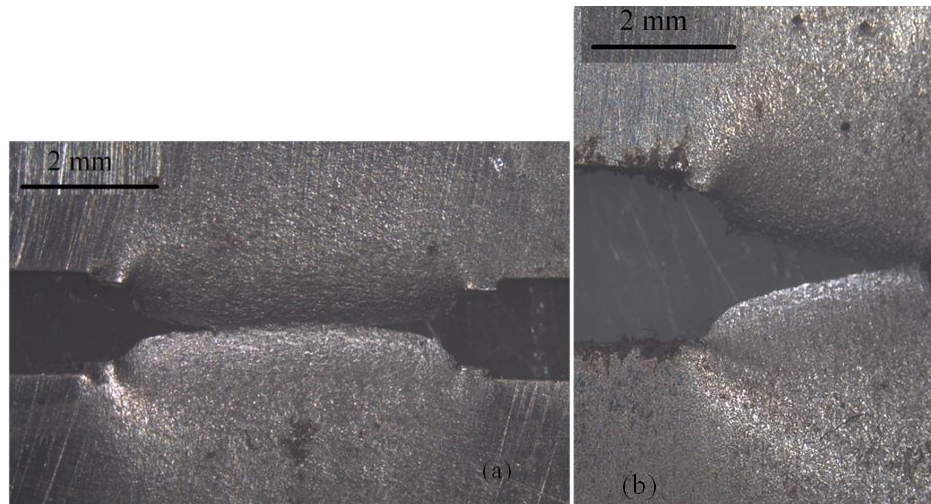


**Figure 6.5:** Different plastic zone shapes for pre-cracked (a) DENT ( $l = 4.6$  mm) and (b) SENT ( $l = 4.3$  mm) specimens

**Table 6.2:** Effect of specimen geometry on the energy based EWF parameters  $w_e, \beta w_p$  (DENT specimen data from Tables 4.1 and 4.2)

Fitted equation: $w_f = \beta w_p l + w_e$							
Ramp rate (mm s <sup>-1</sup> )	Specimen	SENT			DENT		
		$R^2$	$w_e$ (kJ/m <sup>2</sup> )	$\beta w_p$ (MJ.m <sup>-3</sup> )	$R^2$	$w_e$ (kJ/m <sup>2</sup> )	$\beta w_p$ (MJ.m <sup>-3</sup> )
0.006	Notched	0.999	247.1	95.06	0.997	213.6	44.26
0.06		0.998	249.5	103.2	0.997	210.1	55.14
0.6		0.997	257.2	109.1	0.997	238.1	58.10
0.006	Pre-cracked	0.995	133.3	87.03	0.997	132.7	51.83

In contrast, comparison of  $v_f - l$  plots of notched (Fig. 6.6(a)), and pre-cracked DENT and SENT specimens (Fig. 6.6(b)) shows large differences in both slopes and ordinate offsets.

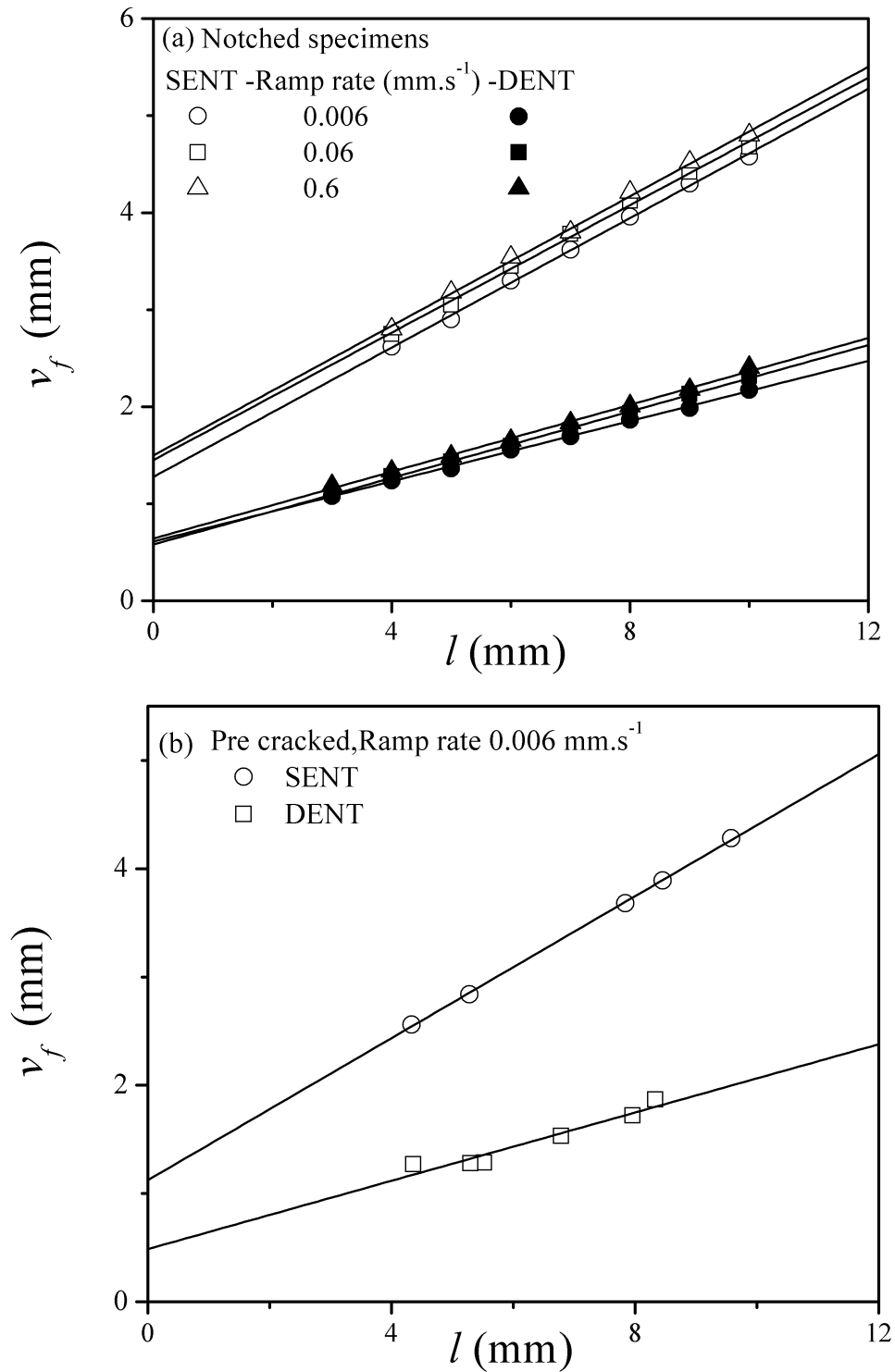


**Figure 6.6.**  $v_f - l$  plots for (a) notched and (b) pre cracked SENT and DENT specimens. (DENT specimen data from Figs. 4.3(b), 4.5(b)).

The differences in slopes is rationalized by noting that for SENT specimens, the modified equation, Eq. 6.1 proposed in the Section 6.1, is required. In Table 6.3.  $\psi^e$  calculated accordingly were only were 3.6 - 5.2% higher for the SENT specimens than for DENT specimens. It may be therefore be concluded that  $\psi^e$  is a material property, independent of specimen geometry, and also notch tip radius, at least up to  $\rho = 0.1$  mm. Also, the  $\psi^e$  parameter was almost independent of ramp rate in the tested range for both the specimen geometries. The situation, however, is different for the  $\delta_c^e$  estimates: these were higher for the SENT specimens by a factor in the range 2.13 - 2.26 for the notched specimens and by a factor 2.3 for the pre-cracked specimens. This mismatch is considered further in Section 6.3.3.1.

**Table 6.3:** Comparison of  $\delta_c^e$  and  $\psi^e$  for SENT and DENT specimens

Ramp rate (mm s <sup>-1</sup> )	Specimen	SENT $v_f = \psi^e l + \delta_c^e$ (Eq. 6.1)			DENT $v_f = (\psi^e/2)l + \delta_c^e$ (Eq 2.9)		
		$\delta_c^e$	$\psi^e$	$R^2$	$\delta_c^e$	$\psi^e$	$R^2$
0.006	Notched	1.27	18.9°	0.999	0.572	17.9°	0.999
0.06		1.45	18.8°	0.998	0.64	18.10°	0.999
0.6		1.49	18.9°	0.997	0.7	18.22°	0.999
0.006	Pre-cracked	1.12	18.67°	0.999	0.487	17.99°	0.967

### 6.3.2 CTOA ( $\varphi$ ) determination by optical method

As with DENT specimens (Section 4.3.3), SENT specimens were used for CTOA determination, following the procedure described in Section 3.2.4. For this purpose, fatigue pre-cracked SENT specimens ( $l \sim 24$  mm) were tested under displacement-controlled mode at three different ramp rates, 0.6, 0.06 or 0.006 mm.s<sup>-1</sup>. Each test generated a series of photographs. From each photograph, CTOA was measured along with the crack extension,  $\Delta a$ , on the specimen surface, using the two-point method described in Section 4.3.3. In order to select the proper measurement basis,  $L$ , initially different  $L$  values, namely 0.5 mm, 1 mm and 1.5 mm, were chosen, and accordingly, three sets of measurements for  $\varphi$  were carried out for each photograph of the SENT specimen tested at ramp rate 0.006 mm.s<sup>-1</sup>

(Fig. 6.7). For each choice of  $L$ , the plot follows a similar trend: with increasing  $\Delta a$ :  $\varphi$  gradually decreases from a high initial value to eventually a fairly constant value  $\varphi_c$  for a regime of  $\Delta a$ , to be followed by farther decrease in  $\varphi$ . From the trend of all the data presented, the range of  $\Delta a$  over which the CTOA may be considered to be constant have been identified and the mean and standard deviation of the CTOA values measured in this stable range have been computed, Fig. 6.7. The CTOA data for  $L = 1.5$  mm were selected as this choice resulted in the smallest data scatter; the critical CTOA  $\varphi_c$  thus determined was  $17.96^\circ$ . It may be noted that the same value of  $L = 1.5$  mm was selected for DENT specimens following the same procedure, Fig. 4.9.

The  $\varphi$  vs  $\Delta a$  curves (determined with  $L = 1.5$  mm, the best choice) for the three different ramp rates are plotted in Fig.6.8. It may be noted that (i) for all the specimens, critical CTOA value  $\varphi_c$  were attained after a transition regime of crack growth  $\Delta a \sim 6$  mm, and (ii) for the quasi-static strain rates considered,  $\varphi_c$  values were in the range  $17.77^\circ$ - $17.96^\circ$ . With the pre-cracked DENT specimens, the corresponding  $\varphi_c$  range determined was  $17.5^\circ$ - $17.72^\circ$ , Table 4.3. This confirms that  $\varphi_c$  determined by the method adopted is specimen geometry independent. Also, for the quasi-static ramp rates considered,  $\varphi_c$  is practically constant for the present test material. The limited extent of crack tip tunneling in SEM micrographs (Fig. 4.6 for DENT specimen, Fig. 5.9 for SENT specimen) justifies measurements of crack extension optically on the specimen surface from very early during the test. For the different ramp rates, Table 6.4 compares the critical CTOA  $\varphi_c$  determined using pre-cracked specimens (Fig. 6.8) with  $\psi^e$  estimated from linear fits of the EWF test data for notched SENT specimens with  $l = 4 - 10$  mm (from Table 6.2). The maximum difference  $\varphi_c$  and  $\psi^e$  values was only 6%. Clearly as concluded for DENT specimens (Section 4.3.3),  $\psi^e$  determined using the simple EWF method with notched SENT specimens can be used as a measure of  $\varphi_c$  determined from the more complex and time consuming testing of fatigue pre-cracked specimens.  $\psi^e$  values were also estimated using EWF procedure with data for notched SENT specimens with  $l = 6 - 10$  mm, i.e., the lower ligament length set equal to the value of  $\Delta a$  for the initial transient regime (Fig. 6.8). This reduced the maximum difference between  $\psi^e$  and the corresponding  $\varphi_c$  to only 3%, Table 6.4. For



notched DENT specimens also, with  $L = 1.5$  mm (the best choice) and  $l = 6 - 10$  mm, the corresponding maximum difference was 4% (Table 4.3). The possible implication of this result for EWF test data analysis, including desirability of determining the initial CTOA transition regime using notched (rather than pre-cracked) specimens, and determining  $\psi^e$  in absence of information about the extent of initial CTOA transition régime, merits further examination.

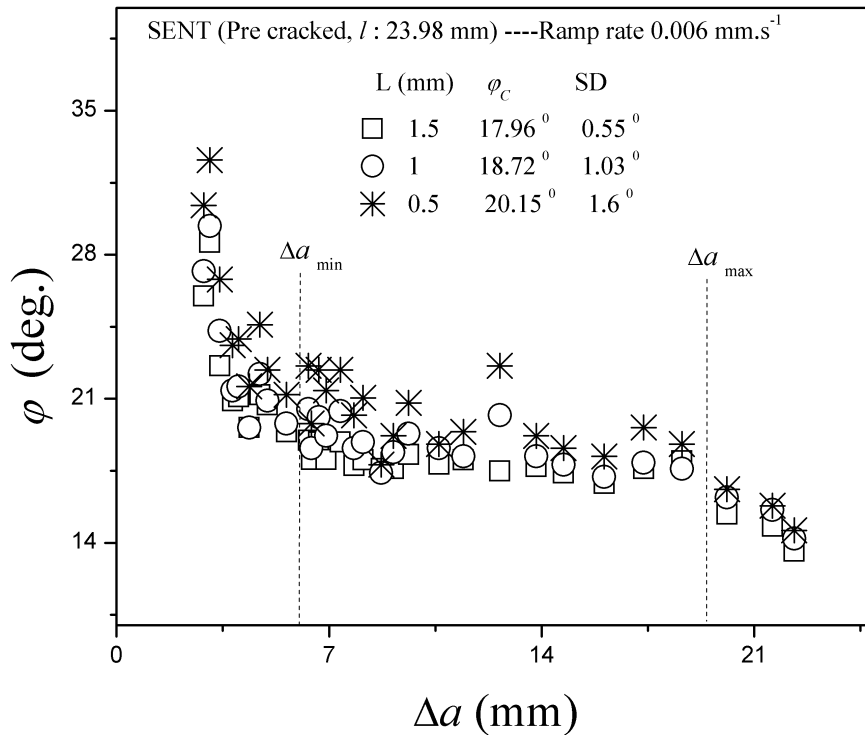


**Figure 6.7:** For SENT specimens. choice of CTOA measurement basis  $L$  for the two point method. SD is the standard deviation computed for the stable CTOA values (determined for the chosen  $L$ ) between the two vertical bars.

**Table 6.4:** Comparison of  $\varphi_c$  for pre-cracked SENT specimens with  $\psi^e$  from EWF tests for notched SENT specimens at three quasi-static ramp rates

Ramp rate (mm.s <sup>-1</sup> )	$\varphi_c$ (pre-cracked specimens)	Data set 1		Data set 2	
		$l$ (mm)	$\psi^e$ from EWF	$l$ (mm)	$\psi^e$ from EWF
0.006	17.96 <sup>0</sup>		18.9 <sup>0</sup>		18.2 <sup>0</sup>
0.06	17.82 <sup>0</sup>	4-10 (Notched)	18.9 <sup>0</sup>	6-10 (Notched)	18.34 <sup>0</sup>
0.6	17.77 <sup>0</sup>		18.8 <sup>0</sup>		18.4 <sup>0</sup>

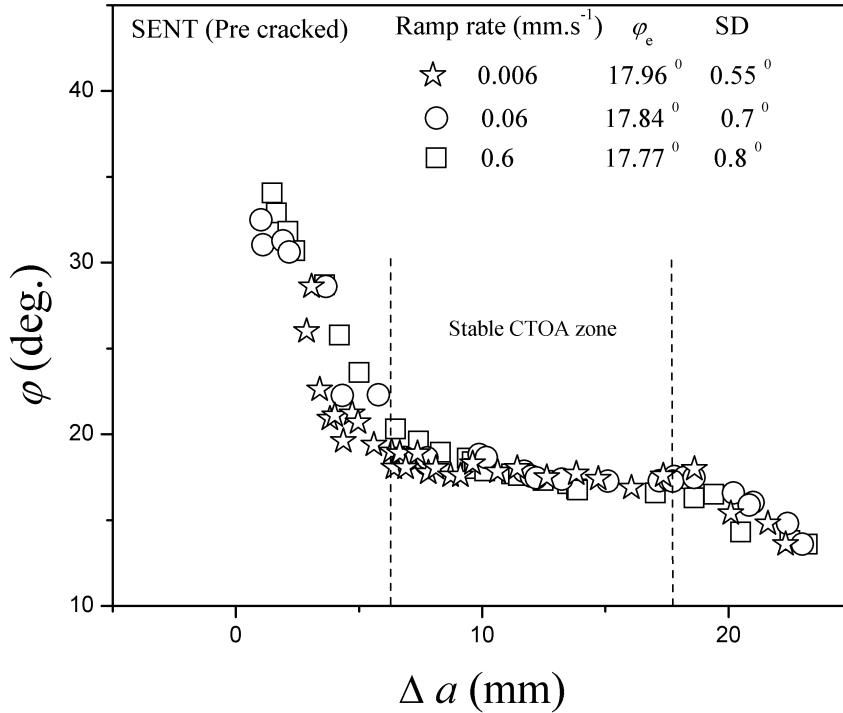


**Figure 6.8:**  $\phi - \Delta a$  plots for pre-cracked SENT specimens at different ramp rates. SD is the standard deviation computed for the stable CTOA values (determined for the chosen  $L = 1.5$  mm) between the two vertical bars.

### 6.3.3 Finite element modelling for non-growing crack

The finite element (FE) simulation reported in this section followed the procedures adopted for the DENT specimens (Section 4.3.4.1), and for SENT specimens (Section 5.3.2). For these analyses, from the  $P - v_a$  data for the tested specimens, the extension values  $v_s$  of the specimen free length  $H$  were determined using the equation,  $v_s = v_a - C_M P$ ;  $C_M = 0.01305 \text{ mm.kN}^{-1}$  is the “machine” elastic compliance. The finite element software, ABAQUS 6.10 was used for these simulations; 3-D 8 node solid hexahedral elements C3D8R with reduced integration and 1 integration point were used. For all FE computations, isotropic hardening model was used. Elastic-plastic tensile material properties and Hollomon strain hardening parameter for nominal strain rate of  $10^{-4} \text{ s}^{-1}$  (Section 3.2.1) which corresponds to the chosen ramp rate were assumed for the entire strain ranges for simulations.

### 6.3.3.1 Notched SENT specimens

3-D time-independent large strain FE simulations for non-growing crack were carried out for all the notched SENT specimens tested at a ramp rate of  $0.006 \text{ mm.s}^{-1}$ . The in-plane dimension of the elements was  $0.2 \text{ mm} \times 0.2 \text{ mm}$  around the notch, gradually increasing to  $1 \text{ mm} \times 1 \text{ mm}$  away from notch. The element width along the thickness direction was  $0.125 \text{ mm}$  (i.e., 8 layers along the thickness direction). The simulations were continued well beyond the maximum loads in each case. Figure 6.9 shows an example: the simulation results matched well with the early portion of the experimental curve but started deviating from the experimental plot at the point “b”, before the maximum load (point “a”) was reached and this deviation point “b” has been ascribed as the point of crack initiation (For details see Fig. 4.12 and Fig.5.7(a)). As Fig.6.9 shows, from the point “b”, a line parallel to the initial elastic loading line was drawn; the enclosed area gives  $W^{in} = w_i l t$ , the (plastic component of the) energy for crack initiation. The remaining area under the  $P - v_s$  plot equals the (total) energy for crack growth,  $W^{gr}$ . Similar identification of the crack initiation points, followed by determining  $W^{in}$  and  $W^{gr}$  were carried out for all the specimens.

The plastic components of critical values of  $J$ - integral at the points of crack initiation,  $J_p^c$ , have been computed using Eq. 4.2 with  $n_p = 0.81$  (see Sections 5.3.1 and 5.3.4) for the ligament lengths used in the present study. The  $J_p^c$  values are plotted against  $l$  in Fig.6.11; the  $J_p^c$  values for  $l = 3, 6, 9, 12, 15 \text{ mm}$  have also been shown in Fig. 5.18. Figure 6.11 clearly shows that  $J_p^c$  gradually increased for  $l$  in the range 1-3 mm, and then remained more or less constant for  $l$  in the range 4-10 mm (the  $l$ -validity range for EWF tests), and even beyond, up to  $l = 15 \text{ mm}$ , and from Fig. 5.18, even beyond, up to  $l = 24 \text{ mm}$ . Within the  $l$ -validity range, the average  $J_p^c$  was obtained as  $193.3 \text{ kJ.m}^{-2}$ ; this is very similar to the average  $J_p^c = 199.8 \text{ kJ.m}^{-2}$  for notched DENT specimens (Fig. 4.14) in the corresponding  $l$ -validity range (3-10 mm).

The initiation CTOD,  $\delta_c$ , at point “b” (Fig. 6.9) has been measured from the FE simulation result following the procedure used in Section 4.3.4.2 (Fig. 4.13).  $\delta_c$  at

point “b” was obtained from the deformed mesh as  $\sim 0.83 - 0.2 = 0.63$  mm, i.e., the total opening (distance between points 1 and 4) minus the initial separation of the flanks (distance between the points 2 and 3), i.e., 0.2 mm (Fig. 6.10).

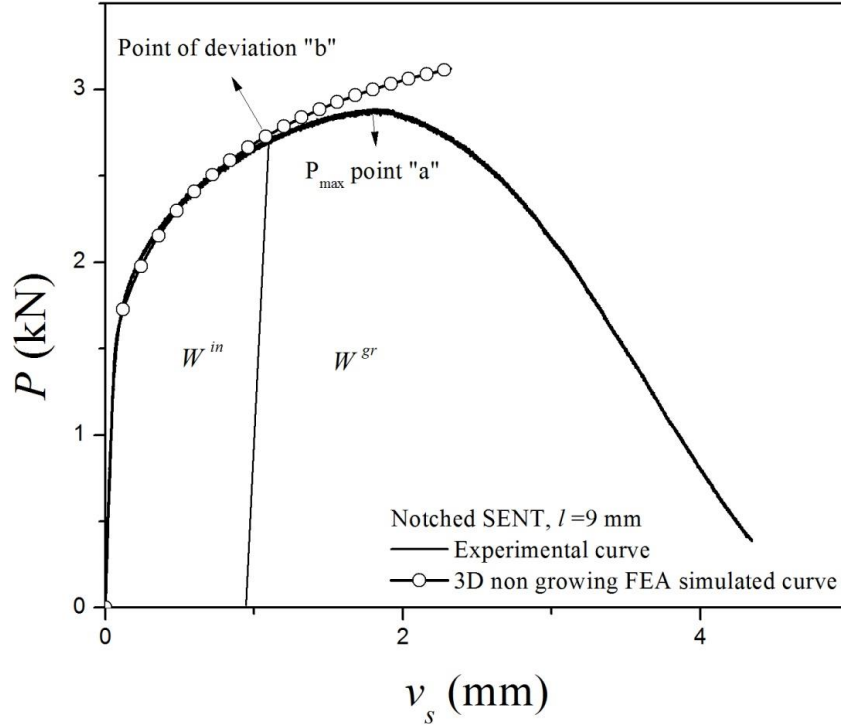


**Figure 6.9:** For notched ( $\rho = 0.1$  mm) SENT specimen with  $l = 9$  mm, FE simulated  $P - v_s$  plot superimposed on the corresponding experimental curve; point ‘b’ is the crack initiation point.

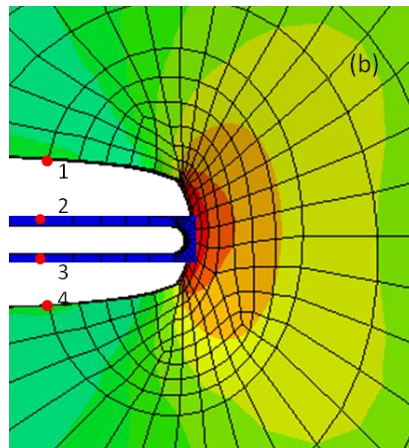


**Figure 6.10:** CTOD determined at point ‘b’ of the Figure 6.9 by the method described in the text.

The  $\delta_c$  value for the different ligament lengths in SENT specimens shows similar trend that of  $J_p^c$  value (Figure 6.11): the average  $\delta_c$  was about 0.63 mm for the  $l$ -valid range. This is almost the same as the average  $\delta_c$  value of 0.64 mm (see Fig.4.13) of notched DENT specimens. That is, for these notched specimens,  $\delta_c$  is a material parameter. Considering the difference in the definitions of  $\delta_c$  (as adopted in the present report) and  $\delta_c^e$  from EWF analysis, this average  $\delta_c \sim 0.63$  mm for notched SENT and DENT specimens from FE simulation may be compared with  $\delta_c^e$  (in the range 0.572 – 0.590 mm for notched DENT specimens (Table 4.1); but it is much smaller than the  $\delta_c^e$  reported in Table 6.1 (1.27 - 1.28 mm for notched SENT specimens).

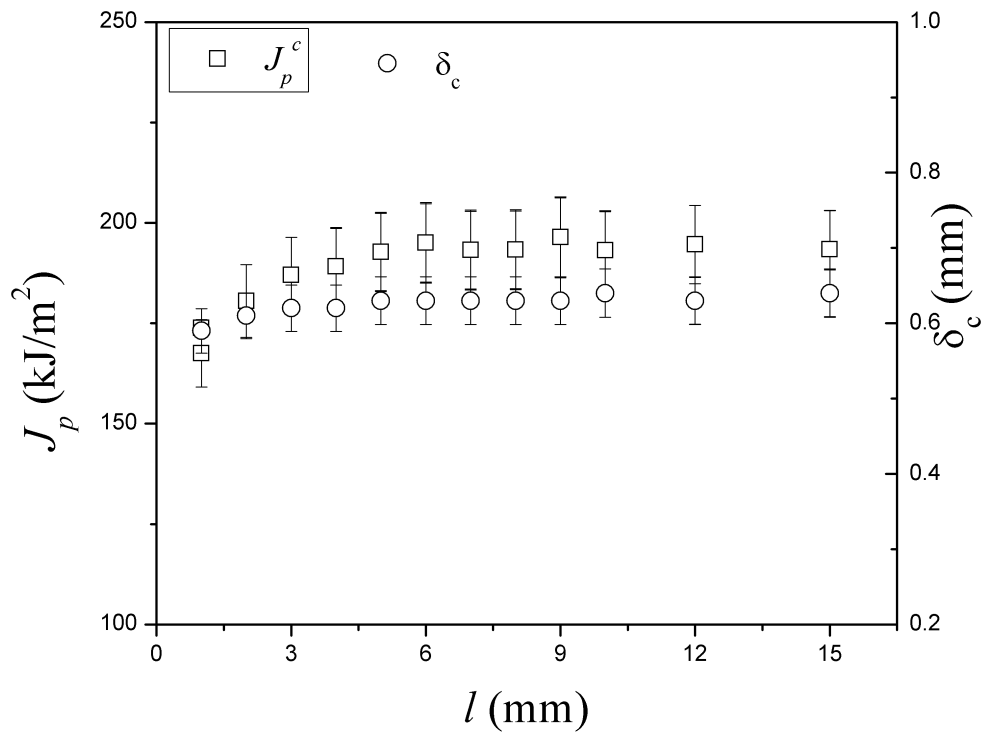


**Figure 6.11:** Variation of  $J_p^c$  and  $\delta_c$  values with ligament length,  $l$  in SENT specimens.

Figure 6.12 shows the  $w_i$  data for the valid  $l$  range ( $l = 4 - 10$  mm) for the notched SENT specimens. For comparison, the  $w_i$  data used in computing plastic components of initiation  $J_p^c$  values for notched DENT specimens (Fig. 4.14) are also presented in this figure. If the modest slopes of these lines are ignored, then the average  $w_i$  for the notched SENT and DENT specimens compute respectively as

237.2 and 252.3 kJ.m<sup>-2</sup>, a difference of about 6%. Using the appropriate  $\eta_p$  values, the corresponding average  $J_p^c$  values are respectively 192.1 and 191.7 kJ.m<sup>-2</sup>, a difference of mere 0.2%, for these SENT and DENT specimens. These results are consistent with  $J_p^c$  for the notched specimens being a material property (see also Fig. 5.18 which includes data from the initial mixed stress regime in SENT specimens, and the related discussion). The  $w_i$ - $l$  data for both these specimen geometries satisfy Eq. 2.8; the dashed lines in this figure show the results from corresponding linear least square fits. The slope for the fitted line (i.e.,  $\beta_i w_{ip}$  in Eq. (2.8)) for the SENT specimens was 1.16 and for DENT specimens was 3.35, reflecting a slightly higher constraint for the DENT geometry (consistent with the conclusion in Section 6.3.1.1 in the context of determining  $l$ -validity range). Values for the ordinate offset  $w_{ie}$  for the two specimen geometries for these lines, obtained from the linear least square fits of  $w_i$ - $l$  data for  $l = 0$ , were respectively 231.7 kJ.m<sup>-2</sup> for the SENT specimens, and 229.04 kJ.m<sup>-2</sup> for the DENT specimens, differing by 1.15%. This shows that for  $\rho = 0.1$  mm,  $w_{ie}$  is independent of specimen geometry. As expected,  $w_{ie}$  values are smaller than the corresponding  $w_e$  values, 247.1 kJ.m<sup>-2</sup> for notched SENT specimens and 213.6 kJ.m<sup>-2</sup> for notched DENT specimens.

Following Mai and Cotterell [15] and other authors [44, 138], extrapolation of the mixed stress regime  $w_f$  data to  $l = 0$  gives a specific essential work of fracture,  $w_e^m$ , corresponding to crack initiation at the highest constraint for the given sheet and notch tip radius. The  $w_f$  data plotted in Fig. 6.13(a), shows that  $w_e^m$  can be approximately determined by simple linear extrapolation of the mixed stress regime  $w_f$  data (for  $l$  ranging from 1-3 mm, only 3 data sets) to  $l = 0$ .  $w_e^m$  thus determined from linear least square fit was 189 kJ.m<sup>-2</sup>, lower than the  $w_{ie}$  value determined as 231.7 kJ.m<sup>-2</sup>. However, a linear extrapolation of  $w_i$  data in mixed stress regime yields the offset value  $w_i^m = 194$  kJ.m<sup>-2</sup>, within about 3% of  $w_e^m$ .

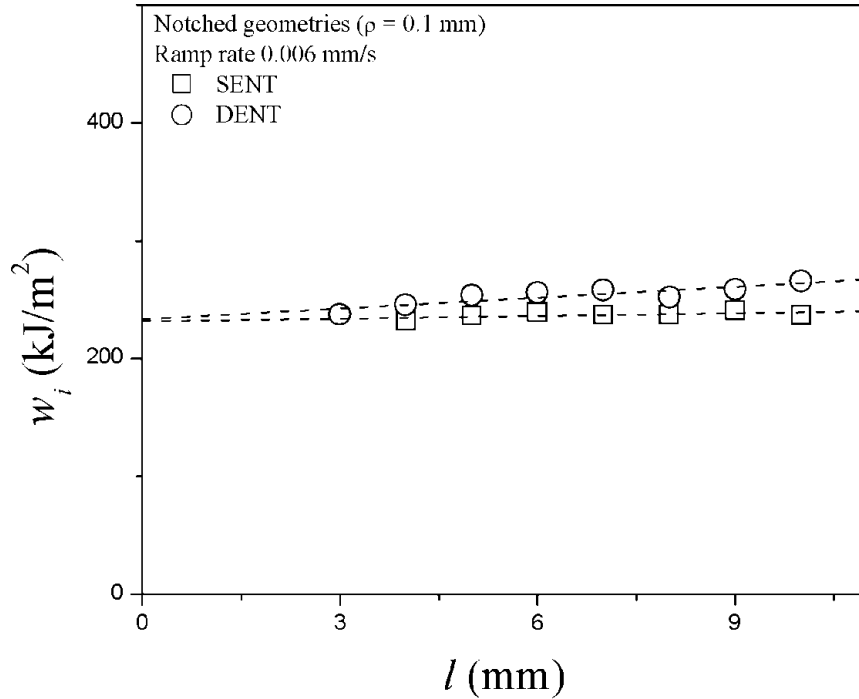


**Figure 6.12:** For notched ( $\rho = 0.1$  mm) SENT specimens ramped at  $0.006 \text{ mm.s}^{-1}$ ,  $w_i - l$  plot for the EWF valid  $l$  range, compared with similar data for DENT specimens (see Fig. 4.14). The dashed lines show linear least square fits for the two sets of data, Eq. 2.8.

For the data shown in Fig. 6.13(b), linear extrapolations of the  $v_f - l$  data in the mixed mode regime to  $l = 0$  mm yielded the ordinate offset,  $\delta_c^{e,m} = 0.6$  mm, while the ordinate offset computed by linear extrapolation of  $\delta_c - l$  data was  $0.595$  mm, about 1.6% lower. Notwithstanding the limitations of the extrapolations carried out in the mixed stress regime, namely availability of only three data sets, and the assumed linear dependencies, the results suggest that at the highest possible constraint with the given sheet thickness and  $\rho = 0.1$  mm in the SENT specimens, initiation energy was  $\sim 194 \text{ kJ.m}^{-2}$  and  $\delta_c \sim 0.6$  mm. Such an exercise with extrapolation of mixed stress regime data to  $l = 0$  was not possible with the notched DENT specimens (Chapter 4), because data were available for only two specimens in this regime. Still, in view of the initiation CTOD values considered in Figs. 6.11 and 6.13(b), and considering that  $\psi^e$  was determined to be (nearly) the same for SENT and DENT geometries (Table 6.3), it appears justified to assume that the kinetic law for crack growth in the mixed stress regime followed by the plane stress regime is identical for SENT and DENT specimens with identical notch

root radius. Then the large difference in the  $\delta_c^e$  values from EWF analysis for SENT and DENT specimens with identical  $\rho$  (Table 6.3) must be ascribed to the difference in the effects of crack growth in the mixed stress regime for these two geometries. This can be seen by considering a simple extension of the derivation leading to Eq. (6.1) in Section 6.1. It is assumed that for both the specimen geometries, the following crack growth law applies:

$$\frac{d(v_f - \delta_c^{e,m})}{dl} = f(l) + \psi^e \quad (6.2)$$

where  $f(l)$  is a suitable decreasing function of  $l$  such that  $f(l) \rightarrow 0$  for large  $l$ . Then, for the SENT geometry,

$$[v_f - \delta_c^{e,m}]_{\text{SENT}} = \int_0^l (f(l) + \psi^e) dl = \int_0^l f(l) dl + \psi^e l$$

On the right hand side of this equation, the first term reflects the influence of the mixed stress regime, while the second term pertains to the plane stress regime. Comparing with Eq. (6.1)

$$[\delta_c^e - \delta_c^{e,m}]_{\text{SENT}} = \int_0^l f(l) dl \quad (6.3)$$

Similarly, for DENT specimens

$$[v_f - \delta_c^{e,m}]_{\text{DENT}} = \int_0^{l/2} (f(l) + \psi^e) dl = \int_0^{l/2} f(l) dl + \frac{1}{2}\psi^e l$$

whence,

$$[\delta_c^e - \delta_c^{e,m}]_{\text{DENT}} = \int_0^{l/2} f(l) dl \quad (6.4)$$

Assuming that  $\delta_c^{e,m}$  is a material property independent of specimen geometry, from Eqs. (6.3) and (6.4),

$$[\delta_c^e]_{\text{SENT}} - [\delta_c^e]_{\text{DENT}} = \int_{l/2}^l f(l) dl \quad (6.5)$$

Even with this simplest formulation,  $[\delta_c^e]_{\text{SENT}} - [\delta_c^e]_{\text{DENT}} > 0$ ; the difference, being determined by the function  $f(l)$ , is expected to be material dependent. To



meaningfully derive an acceptable  $f(l)$  function, however, a larger body of experimental  $v_f$  vs  $l$  data for the mixed stress regime for both the specimen geometries is required.

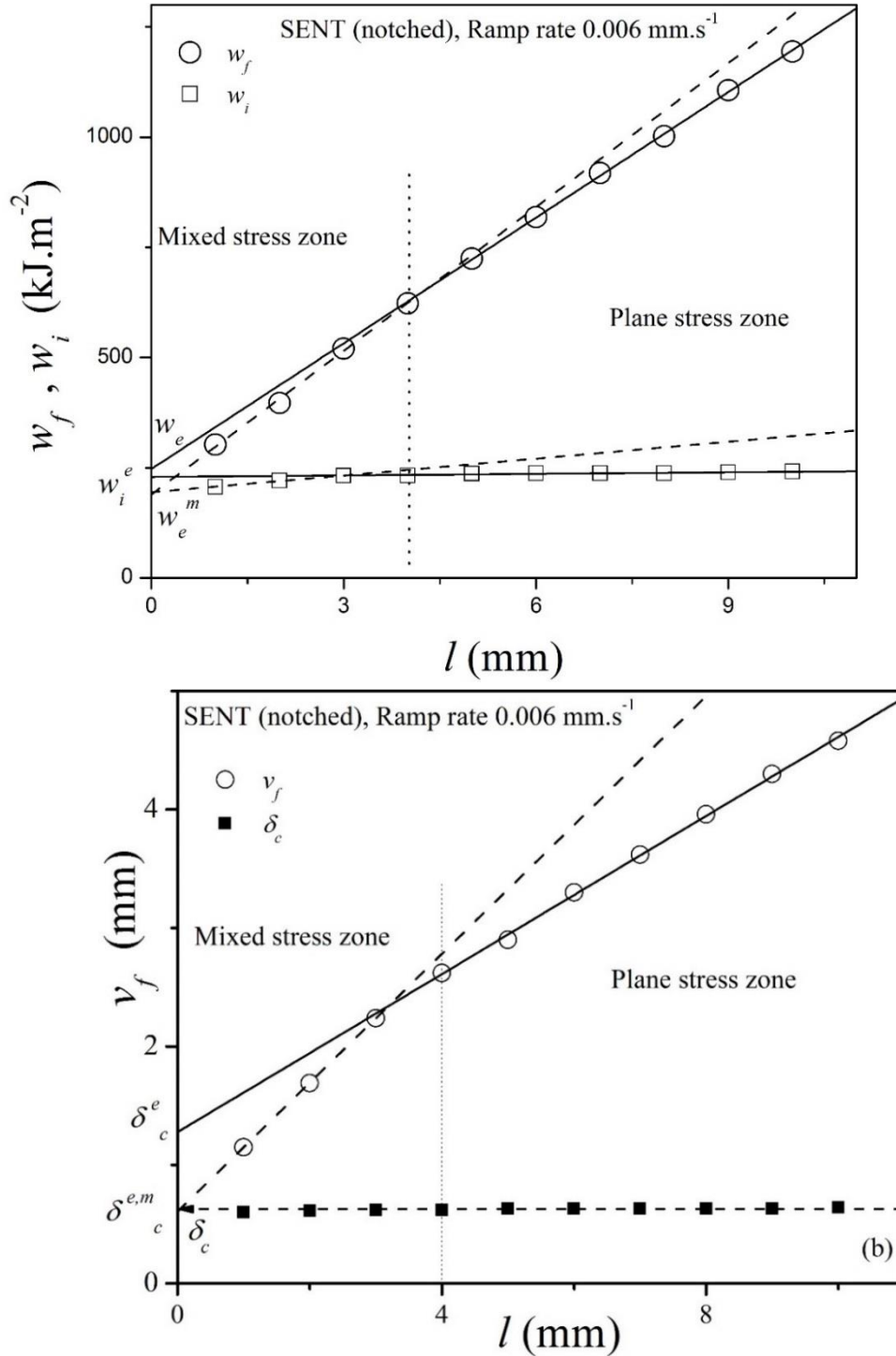


**Figure 6.13:** For notched ( $\rho = 0.1$  mm) SENT specimens, (a) comparison of  $w_e$  for plane stress with  $w_e^m$  and  $w_i^e$  for mixed stress zone; (b) comparison of  $\delta_c^e$  for plane stress with  $\delta_c^{e,m}$  and  $\delta_c$  extrapolated to  $l = 0$  for the mixed stress regime.

### 6.3.3.2 Pre-cracked specimens

3-D FE simulations for non-growing crack in SENT as well as DENT specimens were also carried out at a ramp rate of  $0.006 \text{ mm.s}^{-1}$  with a notch tip radius of  $\rho = 0.02 \text{ mm}$ ; such that the numerical results would be representative of fatigue pre-cracked specimens tested (for details, see Section 5.3.3). The in-plane meshing was same as Section 5.3.3, i.e. the size of the C3D8R elements was  $0.05 \text{ mm} \times 0.05 \text{ mm}$  around the notch gradually increasing to  $1 \text{ mm} \times 1 \text{ mm}$  away from notch; the element thickness was  $0.2 \text{ mm}$  (i.e., 5 layers along the thickness direction). The analysis of results follows the method adopted for the notched specimens. Figures 6.14(a) and 6.14(b) compare the  $P - v_s$  data from experiments and from FE simulations, respectively for a SENT, and a DENT specimen; and the points of onset of deviation, points “b1” marked in these figures, were identified as crack initiation points. Similar results were obtained for all the other pre-cracked SENT and DENT specimens with different ligament lengths. As for the notched specimens, with pre-cracked specimens also, crack initiated before the maximum load was reached. With the crack initiation points thus identified, from plots like Figs. 6.14(a) and 6.14(b), and the corresponding FE simulation data, the  $w_i$  and  $\delta_c$  values were determined for the pre-cracked SENT and DENT specimens with different ligament lengths, as described for notched specimens.

Using the  $w_i$  values, and also the  $\eta_p$  value appropriate for the specimen geometry, the  $J_p^c$  values were calculated. Figures 6.15(a) and 6.15(b) show respectively for the pre-cracked SENT and DENT specimens, the variations of  $J_p^c$  and  $\delta_c$  values with ligament length,  $l$ . It may be noted that for both the specimen geometries, the  $l$  values were in the corresponding  $l$ -validity ranges, i.e., plane stress condition. Expectedly,  $\delta_c$  and  $J_p^c$  values show very modest increase with  $l$ . Ignoring this variations, the mean  $J_p^c$  values were  $115.5 \text{ kJ.m}^{-2}$  for the SENT specimens and  $119.2 \text{ kJ.m}^{-2}$  for the DENT specimen, differing by only  $\sim 3.1\%$ . The mean  $\delta_c$  values were respectively  $0.32 \text{ mm}$  for SENT specimens and  $0.33 \text{ mm}$  for DENT specimens, differing by only  $\sim 3.1\%$ . These results are consistent with the specimen geometry-independence of both  $\delta_c$  and  $J_p^c$  parameters. Comparison of the data in Figs. 6.15(a)-(b) with those presented in Fig. 4.14 for notched DENT

specimens and Fig. 6.11 for notched SENT specimens shows that fatigue pre-cracking drastically reduced the mean  $J_p^c$  by about 40% and mean  $\delta_c$  by about 50%.

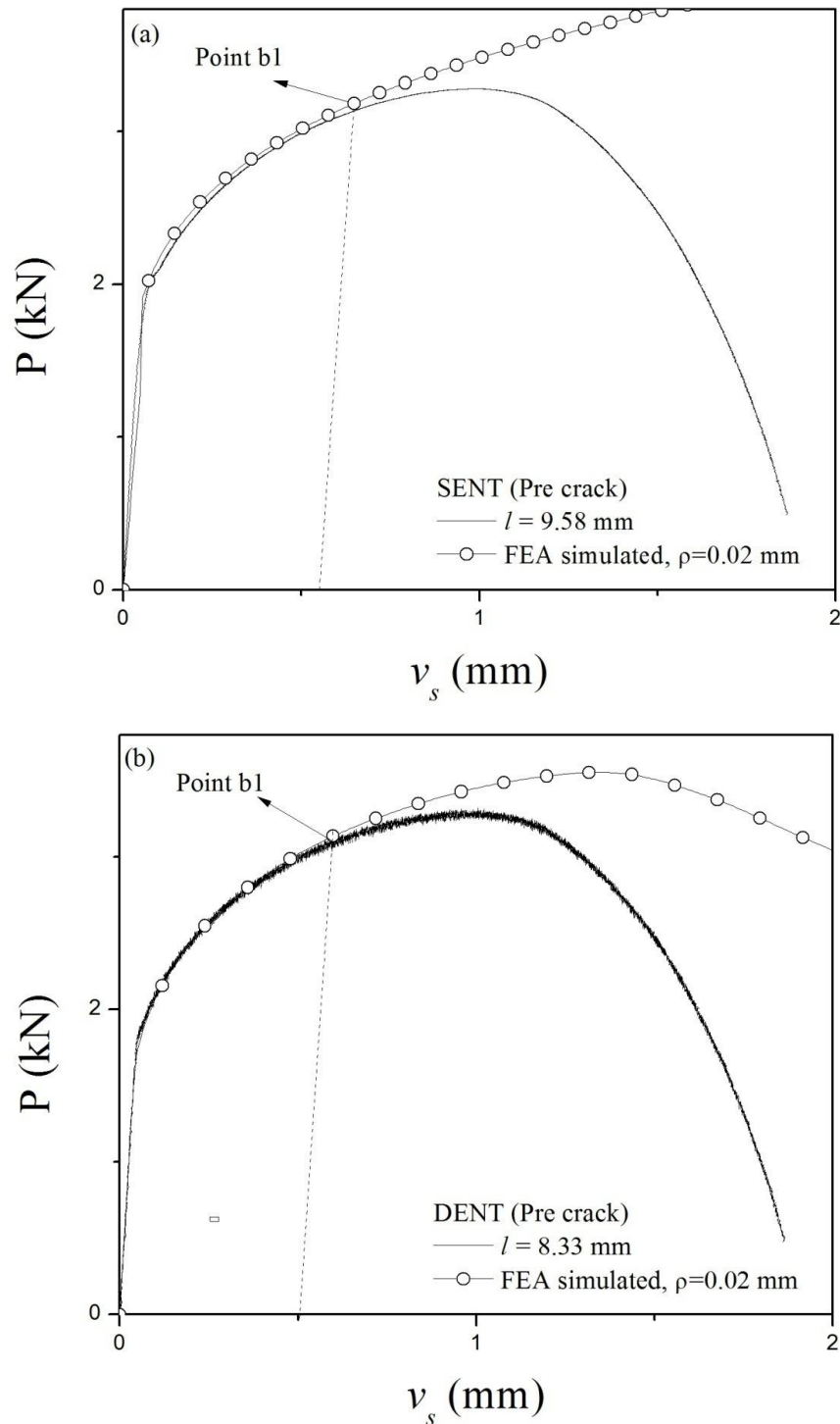


**Figure 6.14:** Representative FE simulated  $P - v_s$  plot superimposed on the corresponding experimental curve for pre-cracked (a) SENT ( $l=9.58$  mm) and (b) DENT ( $l= 8.33$  mm), point “b1” is the crack initiation point.

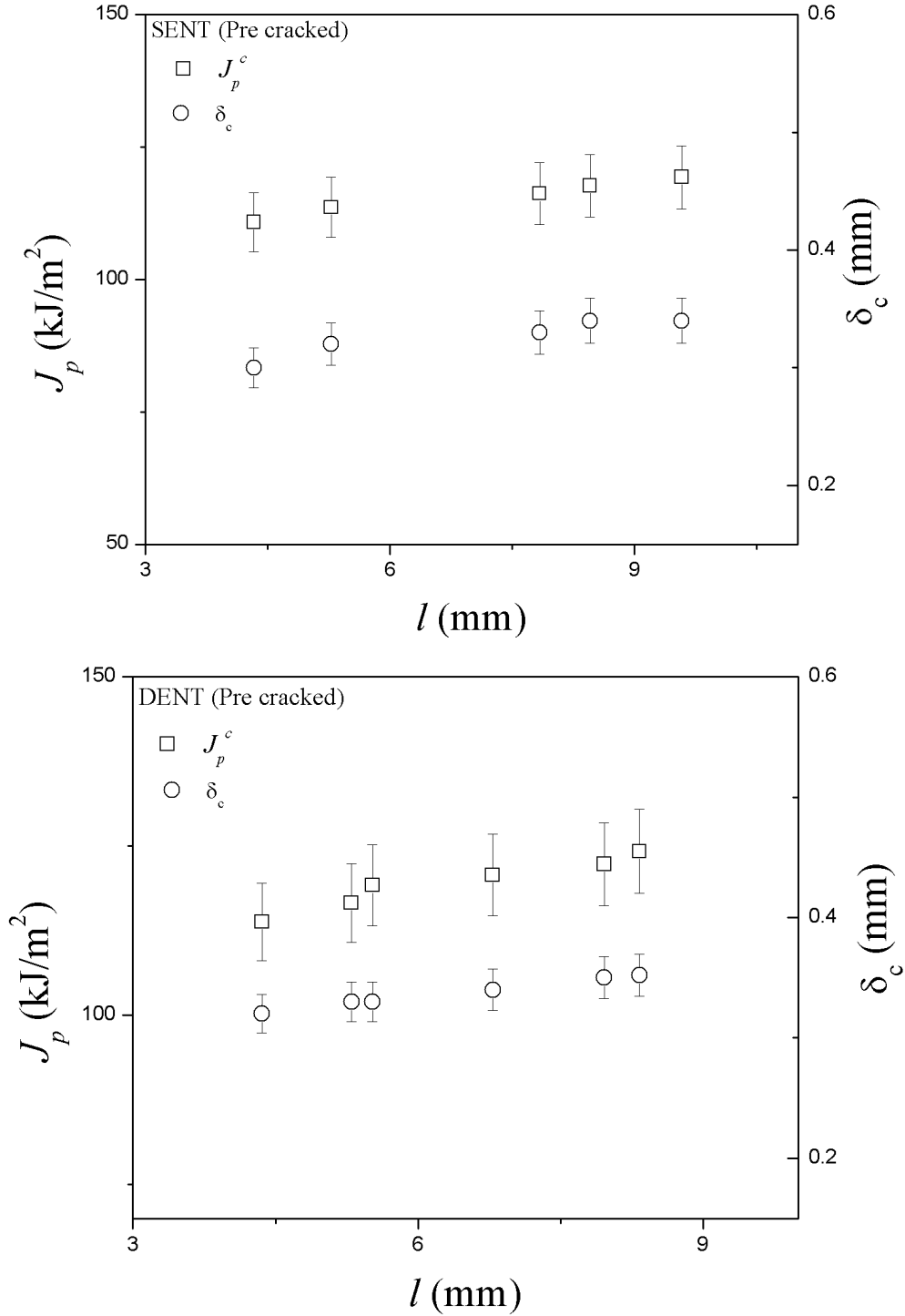


**Figure 6.15:** Variations of  $J_p^c$  and  $\delta_c$  values with ligament length,  $l$  for pre-cracked (a) SENT and (b) DENT specimens

The  $w_i$  values showed very modest increase with  $l$  for both the specimen geometries, Fig. 6.16. The  $w_{ie}$  values computed by least square fitting of the data to Eq. (2. 8) were respectively 128.7 kJ.m<sup>-2</sup> for the SENT geometry and 129.1 kJ.m<sup>-2</sup> for the DENT geometry, differing by 0.3%. The corresponding  $J_p^c$  values computed

using the appropriate  $\eta_p$  values were  $104.3 \text{ kJ.m}^{-2}$  for the SENT specimens, and  $98.1 \text{ kJ.m}^{-2}$  for the DENT specimens, differing by  $\sim 6\%$ . Thus,  $w_{ie}$  for the precracked specimens can also be considered to be a material parameter, independent of specimen geometry. Also, considering the  $w_{ie}$  data for notched specimens presented in Section 6.3.3.1, compared to notched specimens, fatigue pre-cracking reduced  $w_{ie}$  by about 44%.

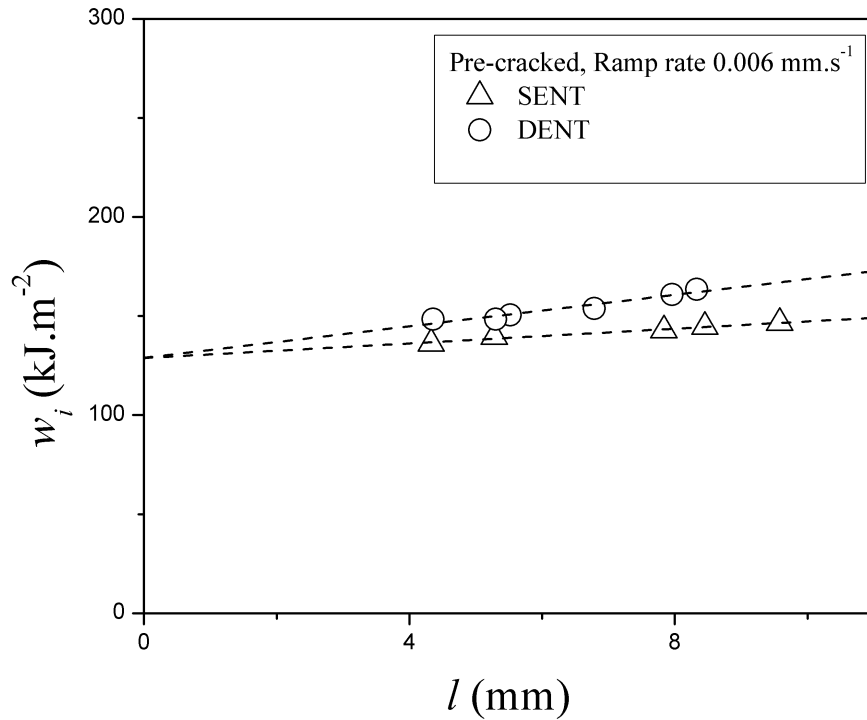


**Figure 6.16:** For pre-cracked SENT and DENT specimens ramped at  $0.006 \text{ mm.s}^{-1}$ ,  $w_i$ - $l$  plots ( $l$  within corresponding valid  $l$  ranges). The dashed lines show linear least square fits for the two sets of data, Eq. 2.8.

## 6.4 Conclusions

1. EWF testing and analysis procedures adopted for DENT specimens (Chapter 4) can very well be adopted with SENT specimens, but with a modified  $v_f$ - $l$  equation, Eq. (6.1). The criterion  $\sigma_n \cong \sigma_u$  has been found suitable for identifying the  $l$ -validity ranges for SENT specimens (Section 6.3.1.1). For the DENT specimens, the criterion was  $\sigma_n \cong 1.15\sigma_u$  (Section 4.3.1.1), suggesting slightly higher constraint level for the DENT specimens.  $w_e$  determined using fatigue pre-cracked specimens, and  $\psi^e$  determined with using fatigue pre-cracked or notched (at least up to  $\rho = 0.1 \text{ mm}$ ) specimens are material

parameters, independent of specimen geometry (Tables 6.2, 6.3). The  $\beta w_p$  is dependent on specimen geometry because of the larger plastic zone size in SENT specimens (Fig.6.5). The large difference in the  $\delta_c^e$  values for SENT and DENT specimens with identical  $\rho$  (Table 6.3) has been tentatively ascribed to the difference in the effects of crack growth in the mixed stress regime for these two geometries. However, further studies with a larger body of experimental  $v_f$  vs  $l$  data for the mixed stress zone is required to clarify this aspect.

2. The  $\varphi_c$  determined by the optical method is identified as a material property, independent of the specimen geometry (Section 6.3.2). Also, as for DENT specimens (Section 4.3.3),  $\psi^e$  determined using the simple EWF method with notched SENT specimens can be used as a measure of  $\varphi_c$  determined from the complex and time consuming testing of fatigue pre-cracked specimens. It appears that for better match with  $\varphi_c$ ,  $\psi^e$  should be computed from least square fitting of  $v_f - l$  data with  $l_{min}$  set higher than the initial transient regime (Figs. 4.9, 4.10 for DENT specimens; Figs. 6.7, 6.8 for SENT specimens). To ensure a wide range of  $l$  for least square data fitting to determine  $\psi^e$ , it should be preferable to use specimen with higher width  $W$  (such as 48 mm for the DENT specimens as in [41] rather than 30 mm for the present study).
3. Successful determination of the crack initiation point for both notched and pre-cracked DENT and SENT specimens permits determining  $\delta_c$ ,  $w_i$  and  $J_p^c$  for these specimens. For either notched ( $\rho = 0.1$  mm) or pre-cracked specimens with  $l$  within the respective  $l$ -validity ranges, average  $J_p^c$ , average  $\delta_c$  and  $w_{ie}$  (determined by linear extrapolation of  $w_i - l$  data to  $l = 0$ ) can be considered to be material parameters (Sections 6.3.3.1 and 6.3.3.2).
4. If an initiation parameter is required for possible use in integrity assessment, then it is advisable to determine it using fatigue pre-cracked specimens; in such a case SENT specimen geometry is for choice.
5. For the notched SENT specimens, the parameters  $w_e^m$  and  $w_i^m$ , determined by linear extrapolation of mixed stress regime data ( $w_f - l$  and  $w_i - l$ ) to  $l = 0$  were within  $\sim 3\%$ , Fig. 6.13(a). Similarly, the parameters  $\delta_c^{e,m}$  by linear extrapolation

of mixed stress  $v_f - l$  data to  $l = 0$  was within  $\sim 1.6\%$  of the ordinate offset computed by linear extrapolation of mixed stress regime  $\delta_c - l$  data, Fig. 6.13(b). These linear extrapolations have been carried out on empirical basis. Further research in this direction is desirable.





# Chapter

## Crack growth characterization: CTOA ( $\varphi$ ) and $\delta_5$ measurements

# 7

### 7.1. Introduction

As reported in Sections 4.3.3 and 6.3.2, pre-cracked DENT and SENT specimens of the present test steel sheet have been successfully tested following the test procedure given in Section 3.2.4 for optical measurement CTOA ( $\varphi$ ) and hence the critical CTOA ( $\varphi_c$ ). In these chapters it was also established that  $\varphi_c$  may be estimated by the EWF parameter  $\psi^e$ , and both these parameters are transferable between the two specimen geometries, as required of a material parameter. Also, both  $\psi^e$  and  $\varphi_c$  decreased marginally on increasing the quasi-static nominal strain rate from  $10^{-4}$  to  $10^{-2} \text{ s}^{-1}$ . These results encouraged additional studies using both DENT and SENT specimens. One objective was to verify that similar to  $\psi^e$  (Tables 4.1, 6.1),  $\varphi_c$  determined by the optical method is independent of notch root radius. Another objective was to characterize crack growth in terms of variation of  $\delta_5$  (determined using an optical method, instead of by using a  $\delta_5$  gage) with  $\Delta a$ . It will be recognized that  $\varphi(\delta_5) - \Delta a$  plot generated using a pre-cracked specimen itself characterizes ductile tearing resistance. The possibility of reducing the experimental burden for determining  $\varphi$  and  $\varphi_c$ , by adopting the  $\delta_5 - \Delta a$  method, has also been examined. .

### 7.2. Experimental

#### 7.2.1 Specimens and testing

Both notched ( $\rho = 0.1 \text{ mm}$ ) and fatigue pre-cracked SENT and DENT specimens with external dimensions identical to specimens tested in the previous chapters were used for the tests reported in this chapter. The  $l$  of the specimen tested were in the range 19.5 mm to 25.5 mm, chosen so that  $l \gg 4t$ , to cover the expected initial transients in  $\varphi$  (cf. [11]) before the regime where  $\varphi$  attains a constant value

$\varphi_c$ . Since a  $\delta_5$  gage (as recommended in [4, 5]) was not available for  $\delta_5$  measurements, it was decided to measure  $\delta_5$  optically on the test specimen, using microhardness indentation marks placed at distance  $\pm 2.5$  mm from crack tip on the crack tip line parallel to the loading axis (A-A1 line in Fig. 7.1). Actually, as shown in Fig 7.1, two more pairs of microhardness indentations placed 0.25 mm apart, at the same distance from the crack path were added. The intention was: in the deformed specimen, on each side of the crack path, the placing of three points would help in unequivocally identifying the gage points for optical measurement. In addition, the tests included a notional  $\delta_7$  measurements, similar to  $\delta_5$  measurements but with gage length 7 mm; accordingly, indentation marks were placed at distance  $\pm 3.5$  mm from crack tip (marked B-B1 in Fig. 7.1) on the line A-A1. The  $\delta_7$  measurement was meant as confirmatory to  $\delta_5$  measurement, and also to protect against the remote possibility of extensive crack tip plastic deformation in particularly notched specimens, distorting the intended interpretation of  $\delta_5$ .

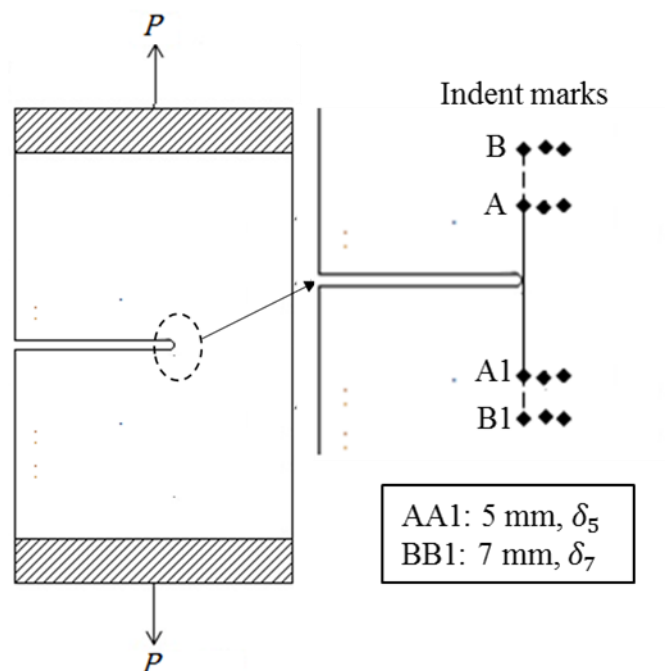


**Fig. 7.1:** Schematic of microhardness indentations for  $\delta_5$  and  $\delta_7$  measurements

For the tests, the specimen was first polished to metallographic quality, and the microhardness indentation marks were placed. Then the testing was carried out following the method prescribed in Section 3.2.4. Each test delivered a series of

photographs for subsequent optical measurements of  $\varphi$ ,  $\delta_5$ ,  $\delta_7$  and  $\Delta a$ . The very limited extent of crack tip tunneling (as reported in Sections 4.3.2 and 5.3.2) justifies measurements of crack extension optically on the specimen surface from very early during the test.

## 7.2.2 CTOA determination

The optical measurement of CTOA from series of photographs was carried out using the two point and the four point method discussed in [4, 23, 87]. The two point method for CTOA measurement has already been presented in detail in Sections 4.3.5 and 6.3.4. In this method, a pair of lines are drawn from the crack tip to reference points on the crack edges back from the crack tip. The four point method was devised for the eventuality when because of plastic deformation, accurately positioning the crack tip become difficult. In this method, lines are drawn from pair of reference points (location 0) on the crack flanks 0.1 mm to 0.2 mm behind the notional crack tip, to a pair of reference points (location  $i$ ) on the crack flanks 0.5 mm to 1.5 mm back from the crack tip. CTOA is determined using the expression

$$(\varphi)_{\Delta a} = \left( \frac{d_i - d_0}{r_i} \right)_{\Delta a} \quad (7.1)$$

where  $d_i$ ,  $d_0$  are respectively the distance between the pairs of points located at the position  $i$ , and 0, and  $r_i$  is the distance between two locations  $i$ , and 0, Fig. 7.2. CTOA from the  $\delta_5$  - $\Delta a$  data, designated as  $\varphi(\delta_5)$  here, can be determined from by numerical differentiation of the test generated  $\delta_5$  - $\Delta a$  data [4]:

$$\varphi(\delta_5) = \frac{\Delta \delta_5}{\Delta a} \quad (7.2)$$

By analogy, it follows that

$$\varphi(\delta_7) = \frac{\Delta \delta_7}{\Delta a} \quad (7.3)$$

It must, however, be noted that  $\varphi(\delta_5)$  (or  $\varphi(\delta_7)$ ) is only an approximation for, and not a true measure of,  $\varphi$ . This is because with increasing crack growth, the sensitivity of  $\delta_5$  (or  $\delta_7$ ) measured at the initial crack tip location reflecting the

deformation and fracture behaviours dictated by the crack with its tip at the current location gradually weakens [87].

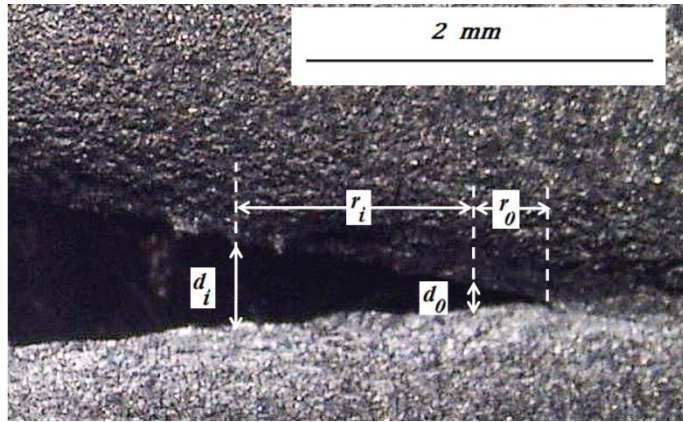


**Fig.7.2:** Four point method for determining the CTOA.

## 7.3 Results and discussion

### 7.3.1 Selection of optical CTOA ( $\varphi$ ) determination method

The successive photographs recorded from the testing of pre-cracked SENT specimen at a ramp rate  $0.006 \text{ mm.s}^{-1}$  were analyzed for CTOA measurement. The  $\varphi - \Delta a$  results from the two point method were presented in Figs. 6.7 (with  $L = 1.5 \text{ mm}$  as the best choice. The corresponding  $\varphi - \Delta a$  data from the four-point method (Eq. (7.2)) were obtained using  $r_0 = 0.2 \text{ mm}$  and  $r_i = 1.3 \text{ mm}$ . The results are compared in Fig. 7.3. The excellent agreement shows that either of the methods, of course with proper choice for  $L$  for the two point method, and  $r_0, r_i$  for the four point method, could be used. Further analyses in the present report adopted the two point method, as the accurate identification of the crack tip was not a problem in the present case.

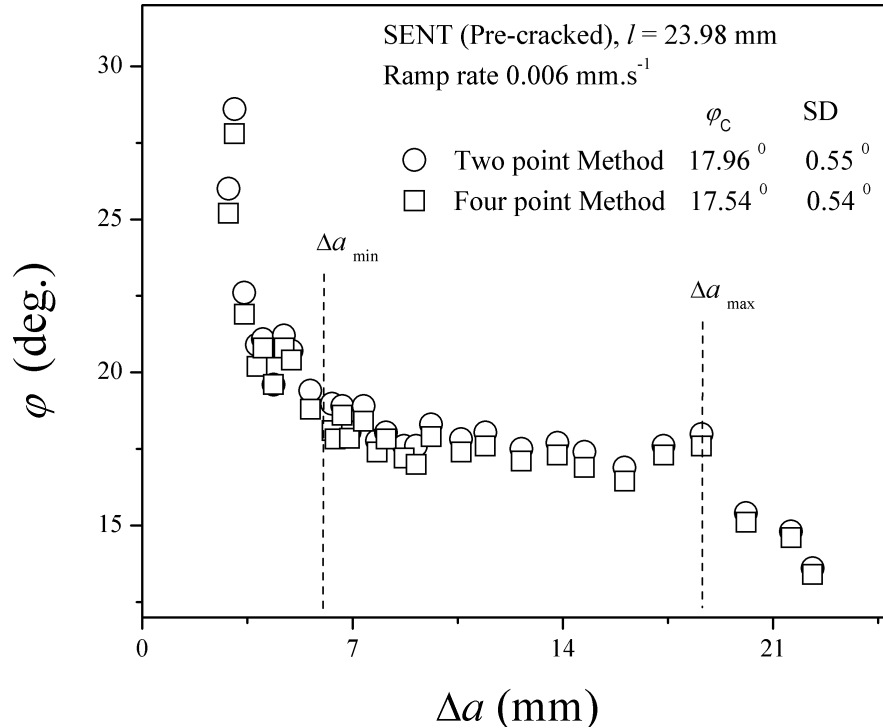


**Fig. 7.3:** For a pre-cracked SENT specimen,  $\varphi - \Delta a$  curves using two point method (data from Fig. 6.7, with  $L = 1.5$  mm, the best choice) and four point method.

### 7.3.2 Effect of notch root radius ( $\rho$ ) and ligament lengths ( $l$ ) on $\varphi - \Delta a$ plots

As indicated in Section 7.1, one of the objectives of the present chapter is to determine the effect of notch tip radius on the optically measured  $\varphi - \Delta a$  curve, particularly the parameter  $\varphi_c$ . For this purpose, one SENT specimen with ligament length  $l = 26$  mm and notch tip radius  $\rho = 0.1$  mm was tested at a ramp rate  $0.006$  mm.s<sup>-1</sup> and  $\Delta a$  - dependence of  $\varphi$  was measured using the optical two point method. The  $\varphi - \Delta a$  plot of the notched specimen thus obtained has been compared with that for a pre-cracked specimen with  $l = 23.98$  mm, Fig. 7.4.

The  $\varphi_c$  values for the notched and pre-cracked specimens in this figure were very similar, similar to the case of the EWF parameter  $\psi^e$ . The difference of the notched and fatigue pre-cracked specimens in Fig. 7.4 was in the transition regimes. For the pre-cracked specimen, the initial transition persisted to  $\Delta a \cong 6$  mm, i.e.  $6t$ . For the notched specimen on the other hand, the initial transient regime was much larger,  $\Delta a \cong 9t$ .

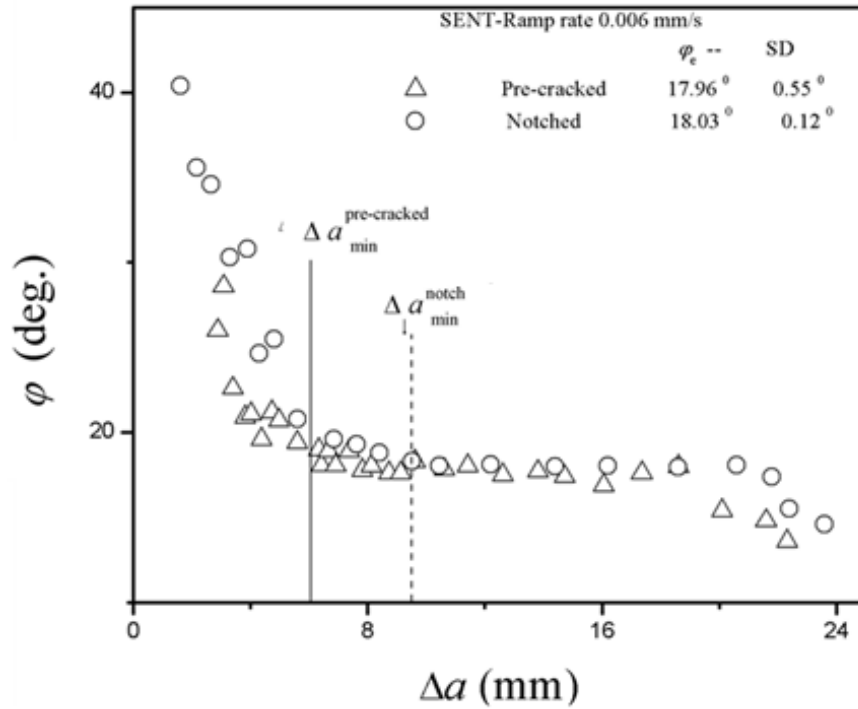


**Fig. 7.4:**  $\varphi - \Delta a$  curves of pre-cracked and notched SENT specimens (pre-cracked specimen data from data from Fig. 6.7 for  $L = 1.5$  mm).

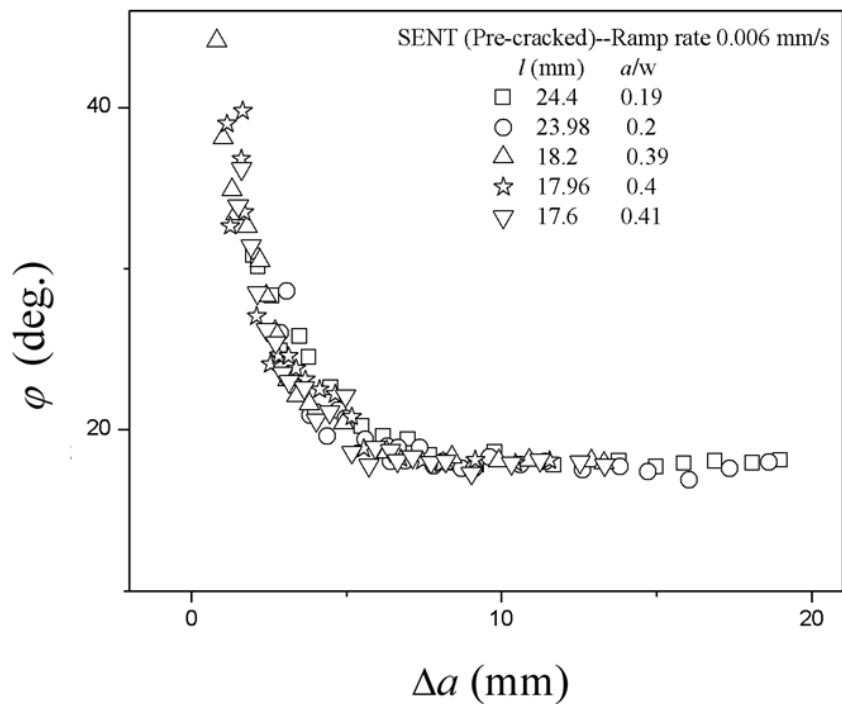


**Fig. 7.5:**  $\varphi - \Delta a$  plots of pre-cracked SENT specimens with different  $l$  (data for  $l = 23.98$  mm from Fig. 6.7 for  $L = 1.5$  mm)

The  $\varphi - \Delta a$  plots for pre-cracked SENT specimens with varying ligament lengths,  $l$ , ranging from 12.8 mm to 24.24 mm, did not show any significant differences, and yielded very similar  $\varphi_c$  values, Fig.7.5. This result is consistent with  $\varphi_c$  for a given sheet material being  $l$ -independent, as expected of a material parameter. The results from Figs. 7.4 and 7.5 taken together show that with judiciously chosen  $l$  to ensure a sufficiently large  $\Delta a$  range for the critical regime, a notched specimen with a sufficiently small notch root radius (such as  $\rho = 0.1$  mm) can very well be used to determine  $\varphi_c$ , thereby avoiding the necessity of pre-cracking the test specimen. This conclusion, reached by testing SENT specimens, should in principle extend to DENT specimens also.

### 7.3.3 $\delta_5 - \Delta a$ and $\delta_7 - \Delta a$ plots: the corresponding $\varphi$ estimates

Figure 7.6(a) shows the  $\delta_5 - \Delta a$  and  $\delta_7 - \Delta a$  plots for a pre-cracked SENT specimen. Clearly, the two plots nearly coincide up to  $\Delta a \cong 20$  mm. From the data presented in this figure,  $\varphi(\delta_5)$  and  $\varphi(\delta_7)$  values were determined using Eq. (7.2) and (7.3) respectively. Expectedly, the  $\varphi(\delta_5) - \Delta a$  and  $\varphi(\delta_7) - \Delta a$  plots also nearly coincided, Fig. 7.6(b). As indicated in section 7.1, the  $\varphi(\delta_5) - \Delta a$  plot generated using a pre-cracked specimen itself characterizes ductile tearing resistance; the same consideration should also apply for the  $\varphi(\delta_7) - \Delta a$  plot. The results presented in Figs. 7.6(a) and 7.6(b) show that in the present instance,  $\delta_7$  measurements merely served to confirm the  $\delta_5$  measurements. Further discussions are therefore restricted to the  $\delta_5 - \Delta a$  and  $\varphi(\delta_5) - \Delta a$  plots. It is interesting to explore whether these data could be used to obtain an approximation for  $\varphi_c$ . From Fig. 7.6(b), it is clear that this would require an acceptable, but subjective, approximation (recall e.g., estimating steady state creep rate from creep strain - time data when true steady state does not obtain). One such approximation is shown in Fig. 7.6(b) - a reasonable extended range of  $\Delta a$  for which the variation of  $\varphi(\delta_5)$  is small. The average  $\varphi(\delta_5)$  over such a range, designated  $\varphi_c(\delta_5)$  could be considered as an approximate measure of  $\varphi_c$ .

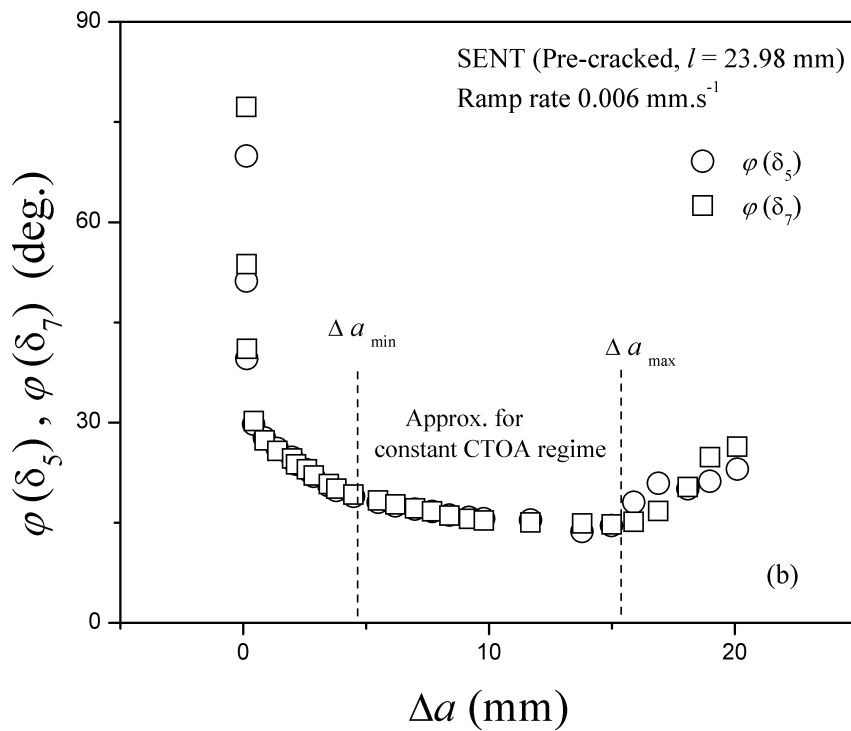
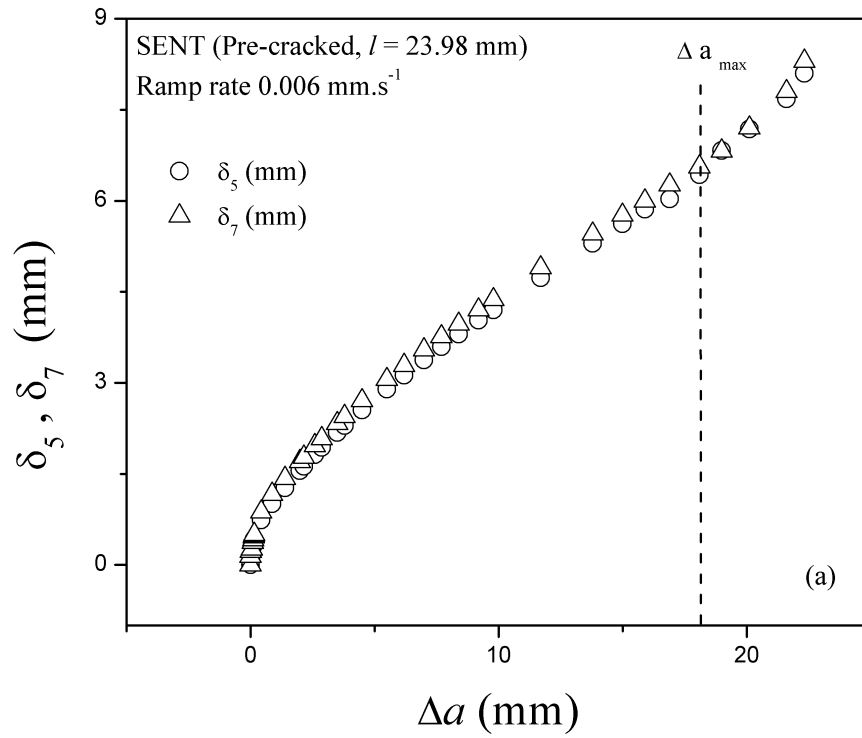


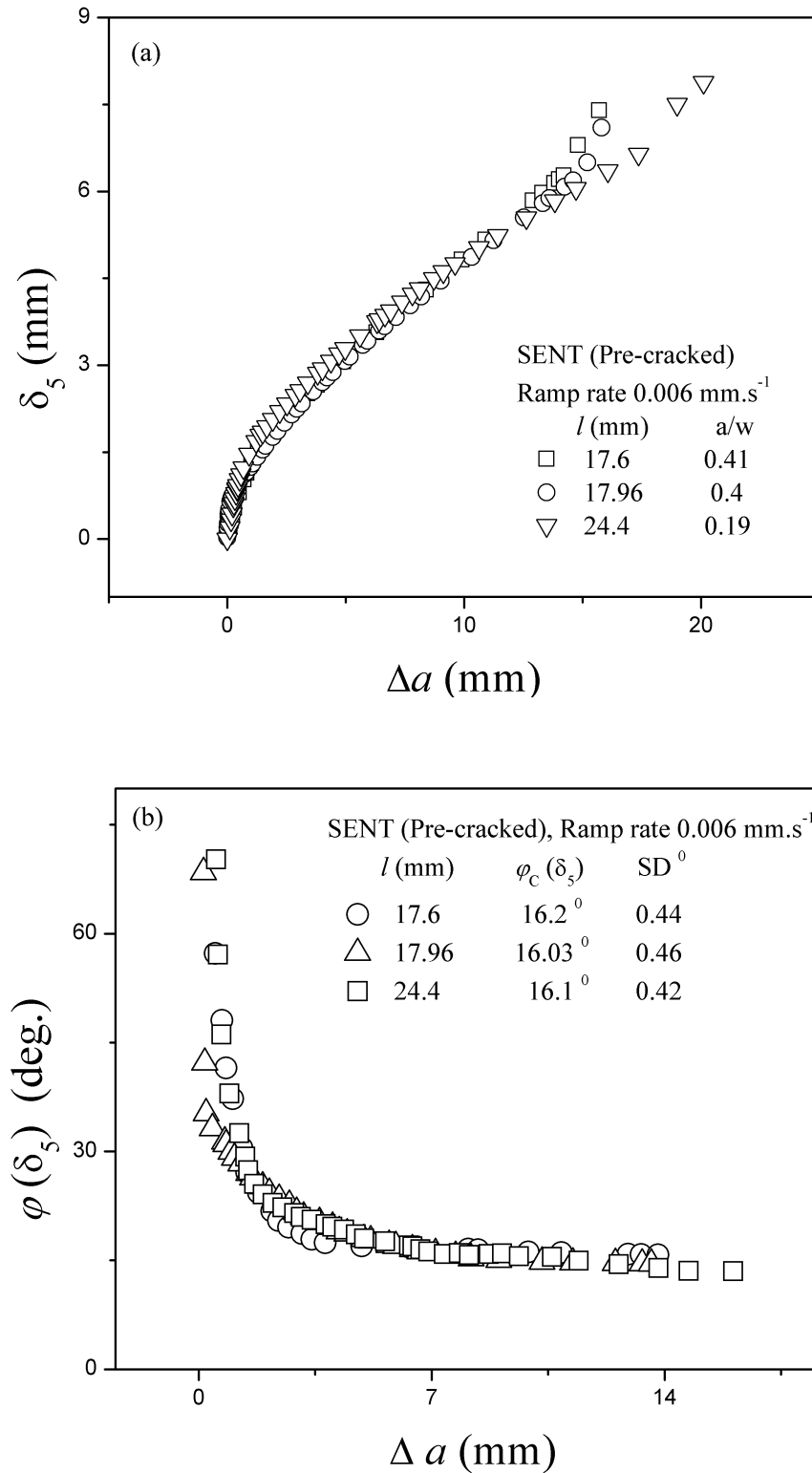
**Fig. 7.6:** For a pre-cracked SENT specimen (a)  $\delta_5 - \Delta a$  and  $\delta_7 - \Delta a$  plots and (b) the corresponding  $\varphi(\delta_5) - \Delta a$  and  $\varphi(\delta_7) - \Delta a$  plots.



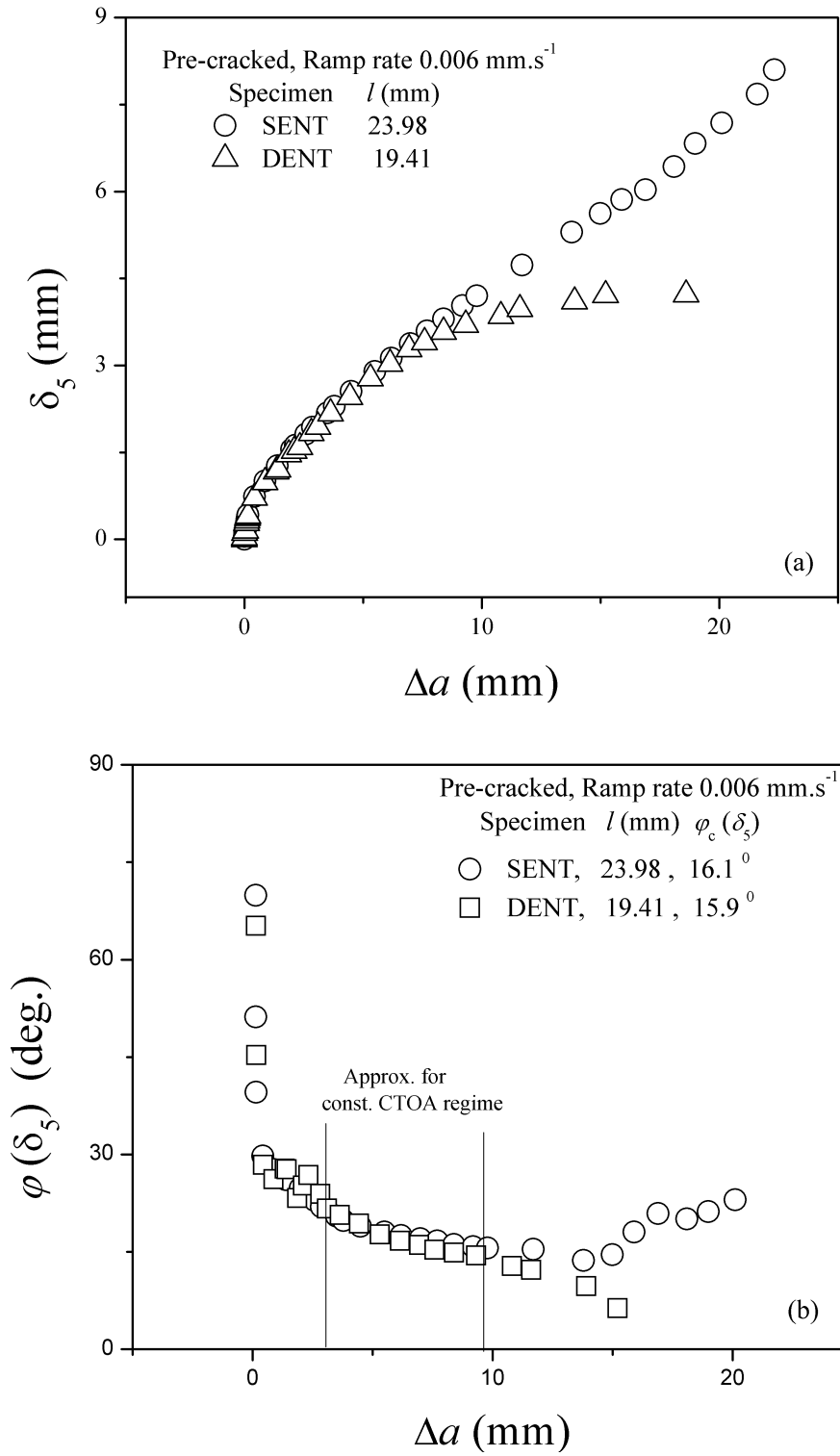
The  $\delta_5 - \Delta a$  curves obtained from pre-cracked SENT specimens with varying ligament lengths  $l$  ranging from 12.8 mm to 24.24 mm, shown in Fig.7.7(a), demonstrates “peeling-off” of the curves for smaller  $l$  values from those for the larger  $l$  values beyond some extents of crack extensions, cf. [87]. The  $\Delta a$  at which the curvature in a  $\delta_5 - \Delta a$  curve changes may be identified as the maximum crack extension,  $\Delta a_{max}$  for determining  $\varphi_c(\delta_5)$ . To improve statistical reliability of the  $\varphi(\delta_5)$  values computed, instead of Eq. (7.2),  $\varphi(\delta_5)$  for a chosen  $\Delta a$  value was determined by linear least square fit of the set of three  $\delta_5, \Delta a$  data sets: the object point, and the two adjacent points with lower and higher  $\Delta a$  values. This method, recommended in [4, 87], requires  $\delta_5, \Delta a$  data with small  $\Delta a$  intervals. The  $\varphi(\delta_5)$  values thus obtained attain a steady value,  $\varphi_c(\delta_5)$  starting from a higher  $\varphi(\delta_5)$  value after the the initial transient, Fig 7.7(b).

Figure 7.8(a). shows that the  $\delta_5 - \Delta a$  curves for pre-cracked SENT and DENT specimen show good match up to a certain extent of crack growth  $\Delta a$ , but progressively increasing deviation with increasing  $\Delta a$  beyond this point.  $\varphi(\delta_5) - \Delta a$  data for both the specimens were computed using the entire sets of data, Fig. 7.8(b). However, for identifying the approximate range for  $\varphi_c(\delta_5)$  measurements, only the initial data sets up to the point of matching in Fig. 7.8(a) could be considered. The results basically confirm the transferability of  $\delta_5 - \Delta a$  data between these two geometries. The increasing difference with increasing  $\Delta a$  beyond the matching point may be attributed to the difference in the geometry dependences beyond the respective critical CTOA regimes in these two geometries.

Figures 7.9(a) and 7.9(b) compare respectively the  $\delta_5 - \Delta a$  plots and the corresponding  $\varphi(\delta_5) - \Delta a$  plots for a notched ( $\rho = 0.1$  mm) and a pre-cracked SENT specimens with comparable ligament lengths. As expected from results presented in Fig. 7.4, the initial transient regime persists to higher  $\Delta a$  level for the notched specimen, Fig. 7.9 (b); for higher levels of  $\Delta a$ , the plots for notched and pre-cracked specimens show good agreement.



**Fig. 7.7:** (a)  $\delta_5 - \Delta a$  and (b) corresponding  $\varphi(\delta_5) - \Delta a$  plots for pre-cracked SENT specimens with different ligament lengths.



**Fig. 7.8:** (a)  $\delta_5 - \Delta a$  and (b) the corresponding  $\varphi(\delta_5) - \Delta a$  plots for pre-cracked SENT and DENT specimens

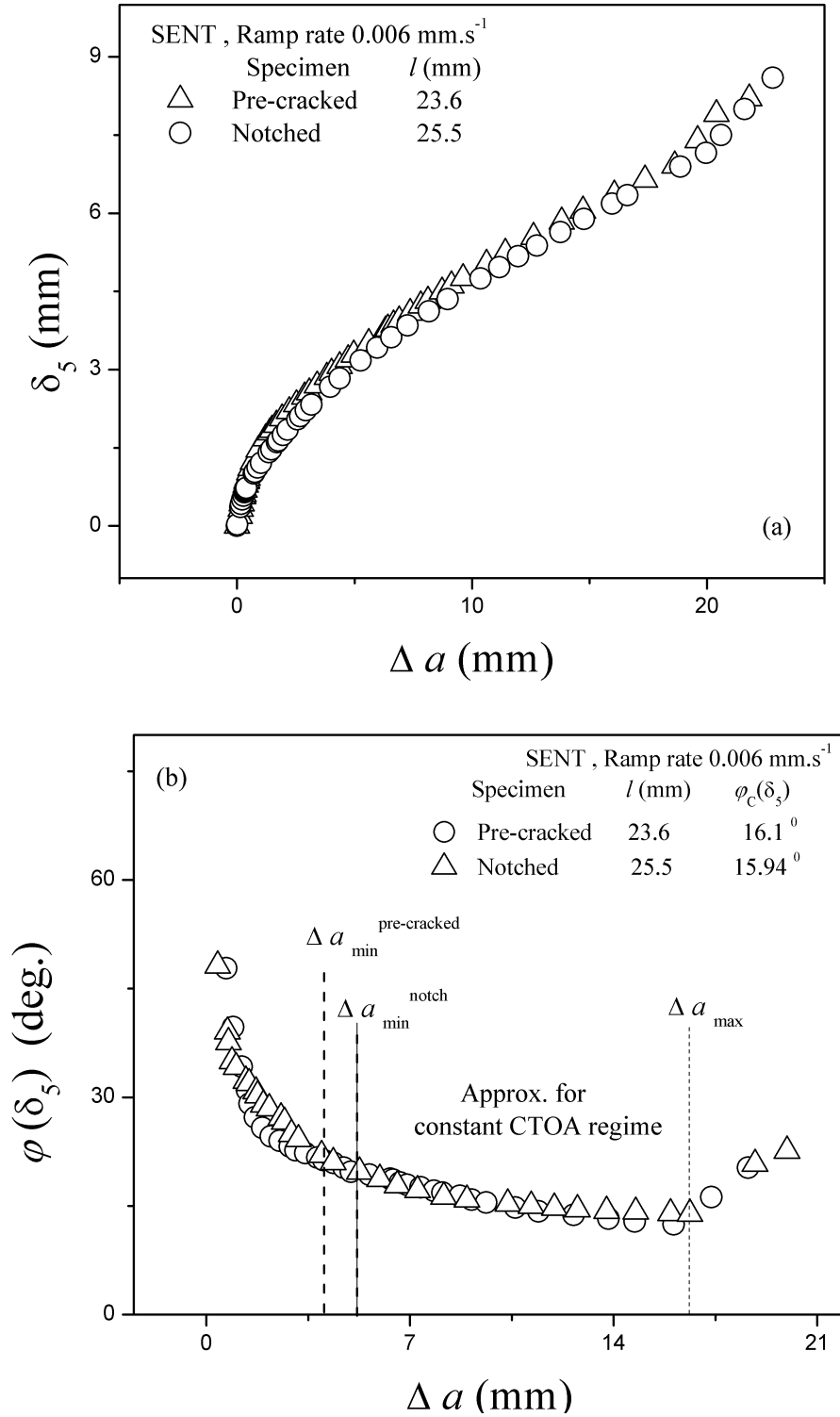


**Fig. 7.9:** (a)  $\delta_5 - \Delta a$  and (b) the corresponding  $\varphi(\delta_5) - \Delta a$  plots for pre-cracked and notched SENT specimens.

Figure 7.10 gives one example demonstrating that  $\varphi(\delta_5)$  is only an approximation for, and not a true measure of,  $\varphi$ , as indicated in Section 7.2.2. At relatively small  $\Delta a$  levels,  $\varphi$  - and  $\varphi(\delta_5)$ -resistance curves exhibit reasonable

matching. However, with increasing  $\Delta a$ , the plots increasingly deviate and consequently  $\varphi_c(\delta_5)$ , the average of  $\varphi(\delta_5)$  values in the approximately constant CTOA regime, becomes smaller than  $\varphi_c$ . As the data in Table 7.1 show,  $\varphi_c(\delta_5)$  values thus computed are significantly ( $\sim 11\%$ ) lower than  $\varphi_c$ . From the disposition of the  $\varphi(\delta_5)$  data in this figure, it is also clear that similar results would be obtained with any plausible alternative criterion. Still, the  $\varphi(\delta_5) - \Delta a$  plot may be useful in approximately determining the end of the initial transient regime. This may be useful in setting the lower ligament length in determining the EWF parameter  $\psi^e$  in better agreement with  $\varphi_c$ , see Table 4.3 and Table 6.4. This, however, requires further investigation.

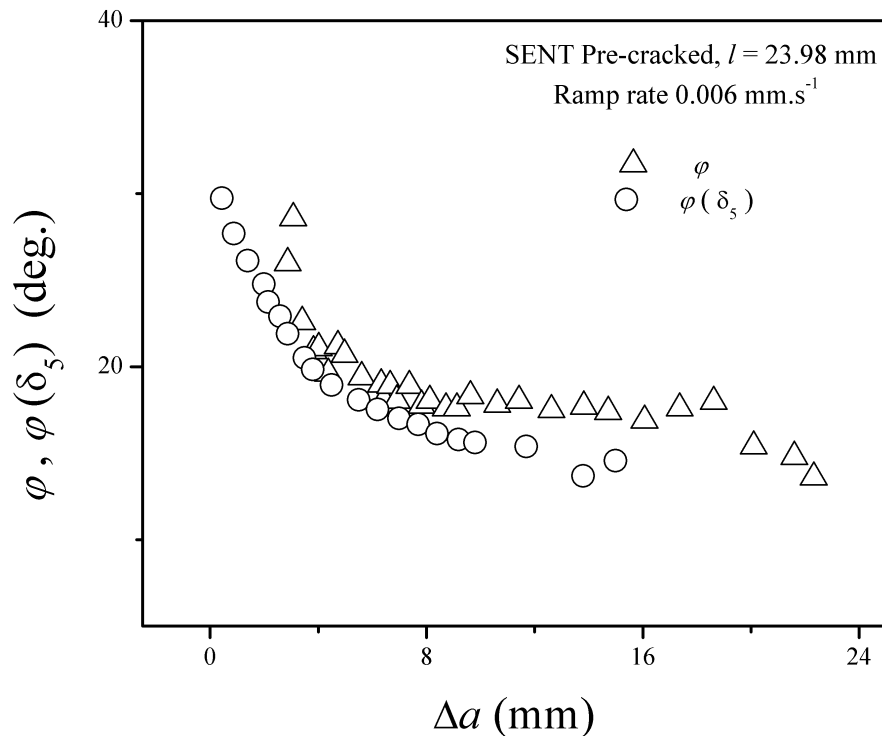


**Figure.7.10:** Comparison of  $\varphi - \Delta a$  and  $\varphi(\delta_5) - \Delta a$  curves of pre-cracked SENT specimen

**Table 7.1:** Comparison of  $\varphi_c$  and  $\varphi_c(\delta_5)$

Specimen geometry	Ramp rate (mm.s <sup>-1</sup> )	$\varphi_c$	$\varphi_c(\delta_5)$
SENT Pre-cracked		17.96°	16.1°
Notched ( $\rho = 0.1$ mm)	0.006	18.03°	15.94°
DENT Pre-cracked		17.72°	15.9°

## 7.4 Conclusions

1. For determining  $\varphi_c$ , either notched or fatigue pre-cracked specimens may be used. Increasing crack tip radius increased the initial transition  $\Delta a$  range, but the value of  $\varphi_c$  was unaffected.
2. For the present test specimens, the 4-point optical method for CTOA measurement gave results identical to those from the 2-point optical method.
3. Optical measurement of  $\delta_5$  was generally successful. Experimental results indicated that the  $\varphi(\delta_5) - \Delta a$  plots qualify as material property for the given sheet thickness. The experimental procedure for this method is also considerably simpler compared to the two-point or four-point method for optical determination of  $\varphi - \Delta a$  plots. However estimating critical CTOA from  $\varphi(\delta_5) - \Delta a$  plots involves a degree of subjectivity, and yielded estimates about 11% lower than the values measured by the optical method.
4. It appears that  $\varphi(\delta_5) - \Delta a$  plots can be used to measure the initial transient regime length. This information may be useful in setting the  $l$  range for determine the EWF parameter  $\psi^e$  in better agreement  $\varphi_c$ . This, however, merits further investigation.

# Chapter

## Crack growth characterization: Energy dissipation rate

8

### 8.1 Introduction

The energy dissipation rate parameter  $R$  proposed by Turner and co-workers [37, 65, 66] for characterizing extensive crack growth was briefly reviewed in Section 2.3. The main problem of  $R - \Delta a$  curve method is that  $R$  (and therefore the “crack propagation energy” for steady state growth,  $R_\infty$ ) depends upon specimen geometry and therefore is not a material property. The use of a normalised energy dissipation rate has been suggested for resolving this problem of specimen geometry dependence of  $R - \Delta a$  curves or of  $R_\infty$ . Though the  $R - \Delta a$  curve has the potential for characterizing crack growth in sheet material, its application has been essentially limited to thick plates. The present chapter focuses on determining the  $R - \Delta a$  curve and also  $R_\infty$  by analyzing test data for DENT and SENT specimens for the present sheet material already generated in the course of deriving some of the results reported in Chapters 4, 6 and 7. Preliminary attempts are also made for identifying a normalization method for the present test data.

### 8.2 Experimental

As reported in the previous chapters,  $\varphi - \Delta a$  plot for a sheet SENT or DENT specimen has been derived by (i) carrying out the test following the procedure described in Section 3.2.4, and then (ii) analyzing the test data, by the procedures illustrated in Sections 4.3.3, 6.3.2 and 7.2.2, generating the  $P - v_s - \Delta a$  data set in the process. Method 1 proposed in Section 8.3.1 involves analysing such a  $P - v_s - \Delta a$  data set for deriving the corresponding  $R - \Delta a$  plot. The  $P - v_s - \Delta a$  test data considered are for (i) one notched ( $\rho = 0.1$  mm) SENT specimen ( $l = 25.5$  mm); (ii) six pre-cracked SENT specimens ( $l$  ranging from 11.88 to 24.3 mm); and (iii) three pre-cracked DENT specimens ( $l$  ranging from 19.41 to 20.06 mm). The quasi-static ramp rates for the tests were 0.6, 0.06 or 0.006 mm.s<sup>-1</sup>. Of these tests, only

the one with fatigue pre-cracked SENT specimen with  $l = 11.88$  mm (see Fig. 8.4) was carried out specifically for the results reported in the present chapter.

EWF testing involves testing a set of notched/pre-cracked SENT/DENT specimens following the procedure prescribed in Section 3.2.2. The EWF analyses with data for notched/pre-cracked DENT specimens have been reported in Section 4.3.1, and for SENT specimens in Section 6.3.1. Method 2, discussed in Section 8.3.2, aims at determining  $R_\infty$  from the  $P - v_s$  data already generated in the course of EWF testing such a set of specimens, with the additional inputs namely identification of the crack initiation points in for these specimens.

## 8.3 Results and discussion

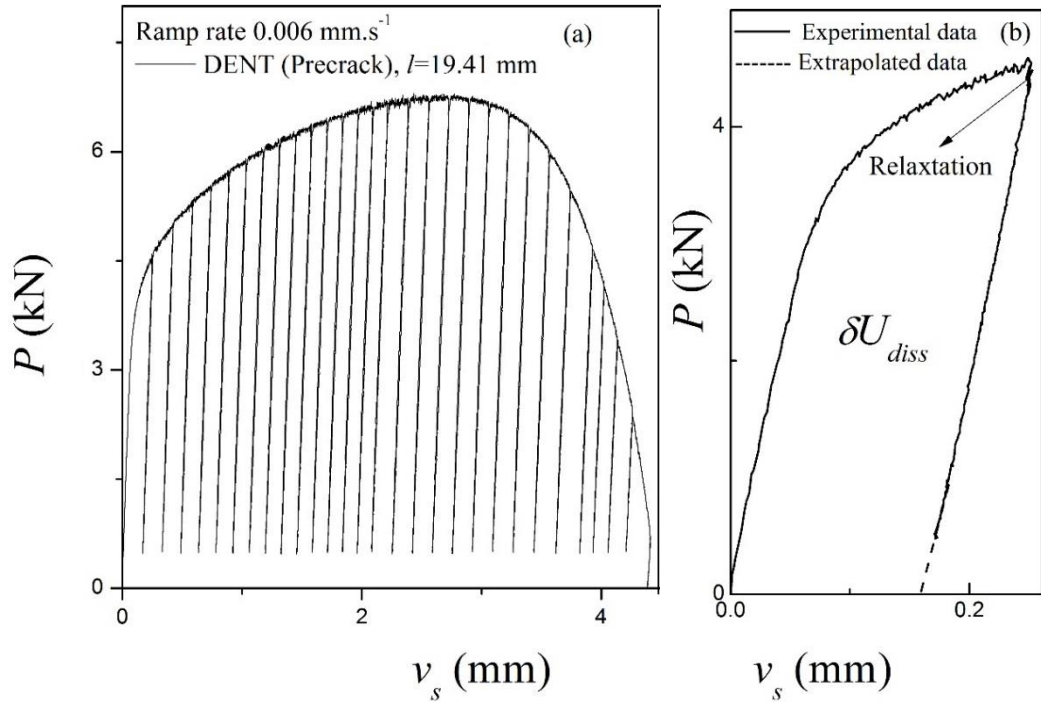
### 8.3.1 Method 1: $R - \Delta a$ plot from $P - v_s - \Delta a$ data

In this method,  $R$  is evaluated from the numerical derivative of the measured plastic area with crack length, Eq. (2.2). Figure 8.1(a) shows an example of  $P - v_s$  plot generated by applying repeated cycles of load-relax-unload imposed on a specimen in the course of generating a  $\varphi - \Delta a$  curve. The unloading segment from each of these cycles was extrapolated to zero load. The enclosed area then gives the increment in energy dissipated,  $\delta U_{diss}$  for this cycle. Figure 8.1(b) illustrates this for the very first cycle in Fig. 8.1(a). Beyond crack initiation, the corresponding total crack length increment  $\delta a$  during the current cycle is measured by comparing the high resolution photographs of crack tip captured during the current and the immediately preceding load relaxation steps. Then, from Eq. (2.2),  $R$  value can be determined.

Figure 8.2 shows the  $R - \Delta a$  plots for one each of pre-cracked SENT and DENT specimens for a ramp rate of  $0.006 \text{ mm.s}^{-1}$  computed in this manner. For both the specimens, the trend of the plots are identical: starting from high values corresponding to very small  $\Delta a$  values,  $R$  decreases with increasing  $\Delta a$  to reach steady values  $R_\infty$ , which remains constant for a regime of crack growth. The high initial value of  $R$  is generally associated with the considerable amount of energy spent for a vanishingly small amount of crack growth during the initial blunting phase of crack deformation [38, 76]. From the  $R - \Delta a$  curves, the  $R_\infty$  values were

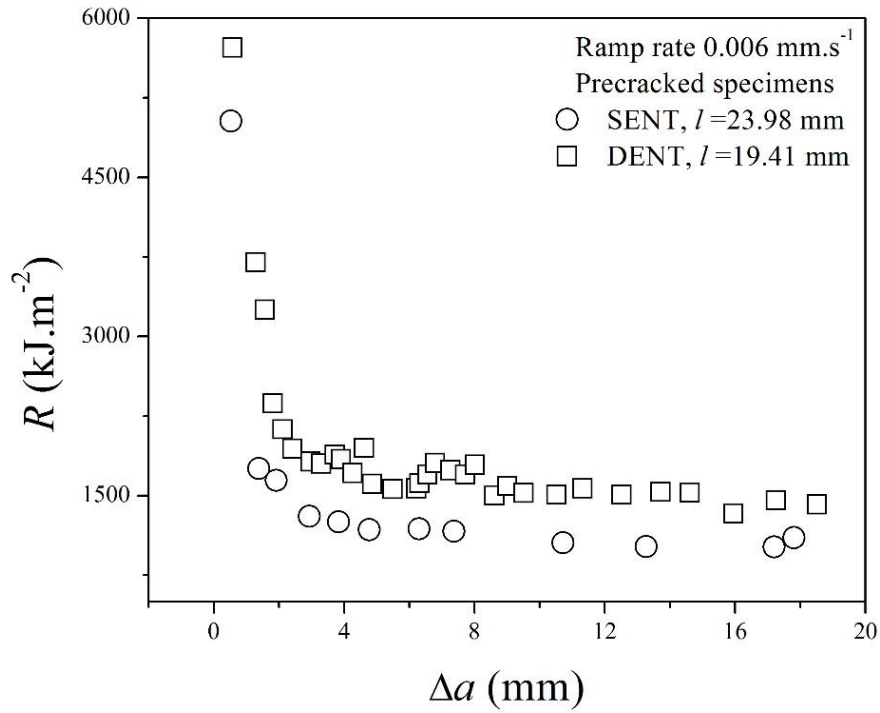


estimated from approximate fits to Eq. (2.3). In Fig. 8.2,  $R_\infty$  value for the DENT specimen thus estimated is  $1104 \text{ kJ.m}^{-2}$ , 30.1% lower than that of the  $R_\infty = 1578 \text{ kJ.m}^{-2}$  estimated for the SENT specimen. This shows the specimen geometry dependence of  $R_\infty$ . The higher  $R_\infty$  value in case of SENT specimens may be ascribed to the larger plastic zone in SENT specimen compared to the DENT specimen (see e.g., Fig. 6.5).

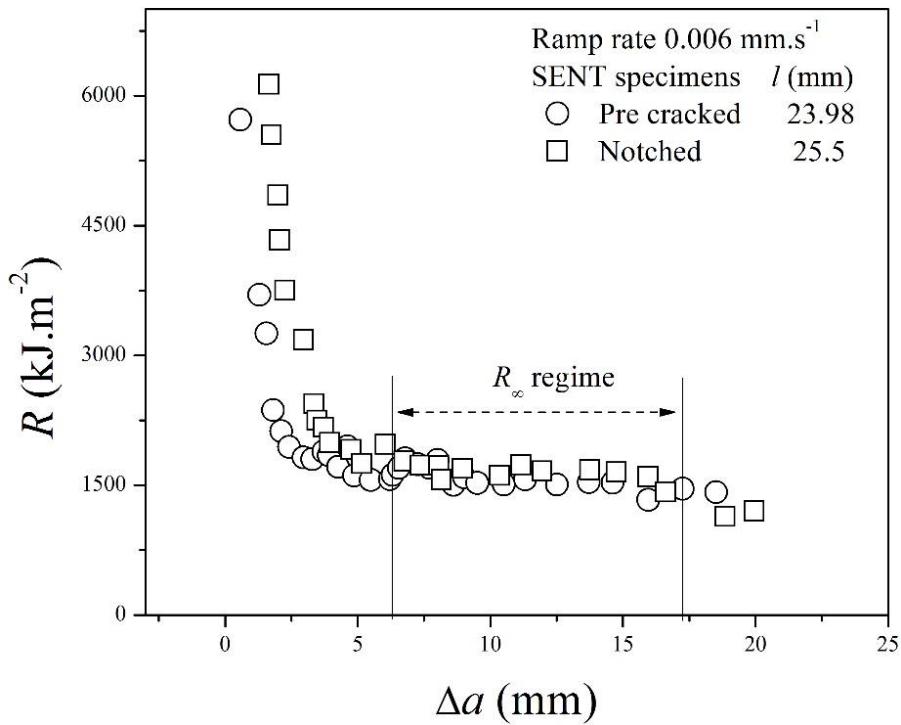


**Figure 8.1:** (a) A representative  $P - v_s$  plot for repeated cycles of loading-relaxation-unloading imposed on a specimen. (b) Illustrating measurement of increment in energy dissipated ( $\delta U_{diss}$ ) for the very first cycle in Fig. 8.1(a).

Figure 8.3 compares  $R - \Delta a$  curves for ramp rate  $0.006 \text{ mm.s}^{-1}$  for a notched ( $\rho = 0.1 \text{ mm}$ ) SENT specimen with that for the fatigue pre-cracked SENT specimens shown in Fig. 8.2; the two specimens had comparable ligament lengths. Compared to the pre-cracked specimen, the notched specimen has higher initial  $R$  at crack initiation, and larger transient crack growth  $\Delta a$  to reach the stable energy dissipation rate ( $R_\infty$ ) regimes; but  $R_\infty$  value for the notched specimen is computed as  $1582 \text{ kJ.m}^{-2}$  within 0.25% of the  $R_\infty = 1578 \text{ kJ.m}^{-2}$  for the pre-cracked specimen, Fig. 8.2. This confirms that for determining  $R_\infty$ , one can use a sharp notched instead of a fatigue pre-cracked specimen [37, 65, 67].

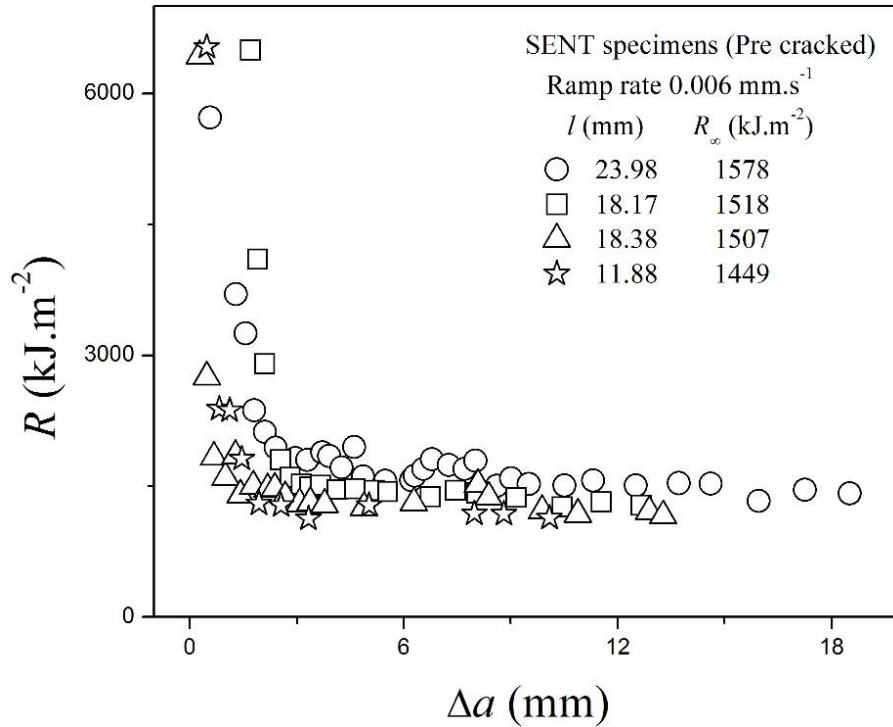


**Figure 8.2:**  $R - \Delta a$  curves for pre-cracked SENT and DENT specimens at ramp rate  $0.006 \text{ mm.s}^{-1}$



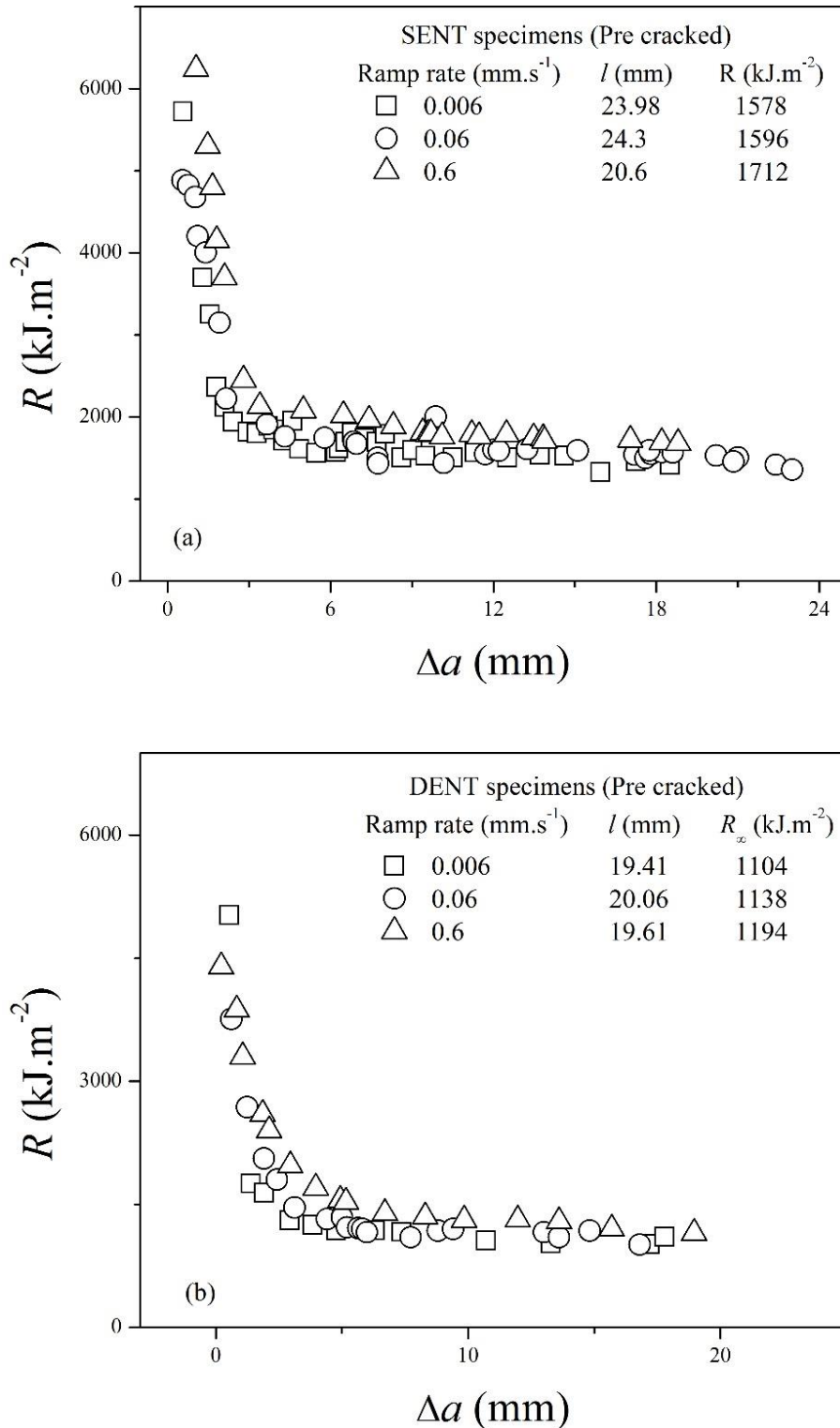
**Figure 8.3:**  $R - \Delta a$  curves for notched and pre-cracked SENT specimens at ramp rate  $0.006 \text{ mm.s}^{-1}$ .

Figure 8.4 compares  $R - \Delta a$  curves for pre-cracked SENT specimens with  $l$  increasing from 11.88 mm to 23.98 mm ( $a/W$  increasing from 0.2 - 0.6). For  $l$  being more than doubled, the corresponding estimates of  $R_\infty$ , also shown in Fig. 5, increase by only  $\sim 9\%$ .



**Figure 8.4:**  $R - \Delta a$  curves for SENT specimens with different ligament lengths for ramp rate 0.006 mm.s<sup>-1</sup>.

For pre-cracked DENT and SENT specimens, the  $R - \Delta a$  curves for three quasi-static ramp rates of 0.006, 0.06 and 0.6 mm.s<sup>-1</sup> are shown in Figs. 8.5(a) and 8.5(b) respectively. The estimated  $R_\infty$  values from these  $R - \Delta a$  plots are also shown in these figures, and also recorded in Table 8.2. For either SENT or DENT specimens, this 100 fold increase in the quasi-static ramp rate increased  $R_\infty$  by only about 8%. This is very close to the 7.4% increase in  $\sigma_u$  for the same increase in ramp rate (see Table 3.1). The implication, if any, of this close match, deserves a careful scrutiny. In comparison, using notched ( $\rho = 0.1$  mm) DENT and SENT specimens, for ramp rate increasing from 0.006 to 0.6 mm.s<sup>-1</sup>,  $\psi^e$  values increased by  $\sim 1$ -2%, and  $\varphi_c$  decreased by  $\sim 1\%$ , Tables 4.2 and 6.4.



**Figure 8.5:** Effect of ramp rates on  $R - \Delta a$  plots of fatigue pre-cracked (a) SENT and (b) DENT specimens

As Figs 8.6(a) and 8.6(b) show, for pre-cracked SENT and DENT specimens of the present test material tested at three quasi-static ramp rates, the  $R - \Delta a$  curves are similar in nature to the previously determined  $\phi - \Delta a$  curves, reported in Fig. 4.10

in and Fig. 6.8. For both the specimen geometries, however, the initial  $\Delta a$  regime for  $R$  to decrease to  $R_\infty$  was smaller than that for  $\varphi$  to decrease to  $\varphi_c$ .

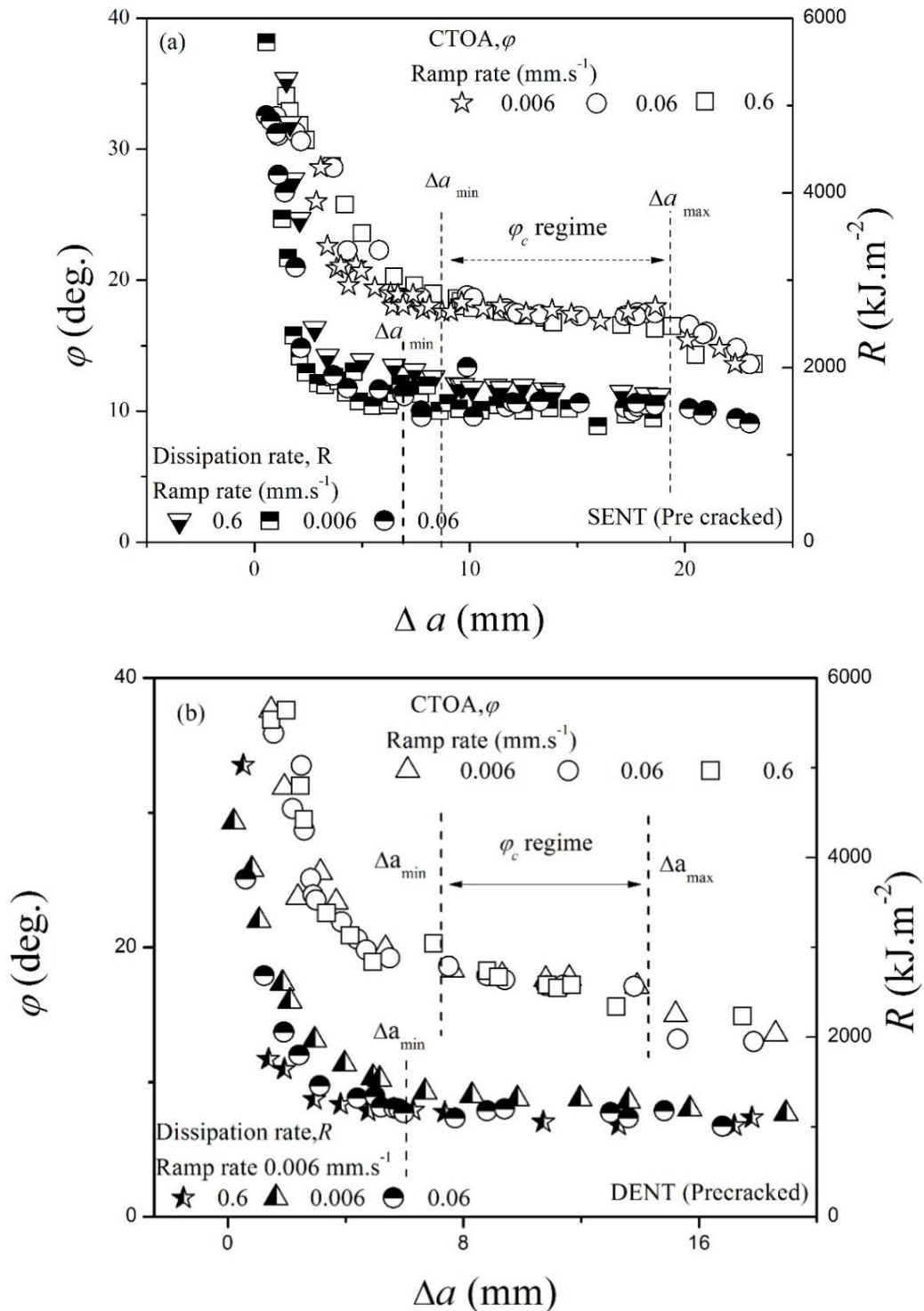


**Figure 8.6:**  $\varphi - \Delta a$  curves and  $R - \Delta a$  curves for (a) SENT and (b) DENT specimens for three quasi-static ramp rates. ( $\varphi - \Delta a$  data for SENT specimens from Fig. 6.8 and for DENT specimens from Fig. 4.10).

### 8.3.2 Method 2: Determining $R_\infty$

Sections 4.3.5 and 6.3.4 showed that the optically measured stable CTOA value,  $\varphi_c$  can be estimated by the EWF parameter  $\psi^e$ , the slope of the linear fit of the  $v_f$ - $l$  data (within  $l$ -validity ranges), for both DENT and SENT specimens. As the  $R$  -  $\Delta a$  curves and  $\varphi$  -  $\Delta a$  curves show similar trends (Figs. 8.6(a) and 8.6(b)), it is tempting to check out whether the stabilized dissipation rate value,  $R_\infty$  can be obtained by linear fitting of the  $U_{diss}$ - $l$  data of the EWF tested notched as well as pre-cracked SENT and DENT specimens. This method is designated as Method 2 in the present investigation. It aims at determining  $R_\infty$  from the  $P$  -  $v_s$  data of a number of specimens with different  $l$  values ramp loaded to fracture, with additional input of the points of crack initiation in these specimens. Integrating Eq. (2.3)

$$U_{diss}(\Delta a)/t = \int_0^{\Delta a} \left[ R_\infty + (R_0 - R_\infty) \cdot \exp\left(-\frac{\lambda \Delta a}{W}\right) \right] \cdot da \quad (8.1)$$

For  $\Delta a$  beyond the initial transient regime (see e.g., Figs. 8.6(a), 8.6(b)), contribution from the exponentially decaying term to  $U_{diss}(\Delta a)$  should be a constant. Writing this constant contribution as  $U_{tr}/t$ , a linear relation is obtained:

$$U_{diss}(\Delta a)/t = U_{tr}/t + R_\infty \Delta a \quad (8.2)$$

Consider now the upper limit of  $\Delta a$  for applicability of Eq. (8.2). In a sheet SENT specimen very close to fracture, additional contributions to  $U_{diss}$  arise from the proximity of the crack tip to the free boundary. Similarly, in a DENT specimen approaching fracture, stress fields of the two approaching crack tips increasingly interact. However, for either specimen geometry, it appears reasonable to assume that with large  $l$ , the corresponding additional contributions to  $U_{diss}$  may be approximated as a constant contribution that gets added to the  $U_{tr}/t$  term. That is, provided  $l$  is sufficiently large, Eq. (8.2) may be assumed to apply to complete fracture, corresponding to  $\Delta a = \Delta a_{max}$ . It will be noted that  $U_{diss}(\Delta a_{max}) = W^{gr}$ , the energy spent in complete fracturing of a specimen (see Fig. 8.8 below). For a SENT specimen with ligament length  $l$ ,  $\Delta a_{max} = l$ , and

$$W^{gr}/t \approx U_{tr}/t + R_\infty \cdot l \quad (8.3(a))$$

For a DENT specimen with ligament length  $l$ ,  $\Delta a_{max} = l/2$  (because of crack growth from two notches), and

$$W^{gr}/t \approx U_{tr}/t + R_{\infty} \cdot \frac{l}{2} \quad (8.3(b))$$

Equations (8.3 (a)) and (8.3 (b)) show that the slope of the linear fit of  $W^{gr}/t - l$  data yields the  $R_{\infty}$  value for SENT specimens and  $R_{\infty}/2$  value in DENT specimens; obviously, the offset values  $U_{tr}/t$  is expected to vary with specimen geometry, and also with notch tip radius  $\rho$ .

For both the notched and pre-cracked SENT as well as DENT specimen sets EWF tested at ramp rate of  $0.006 \text{ mm.s}^{-1}$ , the crack initiation points have already been determined by comparing the  $P - v_s$  plots from mechanical tests and from 3-D FE simulation. The details of this simulations and meshing strategies may be found in Sections 4.3.6, 5.3.5 and 6.3.5. Figure 8.7 shows an example; the crack initiation point is marked as point 'b' in this figure. From this point, a line parallel to the initial loading line is drawn. This is assumed to be the elastic unloading line; the resultant error incurred in ignoring increase in specimen compliance from the initial value to crack initiation is considered negligible for the plasticity dominated processes. The area under the  $P - v_s$  plot from the mechanical test to the left of this line is  $W^{in}$ , and the area to the right of this up to (near) fracture equals  $W^{gr}$ . It may be recalled that in these tests the ramping had been continued not to complete fracture, but up to 90% drop from peak load, after which the specimens were unloaded. However, as can be seen from Fig. 8.7, and also as established in Chapters 4 and 6, the consequent error in energy calculations may be ignored.

The plots of  $W^{gr}/t$  against  $l$  for notched and pre-cracked SENT and DENT specimens (ramp rate  $0.006 \text{ mm.s}^{-1}$ ) are shown in Figs. 8.8(a) and 8.8(b) respectively. The  $l$  ranges covered by these data are the  $l$ -valid ranges identified for applying EWF equation. Consequently the highest value of  $l$  covered in these analyses is  $W/3 = 10 \text{ mm}$ . For each case, data from 2 different but plausible  $l$  ranges were taken for least square fit, and the corresponding  $R_{\infty}$  computed by Method 2. The results are recorded in Table 8.1; this Table also includes

representative  $R_\infty$  data by Method 1 for three of these specimens for comparison (see Figs. 8.2 and 8.3).

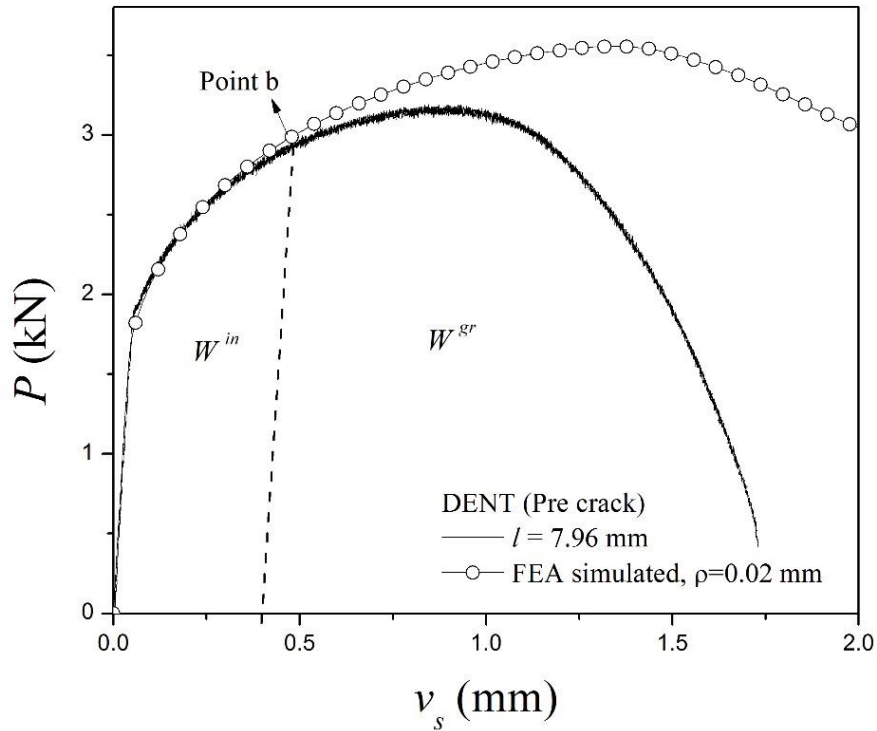


**Figure 8.7:**  $P - v_s$  plot from 3-D FE simulation for non-growing crack superimposed on the  $P - v_s$  plot from mechanical test for a pre-cracked DENT specimen. The point of onset of deviation between the plots, point ‘b’, is the crack initiation point, and  $W^{gr}$  is the dissipation energy to (nearly) complete fracture.

**Table 8.1:** Comparison of  $R_\infty$  computed using Methods 1 and 2. (Ramp rate 0.006 mm.s<sup>-1</sup>)

Specimen	Method 1		Method 2			
	$l$ mm	$R_\infty$ kJ.m <sup>-2</sup>	$l$ mm	$R_\infty$ kJ.m <sup>-2</sup>	$l$ mm	$R_\infty$ kJ.m <sup>-2</sup>
	Set 1		Set 2			
SENT (notched)	25.5	1582	4-10	1479	6-10	1543
SENT (pre-cracked)	23.98	1578	4.3-9.6	1417	5.28-9.6	1520
DENT (notched)	-	-	3-10	1007	5-10	1196
DENT (pre-cracked)	19.41	1104	4.36-8.34	1160	5.3-8.34	1182



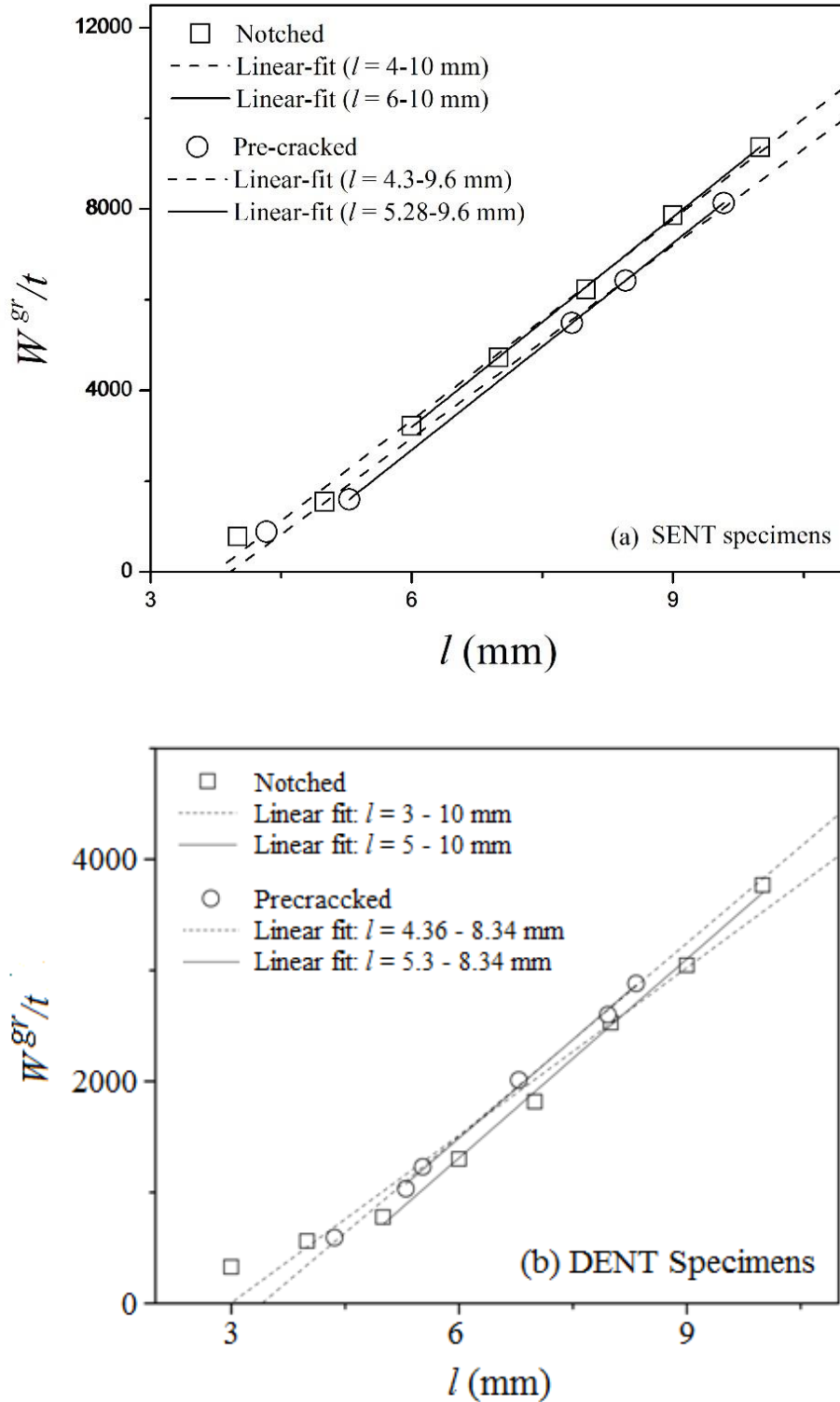


**Figure 8.8:**  $R_{\infty}$  determination from EWF tested notched and pre-cracked (a) SENT and (b) DENT specimens (ramp rate  $0.006 \text{ mm}\cdot\text{s}^{-1}$ ).

From Figs. 8.8(a) and 8.8(b), it is clear that in each case, better linear fits are obtained for the Set 2 data, with lower  $l$  value set as  $\sim 5t$  or higher. For either specimen geometry, the ratio of  $R_{\infty}$  values for notched and pre-cracked specimens

moves closer to the ideal value of 1 with the Set 2 data. For the SENT specimens, this ratio is 1.044 with Set 1 data and 1.015 with set 2 data; for the DENT specimens, the corresponding ratios are 0.868 with Set 1 and 1.012 with Set 2 data. Similar observations had also been made for the case of estimating  $\varphi_c$  using the EWF parameter  $\psi^e$ , see Table 4.3 for DENT specimens and Table 6.4 for SENT specimens. Again, the agreement between  $R_\infty$  by Method 1 and Method 2 (Set 2) is  $\sim 4\%$  for SENT specimens,  $\sim 8\%$  for DENT specimens. From the results presented for Method 2, and also considering the  $R - \Delta a$  plots from Method 1 such as Figs. 8.2, 8.3 and 8.6 (a-b), the lower cut off  $l$  value should be set as  $\sim 5t$  or higher. From the figures for Method 1 cited, it appears that the linearity of Eq. 8.6(a) or 8.6(b) could extend to  $l \sim 15$  mm. However, there is a need to experimentally establish the upper validity bound(s) of  $l$  for both SENT and DENT geometries, adopting rigorous statistical criteria. Also considering the small extents of linear regimes in Figs. 8.8(a) and 8.8(b), specimens with higher  $W$  appear preferable for these studies.

### 8.3.3 Normalization of the $R$ -resistance curve

As considered in Section 2.3,  $R$  has been normalized using a factor  $R_{ref}$  in attempts to obtain a normalized energy dissipation rate  $R_N$  that would be independent of specimen geometry [38, 50, 75, 77, 139]:

$$R_N(\Delta a) = \frac{R(\Delta a)}{R_{ref}} \quad (8.4)$$

The normalization factor  $R_{ref}$  is defined as ( $a_0$  is the initial crack length)

$$R_{ref} = \sigma_y \cdot (W - a_0) \cdot \frac{\sigma_y}{E} \cdot f_Y \left( \frac{a_0}{W} \right) \quad (8.5)$$

Anuschewski et al [38] defined the “geometry function”  $f_Y$  in Eq. (8.5) as the ratio of the plastic limit load of the cracked structure to the yield load of an uncracked structure with the same net section. Memhard et al [140], in the course of research on an 20 mm thick plate of StE 460 German standard steel, proposed that for a high work hardening material, the maximum load  $P_{max}$  reached during loading may be used in place of the plastic limit load of the cracked structure, so that

$$f_Y \left( \frac{a_0}{W} \right) = \frac{P_{max}}{\sigma_y t l} \quad (8.6)$$

Figures 8.5(a) and 8.5(b) presented the  $R - \Delta a$  plots for fatigue pre-cracked SENT and DENT specimens for three quasi-static ramp rates of 0.006, 0.06 and 0.6  $\text{mm.s}^{-1}$ . Figure 8.9 present the corresponding  $R_N - \Delta a$  plots for both SENT and DENT specimens, computed using  $f_Y$  defined by Eq. 8.6. The corresponding  $R_\infty/R_{ref}$  values are recorded in Table 8.2. As Fig. 8.9 shows, this normalization does reduce to a large extent, but does not eliminate, the specimen geometry dependence. A quantitative assessment of the efficacy of normalization may be obtained from Table 8.2: for these test ramp rates,  $R_\infty$  of SENT specimens are 1.40 - 1.43 times the  $R_\infty$  of DENT specimen and the  $R_\infty/R_{ref}$  values of SENT specimens are 0.92 - 0.95 of the  $R_\infty/R_{ref}$  values for DENT specimens.

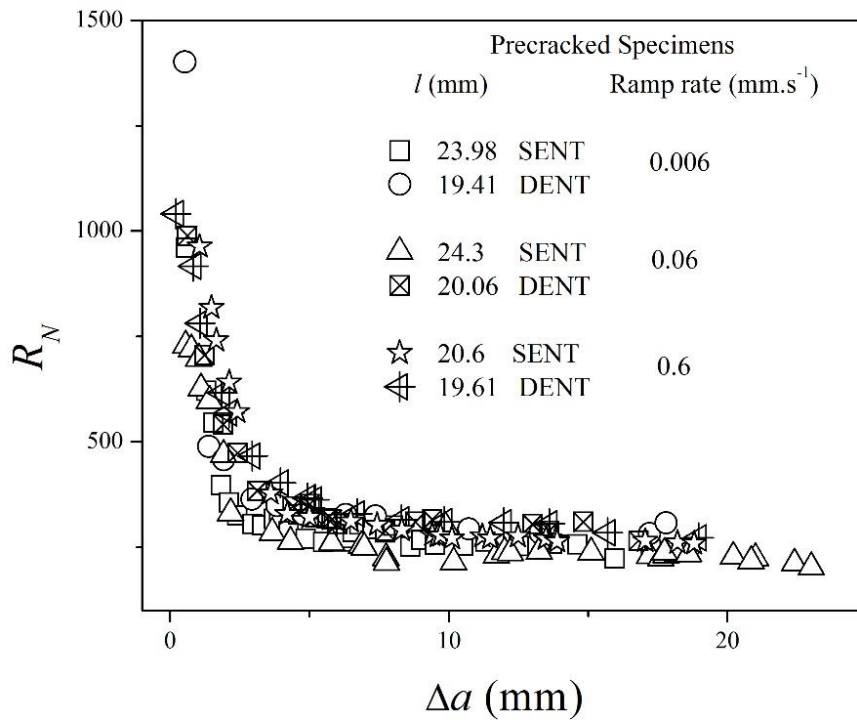


**Figure 8.9:**  $R_N - \Delta a$  curve of pre-cracked SENT and DENT specimens at ramp rate range of 0.006 - 0.6  $\text{mm.s}^{-1}$ . ( $R_{ref}$  defined by Eqs. (8.5) and (8.6)).

**Table 8.2:** Effect of ramp rate and normalization on  $R_\infty$  of pre-cracked SENT and DENT specimens. ( $R_{ref}$  defined by Eqs. (8.5) and 8.6))

Ramp Rate (mm.s <sup>-1</sup> )	SENT (pre-cracked)			DENT (pre-cracked)		
	$l$ (mm)	$R_\infty$ kJ.m <sup>-2</sup>	$\frac{R_\infty}{R_{ref}}$	$l$ (mm)	$R_\infty$ kJ.m <sup>-2</sup>	$\frac{R_\infty}{R_{ref}}$
0.6	20.6	1712	271.5	19.61	1194	293.8
0.06	24.3	1596	263.1	20.06	1138	275.4
0.006	23.98	1578	238.7	19.41	1104	257.4

## 8.4 Conclusions

1. For sheet materials, Method 1 is the simplest method for determining  $R - \Delta a$  curves, and is best adopted as an addition to the optical method adopted in the study for determining  $\varphi - \Delta a$  curves and thus  $\varphi_c$ , using notched or pre-cracked SENT or DENT specimens. Once an  $R - \Delta a$  curve is determined, the corresponding  $R_\infty$  is estimated, cf. Eq. (2.3).
2. The results confirmed that  $R_\infty$  value does not vary with initial notch tip radius – a sharp mechanical notch or a fatigue pre-crack. For the notched specimen, however, the initial  $R$  at crack initiation, and also the extent of crack growth  $\Delta a$  preceding the stable energy dissipation rate ( $R_\infty$ ) regimes are higher. For pre-cracked SENT specimens with  $l$  increasing from 11.88 mm to 23.98 mm,  $R_\infty$  showed a modest increase of only ~9%. For pre-cracked SENT and DENT specimens, tested at three quasi-static ramp rates 0.006, 0.06 and 0.6 mm.s<sup>-1</sup>, the  $R - \Delta a$  curves are similar in nature to the  $\varphi - \Delta a$  curves previously reported, but the initial transient  $\Delta a$  regimes for  $R$  to decrease to  $R_\infty$  were smaller than those for  $\varphi$  to decrease to  $\varphi_c$ . For either SENT or DENT specimens, increase in ramp rate from 0.006 to 0.6 mm.s<sup>-1</sup> increased  $R_\infty$  by only about 8%; very close to 7.4% for increase in  $\sigma_u$  for the same increase in ramp rate. The implication, if any, of this close match deserves a careful scrutiny.

3. Method 2 as designated in this report is suitable only for determining  $R_{\infty}$ . It is very simple but requires that the crack initiation event must be identified for each tested specimen. Also, for either notched or pre-cracked specimens, it is desirable to determine the  $l$ - ranges for Eqs. (8.3(a)) or (8.3(b)) to apply.
4. For the present test materials, normalization defined by Eqs. (8.5) and (8.6) did reduce, but did not eliminate, the specimen geometry dependence of  $R_{\infty}$ , Table 8.2. Further research, with different sheet materials and thickness, is required in this direction.



## 9.1 Introduction

Cohesive zone modeling (CZM) has been introduced in Section 2.7, where it has been mentioned that the literature on application of CZM simulation of crack propagation in thin sheets appears to be very limited. In particular, there are no reports on CZM simulation of crack growth in sheet DENT or SENT specimens. The chapter reports results from some CZM simulations of crack growth in DENT and SENT specimens of the present test material. These simulations have been carried out with the expectation that such study should shed light on issues like crack tunneling, determining crack initiation, and transferability of tearing resistance parameters. Experience has shown that in DENT and SENT specimens of the present test material, the crack grows along the symmetric plane passing through the tip(s) of notch(es)/crack(s) normal to the loading axis, and shows flat (mode I) fracture. Therefore, mode I (i.e., normal) CZM has been used for simulating crack growth on this symmetry plane (the crack growth path) in notched ( $\rho = 0.1$  mm) or fatigue pre-cracked DENT or SENT specimens of the present test material. For these simulations, the normal cohesive traction ( $T_n$ ) - normal opening displacement ( $\Delta_n$ ) for the PPR model proposed by Park et al. [118, 119] presented in Section 2.7 has been used, see Eqs. (2.9), (2.10). This model has four independent parameters. However, for the present study, the mode I cohesive energy parameter  $\Gamma_0$  was calculated using the relation given by Cornec et al. [117]

$$\Gamma_0 = 0.87T_0\delta_c \quad (9.1)$$

This reduces the 4-parameter PPR model, Eq. (2.9), to a 3 - parameter model

$$T_n = \left(\frac{0.87T_0\delta_c}{\delta_n}\right) \left(\frac{\alpha}{m}\right)^m \left(1 - \frac{\Delta_n}{\delta_n}\right)^{\alpha-1} \left(\frac{\alpha}{m} + \frac{\Delta_n}{\delta_n}\right)^{m-1} (\alpha + m) \left(\frac{\Delta_n}{\delta_n}\right) \quad (9.2)$$

with  $m$  given by Eq. (2.10). The three independent parameters in Eq. (9.2) are: (i)  $T_0$ , the maximum traction, corresponding to  $\Delta_n = \delta_c$ , the critical crack opening displacement at crack initiation; (ii)  $\delta_n$  = final value of  $\Delta_n$  at which  $T_n = 0$ ; and (iii)  $\alpha$ , a shape parameter defining the softening part of the traction-separation law. Once the values for these parameter are determined following the procedure elaborated in Section 9.2, it becomes possible carry out CZM simulation of crack growth for the intended purpose, as illustrated in Sections 9.3 - 9.7. All the FE analyses reported in this chapter were carried out using the FE code ABAQUS 6.10.

## 9.2 Determination of the CZM parameters

### 9.2.1 Notched ( $\rho = 0.1$ mm) specimens

For the studies reported in the previous chapters, the crack initiation event for a ramp loaded DENT or SENT specimen has been identified as the point of onset of deviation between the  $P$ - $v_s$  plot from the mechanical test and the corresponding  $P$ - $v_s$  plot of the specimen from 3-D large strain rate-independent FE simulation for non-growing crack. The details may be found in Sections 4.3.4.1 and 6.3.3.1 for notched specimens and Sections 5.3.3 and 6.3.3.2 for pre-cracked specimens.

The cohesive parameters  $T_0$  and  $\delta_c$  were determined for a notched ( $\rho = 0.1$  mm) DENT specimen with  $l = 10$  mm. For this specimen, the FE meshing used solid hexahedral elements with reduced integration (C3D8R elements; 1 integration point at the centre of the element) with in-plane dimensions  $0.2$  mm  $\times$   $0.2$  mm around the notch gradually increasing to  $1$  mm  $\times$   $1$  mm away from notch, and  $0.125$  mm width along the thickness of the sheet specimen (see Sections 4.3.4.1 and 6.3.3.1 for details on meshing). The elastic plastic material property for nominal strain rate  $10^{-4}$  s $^{-1}$  (Table 3.1) were ascribed to the elements, with the assumption that the tensile data were applicable for the entire strain range covered by the simulation. At the identified point of crack initiation (point ‘b1’ in Figure 4.12) the axial stress, and the corresponding  $\Delta_n$  were extracted from the simulation results, and taken as  $T_0$  and  $\delta_c$  respectively. These were then used to compute  $\Gamma_0$  using Eq. 9.1.

For the CZM simulations a single layer of  $0.01$  mm thick 3-D 8-node cohesive hexahedral elements (COH3D8 element, 4 integration points per element) was



placed on the crack growth path, implementing the selected cohesive law. The rest of the specimen was modelled with the C3D8R solid elements as described above. Cohesive element nodes are shared with solid elements; this determines the length (along the crack growth path) and width (along the specimen thickness direction) of the cohesive elements. Sweep meshing was performed with assigning mesh stack to correct numbering of the nodes of cohesive elements and solid elements. This is essential for the proper bonding of cohesive elements with the continuum element. Moreover, to generate elements of good quality mapped meshing was used; this actually removed the need of finer meshing around the notch. The shape parameter  $\alpha$  was estimated by trial and error, choosing the  $\alpha$  value that led to matching between the experimental and CZM simulated  $P$ - $v_s$  plots to large  $v_s$  levels corresponding to extensive crack growth.

Following this procedure, the CZM parameter values determined for notched DENT specimen with  $l = 10$  mm were:  $\delta_c = 0.66$  mm and  $T_0 = 523$  MPa (i.e.,  $\Gamma_0 = 300$  kJ.m<sup>-2</sup>), and  $\alpha = 1.15$ . These values have been used in all the 3-D CZM analyses of all notched specimens of both DENT and SENT geometries.

## 9.2.2 Pre-cracked specimens

The procedure adopted in Section 9.2.1 was adopted also for determining CZM parameters of a pre-cracked SENT specimen of ligament length,  $l = 9.58$  mm. For deriving the  $P$  -  $v_s$  plot for this specimen for the case of non-growing crack using FE simulation, (i) the notch tip radius was chosen as  $\rho = 0.02$  mm; (ii) the in-plane dimension of the hexahedral C3D8R elements was  $0.05$  mm  $\times$   $0.05$  mm around the notch gradually increasing to  $1$  mm  $\times$   $1$  mm away from notch; and (iii) the element thickness was  $0.2$  mm (i.e., 5 layers along the thickness direction). The elastic-plastic properties of the elements were chosen as described in Section 9.2.1 (see Sections 5.3.3 and 6.3.3.2 for details of the FE computation). Determination of the crack initiation point is illustrated in Fig. 6.14(a). As with the notched specimen, the values for the parameters  $T_0$  and  $\delta_c$  were determined from the simulation data for the crack initiation point. (point 'b1' in Figure 6.14(a)).

The meshing method for the CZM simulations followed that for the notched specimen described in Section 9.2.1, with a single 0.01 mm thick layer of cohesive COH3D8 elements placed on the defined crack growth path, sharing nodes with solid C3D8R elements with dimensions as described in the previous paragraph. The shape parameter  $\alpha$  was determined by trial and error so as to obtain for the specimen considered in Fig. 6.14(a) good matching between the experimental and simulated  $P - v_s$  plots to large  $v_s$  levels corresponding to extensive crack growth. The CZM parameter values thus determined for the pre-cracked SENT specimen ( $l = 9.58$  mm) were:  $\delta_c = 0.34$  mm and  $T_0 = 448$  MPa (i.e.,  $\Gamma_0 = 143$  kJ.m<sup>-2</sup>), and  $\alpha = 1.15$ . These CZM parameters values were used in all the 3-D CZM analyses of pre-cracked specimens of DENT and SENT geometries. It is interesting to note that compared to notched specimens, fatigue pre-cracking reduced  $\Gamma_0$  by as much as ~52% and  $\delta_c$  by ~48% , while  $T_0$  was reduced by ~15% and  $\alpha$  remained essentially unchanged.

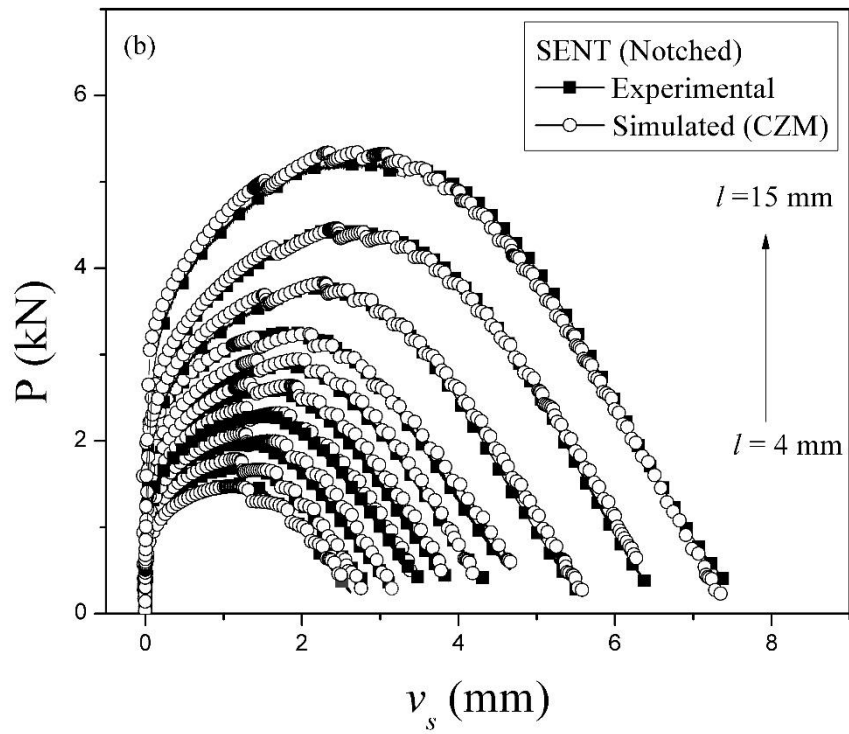
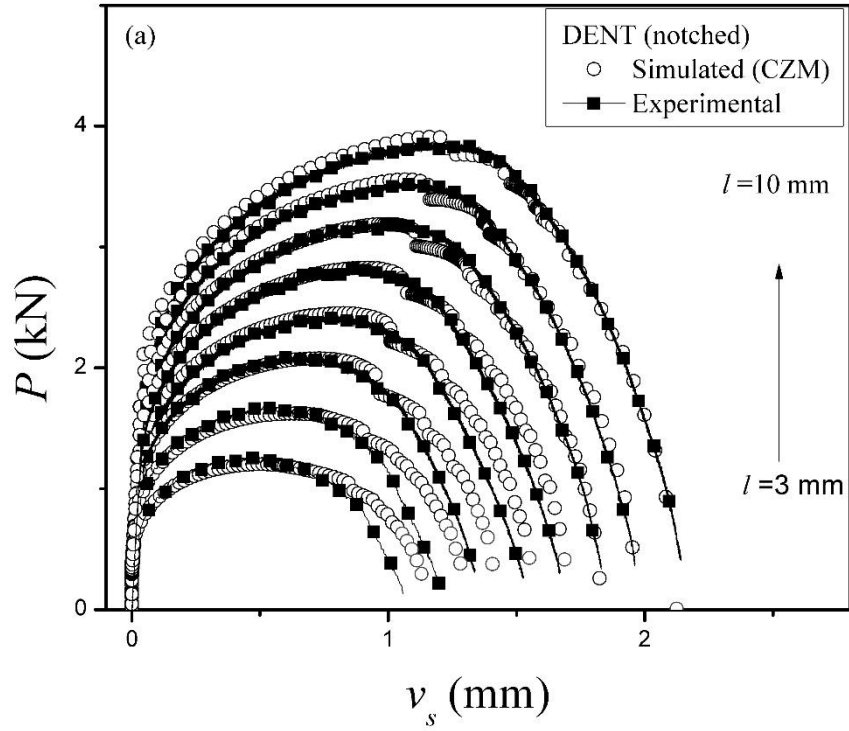
### 9.3 Transferability of CZM parameters

The CZM parameters ( $\Gamma_0 = 300$  kJ.m<sup>-2</sup>,  $\delta_c = 0.66$  mm,  $T_0 = 523$  MPa, and  $\alpha = 1.15$ ; Section 9.2.1) determined from notched ( $\rho = 0.1$  mm) DENT specimen with  $l = 10$  mm. have been used for CZM simulation for extensive crack growth in notched ( $\rho = 0.1$  mm) (i) DENT specimen with  $l = 3 - 10$  mm, and (ii) SENT specimen with  $l = 4 - 15$  mm, tested at a ramp rate 0.006 mm.s<sup>-1</sup>. It was decided to simulate 1 mm thickness of the specimen using 5 layers each of thickness 0.2 mm. The meshing for CZM simulation followed the method described in Section 9.2.1. A single layer of cohesive COH3D8 elements of height 0.01 mm, width (along specimen thickness direction) of 0.2 mm, and length (along crack growth direction) of 1 mm was placed on the crack growth path. The cohesive elements shared nodes with the 3-D solid C3D8R elements with reduced integration used for meshing the rest of the specimen. The C3D8R elements mesh size was  $1 \times 1 \times 0.2$  mm (along the sheet thickness direction), with the exception of two layers, having heights respectively 0.1 mm in the immediate vicinity of the notch and 0.15 mm in the next layer. Other details of meshing may be found in Section 9.2.1. As before, the elastic plastic material property for nominal strain rate  $10^{-4}$  s<sup>-1</sup> (Table 3.1) were ascribed

to the elements, with the assumption that the tensile data were applicable for the entire strain range covered by the simulation. The results from these simulations are compared with the corresponding experimental results in Fig. 9.1(a) for notched DENT specimens and Fig. 9.1(b) for notched SENT specimens respectively.

Similarly, the CZM parameter values determine for fatigue pre-cracked SENT specimen with  $l = 9.58$  mm, viz.,  $T_0 = 448$  MPa and  $\delta_c = 0.34$  mm (i.e.,  $\Gamma_0 = 143$  kJ.m<sup>-2</sup>), and  $\alpha = 1.15$  (Section 9.2.2), have been used to simulate crack growth in fatigue pre-cracked (i) DENT specimens with  $l = 4.33 - 9.58$  mm, and (ii) SENT specimens with  $l = 4.33 - 9.58$  mm, tested at a ramp rate  $0.006$  mm.s<sup>-1</sup>. For FE simulation of fatigue pre-cracked specimens,  $\rho = 0.02$  mm was used (see Sections 5.3.3, 6.3.3.2 and 9.2.2). The meshing strategy was identical to that for the CZM simulations of notched specimens, Figs.9.1(a)-(b). The results for these simulations are compared with the corresponding experimental results in Fig. 9.1(c) for pre-cracked SENT specimens and Fig. 9.1(d) for pre-cracked DENT specimens respectively. The numerically simulated  $P - v_s$  plots for notched as well as pre-cracked DENT and SENT specimens show reasonably satisfactory agreement with the corresponding mechanical test results, Figs. 9.1(a)-(d).

The ability of CZM parameters i) for the notched DENT specimen to simulate crack growth in notched SENT specimens and ii) for the pre-cracked SENT specimen to simulate the crack growth in pre-cracked DENT specimens, establish the transferability of the CZM parameters for given  $\rho$ . That is, at least for the present test material, sheet thickness and notch tip radius  $\rho$ , CZM parameters are material parameters, independent of specimen geometry.



(Continued)

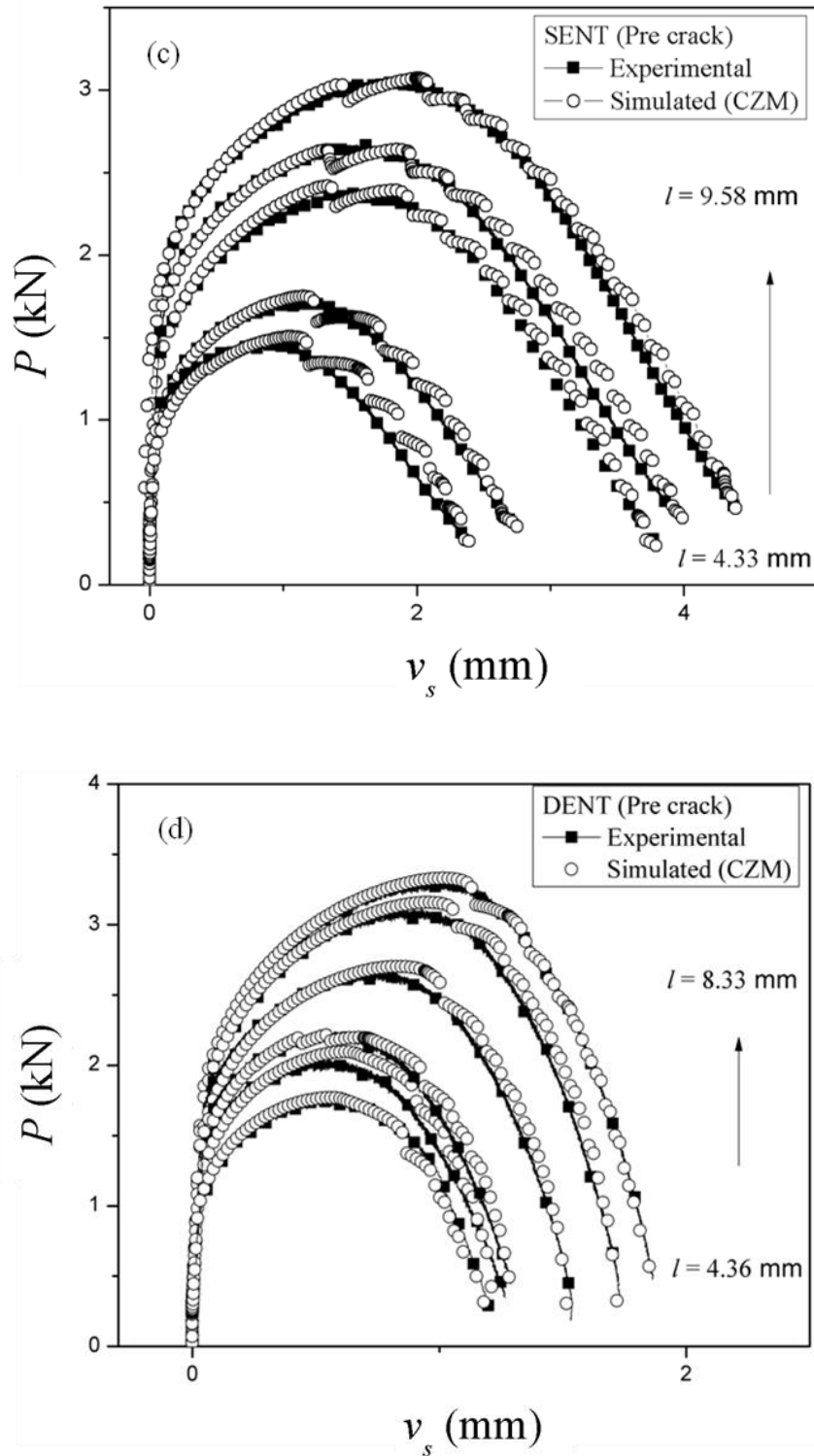


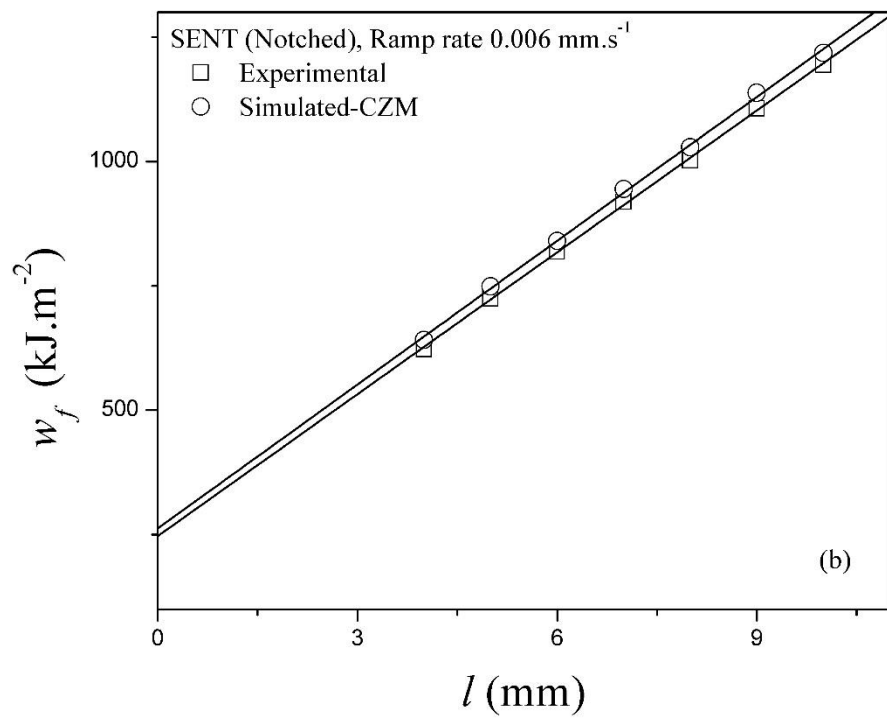
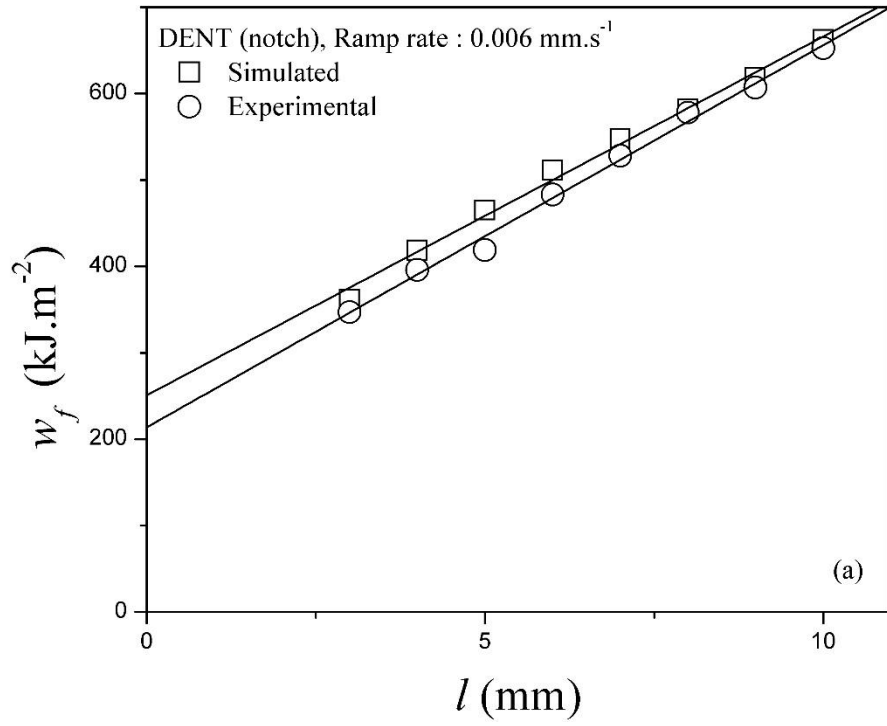
**Figure 9.1:** CZM simulated  $P - v_s$  plots of (a) notched DENT specimens ( $l = 3$ - $10$  mm), (b) notched SENT specimens ( $l = 4$ - $15$  mm), (c) pre-cracked SENT specimens ( $l = 4.33$ - $9.58$  mm), (d) pre-cracked DENT specimens ( $l = 4.36$ - $8.33$  mm), superimposed on the corresponding experimental  $P$ - $v_s$  plots at deformation rate  $0.006 \text{ mm s}^{-1}$ .

## 9.4 Verification of EWF results

The EWF analyses of the simulated  $P - v_s$  plots of the notched as well as pre-cracked DENT and SENT specimens (Figs. 9.1 (a)-(d) with valid ligament lengths within corresponding EWF validity ranges (see Sections 4.3.1.1, 6.3.1.1) were carried out. The  $w_f - l$  and  $v_f - l$  plots are presented in Figs. 9.2 and Figs. 9.3 respectively; the EWF parameters ( $w_e$ ,  $\beta w_p$ ,  $\delta_c^e$  and  $\psi^e$ ) computed from these data showed good correspondence with the results from mechanical test, Table 9.1. The consequence of small mismatch between the simulated and mechanical tested  $P - v_s$  plots at lower ligament lengths, particularly for notched DENT specimens with  $l = 3$  and 4 mm (Fig.9.1(a)), is more significant for the energy based parameters  $w_e$  and  $\beta w_p$  than for the displacement based parameters  $\delta_c^e$  and  $\psi^e$ .

**Table 9.1:** Comparison of EWF results computed using data from mechanical tests and data from CZM simulations

SPECIMN.	Fit to Eq.	$w_f = \beta w_p l + w_e$			$v_f = (\psi^e/2)l + \delta_c^e$		
	$P - v_s$ data from	$R^2$	$\beta w_p$ (MJ.m <sup>-3</sup> )	$w_e$ (kJ/m <sup>2</sup> )	$R^2$	$\psi^e$	$\delta_c^e$ (mm)
DENT Notched	Mech. test	0.997	44.26	213.62	0.990	17.71°	0.58
	CZM model	0.994	41.6	250.2	0.990	17.76°	0.576
DENT Pre-cracked	Mech. test	0.997	51.83	132.7	0.967	17.99°	0.487
	CZM model	0.994	52.6	120.6	0.97	18.02°	0.463
	Fit to Eq.	$w_f = \beta w_p l + w_e$			$v_f = \psi^e l + \delta_c^e$		
SENT Notched	Mech. test	0.999	95.06	247.05	0.999	18.9°	1.27
	CZM model	0.998	96.36	262.5	0.988	19.48°	1.13
SENT Pre-cracked	Mech. test	0.995	87.03	133.3	0.999	18.67°	1.12
	CZM model	0.995	87.1	119.08	0.998	18.68°	1.1



(Continued)

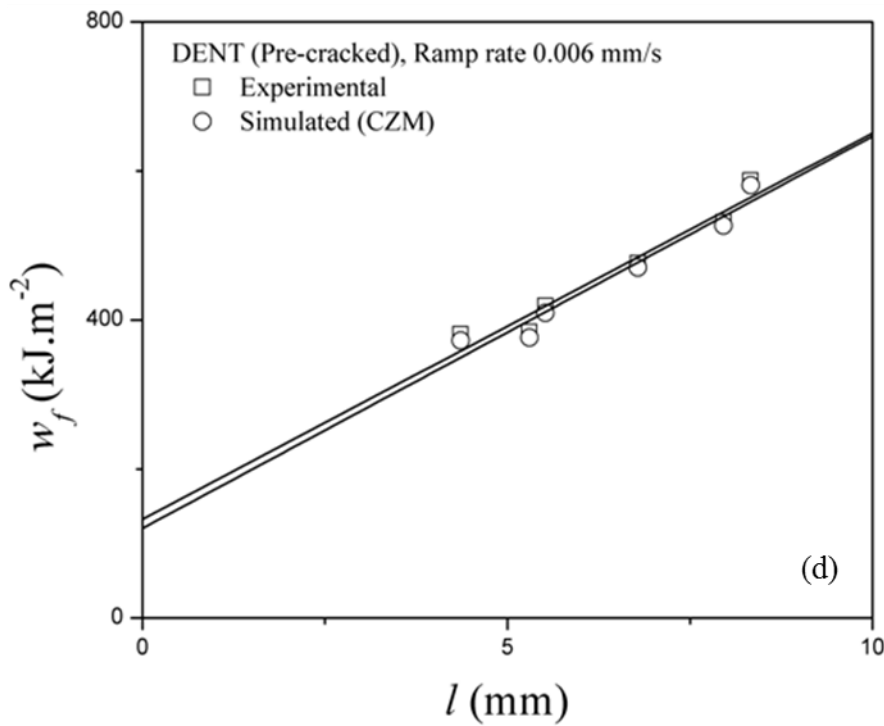
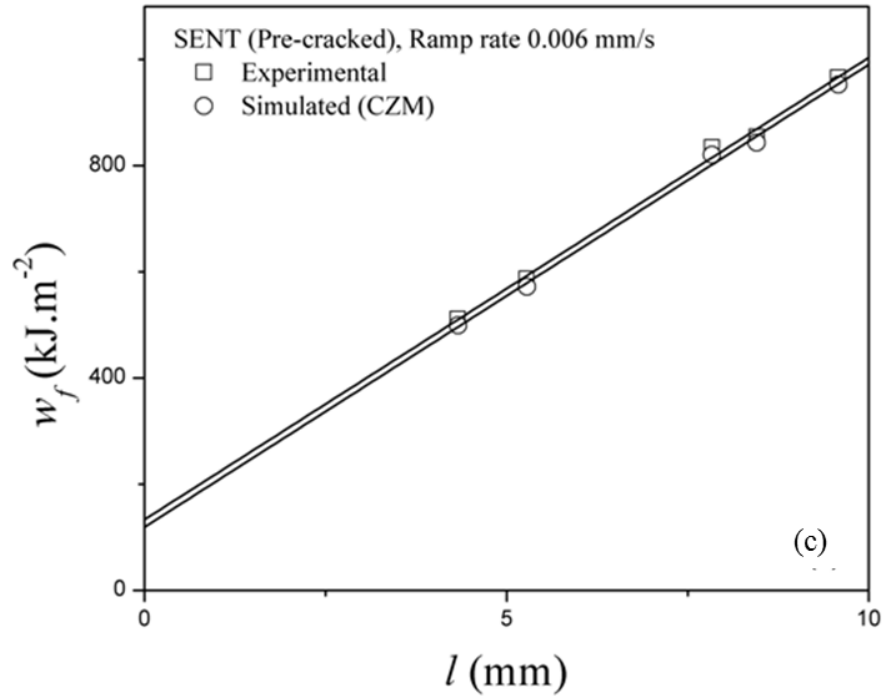
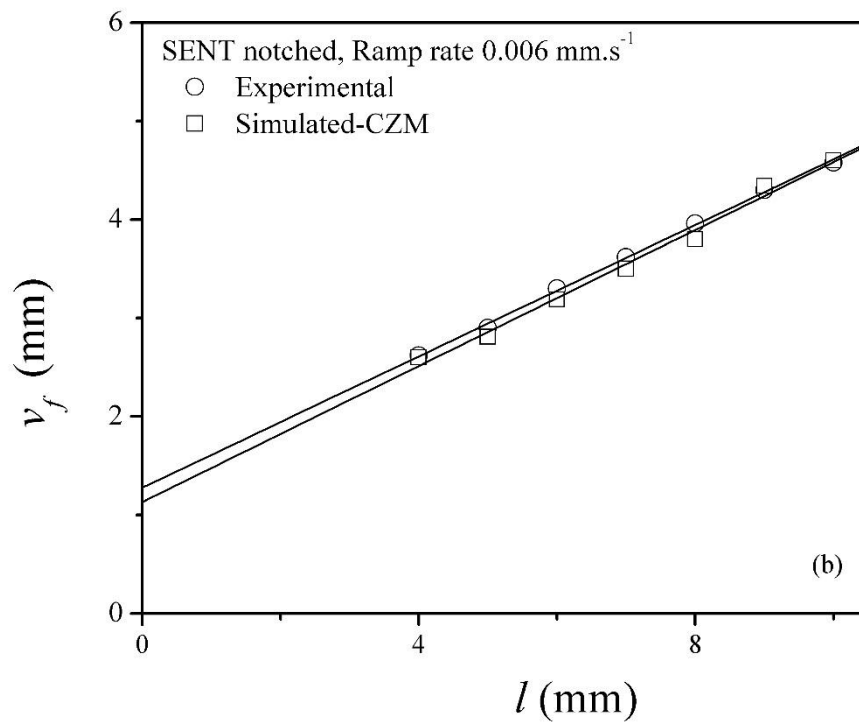
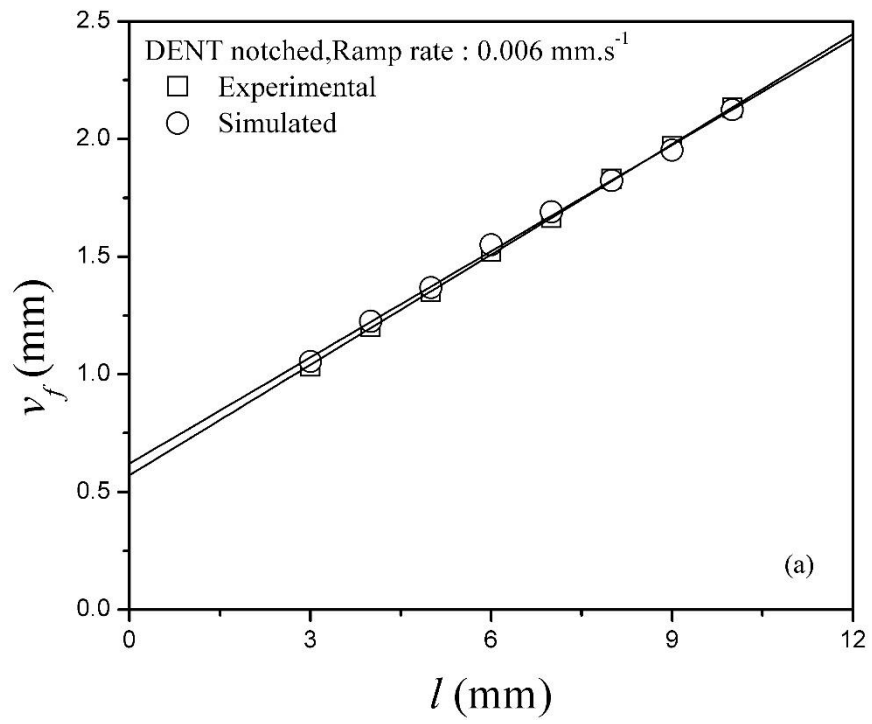


**Figure 9.2:** Comparison of CZM simulated and experimental  $w_f$ - $l$  plots for (a) notched ( $\rho = 0.1$  mm) DENT specimens; (b) notched ( $\rho = 0.1$  mm) SENT specimens; (c) pre-cracked SENT specimens; and (d) pre-cracked DENT specimens. (Ramp rate  $0.006 \text{ mm.s}^{-1}$ ).





(Continued)

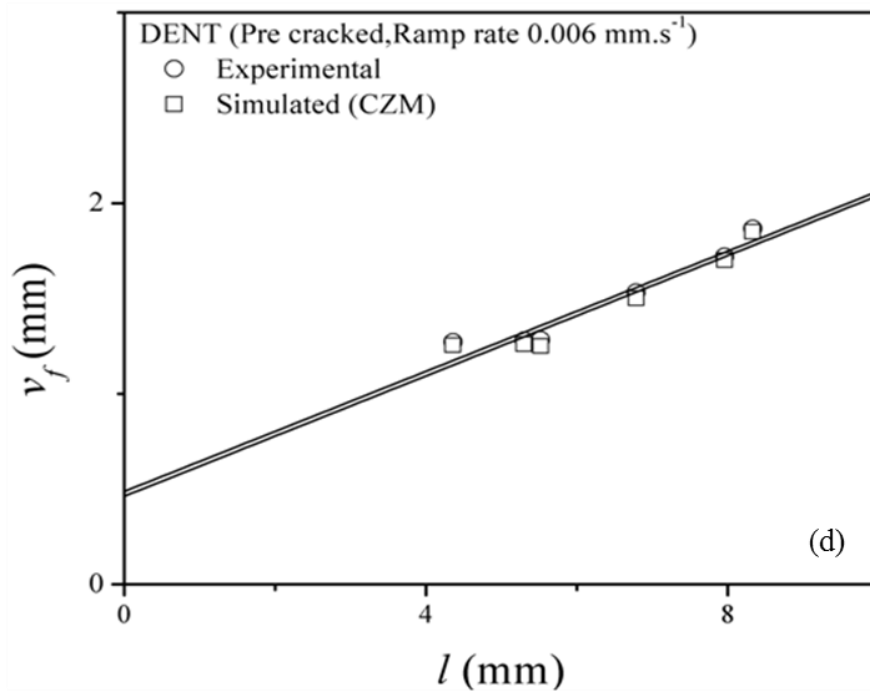
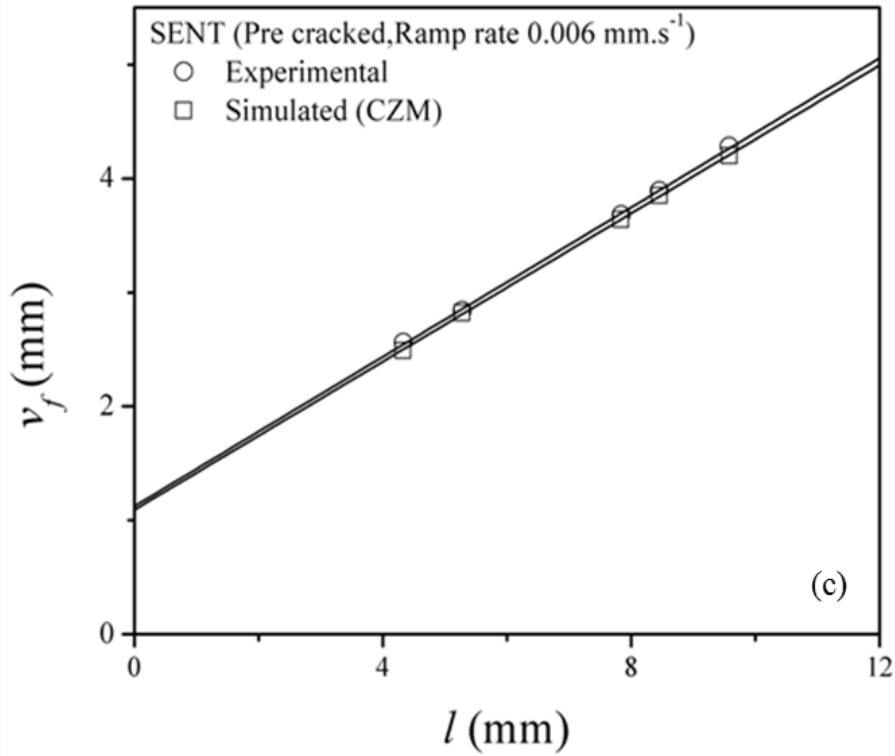


**Figure 9.3:** Comparison of CZM simulated and experimental  $v_f$ - $l$  plots for (a) notched ( $\rho = 0.1 \text{ mm}$ ) DENT specimens; (b) notched ( $\rho = 0.1 \text{ mm}$ ) SENT specimens; (c) pre-cracked SENT specimens; and (d) pre-cracked DENT specimens. (Ramp rate  $0.006 \text{ mm.s}^{-1}$ ).

## 9.5 CZM simulation for $\varphi(\delta_5) - \Delta a$ and $\varphi - \Delta a$ plots for pre-cracked specimens

The critical CTOA,  $\varphi_c$ , and  $\delta_5 - \Delta a$  plots have been determined using SENT and DENT specimens of the present test material, following the test procedure described in Section 3.2.4. In this section, an attempt has been made to generate some of these results by employing 3-D CZM simulation of two specimens investigated in Chapter 7, namely a pre-cracked SENT specimen ( $l = 23.98$  mm), and a pre-cracked DENT specimen ( $l = 19.41$  mm). The ramp rate was  $0.006$  mm.s<sup>-1</sup>. For these simulations, the CZM parameters used are those determined in Section 9.2.2 for a fatigue pre-cracked SENT specimen ( $l = 9.58$  mm), viz.  $T_0 = 484$  MPa,  $\delta_c = 0.34$  mm,  $\Gamma_0 = 143$  kJ.m<sup>-2</sup> and  $\alpha = 1.15$ . The FE meshing was similar to those for pre-cracked specimens described in Sections 9.2.2, 9.3: a single layer of cohesive COH3D8 elements of height 0.01 mm on the crack path sharing nodes with the 3-D solid C3D8R elements with reduced integration used for meshing the rest of the specimen. In addition, two points were marked on the specimen surface ( $z = t$ ) 2.5 mm above and below the initial crack tip in the undeformed FE mesh. The  $\delta_5 - \Delta a$  plot from CZM simulation simply means determining from the simulation data the separation of this point pair as a function of crack length increment ( $\Delta a$ ). The numerically simulated  $P - v_s$  curves for both the specimens show reasonably good agreement with the loading segments of the corresponding plots from mechanical tests comprising load-relax-unload cycles (see Section 3.2.4), Fig. 9.4. This again confirms that CZM parameters are independent of specimen geometry.

For the pre-cracked SENT specimen, the  $\delta_5 - \Delta a$  curve determined by CZM simulation is shown in Fig. 9.5(a); and the corresponding  $\varphi(\delta_5) - \Delta a$  curve determined using the equation  $\varphi(\delta_5) = \Delta\delta_5/\Delta a$ , Eq. (7.2), is shown in Fig. 9.5(b). The estimate for the critical CTOA regime in Fig. 9.5(b) corresponds to an approximation where variation of  $\varphi(\delta_5)$  is small for a reasonably large range of  $\Delta a$ . The results in Figs. 9.5(a) and 9.5(b) show that CZM simulations can successfully substitute for experimental measurements of  $\delta_5$ , and therefore  $\varphi(\delta_5)$ , for the present test material.

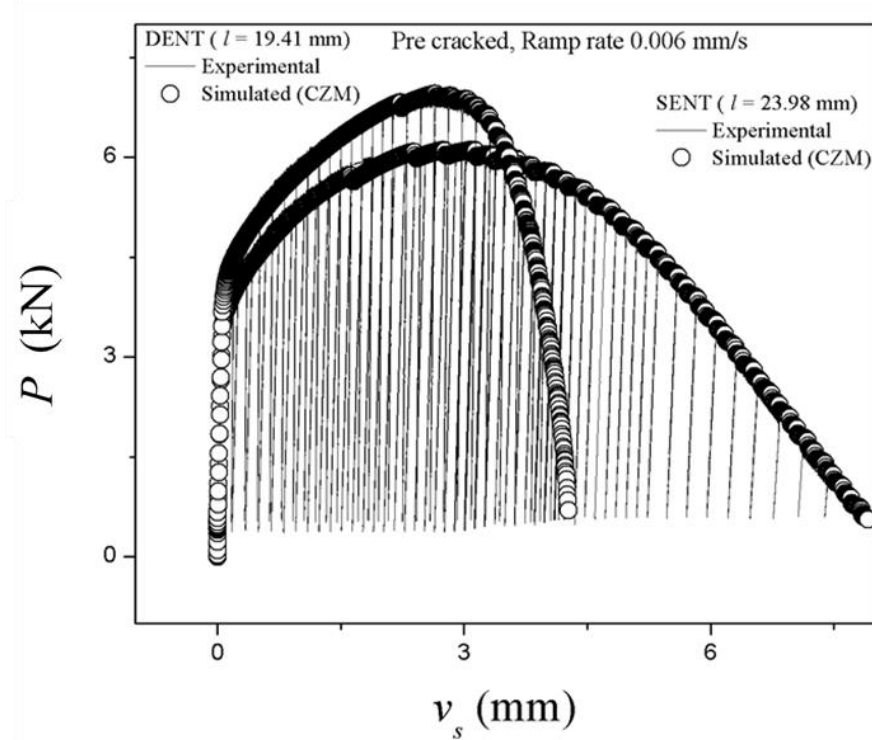


**Figure 9.4:**  $P - v_s$  plots for pre-cracked SENT ( $l = 23.98$  mm) and DENT ( $l = 19.41$  mm) specimens from mechanical tests and CZM simulations. (Ramp rate  $0.006 \text{ mm}\cdot\text{s}^{-1}$ ).

CTOA,  $\varphi$ , values from CZM simulation were determined using the four point method (Section 7.2.2) with measurement basis  $L = 1$  mm, placing these four points on the specimen surface ( $z = t$ ), and measuring the corresponding displacements from the simulation data. Results from such analyses for a pre-cracked SENT specimen ( $l = 23.98$  mm), and also a pre-cracked DENT specimen ( $l = 19.41$  mm) (using identical set of CZM parameters) are presented in Figs. 9.6(a) and 9.6(b). The CZM simulated  $\varphi - \Delta a$  curves were in good agreement with the corresponding optical experimental data reported in Chapter 7.

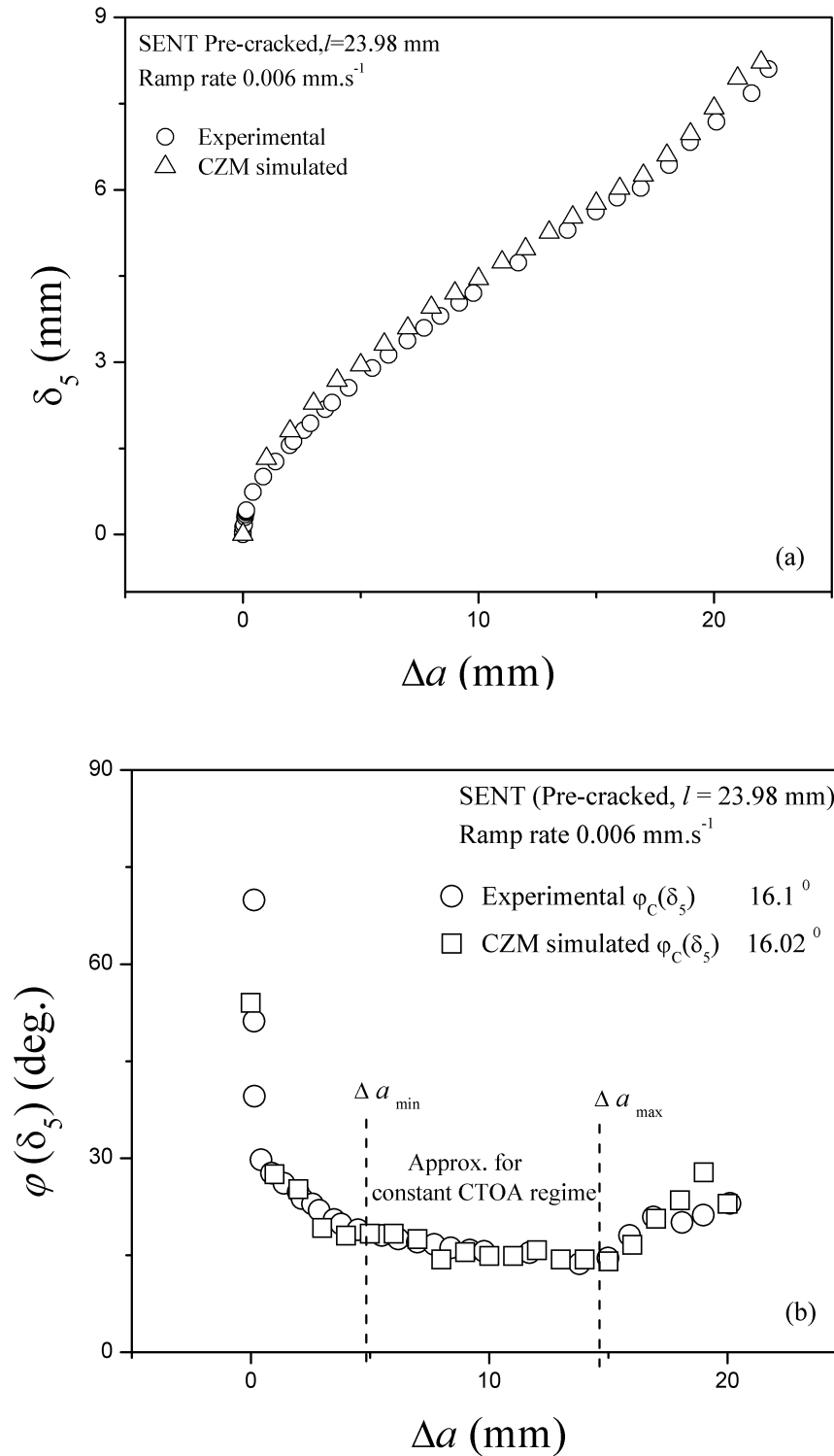


**Figure 9.5:** Comparison of experimental and CZM simulated (a)  $\delta_5 - \Delta a$  and (b)  $\varphi(\delta_5) - \Delta a$  curves. (Experimental data from Figs. 7.6(a) and 7.6(b)).

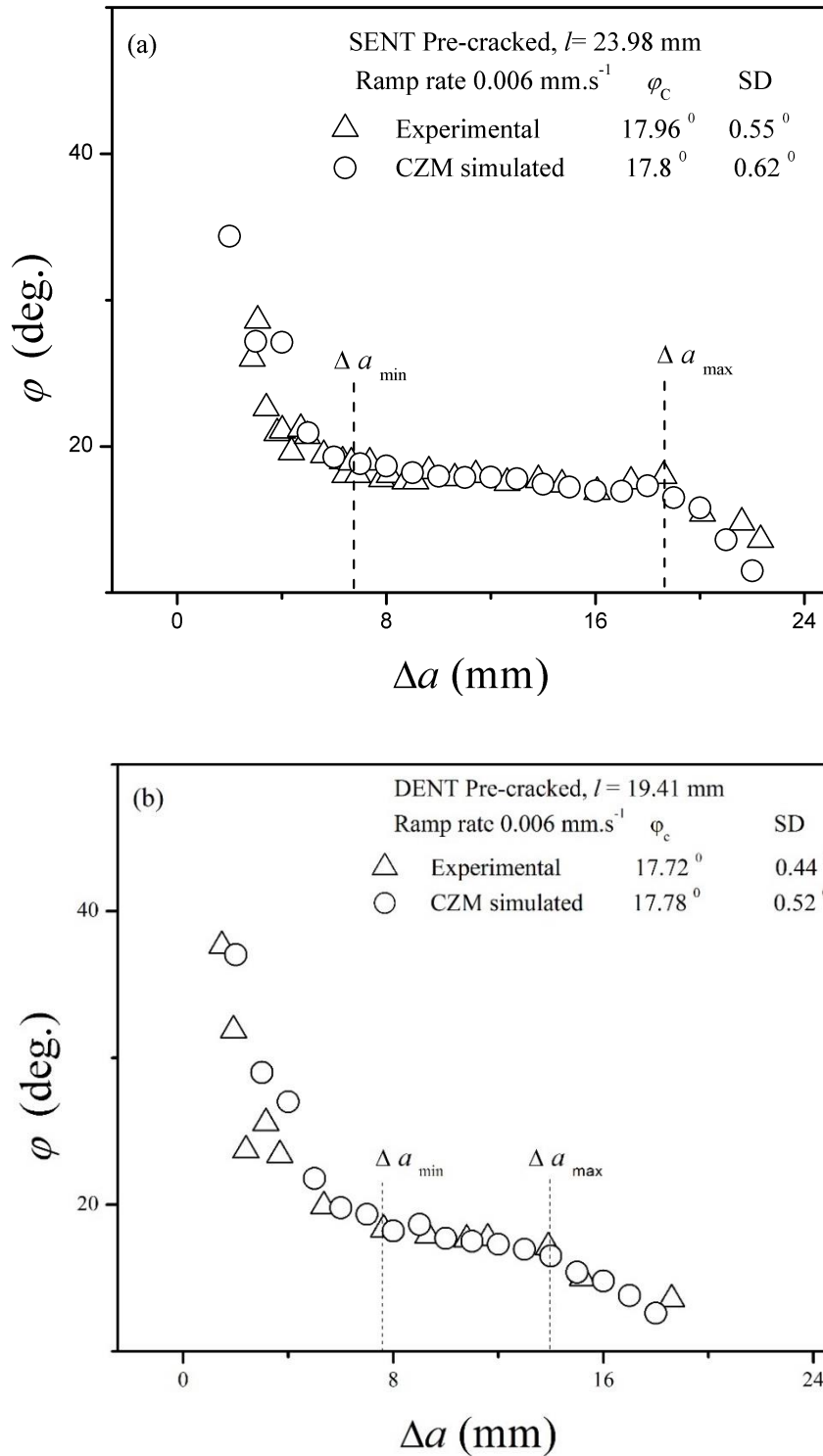


**Figure 9.6:** Comparison of  $\phi - \Delta a$  curves using data from mechanical tests (2-point method) and from CZM simulation (4-point method) for (a) SENT and (b) DENT specimens. (SENT specimen data by 2-point optical method from Fig.6.7; DENT specimen data from Fig 4.10).

## 9.6 Effect of crack tunneling on $\varphi - \Delta a$ curves

Scanning electron microscopic studies (Sections 4.3.2 and 5.3.2) of fractured specimens had shown predominantly flat fracture with very limited tunneling. In order to assess the effect of tunneling on the CTOA values, the CZM simulation of the pre-cracked SENT specimen with  $l = 23.98$  mm was carried out following the method in Section 9.2.2, but with cohesive COH3D8 element size  $0.1 \times 0.1 \times 0.01$  mm (i.e., 10 layers) and C3D8R solid elements of size 0.1 mm in the sheet thickness direction, with in plane size  $0.05 \times 0.05$  around the notch gradually increasing to  $0.1 \times 0.1$  mm away from the notch. The CZM simulated  $\varphi - \Delta a$  curves for this SENT specimen calculated for the free surface ( $z = t$ ), at the mid-plane ( $z = t/2$ ) and at a nearby plane ( $z = 2t/5$ ) are shown in Fig. 9.7. The  $\varphi - \Delta a$  plots for surface and mid-section show the expected opposite curvatures in the initial transient regime (cf. [33]), and the length of this regime is found to be  $\Delta a \approx 6t$ , similar to the initial transient regime measured by optical method for pre-cracked specimens, see e.g., Fig. 7.5. It is interesting to note, however, that in the initial transient regime in Fig. 9.7, the  $\varphi - \Delta a$  plot for  $z = 2t/5$  is very similar to that for the surface,  $z = t$ , even though the  $z = 2t/5$  plane is actually closer to the mid-plane with the highest constraint. This may be attributed to the very limited crack tip tunneling in the present specimen.

A more thorough examination of the CZM simulated  $P - v_s$  plot for this specimen (using the meshing strategy as adopted for the results in Fig. 9.7) shown in Fig. 9.8, with details shown in the inset, proves interesting. The details show that the crack initiated at the mid-section (point 'b' corresponding to the highest constraint) and subsequently the surface crack appeared (point 'c'; corresponding to the lowest constraint). The crack initiation point determined from 3-D FE simulations for non-growing crack (Sections 4.3.4.1, 5.3.2, 6.3.3.1 and 6.3.3.2) is actually an averaged value, that falls between the points 'b' and 'c'. Also, in the present test, the surface crack initiation point determined experimentally by taking successive photographs (point 'd') clearly overshoot the crack initiation point identified by FE computations.

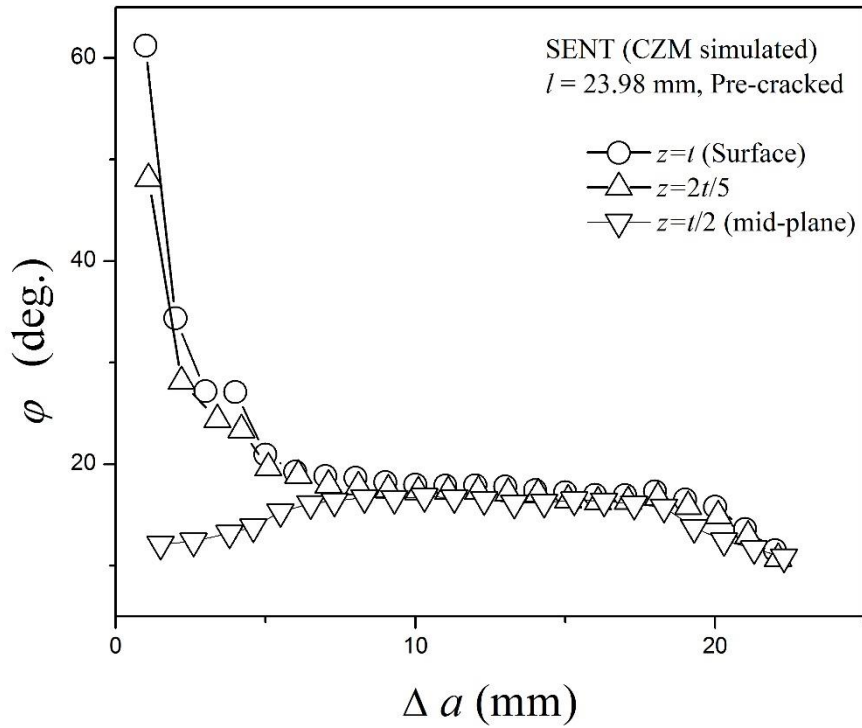


**Figure 9.7:** Effect of crack tunneling on  $\varphi - \Delta a$  curves

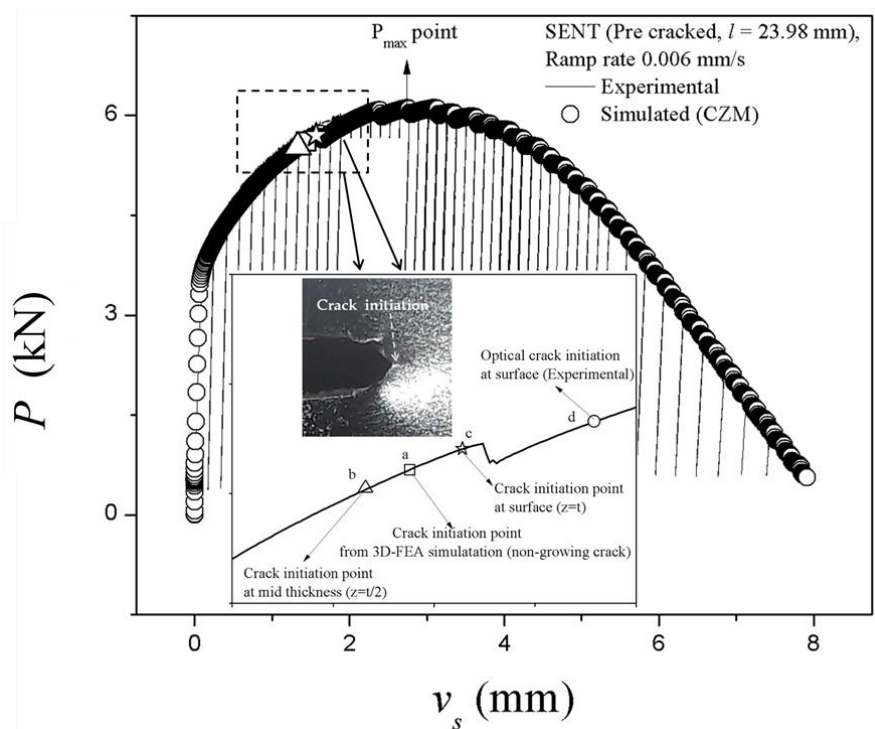


**Figure 9.8:** The crack initiation point (through thickness and on the surface) determined from the CZM model, and from surface photography.



The method of determining the crack initiation point used in the present study (Sections 4.3.4.1, 5.3.2, 6.3.3.1 and 6.3.3.2) does not remove the subjectivity of the conventional crack initiation determination methods e.g., surface detection of crack initiation with videography [2]. However it appears to be a better method as it is less susceptible to crack tip tunneling.

## 9.7 Simulation of dissipation energy rate ( $R$ ) resistance curve

Brocks and Siegmund [77] had used a two parameter CZM simulation for determining dissipation rates for a 1 mm thick and 508 mm wide centre cracked Al panel (Al 2024 T3) with different initial  $a/W$  ratios. In this section, the three parameters cohesive PPR model [118, 119], has been used to simulate the  $R - \Delta a$  curves for both pre-cracked SENT and DENT specimens. For this, the  $P - v_s$  data from CZM simulation presented in Fig. 9.4 have been analysed according to Method 1 as presented in Section 8.3.1. However, unlike the experimental data, the CZM simulated data did not have the unloading segments which are necessary for computing the  $\delta U_{diss}$  values (see Fig. 8.1). Therefore, for each of the two specimens, the values of elastic compliance computed for each unload from the  $P - v_s$  data from mechanical test, and the corresponding optically measured crack length, were used to generate the table of unloading compliance versus crack length. The crack length data from the CZM simulation was then used to determine the corresponding unloading compliance by interpolation from the table. With the unloading lines thus computed, it became possible to complete the computations following Method 1. An alternative method to achieve the objective would be to introduce cycles of load-unload in the CZM simulation itself; since rate-independent material model is used in FE simulation adopted, it is not possible to introduce the relaxation step.

With these unloading lines available, the computation follows the Method 1 in Section 8.3.1. Figure 9.9 compares the  $R - \Delta a$  curves from CZM simulations with the corresponding experimental curves; clearly the agreement for either of these specimens is quite satisfactory. Specifically for the SENT specimen,  $R_\infty$  values determined were  $1550 \text{ kJ.m}^{-2}$  by CZM simulation and  $1578 \text{ kJ.m}^{-2}$  from mechanical

test data. For the DENT specimen, the corresponding figures were  $1093 \text{ kJ.m}^{-2}$  and  $1104 \text{ kJ.m}^{-2}$  respectively. The close agreements, within 1.8% for the SENT specimen and 1% for the DENT specimen show that the CZM simulation can very well be adopted for generating  $R - \Delta a$  curves. Also, the cohesive energy  $\Gamma_0$ , is only about 9% of the  $R_\infty$  for the SENT specimens and 12% of  $R_\infty$  for the DENT specimens, Fig. 9.9. This confirms that for the present sheet material, most of the energy dissipated is for the plastic deformation process, and therefore  $R_\infty$  depends on specimen geometry, and also choosing  $\Gamma_0$  as a ( $\rho$ -dependent) material parameter for integrity assessment purposes will be unduly conservative.

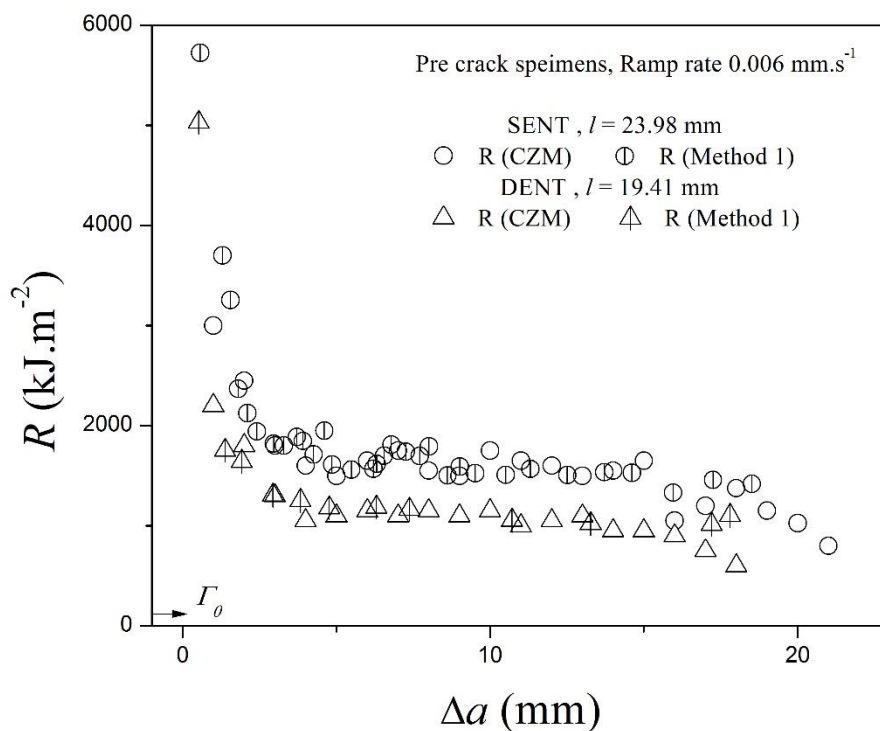


**Figure 9.9:** Comparison of  $R - \Delta a$  curves for pre-cracked SENT and DENT specimens from experiments and CZM simulations. (Data for experiments from Fig. 8.2).

## 9.8 Conclusions

1. For the present test material which undergoes flat fracture, the 3-parameter mode I cohesive zone model given by Eq. (9.2) proved reasonably successful in describing the crack growth behavior. Results showed that at least for the

present test material, sheet thickness and notch tip radius  $\rho$ , CZM parameters are transferable between SENT and DENT specimen geometries.

2. Using CZM simulations, it was possible to derive values for EWF parameters for notched and pre-cracked DENT and SENT specimens matching with those determined from experiments. By simulating crack growth using CZM, it was possible to simulate some  $\varphi(\delta_5) - \Delta a$ ,  $R - \Delta a$  and  $\varphi - \Delta a$  curves in good agreement with the corresponding experimental plots, and also to assess the effects of tunneling, all without the need of laborious measurements from photographs. These encouraging results from essentially exploratory studies suggest that more extensive researches in these directions should be undertaken.
3. These successes notwithstanding, as remarked in the context of Figs. 9.1(a)-(d), the best method for tuning CZM deserves a critical examination.
4. The demonstrated preliminary successes of CZM simulation for the present flat fracture material is an encouragement for undertaking CZM simulation for the more difficult problem of crack growth in other automotive grade steel sheets, such as the dual phase (DP) grades, that undergo transition from flat to predominately shear mode during crack growth.



### 10.1 Thesis conclusions

The present research is aimed at a comprehensive characterization of crack initiation and growth in a 1 mm thick interstitial-free (IF) automotive grade steel sheet. This steel has a high strain hardening index  $n = 0.24$  (Table 3.1), and shows flat fracture with 36% necking (Fig. 4.6). The test variables are **(i)** specimen geometry (DENT and SENT specimens, clamped on both edges), with width  $W = 30$  mm, (Fig. 3.1), **(ii)** notch acuity (specimens with notch tip radius  $\rho = 0.1$  mm or with fatigue pre-cracks), **(iii)** specimen ligament length, and **(iv)** quasi-static ramp rate. The basic ramp rate for the tests was  $0.006 \text{ mm.s}^{-1}$ ; additional tests at ramp rates  $0.06$  and  $0.6 \text{ mm.s}^{-1}$  were carried out when examining the effect of quasi-static ramp rates on a parameter. Section 1.3 identified some key issues to be addressed in the course of this research. Chapters 3 - 9 presented the details of the experimental and computational methods adopted, the results obtained and the conclusions drawn. In this section the main results are briefly recounted.

The crack initiation parameters considered are  $\delta_c$ ,  $w_i$  and  $J_c$ . For plasticity dominated deformation in highly ductile sheet metals,  $w_i$  nearly equals its plastic component, and similarly,  $J_c \cong J_p^c$ . A new method has been devised for detecting the crack initiation event in a ramp loaded specimens (Issue # 2, Section 1.3) by comparing the  $P - v_s$  plot from mechanical tests with the corresponding  $P - v_s$  plot from 3-D rate independent large strain FE simulation for non-growing crack (Sections 4.3.4, 6.3.3). This method is more objective compared to the other methods based on visually detecting crack initiation on the specimen surface, and also less susceptible to crack tip tunnelling (Section 9.5.1). Then  $\delta_c$  (as defined in Section 4.3.4.2) is determined from the deformed FE mesh at this initiation point (cf. Figs. 4.13, 6.10), and (the plastic component of)  $w_i$  is determined from the  $P -$

$v_s$  plot (cf. Figs. 6.9 and 6.14). For determining  $J_p^c$  for SENT sheet specimens, it was also necessary to determine  $\eta_p$  for these specimens (Issue # 3, Section 1.3). Table 5.1 records the  $\eta_p$  values for  $0.2 \leq a/W \leq 0.9$  computed from different  $P - v_s$  data sets; a mean  $\eta_p$  value of 0.81 ( $\pm 7\%$ ) may be considered for the entire  $a/W$  range. Also,  $\eta_p$  thus determined has been validated for one specimen by FE simulation that computes  $J$ -integral invoking its fundamental path independent line integral definition. For either notched or fatigue precracked specimens with  $l$  in EWF validity range or even higher, the parameters  $w_{ie}$ ,  $J_p^c$  and  $\delta_c$  can be considered as material parameters, independent of specimen geometry, DENT or SENT (Sections 6.3.3.1 and 6.3.3.2). Only, compared to the notched specimens, fatigue pre-cracking reduced  $w_{ie}$  by  $\sim 44\%$ , mean  $J_p^c$  by  $\sim 40\%$  and mean  $\delta_c$  by  $\sim 50\%$ .

The crack growth parameters examined are the CTOA ( $\varphi$ ) and its critical value for stable crack growth ( $\varphi_c$ ), the  $\delta_5$  parameter, and also the energy dissipation rate parameter ( $R$ ) and its critical value ( $R_\infty$ ). Test procedures have been devised in the course of the present research for optical measurements of  $\varphi - \Delta a$  plots and  $\delta_5 - \Delta a$  plots with DENT or SENT specimens (Section 3.2.4). It is also shown (Section 8.3.1) that the  $P - v_s - \Delta a$  data set generated in the process of determining  $\varphi - \Delta a$  plot (by the test method in Section 3.2.4) can be analysed for deriving the corresponding  $R - \Delta a$  plot, and hence for determining  $R_\infty$ .  $\varphi_c$  determined from the  $\varphi - \Delta a$  plot is identified as a material property, independent of specimen geometry (Section 6.3.2) or initial ligament length (Fig. 7.5).  $\varphi_c$  is also independent of specimen notch tip radius: only, the initial transient regime of crack growth increases with increasing notch tip radius (e.g., Fig. 7.4). Crack growth may also be characterized by  $\delta_5 - \Delta a$  plot and hence  $\varphi(\delta_5) - \Delta a$  plots (cf. Eq. (7.2)). However,  $\varphi(\delta_5)$  is only an approximation of  $\varphi$ ; this results in mismatch between  $\varphi_c$  and  $\varphi_c(\delta_5)$  (cf. Table 7.1). Similar to  $\varphi_c$ ,  $R_\infty$  is also independent of specimen notch tip radius: here too, the initial transient regime of crack growth increases with increasing notch tip radius. For fatigue pre-cracked SENT or DENT specimens, for increase in ramp rate from 0.006 to 0.6 mm.s<sup>-1</sup>,  $\varphi_c$  was practically constant (Tables 4.3 and 6.4 respectively for pre-cracked DENT and SENT specimens), whereas  $R_\infty$  increased by about 8% (Table 8.2). A new method has been proposed (Section 8.3.2) for

directly determining  $R_\infty$  from the slope of the linear least square fit of crack growth energy  $W^{gr}/t$  with ligament length  $l$ , Figs.8.8(a) and 8.8(b). An attempt at normalizing  $R$  in order to obtain normalized dissipation energy that would be independent of specimen geometry was only partially successful (Section 8.3.3).

EWF testing and analysis procedures originally proposed with DENT specimens (Section 2.6) and adopted with the present test material (Chapter 4), can very well be adopted with SENT specimens as well, but with a modified  $v_f$ - $l$  equation, Eq. (6.1), (Issue # 1, Section 1.3). It was confirmed that with the testing method given in Section 3.2.2, the EWF parameters can be determined using actuator displacement data with either specimen geometry (Tables 4.11 and 6.1). For identifying the  $l$ -validity range for EWF analysis with notched or pre-cracked specimens, the proposed new criteria  $\sigma_n \cong 1.15\sigma_u$  for the DENT specimens and  $\sigma_n \cong \sigma_u$  for the SENT specimens proved efficacious (Sections 4.3.1.1 and 6.3.1.1).  $w_e$  determined using fatigue pre-cracked DENT and SENT specimens proved to be a specimen geometry independent material parameter (Table 6.2). In contrast,  $\delta_c^e$  value for pre-cracked SENT specimens proved to be about 2.3 times the  $\delta_c^e$  value for DENT specimens (Table 6.3); this has been tentatively ascribed to the difference in the effects of crack growth in the mixed stress zone for these two specimen geometries (Section 6.3.3.1; Eq. (6.5)). Similar to  $\varphi_c$ ,  $\psi^e$  also proved to be essentially independent of specimen geometry, notch tip radius (at least up to  $\rho = 0.1$  mm) and quasi-static ramp rate in the range 0.006 to 0.6 mm.s<sup>-1</sup>. In fact, for the three quasi-static ramp rates, the maximum difference between  $\varphi_c$  values (determined using pre-cracked specimens) and  $\psi^e$  values (determined using notched specimens) was as small as 4% for the DENT specimens (Table 4.3) and 6% for the SENT specimens (Table 6.4). Further, for both these cases, the agreement between  $\varphi_c$  and  $\psi^e$  improved with  $\psi^e$  being computed using data sets with minimum value of  $l$  set equal to the value of  $\Delta a$  for the initial transient regime in the  $\varphi - \Delta a$  plot. Similarly, agreement between  $R_\infty$  determined from the  $R - \Delta a$  plot (Section 8.3.1) and from the linear fit of  $W^{gr}/t - l$  data (Section 8.3.2) improved, when the lower bound of  $l$  in the  $W^{gr}/t - l$  data set was increased to be more consistent with the value of  $\Delta a$  for the initial transient regime, cf. Table 8.1. The results thus show that  $\psi^e$  determined by the simple EWF testing of notched

DENT or SENT specimens (with judiciously chosen ligament lengths) can very well represent with sufficient accuracy  $\varphi_c$  determined from a more elaborate and time consuming test, (Issue # 5, Section 1.3).

For the notched SENT specimens, with  $l$  corresponding to the initial mixed stress regime, linear extrapolations to  $l = 0$  (i) of the  $w_f - l$  data yielded the parameter  $w_e^m$ ; and (ii) of the  $w_i - l$  data yielded the parameter  $w_i^m$ , Fig. 6.13(a).  $w_e^m$  and  $w_i^m$  values were within 3%. Similarly, the parameter  $\delta_c^{e,m}$  by linear extrapolation of mixed stress regime  $v_f - l$  data to  $l = 0$  was within  $\sim 1.6\%$  of the ordinate offset computed by linear extrapolation of mixed stress regime  $\delta_c - l$  data, Fig. 6.13(b). The choice of linear relations for these extrapolations was empirical. The four parameters determined from extrapolation to  $l = 0$  correspond to the highest possible constraint for the given sheet material and thickness (Issue # 1, Section 1.3).

For the present test sheet material, the 3-parameter Mode I CZM given by Eq. (9.2) proved reasonably successful in describing the crack growth behavior in notched or fatigue pre-cracked DENT or SENT specimens. For given notch tip radius  $\rho$ , the parameters of the model can be taken to be material parameters, independent of specimen geometry, Figs 9.1(a)-(d). By simulating crack growth using CZM simulations, it was possible to (i) derive values for EWF parameters for notched and pre-cracked DENT and SENT specimens, matching with those determined from experiments, Table 9.1; (ii) simulate for one each of pre-cracked SENT and DENT specimens,  $\varphi(\delta_5) - \Delta a$ ,  $\varphi - \Delta a$  and  $R - \Delta a$  plots which were in good agreement with the corresponding experimentally derived plots; and (iii) assess the effects of crack tunneling; (Issue # 6, Section 1.3). These results from an preliminary exploratory study are sufficiently encouraging for more extensive research in this direction.

## 10.2 Recommendations

A perusal of the conclusions presented above provides some guidelines for planning tests on other automotive grade and similar steel sheets for specific requirements.



1. For the EWF tests carried out following the prescription of Section 3.2.2, an extensometer is not necessary - actuator displacement very well serves the purpose.
2. For determining the valid  $l$ - range for EWF test data, the linearity of  $w_f - l$  and  $v_f - l$  plots and also the variation of  $\sigma_n$  with  $l$  should be checked. A (nearly) constant  $\sigma_n$  over a range of  $l$  appears to be a good indicator for this range.
3. For potential application in integrity assessment, initiation parameters  $w_{ie}$ ,  $\delta_C$  or  $J_p^c$  are to be determined using fatigue pre-cracked specimens. In this case,
  - (a) SENT specimens are for choice, because compared to DENT specimens, SENT specimens are considerably easier to fatigue pre-crack.
  - (b) Only, for determining  $J_p^c$  with SENT specimens, it is also necessary to determine  $\eta_p$  value(s) applicable for the specific sheet metal with the given thickness, following the guidelines of Chapter 5.
  - (c) For determining these crack initiation parameters, it is necessary to determine the crack initiation points. As of now, the method adopted in this research, though computation intensive, appears to be the best choice.
4. For the purposes of material qualification or quality control on the other hand, it should be adequate to determine  $w_e$  with notched specimens with  $\rho$  fixed at a small value (such as 0.1 mm for the present specimens). Since pre-cracking is not involved, either DENT or SENT specimens may be chosen for these tests. For potential application in integrity assessment,  $w_e$  should be determined with fatigue pre-cracked specimens, because this has been shown to be independent of test specimen geometry.
5. Notched specimens can be used for determining the crack growth parameters ( $\psi^e$ ,  $\varphi_c$ ,  $\delta_5$  or  $R$ ) either for material qualification, or for potential application in integrity assessment. Of these parameters,  $\psi^e$  determined using notched specimens with relatively high  $l$  values closer to  $l_{max}$  (preferably higher than the initial transition regime of crack extension) recommends because **(i)** it can be determined easily, and **(ii)** it is a sufficiently accurate measure for  $\varphi_c$ . Also

for determining  $R_\infty$  from the linear fit of  $W^{gr}/t - l$  data (Section 8.3.2) it appears preferable to use specimens with higher width  $W$  (such as 48 mm as used by [41] )

6.  $\varphi - \Delta a$  plots and  $\delta_5 - \Delta a$  plots can be derived using notched DENT or SENT specimens following the optical method described in Section 3.2.4; also the  $P - v_s - \Delta a$  data set generated in the process of determining  $\varphi - \Delta a$  plot by the prescribed method can be used to compute the  $R - \Delta a$ . Either DENT or SENT specimens may be used for these tests, though the test with SENT specimens has the advantage of reduced experimental burden because there is only one crack to consider.

### 10.3 Suggestions for future research

The scope of the results presented in this thesis for the chosen test material (showing flat fracture) is comprehensive enough to consider extending the present study to other grades of ductile steel sheets, particularly those showing predominately slant fracture. Also in the course of the present study, a few issues have emerged for further studies. The areas deserving further research are indicated below.

1. There is a need to search for a method for identifying crack initiation which is adequately objective, but avoids the extensive FE computations that are necessary for the method developed in the course of the present study (Sections 4.3.4, 6.3.3).
2. Figures 6.13(a)-(b) show linear extrapolations of **(i)**  $w_f$  and  $w_i$  data and **(ii)**  $v_f$  and  $\delta_c$  data (for notched SENT specimens in the initial mixed stress regime) to  $l = 0$  respectively. The values of  $w_e^m$  and  $w_i^e$  were very similar, and so were the values of  $\delta_c^{e,m}$  and  $\delta_c$  extrapolated to  $l = 0$ . It is necessary to verify whether the same key results are also obtained for DENT specimens of the present test material, and with both DENT and SENT specimens of other test materials. Such studies should preferably be carried out with increased number of specimens in the initial mixed stress regime, so that the adequacy of linear

relations for these extrapolations (used in deriving the results in Figures 6.13(a)-(b)) may be examined.

3. In the present study, the specimen geometry independence could not be established for  $\delta_c^e$  determined using fatigue pre-cracked specimens. This mismatch has been tentatively ascribed to the difference in the effects of crack growth in the mixed stress regime for these two specimen geometries (Section 6.3.3.1; Eq. (6.5)). This tentative conclusion, however, should be verified. A 3-D FE simulation of crack initiation and growth covering the initial mixed stress regime could possibly clarify this point.
4. The main hindrance to using  $R$  and in particular  $R_\infty$  for characterizing crack growth is: it is a specimen geometry dependent parameter. The preliminary attempts at normalizing  $R_\infty$  in this research was only partially successful in eliminating this specimen geometry dependence of  $R_\infty$ , Table 8.2. Further research, with different sheet materials and thicknesses, is required in this direction.
5. The results from the initial explorations in the potential of CZM simulations of crack growth in the present test material (Chapter 5) are sufficiently encouraging for more thorough investigations with this method, particularly for the more difficult case of simulating crack growth in a sheet material showing predominantly slant fracture.
6. Apart from the testing variables like ramp rate a notch tip radius considered in this thesis, it is important to consider also the effects of pre-strain and specimen orientation (L-T versus T-L) on the various crack initiation and growth parameters.



## References

- [1] O. Chabanet, D. Steglich, J. Besson, V. Heitmann, D. Hellmann, and W. Brocks, "Predicting crack growth resistance of aluminium sheets," *Computational Materials Science*, vol. 26, pp. 1-12, 2003.
- [2] T. Pardoen, Y. Marchal, and F. Delannay, "Thickness dependence of cracking resistance in thin aluminium plates," *Journal of the Mechanics and Physics of Solids*, vol. 47, pp. 2093-2123, 1999.
- [3] D. Gutierrez, L. Pérez Caro, A. Lara, D. Casellas Padró, and J. M. Prado Pozuelo, "Evaluation of essential work of fracture in a dual phase high strength steel sheet," *Revista de Metalurgia*, vol. 49, pp. 45-54, 2013.
- [4] K.-H. Schwalbe, J. C. Newman, and J. L. Shannon, "Fracture mechanics testing on specimens with low constraint – standardisation activities within ISO and ASTM," *Engineering Fracture Mechanics*, vol. 72, pp. 557-576, 2005.
- [5] K. Schwalbe, B. Neale, and J. Heerens, "The GKSS test procedure for determining the fracture behaviour of materials," *EFAM GTP*, vol. 94, 1994.
- [6] G. Lin, Y.-J. Kim, A. Cornec, and K.-H. Schwalbe, "Fracture toughness of a constrained metal layer," *Computational Materials Science*, vol. 9, pp. 36-47, 1997.
- [7] W. C. ASTM International, "ASTM E1820-17a, *Standard Test Method for Measurement of Fracture Toughness*," 2017.
- [8] J. Sumpter and C. Turner, "Method for laboratory determination of  $J_c$ ," in *Cracks and fracture*, edition: ASTM International, 1976.
- [9] T. L. Anderson, *Fracture mechanics: fundamentals and applications*: CRC press, 2017.
- [10] B. Cotterell, T. Pardoen, and A. Atkins, "Measuring toughness and the cohesive stress–displacement relationship by the essential work of fracture concept," *Engineering Fracture Mechanics*, vol. 72, pp. 827-848, 2005.
- [11] J. Newman, M. James, and U. Zerbst, "A review of the CTOA/CTOD fracture criterion," *Engineering Fracture Mechanics*, vol. 70, pp. 371-385, 2003.
- [12] F. Hachez, "Experimental and numerical investigation of the thickness effect in the ductile tearing of thin metallic plates," *PhD thesis, Université Catholique de Louvain*, 2008.
- [13] T. Pardoen, F. Hachez, B. Marchioni, P. Blyth, and A. Atkins, "Mode I fracture of sheet metal," *Journal of the Mechanics and Physics of Solids*, vol. 52, pp. 423-452, 2004.

- [14] X.-K. Zhu and J. A. Joyce, "Review of fracture toughness (G, K, J, CTOD, CTOA) testing and standardization," *Engineering Fracture Mechanics*, vol. 85, pp. 1-46, 2012.
- [15] Y.-W. Mai and B. Cotterell, "On the essential work of ductile fracture in polymers," *International journal of fracture*, vol. 32, pp. 105-125, 1986.
- [16] Y. Marchal and F. Delannay, "Influence of test parameters on the measurement of the essential work of fracture of zinc sheets," *International journal of fracture*, vol. 80, pp. 295-310, 1996.
- [17] T. Pardoen, Y. Marchal, and F. Delannay, "Essential work of fracture compared to fracture mechanics — towards a thickness independent plane stress toughness," *Engineering Fracture Mechanics*, vol. 69, pp. 617-631, 2002.
- [18] M. Faccoli, G. Cornacchia, M. Gelfi, A. Panvini, and R. Roberti, "Notch ductility of steels for automotive components," *Engineering Fracture Mechanics*, vol. 127, pp. 181-193, 2014.
- [19] M. Torrentallé Dot, "High strength steel fracture: fracture initiation analysis by the essential work of fracture concept," *M.Tech thesis, Universitat Politècnica de Catalunya*, 2015.
- [20] M. James and J. Newman, "The effect of crack tunneling on crack growth: experiments and CTOA analyses," *Engineering Fracture Mechanics*, vol. 70, pp. 457-468, 2003.
- [21] M. T. Kirk and R. H. Dodds, "J and CTOD estimation equations for shallow cracks in single edge notch bend specimens," *Journal of Testing and Evaluation*, vol. 21, pp. 228-238, 1993.
- [22] J. Heerens and M. Schödel, "Characterization of stable crack extension in aluminium sheet material using the crack tip opening angle determined optically and by the  $\delta_5$  clip gauge technique," *Engineering Fracture Mechanics*, vol. 76, pp. 101-113, 2009.
- [23] P. P. Darcis, C. N. McCowan, H. Windhoff, J. D. McColskey, and T. A. Siewert, "Crack tip opening angle optical measurement methods in five pipeline steels," *Engineering Fracture Mechanics*, vol. 75, pp. 2453-2468, 2008.
- [24] R. Reuven, C. McCowan, E. Drexler, A. Shtechman, P. Darcis, M. Treinen, R. Smith, J. Merritt, T. Siewert, and J. D. McColskey, "CTOA results for X65 and X100 pipeline steels: Influence of displacement rate," in *7th International Pipeline Conference*, pp. 279-286, 2008.

- [25] S. Xu, W. Tyson, R. Eagleson, C. McCowan, E. Drexler, J. McColskey, and P. P. Darcis, "Measurement of CTOA of pipe steels using MDCB and DWTT specimens," in *8th International Pipeline Conference*, pp. 269-278, 2010.
- [26] S. Hashemi, R. Gay, I. Howard, J. Yates, and R. Andrews, "Experimental determination of CTOA toughness," *J Pipeline Eng*, vol. 12, pp. 2-7, 2013.
- [27] D. J. Horsley, "Background to the use of CTOA for prediction of dynamic ductile fracture arrest in pipelines," *Engineering Fracture Mechanics*, vol. 70, pp. 547-552, 2003.
- [28] L. Pussegoda, S. Verbit, A. Dinovitzer, W. Tyson, A. Glover, L. Collins, L. Carlson, and J. Beattie, "Review of CTOA as a measure of ductile fracture toughness," in *3rd International Pipeline Conference*, pp. V001T02A021-V001T02A021, 2000.
- [29] B. Seshadri, J. Newman Jr, and D. Dawicke, "Residual strength analyses of stiffened and unstiffened panels—Part II: wide panels," *Engineering Fracture Mechanics*, vol. 70, pp. 509-524, 2003.
- [30] W. Xu, H. Wang, X. Wu, X. Zhang, G. Bai, and X. Huang, "A novel method for residual strength prediction for sheets with multiple site damage: Methodology and experimental validation," *International Journal of Solids and Structures*, vol. 51, pp. 551-565, 2014.
- [31] B. Wang and K.-C. Hwang, "Structural integrity assessment in elastic-plastic fracture," *Engineering Fracture Mechanics*, vol. 54, pp. 471-478, 1996.
- [32] W. Brocks, K. H. Schwalbe, and U. Zerbst, "Structural Integrity Assessment of Thin-Walled Structures," *Advanced Engineering Materials*, vol. 8, pp. 319-327, 2006.
- [33] W. C. ASTM International, "ASTM E2472," *Standard Test Method for Determination of Resistance to Stable Crack Extension under Low-Constraint Conditions*, , PA, 2012,.
- [34] I. Scheider, M. Schödel, W. Brocks, and W. Schönfeld, "Crack propagation analyses with CTOA and cohesive model: Comparison and experimental validation," *Engineering Fracture Mechanics*, vol. 73, pp. 252-263, 2006.
- [35] Y. Kayamori, S. Hillmansen, P. Crofton, and R. A. Smith, "Ductile crack propagation characteristics in steel thin single edge notched tension specimens," in *Materials science forum*, 2007, pp. 2180-2185.
- [36] J. Sumpter, "The energy dissipation rate approach to tearing instability," *Engineering Fracture Mechanics*, vol. 71, pp. 17-37, 2004.

- [37] C. Turner and O. Kolednie, "A micro and macro approach to the energy dissipation rate model of stable ductile crack growth," *Fatigue & Fracture of Engineering Materials & Structures*, vol. 17, pp. 1089-1107, 1994.
- [38] P. Anuschewski, W. Brocks, and D. Hellmann, "Characterisation of Ductile Tearing Resistance by the Energy Dissipation Rate: Effects of Material, Specimen Shape and Size", *GKSS-Forschungszentrum*, 2002.
- [39] B. Cotterell and J. Reddel, "The essential work of plane stress ductile fracture," *International journal of fracture*, vol. 13, pp. 267-277, 1977.
- [40] J. Williams and M. Rink, "The standardisation of the EWF test," *Engineering Fracture Mechanics*, vol. 74, pp. 1009-1017, 2007.
- [41] S. Sahoo, N. Padmapriya, P. S. De, P. Chakraborti, and S. Ray, "Ductile Tearing Resistance Indexing of Automotive Grade DP 590 Steel Sheets: EWF Testing Using DENT Specimens," *Journal of Materials Engineering and Performance*, vol. 27, 2018.
- [42] R. Sarkar, "Characterizing ductile tearing resistance using CTOA estimate from essential work of fracture (EWF) tests," *M.Tech thesis*, Jadavpur University, 2016.
- [43] T. Bárány, T. Czigány, and J. Karger-Kocsis, "Application of the essential work of fracture (EWF) concept for polymers, related blends and composites: A review," *Progress in Polymer Science*, vol. 35, pp. 1257-1287, 2010.
- [44] J. Wu and Y. W. Mai, "The essential fracture work concept for toughness measurement of ductile polymers," *Polymer Engineering & Science*, vol. 36, pp. 2275-2288, 1996.
- [45] Y. Mai and B. Cotterell, "Effect of specimen geometry on the essential work of plane stress ductile fracture," *Engineering Fracture Mechanics*, vol. 21, pp. 123-128, 1985.
- [46] F. Hachez, A. G. Atkins, R. H. Dodds, and T. Pardoen, "Modelling of Ductile Tearing in Thin Plates," in *ECF15*.
- [47] X. Chen, "Plastic tearing energy in tough steels," PhD thesis, University of Maryland, 2005.
- [48] Z. Zheng, "Development, Application and Perspective of high strength steel sheets for automobiles," *Iron and Steel*, vol. 11, 2000.
- [49] J. Rice, "Fracture, vol. 2," edition: Academic Press New York, 1968.
- [50] J. Sumpter, "Size effects in tearing instability: An analysis based on energy dissipation rate," *Engineering Fracture Mechanics*, vol. 74, pp. 2352-2374, 2007.



- [51] S. Cravero and C. Ruggieri, "Estimation procedure of J-resistance curves for SE (T) fracture specimens using unloading compliance," *Engineering Fracture Mechanics*, vol. 74, pp. 2735-2757, 2007.
- [52] G. Shen, J. A. Gianetto, and W. R. Tyson, "Measurement of  $J_R$  curves using single-specimen technique on clamped SE (T) specimens," in *The Nineteenth International Offshore and Polar Engineering Conference*, 2009.
- [53] M. F. Kanninen, "Advanced fracture mechanics", *Oxford University Press*, 1985.
- [54] S. Cravero and C. Ruggieri, "Development of plastic eta factors for deep and shallow cracked bend specimens employed in JR curve testing," in *18th International Congress of Mechanical Engineering, Ouro Preto-MG. Proceedings of the COBEM*, 2005.
- [55] G. Shen, J. Gianetto, and W. Tyson, "Development of procedure for low-constraint toughness testing using a single-specimen technique," *CANMET Materials Technology Laboratory, Technical Report*, 2008.
- [56] L. L. Mathias, D. F. Sarzosa, and C. Ruggieri, "Effects of specimen geometry and loading mode on crack growth resistance curves of a high-strength pipeline girth weld," *International Journal of Pressure Vessels and Piping*, vol. 111, pp. 106-119, 2013.
- [57] G. Ramorino, S. Agnelli, R. De Santis, and T. Riccò, "Investigation of fracture resistance of natural rubber/clay nanocomposites by J-testing," *Engineering Fracture Mechanics*, vol. 77, pp. 1527-1536, 2010.
- [58] H. S. Carvalho and C. Ruggieri, "Significance of the plastic eta factor in J estimation procedures for tensile SE (T) fracture specimens," in *ASME Pressure Vessels and Piping Division/K-PVP Conference*, pp. 991-1000, 2010.
- [59] Y. Huang and W. Zhou, "Investigation of plastic eta factors for clamped SE (T) specimens based on three-dimensional finite element analyses," *Engineering Fracture Mechanics*, vol. 132, pp. 120-135, 2014.
- [60] E. Wang, W. De Waele, and S. Hertelé, "A complementary  $\eta_{pl}$  approach in J and CTOD estimations for clamped SENT specimens," *Engineering Fracture Mechanics*, vol. 147, pp. 36-54, 2015.
- [61] O. Kolednik and P. Kutlesa, "On the influence of specimen geometry on the critical crack-tip-opening displacement," *Engineering Fracture Mechanics*, vol. 33, pp. 215-223, 1989.
- [62] H. Pisarski, "Influence of thickness on critical crack opening displacement (COD) and J values," *International journal of fracture*, vol. 17, pp. 427-440, 1981.

- [63] B. E. Amstutz, M. A. Sutton, D. S. Dawicke, and J. C. Newman, "An experimental study of CTOD for mode I/mode II stable crack growth in thin 2024-T3 aluminum specimens," in *Fracture Mechanics: 26th Volume*, edition: ASTM International, 1995.
- [64] D. Dawicke, M. Sutton, J. Newman, and C. Bigelow, "Measurement and analysis of critical CTOA for an aluminum alloy sheet," in *Fracture Mechanics: 25th Volume*, edition: ASTM International, 1995.
- [65] C. Turner and O. Kolednik, "Application of energy dissipation rate arguments to stable crack growth," *Fatigue & Fracture of Engineering Materials & Structures*, vol. 17, pp. 1109-1127, 1994.
- [66] C. Turner, "A re-assessment of ductile tearing resistance (Part 1 and II), Fracture Behaviour and Design of Materials and Structures (Ed. F. Irrao, D.) Vol. 11," *Proc. ECF8*, pp. 933-949, 1990.
- [67] C. Turner and O. Kolednik, "A simple test method for energy dissipation rate, CTOA and the study of size and transferability effects for large amounts of ductile crack growth," *Fatigue & Fracture of Engineering Materials & Structures*, vol. 20, pp. 1507-1528, 1997.
- [68] O. Kolednik, G. Shan, and D. F. Fischer, "The energy dissipation rate — a new tool to interpret geometry and size effects," in *Fatigue and Fracture Mechanics: 27th Volume*, edition: ASTM International, 1997.
- [69] D. Memhard, W. Brocks, and S. Fricke, "Characterization of ductile tearing resistance by energy dissipation rate," *Fatigue & Fracture of Engineering Materials & Structures*, vol. 16, pp. 1109-1124, 1993.
- [70] J. Stampfl and O. Kolednik, "The separation of the fracture energy in metallic materials," *International journal of fracture*, vol. 101, pp. 321-345, 2000.
- [71] W. Brocks, D. Klingbeil, G. Künecke, and D. Sun, "Application of the Gurson model to ductile tearing resistance," in *Constraint Effects in Fracture Theory and Applications: Second Volume*, edition: ASTM International, 1995.
- [72] A. Needleman and V. Tvergaard, "An analysis of ductile rupture in notched bars," *Journal of the Mechanics and Physics of Solids*, vol. 32, pp. 461-490, 1984.
- [73] A. L. Gurson, "Continuum theory of ductile rupture by void nucleation and growth: Part I — Yield criteria and flow rules for porous ductile media," *Journal of engineering materials and technology*, vol. 99, pp. 2-15, 1977.
- [74] T. Siegmund and W. Brocks, "A numerical study on the correlation between the work of separation and the dissipation rate in ductile fracture," *Engineering Fracture Mechanics*, vol. 67, pp. 139-154, 2000.

- [75] A. Arkhireyeva and S. Hashemi, "Fracture behaviour of polyethylene naphthalate (PEN)," *Polymer*, vol. 43, pp. 289-300, 2002.
- [76] W. Brocks, P. Anuschewski, and I. Scheider, "Ductile tearing resistance of metal sheets," *Engineering Failure Analysis*, vol. 17, pp. 607-616, 2010.
- [77] W. Brocks and T. Siegmund, "Effects of geometry and material on the energy dissipation rate," *Fracture Mechanics: Application and Challenges, Proc. ECF*, vol. 13, pp. 6-9, 2000.
- [78] D. Dawicke and M. Sutton, "CTOA and crack-tunneling measurements in thin sheet 2024-T3 aluminum alloy," *Experimental Mechanics*, vol. 34, pp. 357-368, 1994.
- [79] J. Heerens and M. Schödel, "On the determination of crack tip opening angle, CTOA, using light microscopy and  $\delta_5$  measurement technique," *Engineering Fracture Mechanics*, vol. 70, pp. 417-426, 2003.
- [80] A. Martinelli and S. Venzi, "Tearing modulus, J-integral, CTOA and crack profile shape obtained from the load-displacement curve only," *Engineering Fracture Mechanics*, vol. 53, pp. 263-277, 1996.
- [81] D. Dawicke, J. Newman, and C. Bigelow, "Three-dimensional CTOA and constraint effects during stable tearing in a thin-sheet material," in *Fracture Mechanics: 26th Volume*, edition: ASTM International, 1995.
- [82] K. Čolić, M. Burzić, N. Gubeljak, S. Petronić, and F. Vučetić, "Digital image correlation method in experimental analysis of fracture mechanics parameters," *Scientific Technical Review*, vol. 67, pp. 47-53, 2017.
- [83] W. R. Lloyd, "Microtopography for ductile fracture process characterization: Part 1: Theory and methodology," *Engineering Fracture Mechanics*, vol. 70, pp. 387-401, 2003.
- [84] W. R. Lloyd and F. McClintock, "Microtopography for ductile fracture process characterization Part 2: Application for CTOA analysis," *Engineering Fracture Mechanics*, vol. 70, pp. 403-415, 2003.
- [85] A. Gullerud, R. Dodds, R. Hampton, and D. Dawicke, "Three-dimensional modeling of ductile crack growth in thin sheet metals: computational aspects and validation," *Engineering Fracture Mechanics*, vol. 63, pp. 347-374, 1999.
- [86] I. Scheider, A. Cornec, and K.-H. Schwalbe, "SIAM CM 09 - The SIAM method for applying cohesive models to the damage behaviour of engineering materials and structures," *GKSS-Forschungszentrum Geesthacht GmbH (Germany)*, 2009.

- [87] J. Heerens and M. Schoedel, "Characterization of stable crack extension in aluminium sheet material using the crack tip opening angle determined optically and by the  $\delta_5$  clip gauge technique," *Engineering Fracture Mechanics*, vol. 76, pp. 101-113, 2009.
- [88] K.-H. Schwalbe, "Introduction of  $\delta_5$  as an operational definition of the CTOD and its practical use," in *Fracture Mechanics: 26th Volume*, edition: ASTM International, 1995.
- [89] S. Koley, S. Chatterjee, and M. Shome, "Evaluation of fracture toughness of thin sheet of interstitial free high strength steel through critical crack tip opening angle (CTOA<sub>c</sub>) measurement," *International journal of fracture*, vol. 194, pp. 187-195, 2015.
- [90] Y. Mai and B. Cotterell, "Effects of pre-strain on plane stress ductile fracture in  $\alpha$ -brass," *Journal of materials science*, vol. 15, pp. 2296-2306, 1980.
- [91] B. Chéhab, Y. Bréchet, J. C. Glez, P. J. Jacques, J. D. Mithieux, M. Véron, and T. Pardoen, "Characterization of the high temperature tearing resistance using the essential work of fracture — Application to dual phase ferritic stainless steels," *Scripta Materialia*, vol. 55, pp. 999-1002, 2006.
- [92] R. Sarkar, S. K. Chandra, P. S. De, P. Chakraborti, and S. Ray, "Evaluation of ductile tearing resistance of dual-phase DP 780 grade automotive steel sheet from Essential Work of Fracture (EWF) tests," *Theoretical and Applied Fracture Mechanics*, p. 102278, 2019.
- [93] K. B. Broberg, "Crack-growth criteria and non-linear fracture mechanics," *Journal of the Mechanics and Physics of Solids*, vol. 19, pp. 407-418, 1971.
- [94] M. Rink, L. Andena, and C. Marano, "The essential work of fracture in relation to J-integral," *Engineering Fracture Mechanics*, vol. 127, pp. 46-55, 2014.
- [95] D. Ferrer-Balas, M. L. Maspocho, A. Martinez, and O. Santana, "On the essential work of fracture method: Energy partitioning of the fracture process in iPP films," *Polymer Bulletin*, vol. 42, pp. 101-108, 1999.
- [96] S. Hashemi and D. O'Brien, "The essential work of plane-stress ductile fracture of poly (ether-ether ketone) thermoplastic," *Journal of materials science*, vol. 28, pp. 3977-3982, 1993.
- [97] A. Martinez, J. Gamez-Perez, M. Sanchez-Soto, J. I. Velasco, O. Santana, and M. L. Maspocho, "The essential work of fracture (EWF) method—analyzing the post-yielding fracture mechanics of polymers," *Engineering failure analysis*, vol. 16, pp. 2604-2617, 2009.
- [98] Y. Marchal, J.-F. Walhin, and F. Delannay, "Statistical procedure for improving the precision of the measurement of the essential work of fracture of thin sheets," *International journal of fracture*, vol. 87, pp. 189-199, 1997.

- [99] F. Tuba, L. Oláh, and P. Nagy, "On the valid ligament range of specimens for the essential work of fracture method: The inconsequence of stress criteria," *Engineering Fracture Mechanics*, vol. 99, pp. 349-355, 2013.
- [100] A. Pegoretti, L. Castellani, L. Franchini, P. Mariani, and A. Penati, "On the essential work of fracture of linear low-density-polyethylene. I. Precision of the testing method," *Engineering Fracture Mechanics*, vol. 76, pp. 2788-2798, 2009.
- [101] R. Hill, "On discontinuous plastic states, with special reference to localized necking in thin sheets," *Journal of the Mechanics and Physics of Solids*, vol. 1, pp. 19-30, 1952.
- [102] S. Hashemi, "Determination of the fracture toughness of polybutylene terephthalate (PBT) film by the essential work method: Effect of specimen size and geometry," *Polymer Engineering & Science*, vol. 40, pp. 798-808, 2000.
- [103] E. Clutton, "ESIS TC4 experience with the essential work of fracture method," in *European Structural Integrity Society*. vol. 27, edition: Elsevier, pp. 187-199, 2000.
- [104] A. Saleemi and J. Nairn, "The plane-strain essential work of fracture as a measure of the fracture toughness of ductile polymers," *Polymer Engineering & Science*, vol. 30, pp. 211-218, 1990.
- [105] J. Karger-Kocsis and D. Ferrer-Balas, "On the plane-strain essential work of fracture of polymer sheets," *Polymer Bulletin*, vol. 46, pp. 507-512, 2001.
- [106] S. Hashemi, "Work of fracture of PBT/PC blend: effect of specimen size, geometry, and rate of testing," *Polymer Engineering & Science*, vol. 37, pp. 912-921, 1997.
- [107] L. Xia and C. F. Shih, "Ductile crack growth - I. A numerical study using computational cells with microstructurally-based length scales," *Journal of the Mechanics and Physics of Solids*, vol. 43, pp. 233-259, 1995.
- [108] C. Ruggieri, T. L. Panontin, and R. Dodds, "Numerical modeling of ductile crack growth in 3-D using computational cell elements," *International journal of fracture*, vol. 82, pp. 67-95, 1996.
- [109] S. Wang, Z. Chen, and C. Dong, "Tearing failure of ultra-thin sheet-metal involving size effect in blanking process: Analysis based on modified GTN model," *International Journal of Mechanical Sciences*, vol. 133, pp. 288-302, 2017.
- [110] T. Henseler, S. Osovski, M. Ullmann, R. Kawalla, and U. Prahl, "GTN Model-Based Material Parameters of AZ31 Magnesium Sheet at Various Temperatures by Means of SEM In-Situ Testing," *Crystals*, vol. 10, p. 856, 2020.

- [111] B. Teng, W. Wang, and Y. Xu, "Ductile fracture prediction in aluminium alloy 5A06 sheet forming based on GTN damage model," *Engineering Fracture Mechanics*, vol. 186, pp. 242-254, 2017.
- [112] I. Scheider, "Derivation of separation laws for cohesive models in the course of ductile fracture," *Engineering Fracture Mechanics*, vol. 76, pp. 1450-1459, 2009.
- [113] U. Zerbst, M. Heinemann, C. Dalle Donne, and D. Steglich, "Fracture and damage mechanics modelling of thin-walled structures – An overview," *Engineering Fracture Mechanics*, vol. 76, pp. 5-43, 2009.
- [114] A. Needleman, "A continuum model for void nucleation by inclusion debonding," *Journal of applied mechanics*, vol. 54, pp. 525-531, 1987.
- [115] A. Needleman, "An analysis of tensile decohesion along an interface," *Journal of the Mechanics and Physics of Solids*, vol. 38, pp. 289-324, 1990.
- [116] V. Tvergaard and J. W. Hutchinson, "The relation between crack growth resistance and fracture process parameters in elastic-plastic solids," *Journal of the Mechanics and Physics of Solids*, vol. 40, pp. 1377-1397, 1992.
- [117] A. Cornec, I. Scheider, and K.-H. Schwalbe, "On the practical application of the cohesive model," *Engineering Fracture Mechanics*, vol. 70, pp. 1963-1987, 2003.
- [118] K. Park and G. H. Paulino, "Computational implementation of the PPR potential-based cohesive model in ABAQUS: educational perspective," *Engineering Fracture Mechanics*, vol. 93, pp. 239-262, 2012.
- [119] K. Park, H. Choi, and G. H. Paulino, "Assessment of cohesive traction-separation relationships in ABAQUS: A comparative study," *Mechanics Research Communications*, vol. 78, pp. 71-78, 2016.
- [120] K. Park, "Potential-based fracture mechanics using cohesive zone and virtual internal bond modeling," *University of Illinois*, vol. P.hD thesis, 2009.
- [121] G. H. Paulino, K. Park, and J.R. Roesler, "Concrete fracture predictions using the virtual internal bond model with a modified Morse functional potential," *Multiscale & Functionally Graded Materials Conference 2006, American Institute of Physics, Oahu Island, Hawaii, 724–729.*, 2008.
- [122] K. Park, G. H. Paulino, and J. R. Roesler, "A unified potential-based cohesive model of mixed-mode fracture," *Journal of the Mechanics and Physics of Solids*, vol. 57, pp. 891-908, 2009.
- [123] G. L. M. Alfano, F. Furgiuele, and G. H. Paulino, "On the enhancement of bond toughness for Al/epoxy T-peel joints with laser treated substrates," *International journal of fracture*, vol. 171, pp. 139-150, 2011.

- [124] P. C. L. Gutierrez D, Lara A, Casellas Padró D, Prado Pozuelo JM, "Evaluation of essential work of fracture in a dual phase high strength steel sheet," *Revista de Metalurgia*, vol. 49, pp. 45-54, 2013.
- [125] P. T. Lacroix G, Jacques PJ, "The fracture toughness of TRIP-assisted multiphase steels," *Acta Materialia*, vol. 56, 2013.
- [126] S. P. D. Frómeta, A. Lara, S. Molas, D. Casellas, P. Jonsén, J. Calvo, "Identification of fracture toughness parameters to understand the fracture resistance of advanced high strength sheet steels," *Engineering Fracture Mechanics*, vol. 229, 2020.
- [127] V. M. Martin G, Brechet Y, Chehab B, Fourmentin R, Mithieux J-D "Characterization of the hot cracking resistance using the Essential Work of Fracture (EWF): application to duplex stainless steels," *Rem Rev Esc Minas*, vol. 66, pp. 145-151, 2013.
- [128] E. C. Ching, R. K. Li, and Y. W. Mai, "Effects of gauge length and strain rate on fracture toughness of polyethylene terephthalate glycol (PETG) film using the essential work of fracture analysis," *Polymer Engineering & Science*, vol. 40, pp. 310-319, 2000.
- [129] F. M. Peres, J. R. Tarpani, and C. G. Schön, "Essential work of fracture testing method applied to medium density polyethylene," *Procedia Materials Science*, vol. 3, pp. 756-763, 2014.
- [130] E. C. Ching, W. K. Poon, R. K. Li, and Y. W. Mai, "Effect of strain rate on the fracture toughness of some ductile polymers using the essential work of fracture (EWF) approach," *Polymer Engineering & Science*, vol. 40, pp. 2558-2568, 2000.
- [131] D. R. Moore, J. Williams, and A. Pavan, "Fracture mechanics testing methods for polymers, adhesives and composites", vol. 28: *Elsevier*, 2001.
- [132] J. Begley and J. Landes, "The J integral as a fracture criterion," in *Fracture Toughness: Part II*, edition: ASTM International, 1972.
- [133] C. Turner, "The ubiquitous  $\eta$  factor," in *Fracture Mechanics*, edition: ASTM International, 1980.
- [134] P. C. Paris, H. Ernst, and C. Turner, "A J-integral approach to development of  $\eta$ -factors," in *Fracture Mechanics*, edition: ASTM International, 1980.
- [135] P. P. Ernst HA, Rossow M, Hutchinson JW, "Analysis of load–displacement relationships to determine  $J_R$  curve and tearing instability material properties," In: *Fracture mechanics. ASTM STP 677. American Society for Testing and Materials*, pp. . p. 581–99., 1979.
- [136] M. Sharobeam and J. Landes, "The load separation criterion and methodology in ductile fracture mechanics," *International journal of fracture*, vol. 47, pp. 81-104, 1991.

- [137] "Abaqus 6.10: Analysis user's manual," *Providence, RI: Dassault Systèmes Simulia Corp*, 2010.
- [138] J. Karger-Kocsis, T. Czigány, and E. J. Moskala, "Deformation rate dependence of the essential and non-essential work of fracture parameters in an amorphous copolyester," *Polymer*, vol. 39, pp. 3939-3944, 1998.
- [139] W. Brocks, P. Anuschewski, and D. Hellmann, "A concept for scaling  $J_R$ -curves by plastic constraint factors," *International journal of fracture*, vol. 130, pp. 455-469, 2004.
- [140] W. B. D. Memhard, and S. Fricke, "Characterization of ductile tearing resistance by energy dissipation rate," *ECF-10, structural integrity: experiments, models and applications*, 1996.